The Pennsylvania State University

The Graduate School

TRANSPORT PHENOMENA BASED MODELING OF COMMON DEFECT FORMATION IN METAL PRINTING

A Dissertation in

Materials Science and Engineering

by

Tuhin Mukherjee

Submitted in Partial Fulfillment

of the Requirements

for the Degree of

Doctor of Philosophy

December 2019

The dissertation of Tuhin Mukherjee was reviewed and approved* by the following:

Tarasankar DebRoy
Professor of Materials Science and Engineering
Dissertation Advisor
Chair of Committee

Todd A. Palmer
Professor of Engineering Science and Mechanics and Materials Science and Engineering

Zi-Kui Liu
Distinguished Professor of Materials Science and Engineering

Timothy W. Simpson
Professor of Mechanical and Nuclear Engineering and Industrial and Manufacturing Engineering

John Mauro
Professor of Materials Science and Engineering
Chair of Graduate Program

*Signatures are on file in the Graduate School

ABSTRACT

Additive manufacturing (AM) or 3D printing of metals allows one step, near net shape fabrication of complex and intricate components that cannot be easily and economically produced by other means. Stainless steels, aluminum, titanium and nickel alloys are commonly printed using mainly directed energy deposition (DED) and powder bed fusion (PBF) techniques. However, printed metallic components often suffer from defects such as residual stresses, distortion, composition change due to selective vaporization of alloying elements and lack of fusion voids. These defects largely degrade the mechanical properties of the parts and in extreme cases lead to part rejection. For example, high residual stresses may result in warping, buckling and delamination of the parts and are detrimental to fatigue properties. Changes in composition can affect microstructure, corrosion resistance and mechanical properties of the components. Lack of fusion defects are known to adversely affect the tensile properties of the printed parts. Formation of these defects is affected by the transport of heat, mass and momentum, which include heat absorption by the feedstock material, formation of molten pool, convective flow of liquid metal inside the pool and cooling down by exchanging heat with the surroundings by convection and radiation. Therefore, fabrication of defect free and reliable AM parts requires a better understanding of the effects of heat, mass and momentum transfer on the formation of defects.

The AM process involves rapid heating, melting, solidification and cooling of the part. As a result, different regions of the workpiece experience repeated heating and cooling. The spatially varying thermal cycles result in residual stresses and distortion in the AM parts. Key physical factors responsible for the origin of residual stresses and distortion include spatial temperature gradient, expansion and contraction of the part due to repeated thermal cycles and large coefficient of thermal expansion, solidification shrinkage of molten pool and temperature and strain rate dependent constitutive behavior of plastic material.

At very high temperature, alloying elements may vaporize significantly depending on the equilibrium vapor pressure above the molten pool and the total pressure in the depositing chamber. All elements do not vaporize at the same rate because of the difference in vapor pressures of different elements. Such selective vaporization of alloying elements often results in a significant change in the composition of the part from that of the original feedstock. Composition change is affected by vaporization rates of different alloying elements, temperature distribution on the top surface area of the deposit and molten pool volume.

Lack of fusion defects may result due to insufficient overlap between neighboring tracks of deposits and are affected by the shape and size of the fusion zone. Shape and size of fusion zone are often controlled by heat absorption by the feedstock, heat transfer through the substrate and surface energy on the top surface of the molten pool. For example, in wire arc based DED processes, fusion zone geometry is governed by arc pressure and vapor pressure on the top surface of the molten pool, droplet impingement and surface tension. Fusion zone geometry is also often influenced by convective flow of liquid metal primarily driven by the surface tension gradient on the top surface of the molten pool.

The abovementioned variables related to heat, mass and momentum transfers are required to be estimated in order to predict defects. Therefore, in this research, three-dimensional, transient, heat transfer and fluid flow models for both DED and PBF processes were developed and used. These models calculated 3D, transient temperature and velocity fields, fusion zone shape and size, which affect the defect formation. The models solve equations of conservation of mass, momentum and energy in a discretized solution domain consisting of substrate, deposits, feedstock materials and shielding gas. They also consider the effects of liquid metal convection and thus increased the accuracy in temperature field calculations. The computational efficiency for multi-layer, multi-hatch components is enhanced by implementing a novel traveling grid system. The models were rigorously tested using independent experimental data.

Based on the calculated transient temperature field, residual stresses and distortion for multi-track components were predicted using a finite element based thermo-mechanical model. This model was used to calculate residual stresses and distortion for stainless steel 316, Inconel 718 and Ti-6Al-4V components fabricated using DED and PBF processes. It was shown that fabrication of a graded joint using laser DED between 2.25Cr-1Mo steel and alloy 800H significantly reduced the sharp change in residual stresses at the interface of the dissimilar joint between these two alloys. Changes in compositions were calculated using a vaporization model based on the top surface temperature and volume of the molten pool, which were calculated using the heat transfer fluid flow models. Lack of fusion defect was estimated based on the deposit and fusion zone geometries calculated using the heat transfer and fluid flow model. Easy to use lack of fusion index and dimensionless strain parameter were proposed for practical use in shop floors to predict lack of fusion defects and thermal distortion quickly.

Apart from providing a better understanding of the evolution mechanism of defects based on heat transfer, fluid flow and mechanics of materials, printability or the ability to resist the defects for various alloy-AM process combinations are also evaluated. Quantitative scales are proposed to construct, test and validate the printability of stainless steels, nickel and titanium alloys for DED and PBF processes. It was shown that components printed using PBF are more susceptible to composition change and lack of fusion defects compared to those made by DED. However, fabrication of components with very thin layers made the PBF components less vulnerable to residual stresses and distortion.

This thesis research work represents a contribution to the growing quantitative knowledge base in AM of metallic materials. Expansion of this knowledge base is necessary, if not essential, to fabricate defect free, structurally sound and reliable metallic components using AM. For example, printing of new alloys requires creation of printability database based on the knowledgebase for existing alloys employing the method of this research a critical step forward. In addition, future research is needed to find out the hierarchy of the causative variables affecting defect formation where data-driven machine learning approach could be beneficial.

TABLE OF CONTENTS

LIST OF FIGURES

LIST OF TABLES

LIST OF EQUATIONS

ACKNOWLEDGEMENTS

Over the course of five years (2015-2019) at Penn State, I have met many people who have helped to make the undertaking of this magnitude possible. I would first like to express my sincere gratitude and deep appreciation to my advisor, Dr. Tarasankar DebRoy. His guidance of the research effort, professional expertise, demand for excellence and encouragement brought the best from all involved. He gave me many opportunities to advance my research as well as my professional development.

I am grateful to the invaluable contributions of Dr. Todd A. Palmer at Penn State University during my curriculum. In addition, I consider myself fortunate to have had the opportunity to work with Dr. Amitava De of Indian Institute of Technology, Bombay and Dr. Wei Zhang of The Ohio State University. I would also like to acknowledge Drs. Todd A. Palmer, Zi-Kui Liu and Timothy W. Simpson for their valuable advice and suggestions on my work while serving on my thesis committee. I am very appreciative to them for giving their time to review and comment on this thesis.

Many thanks to my colleagues, Dr. Vinaya D. Manvatkar, Dr. Huiliang Wei, Dr. Jared J. Blecher, Dr. James S. Zuback II, Dr. Tong Liu, Dr. Leilei Wang, Dr. Zhongmei Gao, Dr. Barnali Mondal, Ms. Yang Du, Ms. Qianru Wu, Mr. Gerry L. Knapp, Mr. Nithin Reddy, Mr. Wenmin Ou and Mr. Meng Jiang for their outstanding research and great help. They have made my study at Penn State a rewarding and memorable experience.

I am grateful to my parents, brother and relatives for their love and support. I am deeply indebted to all of my friends who supported and encouraged me during my stay in Penn State.

Finally, I would like to acknowledge a grant from the US Department of Energy NEUP with grant number DE-NE0008280. I am also grateful to the American Welding Society Foundation, which provided me with a graduate fellowship to further my education and research at Penn State.

Chapter 1

INTRODUCTION

1.1 General background

In the past few decades, 3D printing of metals, also known as additive manufacturing (AM), has evolved from the rapid fabrication of functional prototypes to the manufacturing of a wide variety of metallic components that cannot be easily and economically produced by other means [1, 2]. Printing of metals and alloys is the fastest growing sector of additive manufacturing today [2]. Metal printing offers unique advantages and is now widely used in aerospace, consumer products, health care, energy, automotive, marine and other industries [3-6] as shown in Figure 1.1. Customized parts and other important components can be produced on-demand, such as patient specific medical implants [2] and a metallic impeller for the safe operation of a nuclear power plant [7]. The viability of using 3D metal printing in diverse industries, the ability to print unique components and the emerging printing processes that overcome deficiencies of current manufacturing processes, all point to the growing adaptation of 3D printing in industry [2].

Starting with a digital model, metals are deposited layer-by-layer to form a 3D component [1]. Stainless steels, aluminum, titanium and nickel alloys are printed using mainly powder bed fusion (PBF) and direct energy deposition (DED) techniques. The feedstock is typically in the form of metal powder or wire which is melted by a laser beam or an electric arc. Depending on the type of heat source the processes are classified as DED with laser (DED-L), with gas metal arc (DED-GMA) and PBF with laser (PBF-L). The AM process involves rapid heating, melting, solidification and cooling of parts [1]. The spatially varying thermal cycles result in residual stresses and distortion in the AM parts. Key physical factors responsible for the origin of residual stresses and distortion include spatial gradient of temperature, expansion and contraction of parts due to repeated thermal cycles and large co-

efficient of thermal expansion, solidification shrinkage of molten pool and temperature and strain rate dependent constitutive behavior of plastic material [1].

At very high temperatures, alloying elements may vaporize significantly depending on their equilibrium vapor pressures above the molten pool and the total pressure in the depositing chamber [1]. All elements do not vaporize at the same rate because of the difference in vapor pressures of elements. Such selective vaporization of alloying elements often results in a significant change in the composition of the part from that of the original feedstock [1].

Lack of fusion defects may result due to insufficient overlap between neighboring tracks of deposits and are affected by the shape and size of the fusion zone [1]. Shape and size of fusion zone are often controlled by heat absorption by the feedstock, heat transfer through the substrate and surface energy distribution on the top surface of the molten pool. These defects significantly degrade the mechanical properties of the components [1].

Although AM parts have advantages over conventionally manufactured parts in many cases, the aforementioned defects often affect the part quality and in extreme cases lead to part rejection. Therefore, mitigation of these defects by providing a better understanding of their formation mechanisms is a challenge to the community.

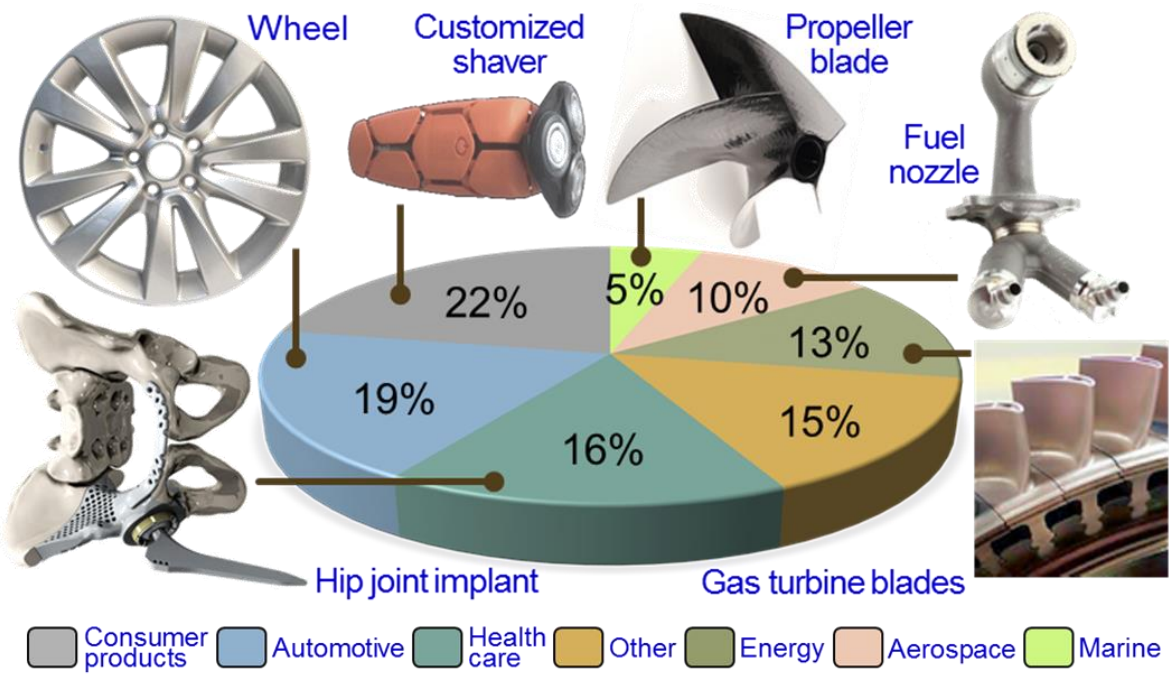

Figure 1.1. Applications of metal printing in various industries [1] and the distribution of revenues [5] from the printed parts among various industries. Adapted from DebRoy et al. [2].

1.2 Research objectives and methodology

Since evolution of defects such as residual stresses, distortion, composition change and lack of fusion depends on heat, mass and momentum transfer during AM, the overall objective of this study is to seek a quantitative understanding of defect formation based on the fundamentals of transport phenomena. To achieve this objective, comprehensive numerical models for DED-GMA, DED-L and PBF-L are developed, tested against independent experimental data and used to calculate transient temperature and velocity fields and fusion zone geometry based on which the macroscopic defect formation is predicted.

The methodology used in the present thesis research is depicted in Figure 1.2. As shown in this figure, three-dimensional, transient heat transfer and fluid flow models for three AM processes considering the AM process parameters and alloy properties are used to calculate the fusion zone geometry and temperature and velocity fields in the molten pool. These models solve equations of conservations of mass, momentum and energy in a solution domain consisting of substrate, deposit, powder bed (in PBF) and shielding gas. The range of process variables for which calculations are performed are adapted from the literature. Calculations are done for commonly used AM alloys such as stainless steel 316, titanium alloy Ti-6Al-4V, nickel based superalloys and aluminum alloy AlSi10Mg.

The 3D, transient temperature field is exported to a finite element based thermo-mechanical model to calculate residual stresses and distortion. The thermo-mechanical model solves constitutive equations where the stresses are calculated from the increment in elastic, plastic and thermal strains. The temperature dependent mechanical properties required for the calculations are either adapted from the literature or calculated thermodynamically. Composition change due to evaporative loss of alloying elements is calculated using a vaporization model. This model first calculates the vaporization flux based on molten pool top surface area, temperature distribution and partial pressures of alloying elements. Then net change in composition is estimated by mass balance. Since lack of fusion defects depend on the extent of overlap between neighboring tracks, it is estimated from the calculated fusion zone geometry. Back of the envelope calculations are performed to deduce two dimensionless numbers to predict the susceptibilities to distortion and lack of fusion defect in real time. These dimensionless numbers consist of AM process parameters, alloy properties, geometry of builds as well as variables computed using the numerical models such as peak temperature and molten pool dimensions.

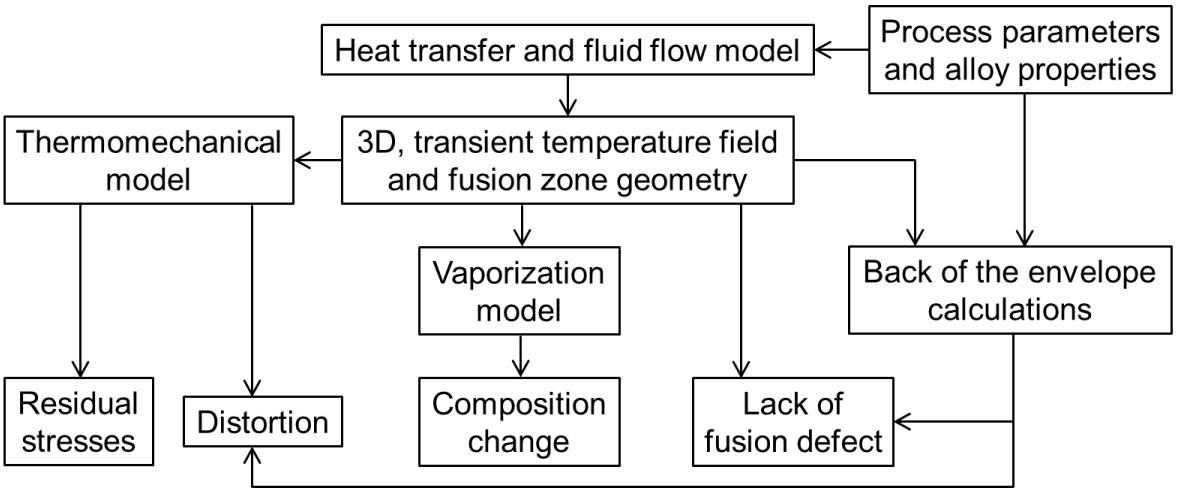

Figure 1.2. Research methodology used in the present thesis study.

1.3 Significance of this research work

Through the synthesis of appropriate concepts of transport phenomena, this doctoral thesis work outlines a completely new direction of exceptional promise to reveal the underlying scientific principles of defect formation during AM. The numerical models developed, tested and used in this thesis work, altogether provide a useful phenomenological framework that can predict defect formation for a wide variety of AM process-alloy combinations. Unlike any other existing models, unique considerations of molten metal convection, vaporization, evaporative loss, curved deposit geometry governed by the energy on the surface of the molten pool and temperature dependent alloy properties make these models accurate and close to the reality. Implementation of a novel, traveling grid system enhances the computational efficiency without sacrificing the calculation accuracy which makes the simulation of multi-layer, multi-hatch components possible in a timely manner. In addition, this thesis work, for the first time, proposes unique dimensionless numbers that can be used to evaluate the propensity of distortion and lack of fusion defects in real time. Furthermore, quantitative scales to evaluate the printability or the ability to resist the macroscopic defects of several alloy-AM process combination are developed. Although the work reported here focuses on DED and PBF using laser and arc heat sources, the method used in this research can be extended for electron beam AM processes in the future.

1.4 Thesis structure

The thesis consists of seven chapters. Chapter 1 describes the subject matter, research objectives, methodology, significance of this work and the thesis contents.

Chapter 2 provides a broad background and literature study on the topics related to this thesis work. The basic working principle of different powder bed fusion (PBF) and directed energy deposition (DED) processes are described. The mechanisms of heat, mass and momentum transport during AM processes are critically reviewed. It includes heat source characteristics, heat absorption mechanisms by the feedstock materials, molten pool formation and convective flow of liquid metal inside the molten pool. Evolution of residual stresses, distortion, composition change and lack of fusion defects are reviewed. Important variables that affect defect formation are also discussed. In addition, the detrimental effects of these defects on structure and mechanical properties of the components are also examined. Different existing transport phenomena based modeling approaches for defect prediction are described. Gaps and current challenges in modeling defect formation are also outlined.

In Chapter 3, the calculations of temperature and velocity fields and deposit geometries using 3D, transient heat transfer and fluid flow models for PBF-L, DED-L and DED-GMA are described. Depending on the different AM processes, modeling of heat sources, implementing boundary conditions, providing alloy properties, defining solution domain are described in detail in this chapter. In addition, this chapter also describes how a novel travelling grid approach is developed and used in this research to enhance the computational efficiency of multi-layer, multi-hatch calculations. Some basic results of temperature and velocity fields and fusion zone geometries are presented with validation against independent experimental data.

In Chapter 4, the calculations of residual stresses and distortion using a finite element based thermomechanical model are described. The results presented in this chapter explain the temporal evolution and spatial non-uniformity in residual stresses and distortion. In addition, based on the modeling results, it was explained how the sharp gradients in residual stresses and strains in the dissimilar alloy joints can be alleviated using a graded joint. Finally, a novel, dimensionless strain parameter was proposed for shop floor usage in order to guide engineers to find suitable conditions to mitigate distortion.

In Chapter 5, the calculations of composition change due to evaporative loss from the molten pool and lack of fusion defect are described. In addition, a novel, dimensionless lack

of fusion number was proposed for shop floor usage in order to guide engineers to find suitable conditions to mitigate lack of fusion defects.

In Chapter 6, printability of different alloys is evaluated for a given AM process using the process conditions. In addition, printability of a particular alloy is evaluated while printing it using three AM processes. The calculations of residual stresses and distortion, composition change and lack of fusion defects are done as described in previous chapters.

The summary and important conclusions of this research are presented in Chapter 7. The suggestions for future work are also documented in this chapter.

1.5 References

1) T. DebRoy et al. Additive manufacturing of metallic components - Process, structure and properties. Prog. Mater. Sci. 92 (2018) 112-224.
2) T. DebRoy et al. Scientific, technological and economic issues in metal printing and their solutions. Nature Mater. (2019) 1.
3) W.E. Frazier. Metal additive manufacturing: a review. J Mater. Eng. Perform. 23 (2014) 1917-1928.
4) T.M. Pollock. Alloy design for aircraft engines. Nature Mater. 15 (2016) 809.
5) A.L. Verhoef et al. The effect of additive manufacturing on global energy demand: An assessment using a bottom-up approach. Energy Policy. 112 (2018) 349-360.
6) T. Duda et al. 3D metal printing technology: the need to re-invent design practice. AI Soc. 33 (2018) 241-252.
7) L.E. Murr. A metallographic review of 3D printing/additive manufacturing of metal and alloy products and components. Metal. Micro. Anal. 7 (2018) 103-132.

Chapter 2

BACKGROUND

The objective of the present thesis research is to provide a better understanding of defect formation mechanism based on transport of heat, mass and momentum during AM processes. In particular, the research work seeks to quantitatively predict residual stresses, distortion, composition change due to evaporative loss of alloying elements and lack of fusion defects from the fundamentals of heat transfer and fluid flow. Since the subject of heat transfer, fluid flow, vaporization and mechanics of materials covers a wide range of topics, it is not possible to review all the aspects in this chapter. Therefore, selected important problems and issues pertinent to the subject of this study are selected to be reviewed here. The intention of this chapter is to briefly review the transport processes during AM and the mechanisms of formation of the macroscopic defects as well as examine some of the existing numerical methods for modeling heat transfer, fluid flow and defect formation during AM of metals and alloys. The following topics are covered in this chapter.

(1) The basic working principle of different powder bed fusion (PBF) and directed energy deposition (DED) processes are described. In this research, PBF with laser source (PBF-L) and DED with laser (DED-L) and gas metal arc (DED-GMA) sources are considered.

(2) The mechanisms of heat, mass and momentum transport during AM processes are critically reviewed. It includes heat source characteristics, heat absorption mechanisms by the feedstock materials, molten pool formation and convective flow of liquid metal inside the molten pool.

(3) Evolution mechanisms of residual stresses, distortion, composition change and lack of fusion defects are reviewed. Important variables related to transport phenomena that affect the defect formations are also identified. In addition, the detrimental effects of these defects on structure and mechanical properties of the components are also discussed.

(4) Different existing transport phenomena based modeling approaches for defect prediction are described. Gaps and current challenges in modeling defect formation are also outlined.

At the end of this chapter, a selection of important unanswered questions in the field of heat transfer, fluid flow, mechanics of materials and defect formation during AM are identified. Seeking answers to these questions is an important goal of the present thesis study, and details of the solution are presented in subsequent chapters.

2.1 Commonly used additive manufacturing (AM) processes for metals

In AM processes feedstock materials such as powder or wire are consolidated into a dense metallic part by melting and solidification with the aid of a heat source such as laser, electron beam or gas metal arc [1]. The AM processes fall into two categories defined by ASTM Standard F2792 [2] as Directed Energy Deposition (DED) and Powder Bed Fusion (PBF). A further distinction is provided as a function of the primary heat source such as laser (L), electron beam (EB), and gas metal arc (GMA) as PBF-L, PBF-EB, DED-L, DED-EB and DED-GMA. Figure 2.1 indicates the commonly used alloys and their various applications in PBF and DED processes. In this research, PBF-L, DED-L and DED-GMA processes are considered. Table 2.1 provides a comparison among these three AM processes [1]. This sub-section provides an introduction to these processes with a particular emphasis on process fundamentals.

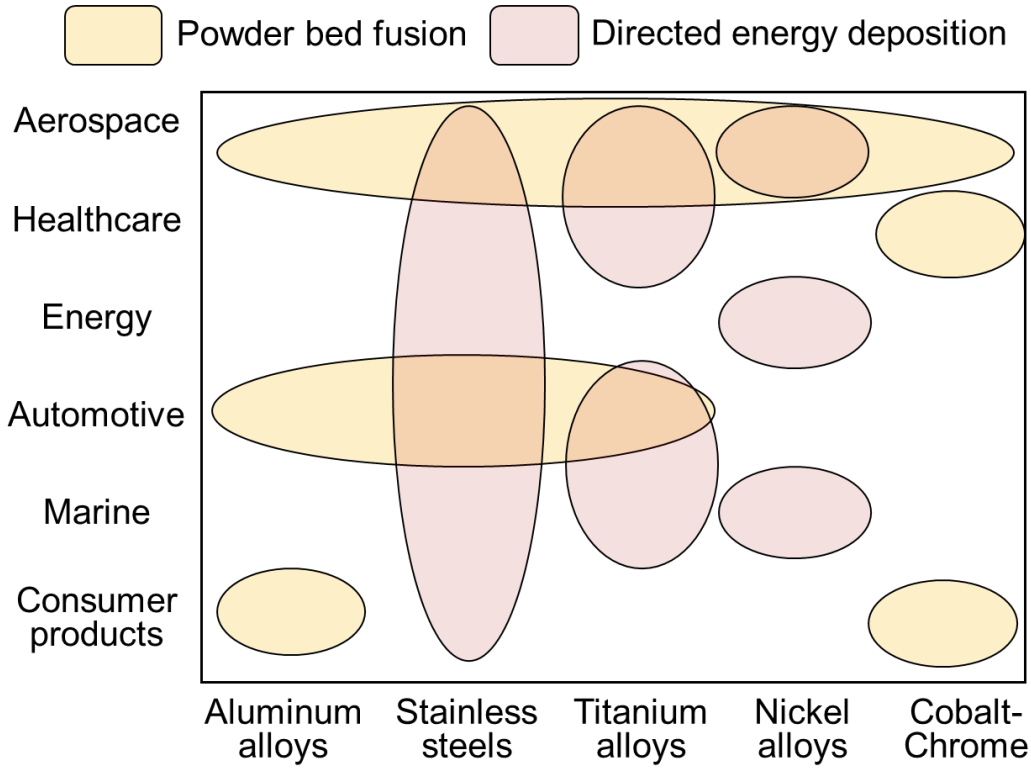

Figure 2.1. Common AM alloys and their applications. Adapted from DebRoy et al. [1]

Table 2.1. Comparison of three different additive manufacturing processes for metallic components: laser assisted powder bed fusion (PBF-L), directed energy deposition with laser (DED-L) and gas metal arc (DED-GMA) sources. Adapted from DebRoy et al. [1]

Process	DED-L	PBF-L	DED-GMA
Feed stock	Powder	Powder	Wire
Power (W)	100 to 3000	50 to 1000	1000-3000
Speed (mm/s)	5 to 20	10 to 100	5-15
Max. feed rate (g/s)	0.1 to 1.0	_	0.2 to 2.8
Max. build size (mm × mm × mm)	2000 × 1500 × 750	500 × 280 × 320	5000 × 3000 × 1000
Production time	High	High	Low
Dimensional accuracy (mm)	0.5 to 1.0	0.04 to 0.2	Intricate features are not possible
Surface roughness (μm)	4 to 10	7 to 20	Needs machining
Post processing	HIP and surface grinding are seldom required	HIP is rarely required to remove the porosities	Machining is essential to produce final parts

2.1.1 Powder bed fusion with laser (PBF-L)

PBF-L begins with a 3D CAD model, orienting it within a build volume and including support structures, slicing into multiple horizontal layers, defining a deposition path and build-file based upon a pre-defined set of parameters and machine configuration [3]. Figure 2.2 (a) schematically represents the working principle of PBF-L process. The part forms by spreading thin layers of powder and fusing layers upon layers of this powder within an inert chamber, incrementally lowering the bed vertically after the deposition of each layer [1]. Fusion occurs by a raster motion of the laser beam using a galvanometer driven mirror, resulting in melting and solidification of overlapping deposit tracks [1]. For PBF-L process, the scanning of the beam for each layer can follow different patterns, also referred to as hatching, such as unidirectional, bidirectional, spiral, zigzag and cross-wise [1].

2.1.2 Directed energy deposition with laser (DED-L)

Figure 2.2 (b) shows a schematic diagram of DED-L with powder used as the feedstock. DED-L typically relies upon the feeding of powder from a nozzle into the depositing track [1]. The powders are melted by the laser beam to form a molten pool. A shielding gas such as argon is used to protect the molten metal from oxidation and to carry the powder stream into the molten pool. The distance between the focused beam and the build surface is maintained by a synchronized multi-axis movement of the workbench that holds the substrate and the heat source during the deposition [3]. The parts with overhanging features may also require appropriate support structure to prevent distortion induced either thermally or under their own weight [1]. The processing conditions such as scanning speed of the heat source and feed rate of the feedstock material are either pre-set or controlled in-process by in-situ sensing and control systems [1]. After the deposition process, the fabricated part is removed from the substrate by machining and often requires further finishing operations to achieve the desired surface quality [4].

2.1.3 Directed energy deposition with gas metal arc (DED-GMA)

DED-GMA is developed from arc welding and suitable for making large components because of high deposition rates, low equipment and feedstock costs [5]. In DED-GMA, an electric arc is used as the heat source with filler wires as feedstock material similar to fusion welding [6]. These processes consist of digital MIG/MAG welding power source, a wire feeding system, and an integrated multi-axis control system for relative movement of the build and the heat source as shown in Figure 2.2 (c). The specimens are often fabricated using a welding robot combined with control box, workbench and wire feed system [1]. The 6-axis independent movements of the robot are programed and controlled by a software-based control system for printing complex components [3]. Because of high deposition rates, DED-GMA components are generally printed using very thick layers. As printed components usually have poor surface finish and require machining and grinding after the process [5].

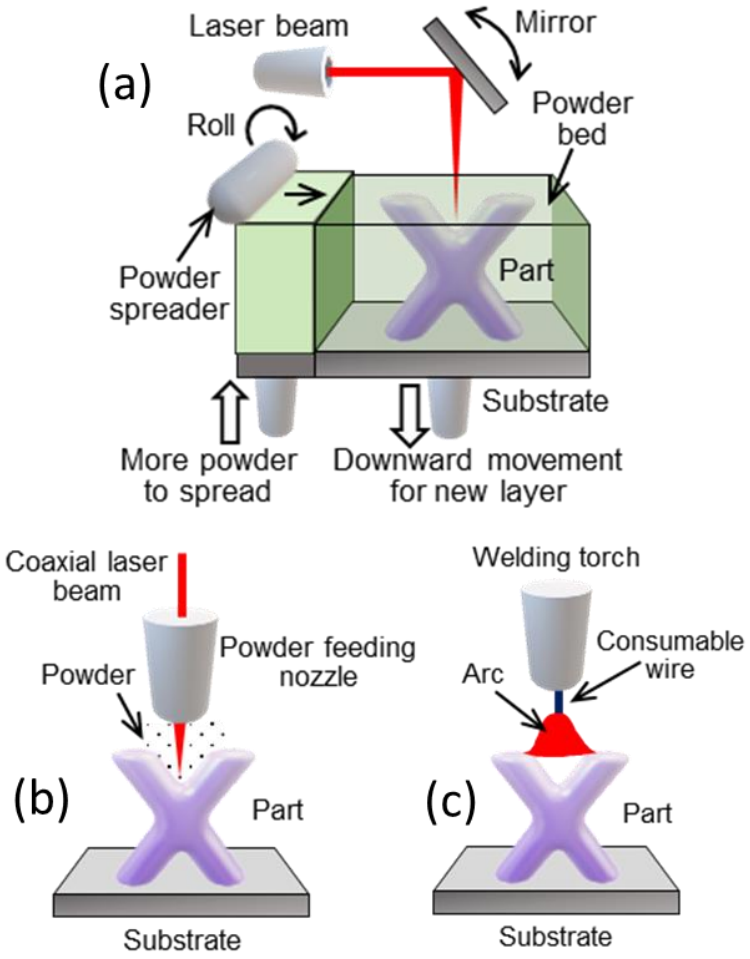

Figure 2.2. Schematic diagrams of (a) DED-L, (b) DED-GMA and (c) PBF-L processes.

2.2 Transport processes during AM

As the laser or arc impinges on the surface of the work piece, the feedstock melts quickly and forms a molten pool. The highest temperature is attained directly below the heat source on the top surface of the molten pool and the temperature decreases with distance away from that location [1]. Inside the pool, the liquid alloy recirculates rapidly at very high velocities primarily driven by the spatial gradient of surface tension on the surface of the pool [1]. This convective flow mixes the liquid metal in different regions and enhances the transport of heat inside the molten pool [6]. Heat absorption and transfer and molten pool dynamics during AM [1] are schematically shown in Figure 2.3.

Physical processes in AM have similarities with those in fusion welding [6]. For example, a moving heat source, formation of a fusion zone that travels along with the heat source and convective flow inside the molten pool are important physical processes that are shared by both welding and most AM processes [6]. However, there are also differences

between welding, DED and PBF-L because the heat source interacts very differently with a stream of powder or wire, a powder bed and solid metal [1]. In addition, solid metal surrounds the fusion zone on both sides of the weld but not so for the AM processes [1]. Absorption of heat depending on the heat source type, interaction of the heat sources with the feedstock material, layer-by-layer deposition, melting and solidification, repeated thermal cycles at any particular location are some of the features that are necessary for the understanding of AM as discussed in this sub-section.

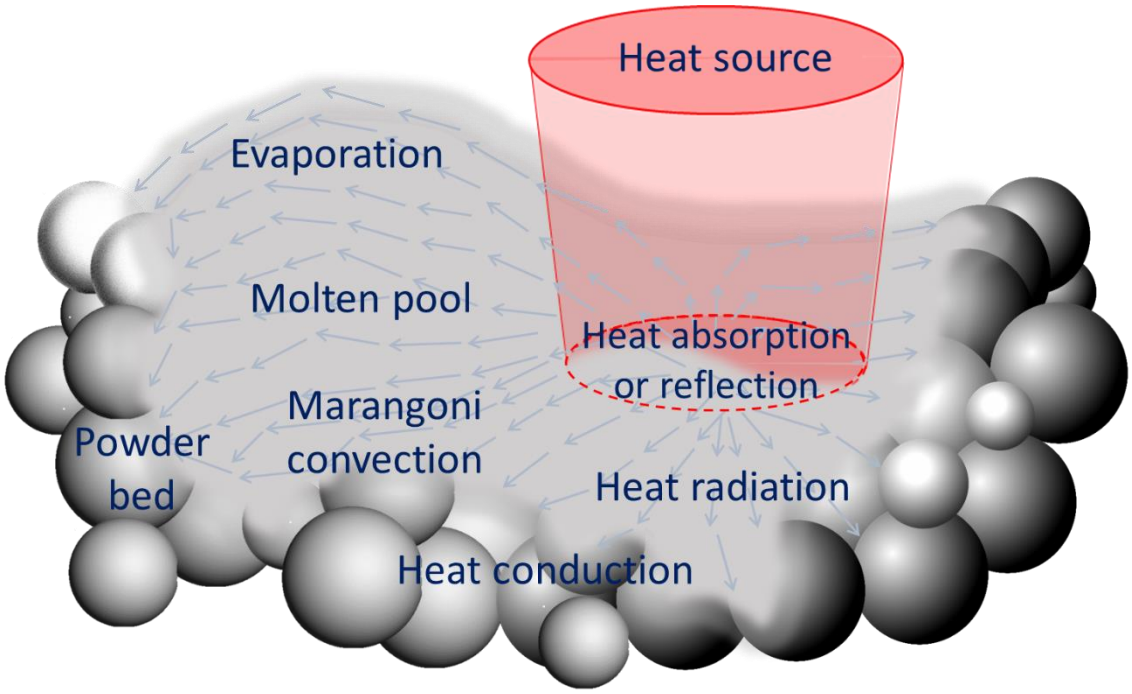

Figure 2.3. Heat transfer and molten pool dynamics during powder based AM [1].

2.2.1 Heat source characteristics

During AM, energy absorption by the feedstock materials depends on the heat source characteristics [1]. For lasers and arc, the power, radius and the power density distribution are important properties of the heat source [1]. For many heat sources, the power intensity varies as a function of radius from the beam axis. For conduction mode AM, the heat input can be described by a Gaussian distribution as a function of distance from its center [7]. Such surface heat flux distributions have been measured for lasers and electric arcs and commonly found to follow the following axisymmetric Gaussian profiles [8]:

$$P_d = \frac{d \in P}{\pi\ r_b^2} \exp\left(-d\,\frac{r^2}{r_b^2}\right) \qquad (2\text{-}1)$$

where d is the power distribution factor, $\in$ is the energy absorptivity, P is the total power of the heat source, r_b is the radius of the heat source, and r is the radial distance of a surface point to the heat source axis. The typical value of the distribution factor varies from 1 to 3; a higher value indicates a more focused power density near the beam axis and, as a result, a higher peak temperature underneath the beam [8]. Figures 2.4 (a-c) compare the power density distributions for a 500 W heat source with a 1 mm radius using distribution factors of 1, 2, and 3, respectively. Depending on the nature of the heat source (e.g., laser beam), the power density distribution can also be roughly uniform which is commonly called a top hat power distribution [1]. In Figure 2.4 (d), power density is represented as a function of horizontal position relative to the heat source axis for different values of distribution factor [7]. With the increase of the distribution factor, the energy becomes more focused resulting in a high peak temperature under the heat source.

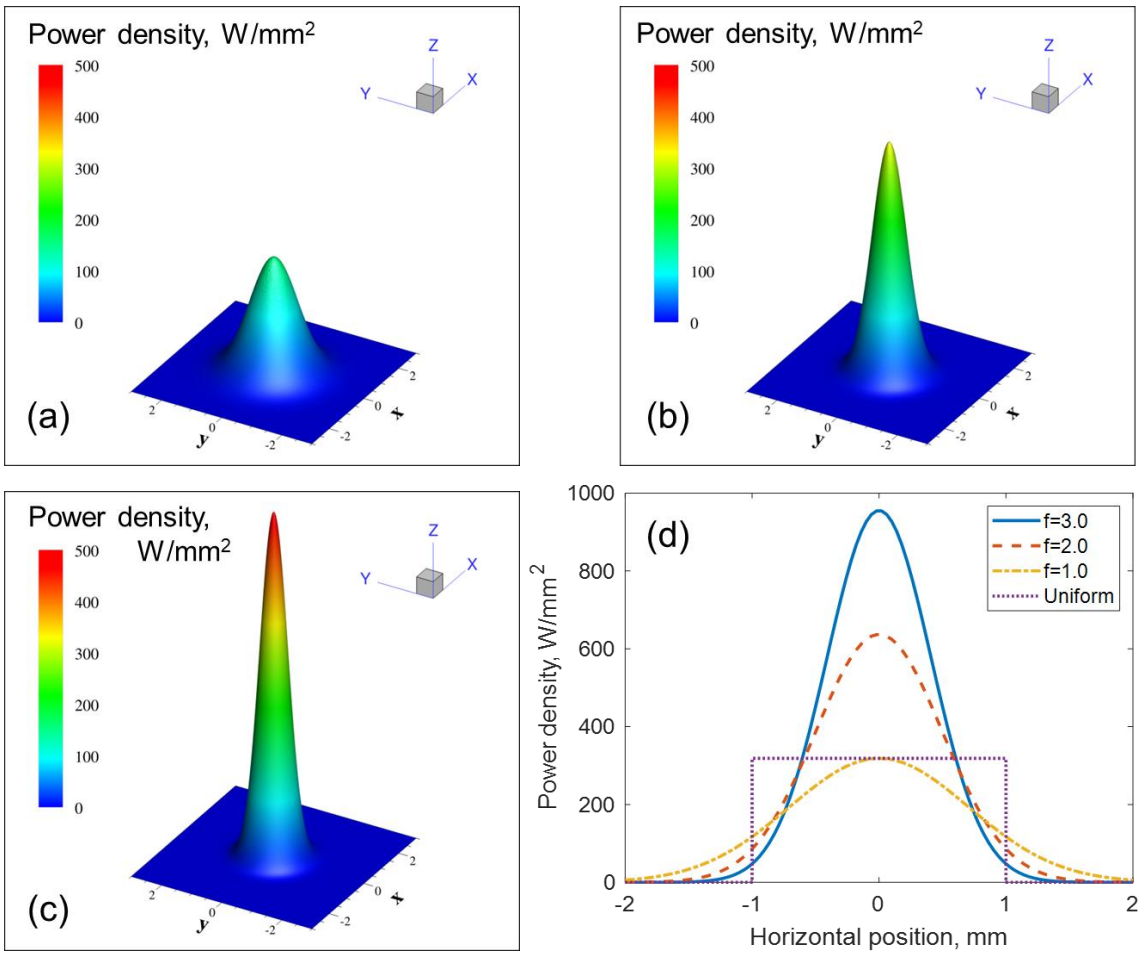

Figure 2.4. Comparison between power density distributions for a 500 W heat source with a 1 mm radius using distribution factors of (a) 1 (b) 2 and (c) 3. (d) The power density distribution with a power source of 1000W and 1 mm radius, as a function of horizontal position relative to the heat source axis for different values of the power distribution factor [1].

Minimum spot sizes depend on the AM process. PBF-L process typically uses laser beam diameters on the order of 50–100 μm for fine resolution, while DED-L process uses larger, defocused, beams with millimeter sized spots for higher deposition rates [1]. In DED-GMA, power density distribution of the arc heat source is affected by the arc length, filler wire diameter, arc current and the nature of the shielding gas [9]. In particular, the pulsed current sources are used for the electric arc assisted wire-fed AM processes. The pulsating nature of current allows high peak pulse for a short duration that helps in superior control on heat input and molten metal transfer [5].

2.2.2 Absorption of heat by feedstock material

In AM, the mechanism of heat absorption depends on the type of feedstock, liquid metal in the molten pool and solid part. In addition, various feedstocks such as powder and wire absorb heat differently. Therefore, an understanding of the absorption of heat from the three main heat sources are critical. This sub-section provides a discussion of the heat absorption mechanisms for different AM process and feed stock combinations.

Absorption of heat from laser heat source

In DED-L process, the powder particles absorb heat in two stages. First, heat is absorbed by the powder during their flight from the nozzle to the substrate [7] as shown in Figure 2.5 (a). This in-flight heating of the particles depends on the type, shape, size and speed of the powders, beam characteristics and shielding gas [1]. The published literature reports significant loss of beam energy due to attenuation and in-flight pre-heating of powder particles in DED-L of various alloys [10, 11]. Second, after the flight, the heated powder particles on the substrate absorb heat and melt to create the molten pool. This absorbed heat depends on the absorptivity of the powder particles [10, 11]. The absorptivity depends on the laser wavelength, nature of the material surface, local temperature of the material, and the nature and size of the plasma present above the molten pool [10]. The dependence of the absorptivity of different metallic materials on the laser wavelength is shown in Figure 2.5 (b) [12]. It shows that the laser energy absorptivity varies significantly for metals and alloys. For example, the energy absorption rate of commonly used fiber laser in AM for aluminum is around 5%, which indicates that 95% of the energy is lost and not actually used to heat the material [12]. In contrast, the fiber laser absorptivity for steels is significantly higher than that for aluminum,

copper and precious metals such as silver and gold. However, depending on the surface roughness and impurities, the laser absorptivity of aluminum could be as high as ~35%, which is significantly higher [13] than the value indicated in Figure 2.5 (b) for flat surfaces.

In PBF-L process, absorption of heat depends on internal-reflection of the laser beam among the powder particles [15] as shown in Figure 2.5 (c). Since the net amount of laser energy absorbed increases with each reflection and subsequent absorption, depending on the packing efficiency of the powder bed, the absorptivity can be significantly higher than that of a flat surface or just a single powder particle [15]. It has been shown that depending on the packing efficiency the absorptivity of the powder bed can be greater than the absorptivity of a flat surface of the same material [16]. For example, it has been shown to be 6 times greater for silver and gold, and around twice for stainless steel and titanium [16].

In both DED-L and PBF-L processes, the heat absorption rate changes drastically as soon as the feedstock melts and forms a molten pool. The absorptivity of the laser beam in the molten pool, i.e. Fresnel absorptivity [7], affects the shape of the molten pool. Figure 2.5 (d) shows that laser processing can take place in conduction, keyhole or mixed mode depending on the laser power intensity [17]. Generally, for DED-L, the power intensity is low because of the large spot size of laser beam. That results in conduction mode with a low depth to width ratio of the molten pool. In PBF-L, due to very small laser spot size and high power density, vaporization of alloying elements often takes place on the pool surface [1]. The resulting recoil force severely depress the liquid metal, forming a deep cavity, or keyhole [18], which is full of vaporized alloying elements. The mechanism of heat absorption in the keyhole mode involves bouncing of the beam within the keyhole surfaces in multiple locations. A portion of the beam is absorbed in each location and the remaining portion is reflected. Because of the geometry of the keyhole and multiple reflections of the beam, absorptivities often exceeding 80% are achieved [19]. However, conduction mode laser based PBF-L is common and widely reported in the literature [20].

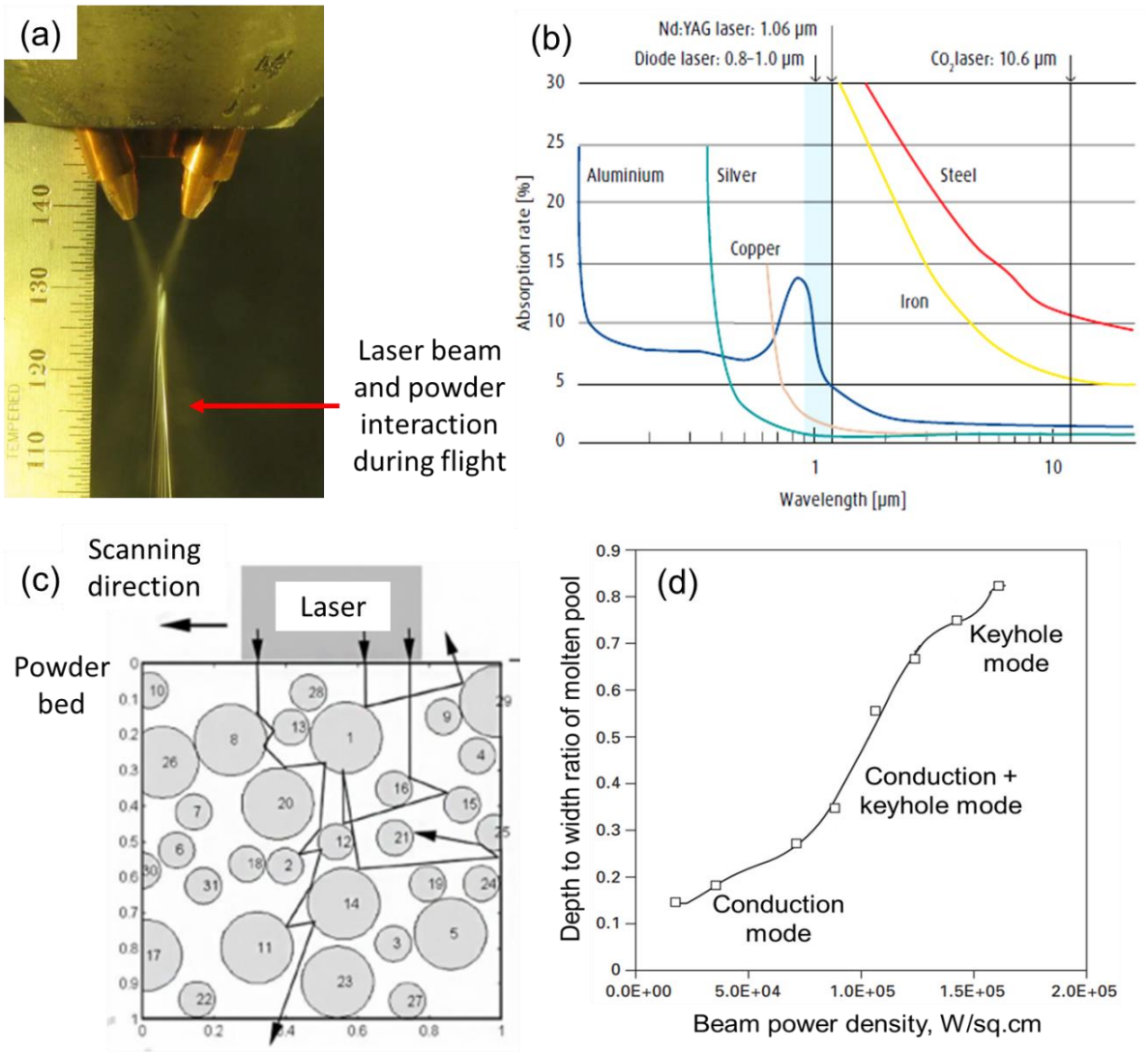

Figure 2.5. (a) Laser beam and powder interaction during the flight of the powder from the nozzle to the substrate [1]. (b) Absorptivity of laser energy for various materials [12]. (c) inter-reflection of laser beam and heat absorption by the powder during powder bed fusion process [15]. (d) Identification of the three modes in laser welding. Adapted from Buvanashekaran et al. [17]

Absorption of heat from arc heat source

The feedstock materials are melted through the arc energy during DED-GMA. The The absorption of heat by the wire feed stock depends on the alloy, arc temperature, surface finish of the wire and metal transfer mode [1]. An electric arc is established between the electrode and the substrate, which serves as the heat source. The arc can be divided into three regions, i.e. the anode, the cathode and the arc column [21]. Depending on the different variants of DED-GMA, the electrode and the substrate serve as the anode and the cathode, respectively, or vice versa. The arc column is electrically neutral and is composed of neutral atoms, electrons

and positive ions [1]. Electrons are emitted from the cathode, accelerated through the arc column, and condensed at the anode. Ions travel along a reversed path, i.e. from the anode to the cathode through the arc column [21]. Both the filler wire and the substrate or solidified deposit are heated and melted by the arc.

The characteristics of the arc are determined by major variables including the polarity of the electrode, the arc voltage and current, arc length as well as other factors such as shielding gas composition and wire diameter [22]. Tungsten is commonly used as non-consumable electrode and cerium or thorium is also added to have better electron emissivity, current-carrying capacity, and contamination resistance [23]. The consumable filler wire is melted during GMA, with three common modes of metal transfer, i.e. globular, spray, and short-circuit, depending on the interactions between the arc and the tip of the filler wire [23]. Because of the considerable amount of heat transported by the liquid metal from the filler wire to the molten pool, the energy efficiency is typically over 80% during the DED-GMA process [23]. The arc heat absorption by the molten pool is similar to that for laser based processes. However, due to low power intensity of the arc source because of its large size, conduction mode is generally observed in arc based DED processes [24].

2.2.3 Molten pool formation and fluid flow

Heat from the laser or arc sources is absorbed by the powder or wire feedstock to form a molten pool. Shape and size of the molten pool are affected by the heat source and feedstock types, feedstock feeding mechanism, flow of shielding gas, heat source power, scanning speed and thermo-physical properties of the material. Non-uniformity in temperature field inside the molten pool results in convective flow of liquid metal which often dominates the heat transfer mechanism inside the fusion zone. In this sub-section, the formation mechanism of various molten pool geometries and role of convective flow in that for different AM processes are discussed.

Molten pool geometry

Figure 2.6 compares the shape and size of the molten pools at the transverse section during printing of SS 316 components using DED-GMA, DED-L and PBF-L processes [25-27]. The shape of the molten pool varies for the three printing processes because of the unique features of the processes. For example, in DED-GMA, the molten metal near the arc axis is

depressed by the arc pressure and the impact of the impinging droplets [4]. The liquid metal is pushed to the rear part of the molten pool and forms the curved deposit as it solidifies. The impinging effect of the droplets also result in deep finger-like penetration in DED-GMA [25], as shown in Figure 2.6 (a). However, in DED-L the curved pool surface is formed immediately under the laser beam axis due to the accumulation of the powder particles [26], as shown in Figure 2.6 (b). In contrast, Figure 2.6 (c) shows that the top surface of the molten pool in PBF-L is flat because of the addition of thin flat layers of powders [27]. The size of the molten pool in the three printing processes varies widely depending on the heat sources and heat input. The linear heat input (power/speed) in PBF-L is in the order of 0.1 J/mm [1] that results in very small pool whose dimensions are in micrometers. However, linear heat inputs in DED-L and DED-GMA are on the order of 10 J/mm and 100 J/mm, respectively [1]. Therefore, the molten pool width in DED-GMA is the largest followed by that in DED-L. Figure 2.6 shows that the pool dimensions in PBF-L are around 10% and 30% of those for DED-GMA and DED-L respectively. These aforementioned variations in molten pool shape and size and the differences in heat input play a critical role in determining the relative susceptibilities to defect formation for the three printing processes.

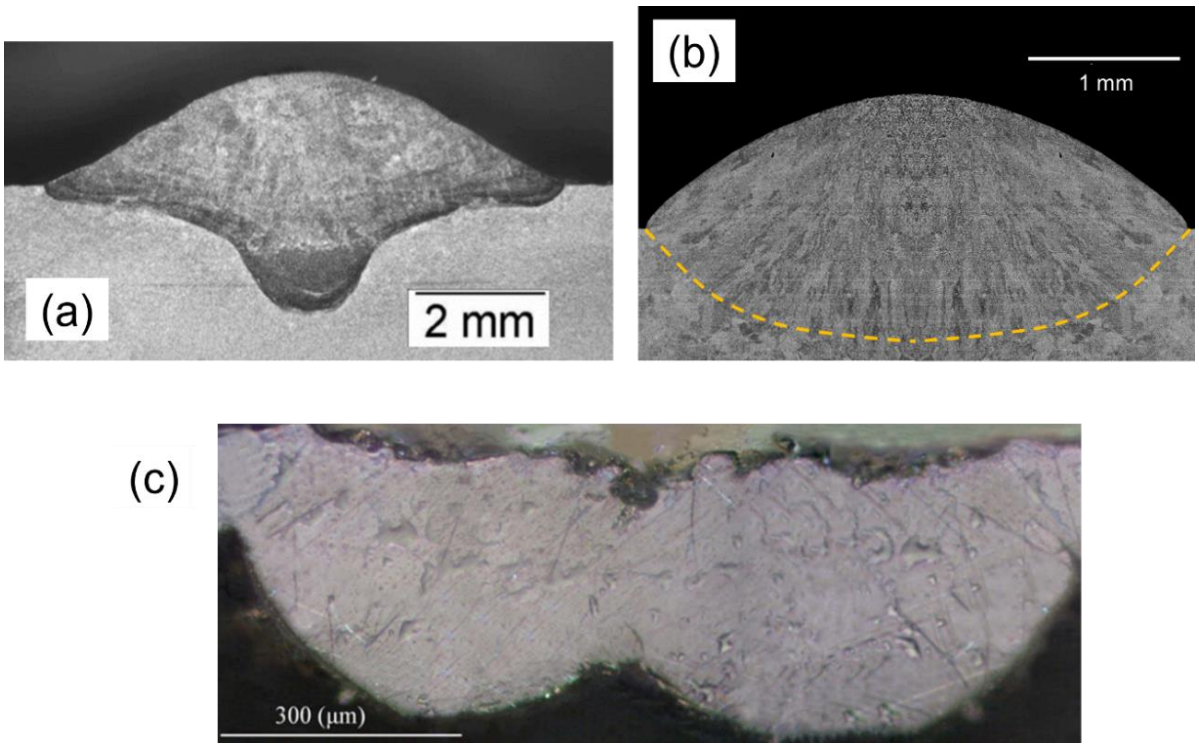

Figure 2.6. Shape and size of the fusion zone at the transverse section for (a) DED-GMA [25]. (b) DED-L [26] and (c) PBF-L [27]. All deposits are made of stainless steel 316.

Convective flow inside the molten pool

Convective flow of liquid metal inside the molten pool is primarily caused by the combined effects of the Marangoni, electromagnetic and buoyancy forces [28]. Both the Marangoni and buoyancy forces are common in all AM processes [1], whereas the electromagnetic force is important only for the DED-GMA process [1]. However, the buoyancy force is significantly lower than that of Marangoni force [1].

Surface tension is temperature-dependent and therefore varies spatially on the surface of the fusion zone [28]. This variation of surface tension drives fluid flow tangential to the pool surface, commonly known as the Marangoni flow [26]. Marangoni shear stress on the top surface of the molten pool can be represented as [28]:

$$\frac{d\gamma}{dT}\cdot\frac{dT}{d\vec{s}} = \mu\frac{\partial u_s}{\partial\vec{n}} \qquad (2\text{-}2)$$

where $\frac{d\gamma}{dT}$ is the temperature coefficient of surface tension (γ), $\frac{dT}{d\vec{s}}$ is the temperature gradient along a tangential direction on the surface $\vec{s}$, μ is the viscosity, u_s is the surface velocity along $\vec{s}$, and $\vec{n}$ is the surface normal direction. The right-hand side in Equation (2-2) is the viscous shear stress for a Newtonian fluid [1]. For pure metals, $d\gamma/dt$ is negative that means higher surface tension at lower temperatures and vice versa [29]. The region of the molten pool directly under the heat source will have the highest temperature, typically causing liquid to be pulled to the sides of the pool which has a lower temperature and consequently higher surface tension [30], as shown in Figure 2.7 (a). Therefore, the fusion zone becomes wide and shallow. However, the flow direction may reverse with the presence of a surface-active element such as sulfur or oxygen [30], as shown in Figure 2.7 (b). The variation of surface tension of steels [31] containing low concentrations of sulfur is shown in Figure 2.8. In those cases, $d\gamma/dt$ is positive for a certain range of temperature and the liquid metal flows in a direction opposite to that in the absence of sulfur, as shown in Figure 2.7 (b). The penetration depth of the molten pool is significantly larger in the case of inward flow due to the heat transported to the bottom of the fusion zone, which results in a greater depth-to-width ratio [30].

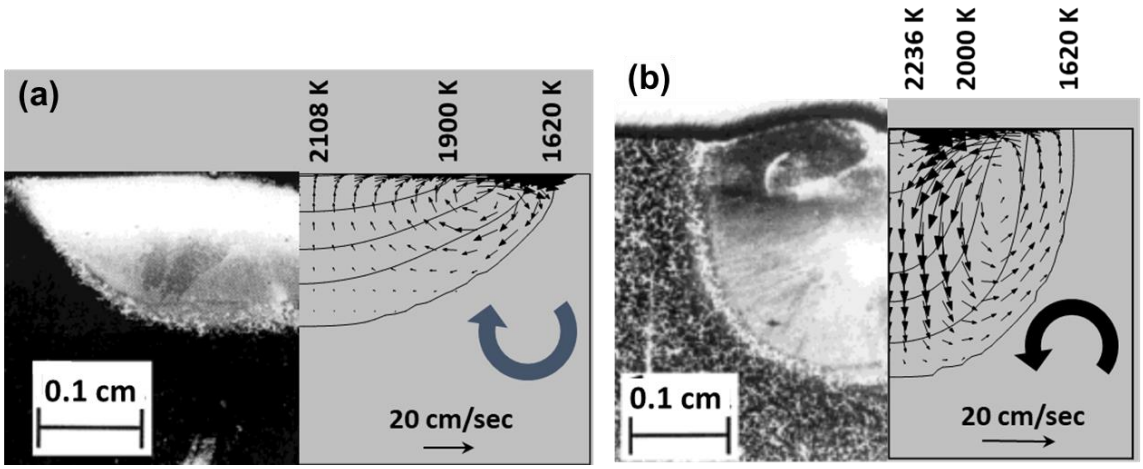

Figure 2.7. Convective flow of liquid metal in the molten pool during laser spot welding. (a) Outward and (b) inward flow from the periphery to the center of the molten pool [30].

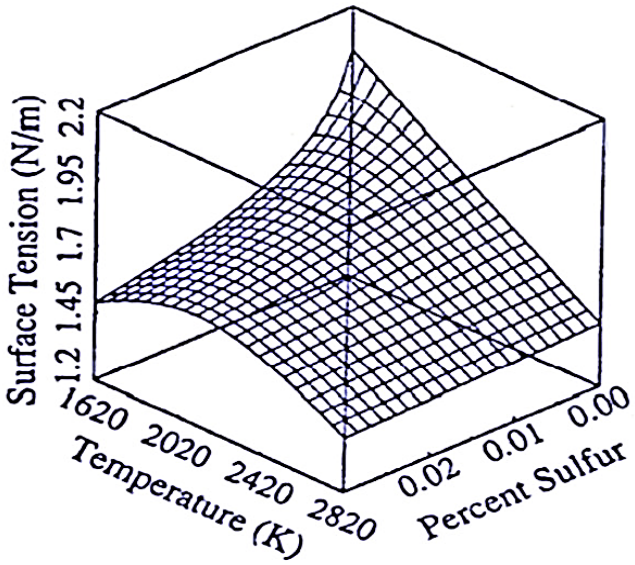

Figure 2.8. Surface tension of Fe-S alloys as a function of temperature and composition [31].

For the joining of alloys containing different concentrations of surface active elements, the aforementioned variations in $d\gamma/dt$ result in different shapes of the molten pool as shown in Figure 2.9. The molten pool shown in Figure 2.9 (a-b) demonstrate a net movement of liquid metal from the high sulfur 303 to the low sulfur 304L stainless steels [32], which originates from the Marangoni convection. The rotational asymmetry of the molten pool shown in Figure 2.9 (c) results from the interaction between the velocity field in the molten pool and its linear motion with the scanning of the laser beam [32]. The variable shapes of the molten pool shown in Figure 2.9 (d-f) are attributed to the heat input parameters and the thermophysical properties of materials [33].

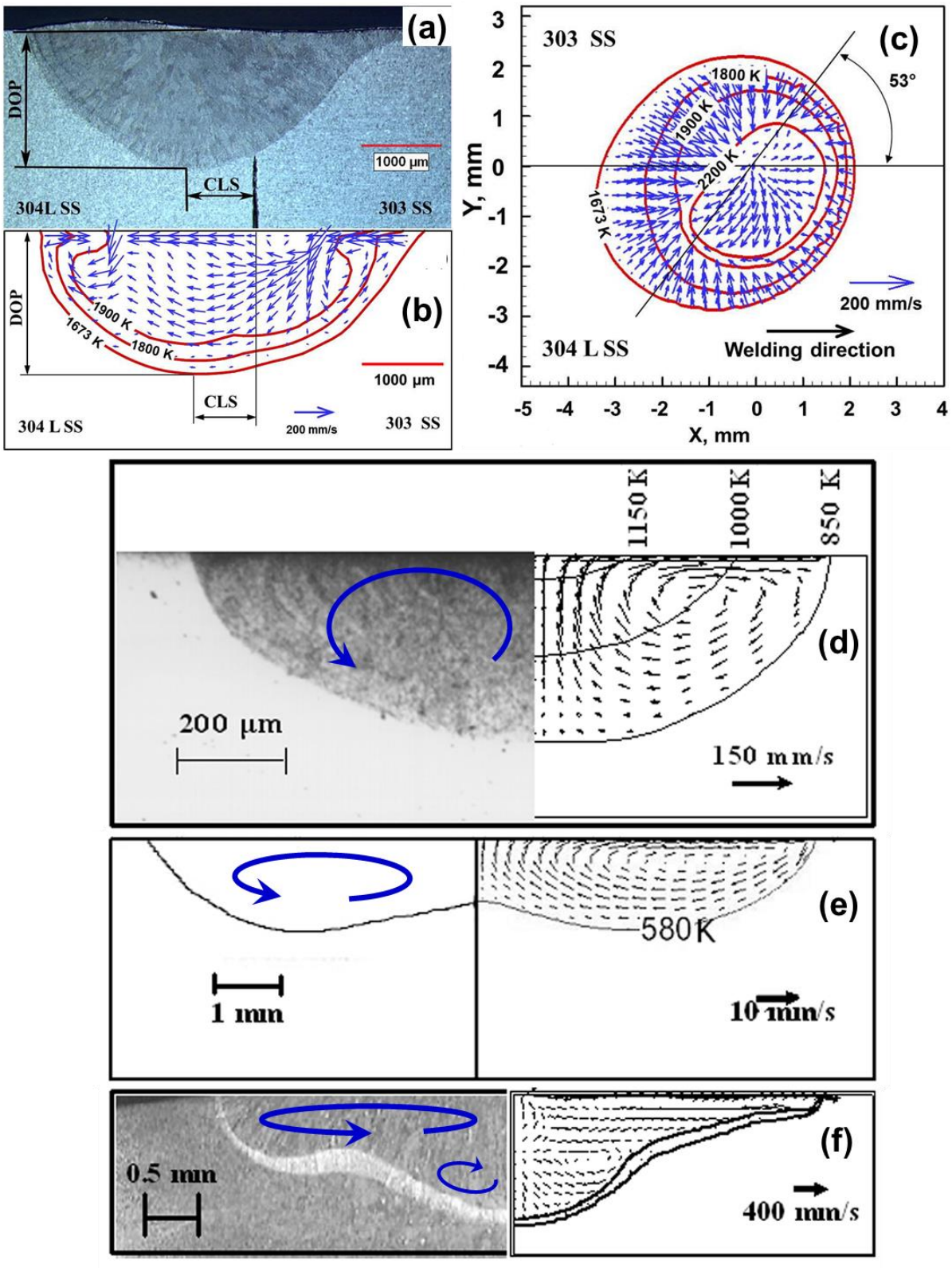

Figure 2.9. Various molten pool shapes resulting from different patterns of flow of the liquid metal. (a)-(c) The center line shift (CLS), rotational and translational asymmetry of the molten pool during welding of two stainless steels with different sulfur concentrations [32]. (d)-(f) Molten pool geometries of Al alloy 5182, NaNO3, and steel, respectively [33].

2.3 Defect formation in AM of metals and alloys

The mechanism of evolution of macroscopic defects in AM, residual stresses, distortion, composition change and lack of fusion defects and their impact on structure and mechanical properties of AM parts are discussed in this sub-section.

2.3.1 Residual stresses and distortion

In all AM processes, the cyclic heating and prolonged build time lead to complex stresses and strains within the solidified part. They originate from thermal expansion and contraction [34] while the part is constrained by the build plate. Key physical factors that affect the evolution of residual stresses and distortion include spatial gradient of temperature due to localized heating and cooling by the moving heat source, thermal expansion and contraction of material depending on the transient temperature field and mechanical properties, and temperature and strain rate dependent constitutive behavior of plastic material [1]. Besides these, in many materials, at least one solid-state phase transformation occurs during the cooling of the part from solidus to room temperature [34]. For example, austenite to ferrite transformation in steel and β to α transformation in Ti-6Al-4V take place. The change of the crystal structure during a phase transformation leads to the development of "transformation plasticity," or the deformation due to the expansion or contraction of the material. For the welding of steels, transformation plasticity was found to have a significant effect on the final residual stresses [35]. Nonetheless, the effect of solid-state phase transformations varies between alloys, which has not been explored in great depth within the AM literature. One of the few examples that consider this form of residual stress is by Bailey et al. for DED-L of AISI H13 tool steel [36]. Another factor contributing to the final residual stresses is the stress relaxation that can occur due to layer-by-layer mass deposition and heating. As materials are heated above a certain temperature, annealing can occur that relieves some of the existing stresses [37].

Residual stresses and distortion affect the mechanical properties as well as the structural integrity and dimensional accuracy of parts. For example, Figure 2.10 (a-d) show that the printed Inconel 718 part can suffer from warping due to very high distortion along the build direction [38]. Warping was observed in the fabricated component and corresponding vertical deformation was calculated using a thermo-mechanical model. Delamination is the separation of two consecutive layers as shown in Figure 2.10 (e), which is caused by the

residual stresses at the layer interfaces exceeding the yield strength of the alloy [39]. Figure 2.10 (f), a plot based on independent literature data [40,41], indicates that the fatigue cracks in additively manufactured Ti-6Al-4V parts grow faster in the presence of a higher tensile residual stress in the component. The maximum tensile residual stress values are estimated from the reported stress distributions [40,41]. The y-intercept of the curve is about 8×10^{-6} mm/cycle which corresponds to the crack growth rate with very low residual stresses (such as the traditionally processed Ti-6Al-4V parts) [42]. Therefore, printed parts with high residual stresses are susceptible to premature failure under dynamic loading.

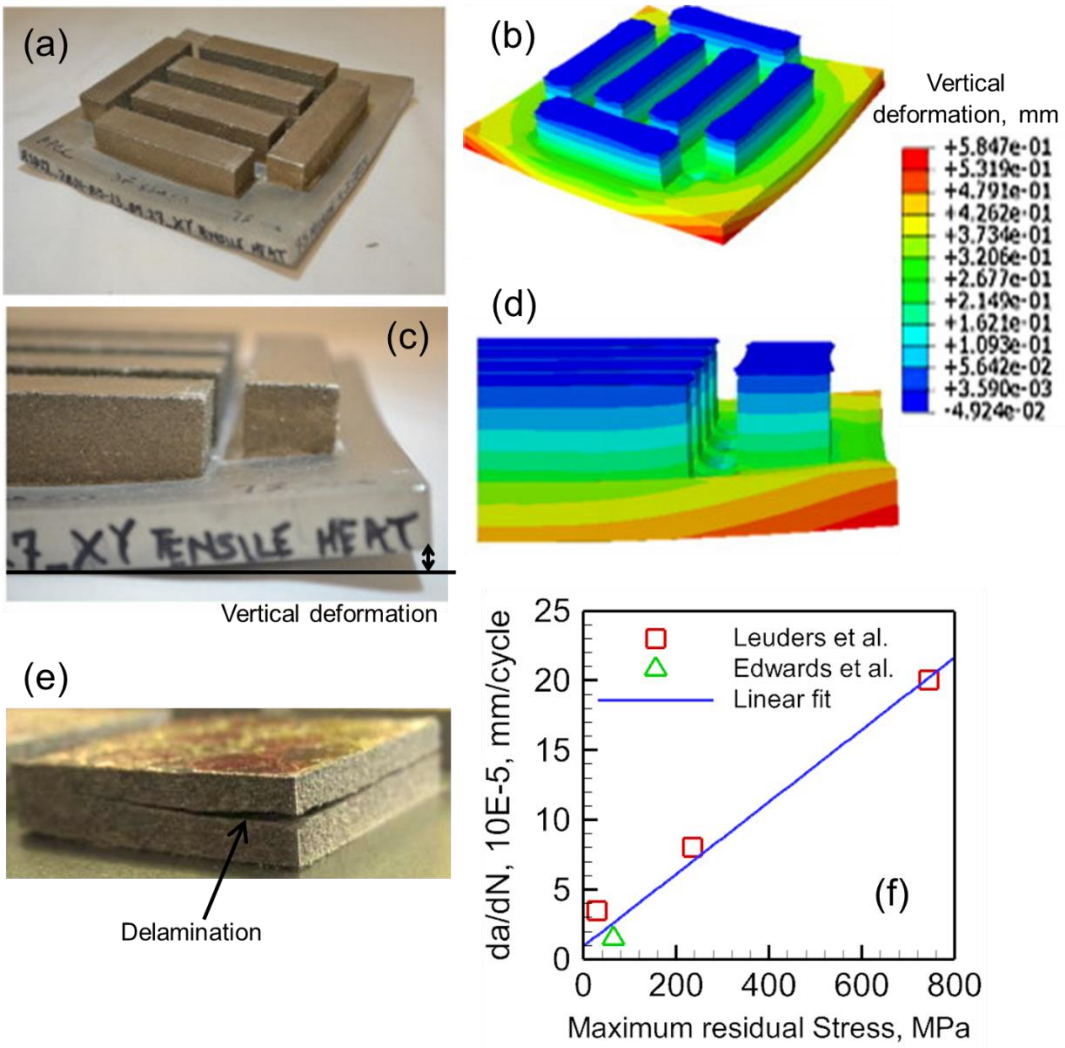

Figure 2.10. Warping due to distortion in AM parts of Inconel 718 [38] (a-b) picture of the part and (c-d) corresponding modeling results showing the vertical deformation in mm. (e) Delamination in additive manufacturing due to high residual stresses [39]. (f) Fatigue crack growth rate (da/dN) for additively manufactured Ti-6Al-4V components as a function of maximum tensile residual stress. The data are obtained from the crack growth rate curves reported in independent literature [40,41]. The stress intensity factor ratio is 0.1 and the stress intensity factor range is 10 MPa $m^{1/2}$.

2.3.2 Composition change due to evaporative loss

At very high temperatures, alloying elements vaporize significantly depending on their equilibrium vapor pressures above the molten pool and the total pressure in the depositing chamber [6]. All elements do not vaporize at the same rate because of the difference in vapor pressures of elements [1]. Such selective vaporization of alloying elements often results in a significant change in the chemical composition of the part from that of the original feedstock [1]. Composition change is affected by vaporization rates of different alloying elements, temperature distribution on the top surface of the deposit, surface area and the molten pool volume [1].

The loss of volatile alloying elements is known to occur during processing of both steels and non-ferrous alloys. Laser welding of high manganese stainless steels is known to result in the depletion of manganese and chromium in the weld metal [43], and aluminum alloys are known to lose magnesium and zinc [44]. These losses often result in the degradation of mechanical properties due to changes in microstructure, as well as the deterioration of the corrosion resistance. Depletion of magnesium [44] in the weld zone in bead-on-plate autogenous conduction mode laser welding of thin aluminum alloy 5182 plates (4.2 wt% Mg, 0.2%Si, 0.35% Mn, 0.07% Zn, 0.15%Cu, 0.1% Ti and balance Al) can be observed in Figure 2.11 (a). These results indicate that elements with relatively low boiling points, such as Al, Mg and Zn, selectively vaporize from the molten pool more readily than other elements. Gaytan et al. [45] have reported a 10–15% reduction in aluminum during powder bed process of Ti-6Al-4V, which corresponded to about a 0.6–0.9 wt% decrease of the aluminum composition. This observation is consistent with that reported by Taminger [46] as shown in Figure 2.11 (b). Experimentally measured concentration of aluminum [47] for various speeds and powers is shown in Figure 2.11 (c). In all cases, the concentration of aluminum in the build was significantly lower than that in the powder. As shown in the figure, both the energy of the beam and the scanning speed were varied and for a given linear energy density, higher scanning speed produced more pronounced change in the concentration of aluminum [47]. Because a faster scanning normally results in a shallower, longer molten pool with a larger surface area, more pronounced composition change occurs for a higher surface area to volume ratio of the molten pool.

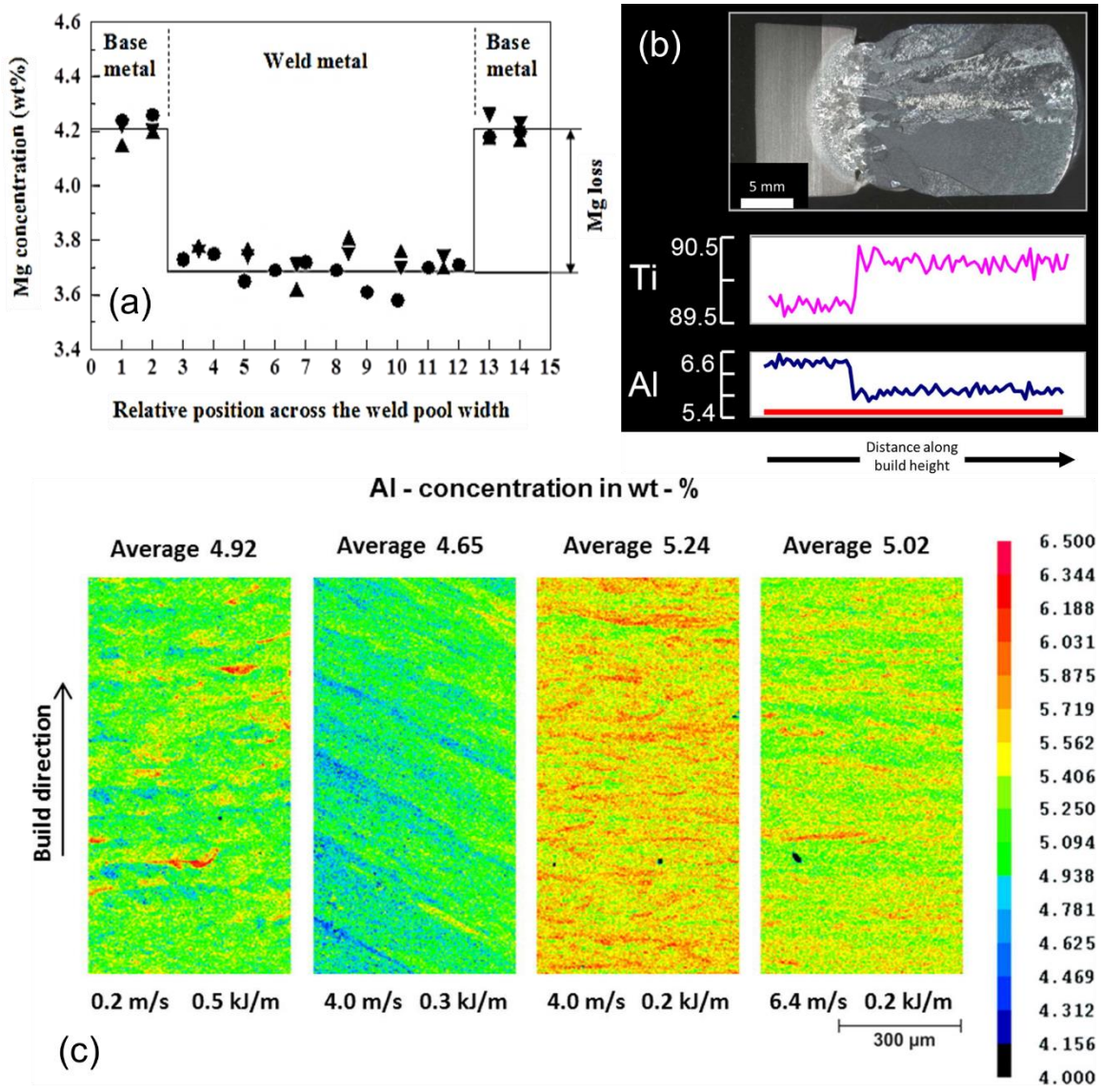

Figure 2.11. (a) Typical magnesium concentration profile across the weld pool width [44] after composition change due to evaporative loss. (b) Measured chemical composition along the build height for a printed Ti-6Al-4V component that shows a depletion in Al concentration and an increase in Ti concentration [46]. (c) Experimentally measured concentration of aluminum [47] for powder bed fusion AM of Ti-6Al-4V at different processing conditions.

2.3.3 Lack of fusion defects

Lack of fusion defects may result due to insufficient overlap between neighboring tracks of deposits and are affected by the shape and size of the fusion zone [48]. Figure 2.12 shows formation of lack of fusion defect during PBF-L of Inconel 718 [49]. The defect was formed due to improper fusional bonding between two successive layers [49]. The void was more than 100 µm long along the scanning direction. Shape and size of fusion zone that control the lack of fusion defect are often controlled by heat absorption by the feedstock, heat transfer

through the substrate and surface energy on the top surface of the molten pool [1]. For example, in wire arc based DED processes, fusion zone geometry is governed by arc pressure and vapor pressure on the top surface of the molten pool, droplet impingement and surface tension [1]. Fusion zone geometry is also often influenced by convective flow of liquid metal primarily driven by the surface tension gradient on the top surface of the molten pool [1]. Figure 2.13 shows that the susceptibility to lack of fusion defect increases at low heat source power and high scanning speed and hatch spacing [50,51]. At low power and rapid scanning speed, smaller molten pools are unable to remelt the previously deposited tracks and cause lack of fusion defects [50,51]. Since it is difficult to achieve proper bonding between two neighboring hatches with a large distance between them, lack of fusion defects increase with hatch spacing [50]. These defects are detrimental to the mechanical properties of printed parts. For example, Figure 2.14 shows tensile properties such as elongation before failure and tensile strength of stainless steel 316 parts printed using PBF-L are degraded with increasing size of pores [52].

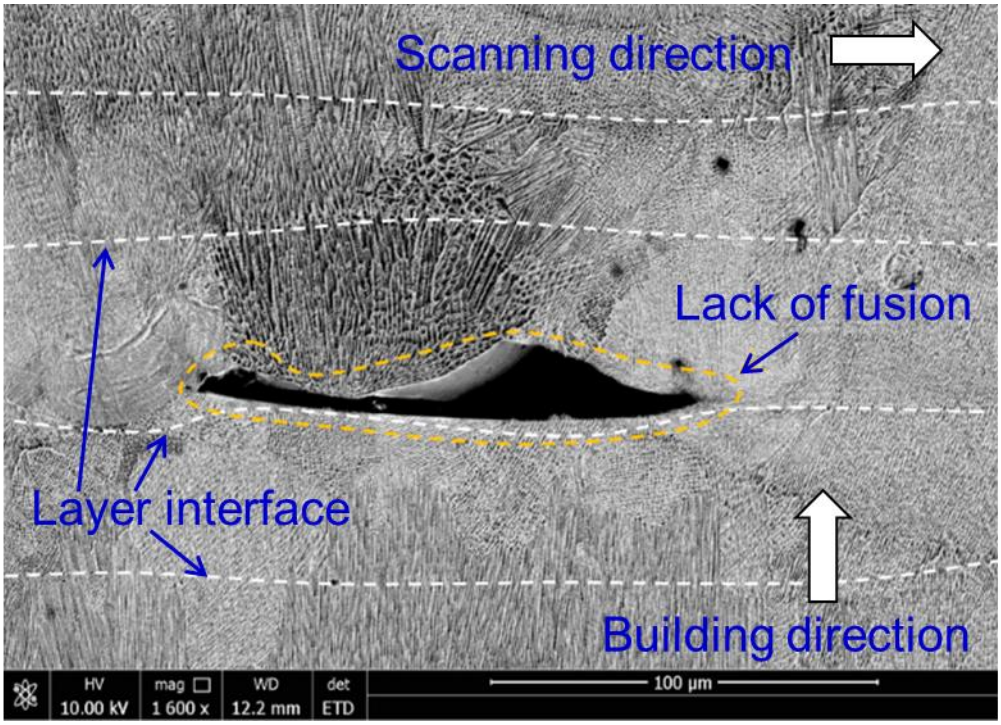

Figure 2.12. Formation of lack of fusion defect during PBF-L of Inconel 718 [49].

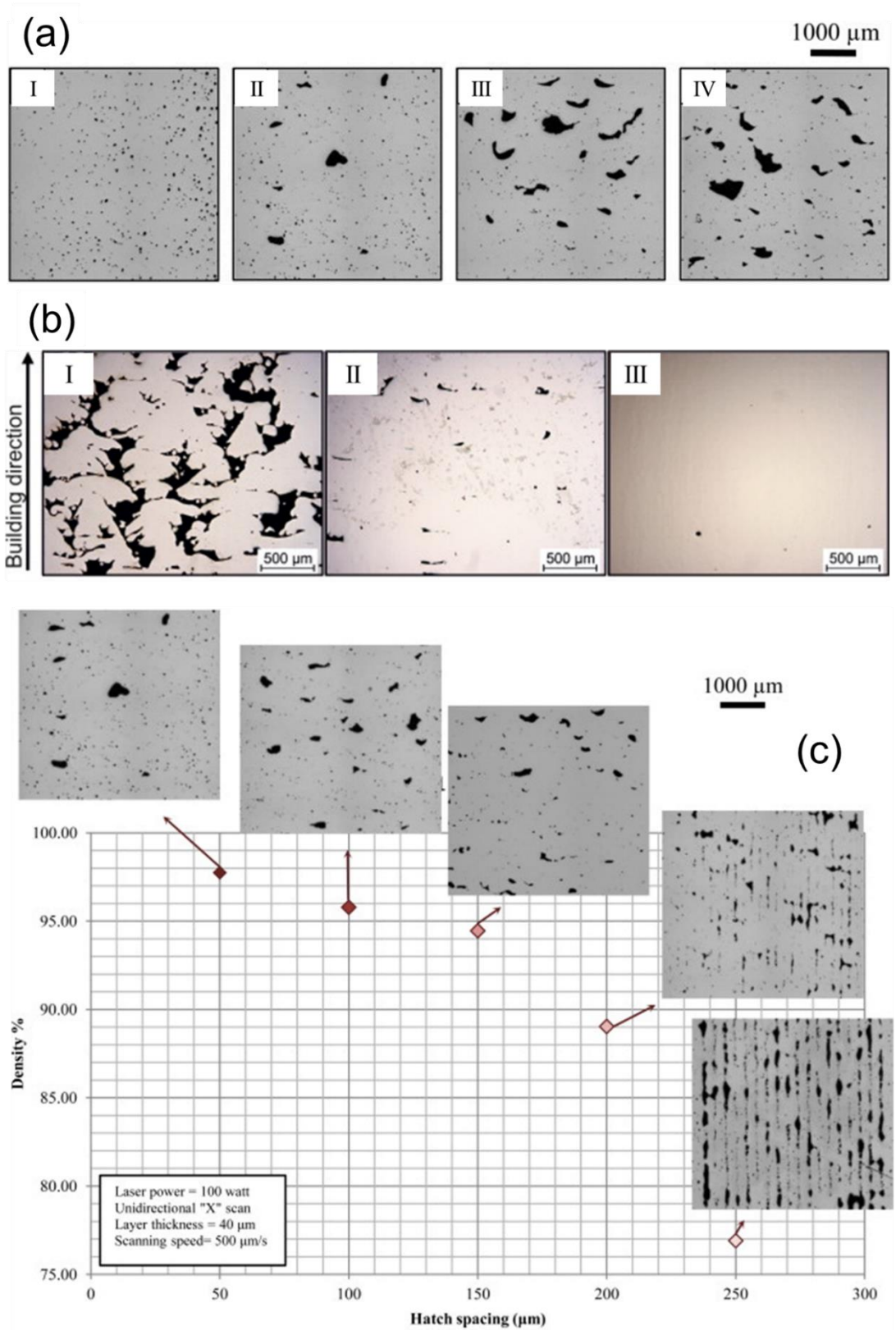

Figure 2.13. (a) Effect of scanning speed on lack of fusion defect (I) 250 (II) 500 (III) 750 and (IV) 1000 mm/s [50] (b) Effect of laser power on lack of fusion defect (I) 90 (II) 120 and (III) 180W [51]. (c) Effect of hatch spacing on density of the printed part [50].

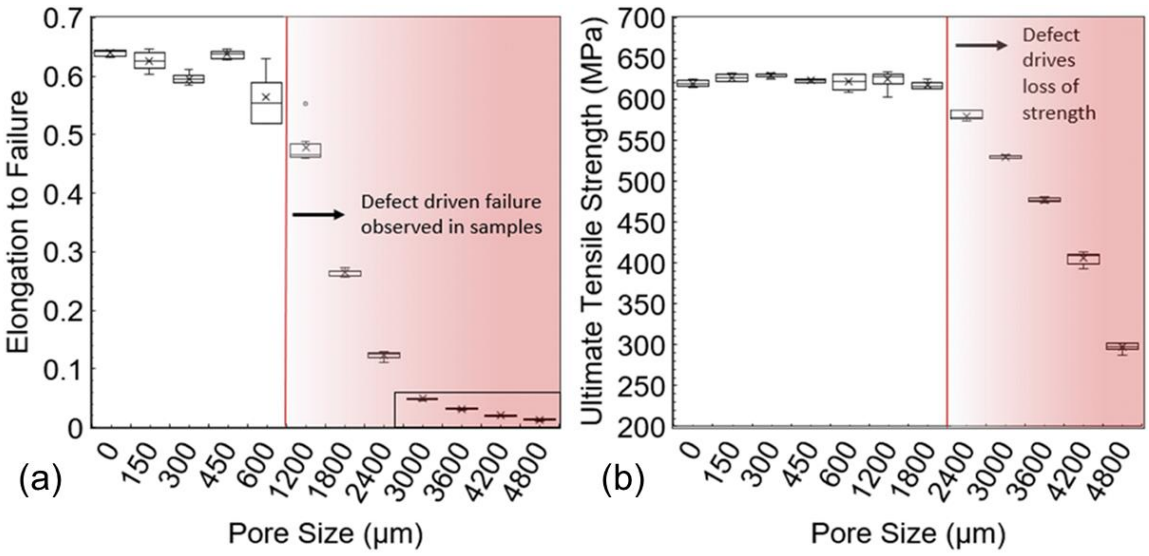

Figure 2.14. Effect of lack of fusion pore size on (a) elongation to failure and (b) ultimate tensile strength of stainless steel 316 parts printed using PBF-L [52].

2.4 Transport phenomena based models for defect prediction

Several attempts have been made to model residual stresses, distortion, composition change and lack of fusion defects with different levels of complexities. In this sub-section, a summary of those models is provided and the existing challenges in the modeling defect formation in AM are outlined.

2.4.1 Different modeling approaches

Currently, there are six main approaches for transport phenomena based modeling of metal printing [1]. These methods and their special features are summarized in Table 2.2. Analytical methods [53] solve heat conduction equation to obtain temperature fields and cooling rates based on several simplified assumptions. However, these methods ignore the dominant mechanism of heat transfer in the liquid pool and produce large errors. Heat conduction models [38] using finite element method (FEM) solve the energy conservation equation to calculate temperature fields, build geometry, cooling rates and the constitutive equations of stress and strain to predict distortion and residual stresses. Although these models are easy to apply and can handle intricate geometries, they often neglect convective flow of liquid metal and often severely overestimate the temperature and pool size. Heat transfer and fluid flow models [7] using finite difference method (FDM) solve conservation equations of mass, momentum and energy to calculate essential variables in AM. Level set method (LSM) and volume of fluid method (VOF) based models track the free deposit surface [54]. Therefore,

the calculated deposit geometries using these models agree well with the experiments. However, these models are often applied in 2D and computationally expensive. Powder scale models [55] using lattice Boltzman method (LBM) and arbitrary Lagrangian-Eulerian (ALE) method solve the heat, mass and momentum conservation equations and involve free surface boundary conditions treating surface tension, thermodynamics, phase transition and wetting. Apart from temperature fields and deposit geometry, these models can accurately predict void formation, spattering and surface roughness. However, these models are computationally expensive and require advanced computational resources. Figure 2.15 shows the calculated temperature fields and deposit geometry using different modeling approaches [55-58].

Table 2.2. Comparison among the current modeling approaches in AM. Adapted from [1].

Approaches	Features
Analytical approach	• Analytically solves Rosenthal's heat conduction equation. • Outputs are temperature fields, build dimensions and cooling rates. • Computationally less expensive, simplified and easy to use. • Ignores the mechanism of heat transfer and known to produce large errors.
Heat conduction models using finite element method	• Solves steady state or transient energy conservation equation • Outputs are 3D temperature distribution and build shape and size. • Easy to implement, can handle intricate geometries. • Does not consider the effects of convective flow of liquid metal, therefore severely overestimates the peak temperature and cooling rate.
Heat transfer fluid flow models using finite difference method	• Solves 3D transient conservation equations of mass, momentum and energy. • Outputs are 3D transient temperature and velocity distributions, build shape and size, solidification parameters. • Considers the effects of molten metal flow inside the pool and therefore provides accurate temperature distribution.
Level set method (LSM)	• Tracks the free surface of the molten pool. • Outputs are 3D temperature and velocity distribution. • The calculated deposit shape and size agree well with experiments. • Computationally intensive and tends to suffer from non-conservation of mass.
Volume of fluid (VOF) method	• Tracks the free surface of the molten pool. • Outputs are 3D temperature and velocity distribution of the deposit with free curved surface. • Computationally intensive.
Lattice Boltzman method (LBM) and arbitrary Lagrangian Eulerian (ALE)	• 2D and 3D numerical methods involving cellular automaton modeling of discrete particle kinetics by discrete space, time, and particle velocities. • It involves free surface boundary conditions treating thermodynamics, surface tension, phase transitions, and wetting. • Can predict the build geometry accurately. Also, the balling phenomenon and surface roughness can be simulated. • Computationally intensive suitable for massive parallel computing.

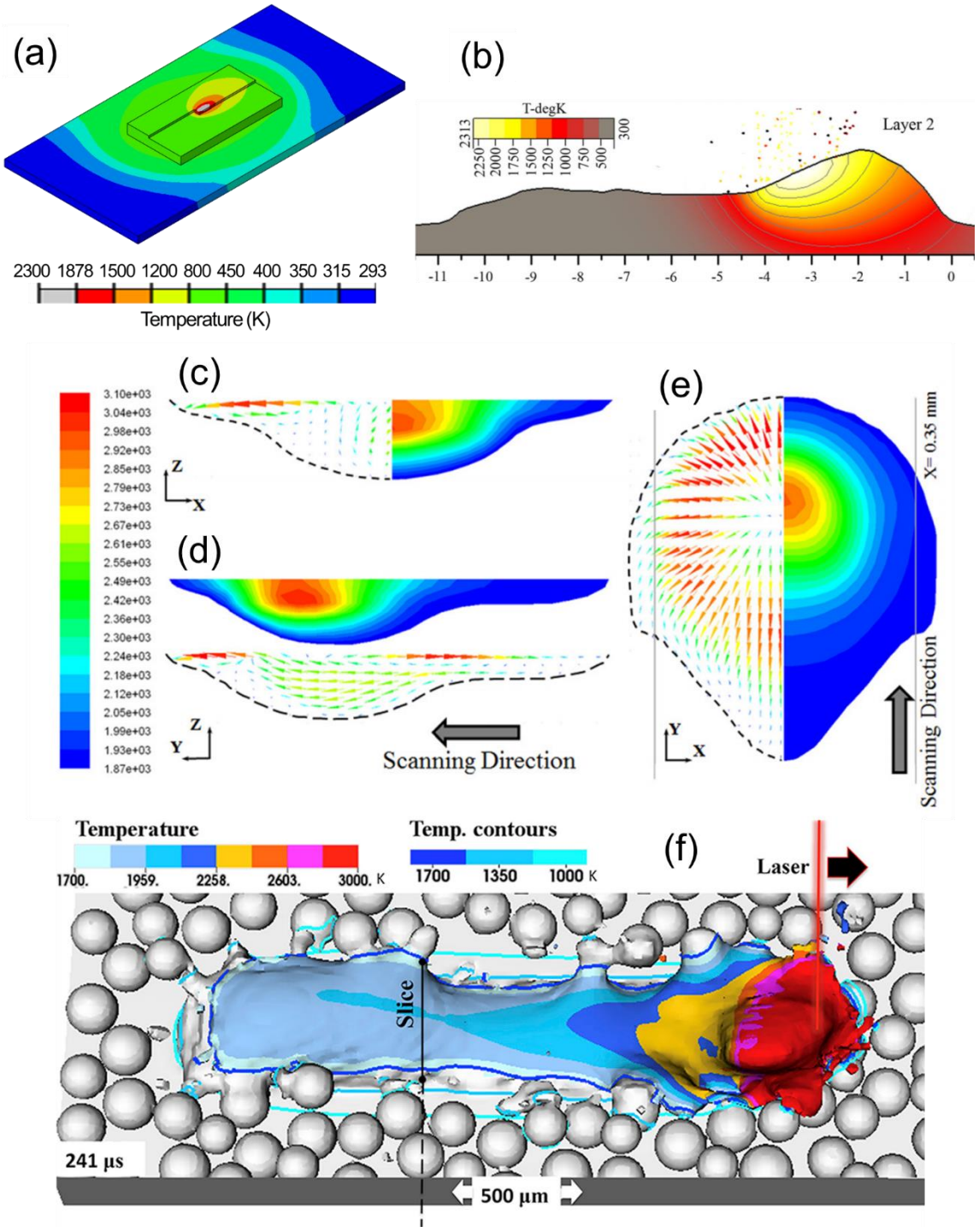

Figure 2.15. Calculations of temperature fields and deposit geometry using different modeling approaches for various AM processes. (a) 3D temperature distribution during DED-GMA calculated using a heat conduction model [56]. (b) Temperature field during DED-L using VOF [57]. Temperature and velocity fields calculated for powder bed fusion using heat transfer fluid flow model [58] (c) transverse view, (d) longitudinal view and (e) top view. (f) Molten pool and powder particles simulated using powder scale model ALE [55] for PBF-L.

2.4.2 Calculation of residual stresses and distortion

Calculations of residual stresses and distortion have been demonstrated using methods of varying complexity. A selection of thermomechanical models [59-64] for various AM processes are shown in Table 2.3. Coupled thermo-mechanical models are common, linking transient temperature fields to thermal strains. For PBF-L, rapid scanning of a small beam makes a myriad of complex scanning strategies and part geometries feasible, leading to differences in the heating and cooling of the material both spatially and temporally [1]. Figure 2.16 shows how different scanning strategies lead to different residual stress states for the same material and processing parameters [65]. Similar models have been developed for DED-GMA processes [56], an example of which is shown in Figure 2.17 The figure shows the residual stresses in Ti-6Al-4V and Inconel 718 fabricated with three deposition patterns after releasing the clamps. For both alloys, the stress distributions in the substrate are the same with high tensile stress near the shorter edge of the deposit and high compressive stress near the longer edge of the substrate. Notably, most of the models show that the edges of the material where the part joins the base plate are subject to the highest residual stresses [56].

Table 2.3 shows that FEM has been successfully implemented for AM of very complex geometries such as impeller, triangular prisms, parts with overhang and compressor blades. However, for large components, FEM is computationally expensive and requires large computational memory. For example, residual stresses and distortion calculations for actual process of 2 seconds can take up to 460 hours [62]. The required calculation time may vary depending on the efficiency and capability of the computing facility. However, there are several ways to reduce computational burden in FEM of large scale systems [66, 67]. Jayanath et al. [66] proposed a dynamic grid system where the grids are updated with the progress of the building process. After the completion of each layer the fine grid region moves up and is applied for the depositing layer. Already deposited layers are discretized with coarser grids. This process reduces the total number of nodes and elements for large components. It is reported that the total calculation time was reduced from 45 hours to 27 hours by using this technique for a cylindrical geometry fabricated using 32 layers. Ding et al. [67] separates the elastically and plastically deformed zone in their thermo-mechanical calculations. In AM, the plastically deformed zone is very small in size but the simulation of this region requires a large amount of computational resources because of the non-linear relation between stress and strain. Confining the plastic deformation calculation in a small region where material yields because

of very high temperature, the total calculation time for a 500 mm long four layers deposit is reduced from 75 hours to 42 minutes [67]. Therefore, selection of a useful numerical model depends not only on the part geometry and types of the calculation, but also computational facilities and availability of the smart algorithms to enhance computational efficiency.

Table 2.3. Selected thermomechanical models for various AM approaches.

Process	Material	Numerical method	Computational features	Ref.
DED-L	H 13 tool steel	FEM (ABAQUS)	• Around 6 hours for 2 × 2 × 3 mm solution domain • 55,455 elements and 60,033 nodes • Rectangular block with multiple layers and hatches	[59]
	Inconel 718	FEM (ABAQUS)	• Compressor blade with complex geometry • 2D longitudinal section • Computational details not given	[60]
PBF-L	Ti-Ni shape memory alloy	FEM (ANSYS)	• Brick elements with size of 0.025 × 0.025 × 0.0125 mm • Rectangular block with multiple layers and hatches	[61]
	Ti-6Al-4V	FEM (COMSOL)	• Total calculation time: 460 hours for 2 seconds of actual manufacturing simulation • Impeller with complex geometry	[62]
	SS 316 L	FEM (DIABLO)	• Triangular prism and 'L' shaped builds • Computational details not provided	[63]
DED-GMA	Low carbon steel	FEM (ANSYS)	• Rectangular block with single layer, multiple hatches • 90,000 8-node brick elements	[63]
	Structural steel grade S355JR-AR	FEM (ABAQUS)	• Single pass multi-layer deposit • 8-node brick elements with size 2 × 0.833 × 0.667 mm • Total deposition length: 500 mm • Total calculation time: 75 hours 25 minutes	[64]

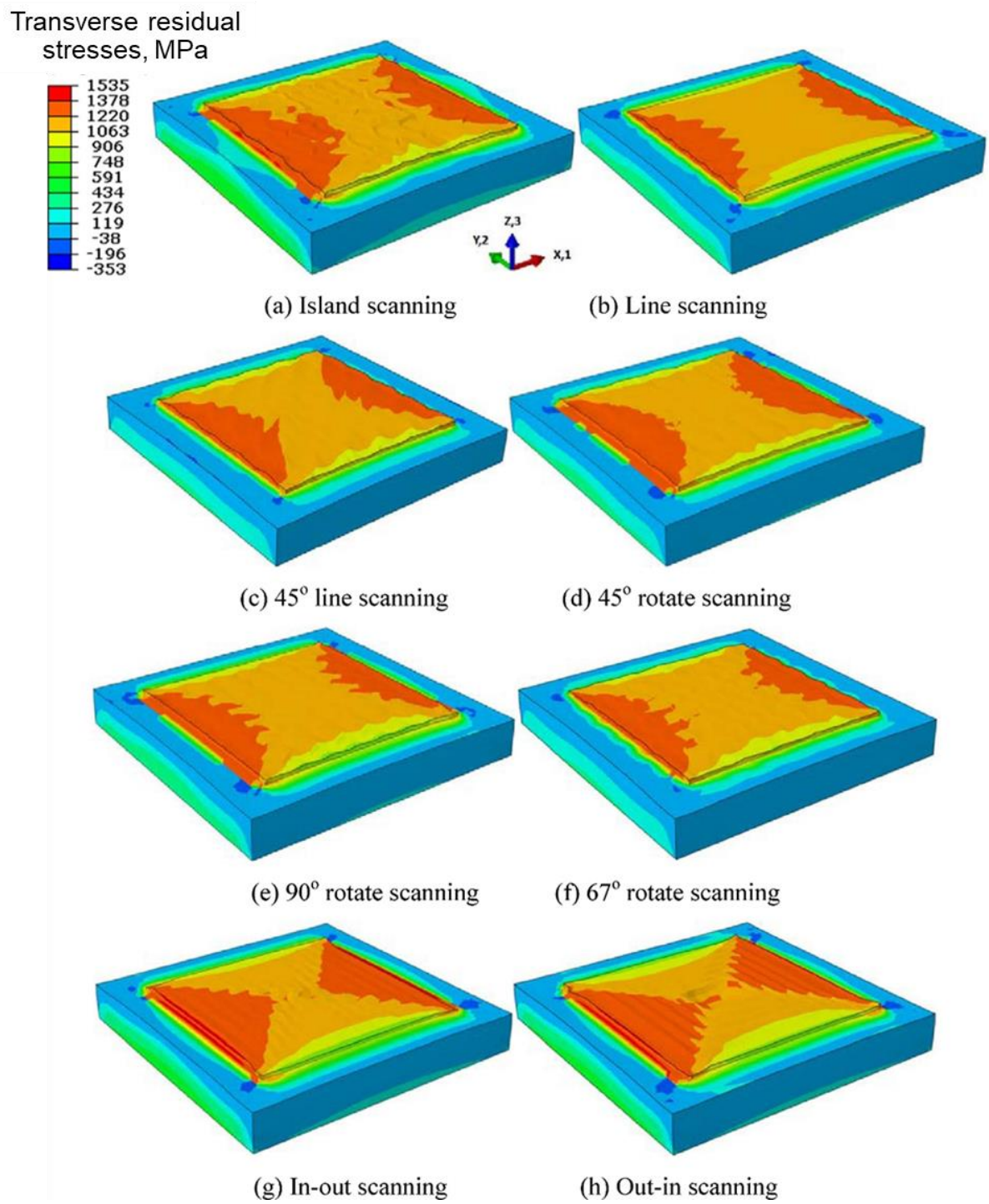

Figure 2.16. Transverse residual stresses along the Y-direction for a variety of different scanning patterns during PBF-L processing of Inconel 718 alloy. Reproduced from [65].

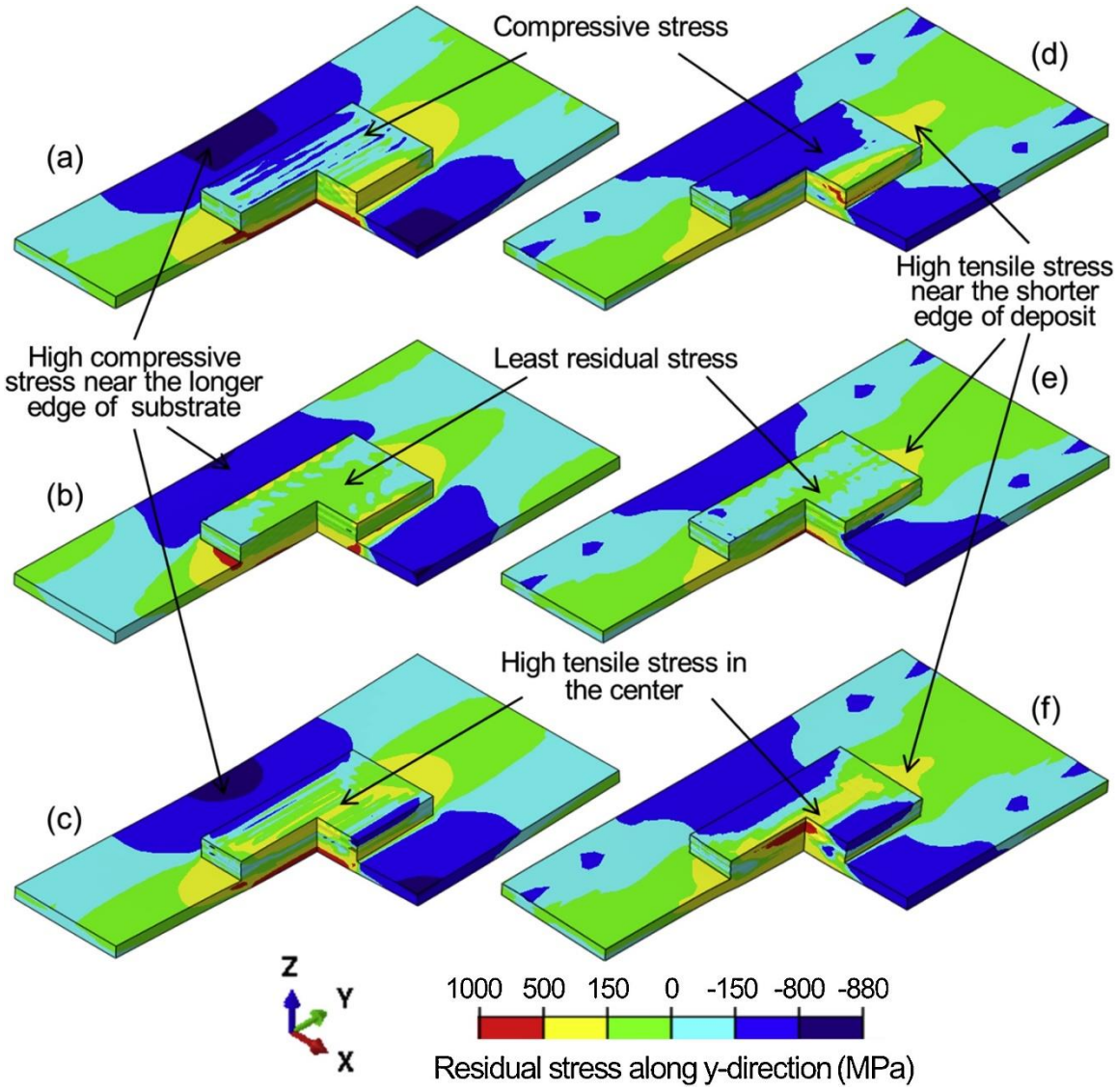

Figure 2.17. Residual stresses along y-direction in the Ti-6Al-4 V components [56] fabricated using (a) long deposition pattern, (b) short deposition pattern and (c) spiral deposition pattern when the deposits cooled down to room temperature and the clamps were released. Residual stresses along y-direction in the Inconel 718 components deposited with (d) long deposition pattern, (e) short deposition pattern and (f) spiral deposition pattern when the deposits cooled down to room temperature and the clamps were released.

2.4.3 Estimation of composition change

Alloying element loss and the resulting composition change are calculated based on mass balance. The decrease in the concentration of an element *i*, such as manganese or magnesium, can be expressed as follows [28]:

$$\Delta\%C_i = 100 \sum(R_i \, dA_s)/(\rho \, V_m) \qquad (2\text{-}3)$$

where $\Delta\%C_i$ is the decrease in the concentration of alloying elements, R_i is the local vaporization rate of *i* per unit surface area, dA_s is the local surface area, ρ is the density of the weld metal, and V_m is the volume of the weld metal melted per unit time. The term $\sum(R_i\, dA_s)$ is the total rate of vaporization of element i per unit time from the top surface of the molten pool. Therefore, the change in the concentration of an element depends on both the vaporization rate of the element and the volume of the molten pool [28].

There are varying levels of complexity that can be used calculate the vaporization flux, depending on the accuracy desired. However, most models are based on the fact that there is some relationship between the vapor pressure of an element above the molten pool and the vaporization rate of that element. A simple approach to calculate the vaporization flux of an element *i* in the alloy, $J_{i,}$ involves applying a modified form of Langmuir equation [68] :

$$J_i = \frac{\xi P_i}{\sqrt{2\pi M_i T}} \tag{2-4}$$

where P_i is the partial pressure of element *i* over the alloy, M_i is the molecular weight, *T* is the local temperature. The P_i can be found from the product of activity of element *i* and the equilibrium vapor pressure of *i* over pure element at temperature *T*. The term ξ is a positive fraction that represents an adjustment factor to account for the condensation of vaporized atoms on the surface. This variable is needed because the original Langmuir equation was derived for evaporation in vacuum where the condensation of the vaporized species could be safely ignored. This calculation overestimates the vaporization rate at ambient pressure when ξ is taken as 1 [69]. However, the equation is useful for the calculation of relative rates of vaporization of various alloying elements from a liquid surface where the value of ξ is considered to be a constant for all alloying elements.

A more accurate model for the calculation of vaporization rate that considers the effects of the ambient pressure was proposed by Anisimov and Rakhmatulina [70] and Knight [71]. Their models solve the equations of conservation of mass, momentum and energy in a thin layer adjacent to the liquid-vapor interface known as the Knudsen layer. Notably, they consider the possibility that some atoms that leave the molten pool as vapor will not escape into the atmosphere, and instead will condense on the molten pool surface. To account for this condensation, the model considers the velocity distribution functions of the metal vapor molecules close to the molten pool [70, 71]. With only a few exceptions, most models of AM do not consider vaporization and the resulting composition change of alloys. There is no significant barrier to the implementation of vaporization models, because the existing theory

from laser welding literature provides computational methods that can be implemented into numerical calculations of AM. Though the trends predicted by these models are qualitatively observed in AM experiments, validation of these models for a quantitative prediction of composition change for a wide range of AM process variables still needs to be undertaken.

2.4.4 Prediction of lack of fusion defects

Models of varying levels of complexity have been applied to predict lack of fusion defects. For example, Tang et al. [72] proposed a simple, geometry-based analytical model to predict lack of fusion defects in PBF-L. Molten pool dimensions were obtained by solving the heat conduction equation. The dependence of lack of fusion defect on molten pool size is explained in Figure 2.18 (a) The lack of fusion defect was mentioned to be formed when the dimension L* (in Figure 2.18 (a)) is less than the layer thickness (L) [72]. The condition was expressed in terms of pool width (W), depth (D), layer thickness (L) and hatch spacing (H) as: $(H/W)^2 + (L/D)^2 > 1$.

Powder scale models of transport phenomena are more accurate than analytical models and can directly compute the shape and size of pores without the use of any empirical relations [73]. These models are often used to predict lack of fusion defects in DED-L and PBF-L. These simulations show the unstable nature of the interaction of a molten pool with the surrounding powders, vapor jets, and the gas flow. Xia et al. [49] used a 3-D powder-scale model to show that lack of fusion defects between two hatches may result from incomplete melting of powders, as shown in Figure 2.18 (b-e). Even with smart algorithms to reduce computational time, simulations are typically limited to only a few passes within a single layer. However, multiple simulations are necessary to obtain reliable results because computational volumes need to be small since three-dimensional powder-scale models are computationally intensive. The need to simulate multiple hatches and layers required for an accurate estimation of lack of fusion porosity limits their applications.

In DED-GMA, lack of fusion defects typically occur due to unexpected variations in the geometry of the deposited bead. For GMA welding, models for the droplet size, shape, temperature, and velocity have been studied [74]. Deflection of the droplets from the wire axis due to the Lorentz force depends on the arc current [75] and any fluctuation of the arc current or the travel speed can affect the stability of the process. Although in DED-GMA, temporal variations of arc current, wire feed rate or gas flow rate can result in spatial variations of track

geometry resulting in porosity similar to welding, research on lack of fusion defect in DED-GMA is scarce in the literature.

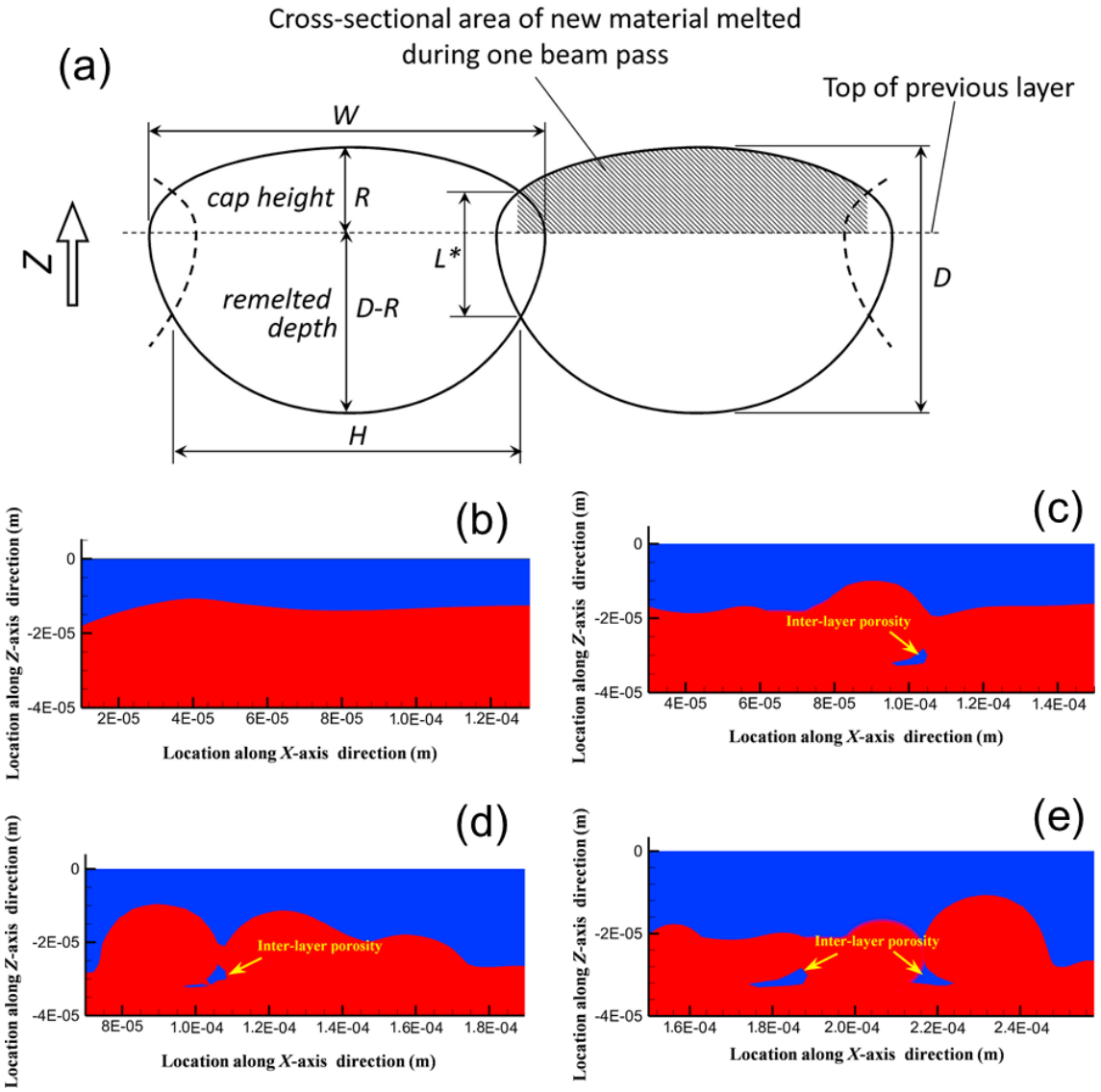

Figure 2.18. (a) Schematic of the melt pools in the analytical model by Tang et al. [72], showing the overlap between two adjacent beads and with relevant dimensions labeled. Evolution of lack of fusion porosity during PBF-L of Inconel 718 at longitudinal section at scanning speeds of (b) 200 (c) 300 (d) 400 and (e) 500 mm/s [49].

2.5 Important unanswered questions

From the aforementioned review of the literature, it is evident that the transport phenomena based understanding of defect formation in AM is a developing field. Better insight about the interconnection between transport phenomena and defect formation is required because many important questions still remain unanswered due to complexity of the process

and scarcity of rigorous phenomenological models. The following is a selection of important unanswered questions that are addressed in this thesis.

(1) Convective flow of liquid metal inside the molten pool often dominates the heat transfer mechanism inside the fusion zone and thus affects the temperature field and fusion zone geometry. What is the role of the convective flow on residual stresses, distortion, composition change and lack of fusion defect? How to include the effects of convective flow in the transport phenomena based mechanistic modeling of defect formation?

(2) How residual stresses and distortion evolve depending on the transient temperature field and temperature dependent alloy properties. For example, in a compositionally graded material printed using AM, the thermo-physical and mechanical properties vary spatially within the part. How to include these effects to calculate residual stresses and distortion for graded components?

(3) All alloys are not equally printable by the AM processes. How to select an appropriate alloy-AM process combination using the fundamental knowledge of transport phenomena that can produce defect free parts?

(4) How to transfer the knowledge obtained from rigorous, transport phenomena based mechanistic models to the shop floor applications in order to predict defects quickly?

2.6 References

1) T. DebRoy et al. Additive manufacturing of metallic components - Process, structure and properties. Prog. Mater. Sci. 92 (2018) 112-224.
2) Standard terminology for additive manufacturing technologies. ASTM Int. (2013) F2792–12a.
3) D.D. Gu et al. Laser additive manufacturing of metallic components: materials, processes and mechanisms. Int. Mater. Rev. 57 (2012) 133–64.
4) W.E. Frazier. Metal additive manufacturing: a review. J Mater. Eng. Perform. 23 (2014) 1917–28.
5) S.W. Williams et al. Wire+ arc additive manufacturing. Mater. Sci. Technol. 32 (2016) 641-647.
6) H.L. Wei et al. Harnessing the scientific synergy of welding and additive manufacturing. Sci. Technol. Weld. Join. (2019) 1-6.

7) V. Manvatkar et al. Heat transfer and material flow during laser assisted multi-layer additive manufacturing. J Appl. Phys. 116 (2014) 124905.
8) P. Farahmand et al. An experimental–numerical investigation of heat distribution and stress field in single-and multi-track laser cladding by a high-power direct diode laser. Opt. Laser Technol. 63 (2014) 154-68.
9) M. Lu et al. Power and current distributions in gas tungsten arcs. Weld. J. 67 (1988) S29–34.
10) A.J. Pinkerton et al. An analytical model of energy distribution in laser direct metal deposition. Proceed. Inst. Mech. Eng. B: J Eng. Manuf. 218 (2004) 363-74.
11) J.P. Andrew et al. Modelling the geometry of a moving laser melt pool and deposition track via energy and mass balances. J Phys. D: Appl. Phys. 37 (2004) 1885.
12) Bergström. The Absorption of Laser Light by Rough Metal Surfaces. Sweden: Luleå University of Technology (2008).
13) A.M. Rubenchik et al. Temperature-dependent 780-nm laser absorption by engineering grade aluminum, titanium, and steel alloy surfaces. Opt. Eng. 53 (2014) 122506.
14) X.C. Wang et al. Direct selective laser sintering of hard metal powders: experimental study and simulation. Int. J Adv. Manuf. Technol. 19 (2002) 351–357.
15) M. Markl et al. Multiscale Modeling of Powder Bed–Based Additive Manufacturing. Ann. Rev. Mater. Res. 46 (2016) 93-123.
16) W.E. King et al. Laser powder bed fusion additive manufacturing of metals; physics, computational, and materials challenges. Appl. Phys. Rev. 2 (2015) 041304.
17) G. Buvanashekaran et al. A study of laser welding modes with varying beam energy levels. Proceed. Inst. Mech. Eng. C: J Mech. Eng. Sci. 223 (2009) 1141-56.
18) W.E. King et al. Observation of keyhole-mode laser melting in laser powder-bed fusion additive manufacturing. J Mater. Process. Technol. 214 (2014) 2915-25.
19) R. Rai et al. Heat transfer and fluid flow during keyhole mode laser welding of tantalum, Ti-6Al-4V, 304L stainless steel and vanadium. J Phys. D-Appl. Phys. 40 (2007) 5753-66.
20) K. Khan et al. Modelling of selective laser melting process with adaptive remeshing. Sci. Technol. Weld. Join. (2019) 1-10.
21) J.F. Lancaster. The physics of welding. Physics in technology. 15 (1984) 73.
22) B. Ribic et al. Problems and issues in laser-arc hybrid welding. Int. Mater. Rev. 54 (2009) 223-44.

23) S. Kou. Welding metallurgy. 2nd ed. Hoboken, NJ: John Wiley & Sons (2003).
24) J. Ding et al. A computationally efficient finite element model of wire and arc additive manufacture. Int. J Adv. Manuf. Technol. 70 (2014) 227-36.
25) N. Rodriguez et al. Wire and arc additive manufacturing: a comparison between CMT and TopTIG processes applied to stainless steel. Weld. World. 62 (2018) 1083-1096.
26) G.L. Knapp et al. Building blocks for a digital twin of additive manufacturing. Acta Mater. 135 (2017) 390-399.
27) A. Foroozmehr et al. Finite element simulation of selective laser melting process considering optical penetration depth of laser in powder bed. Mater. Des. 89 (2016) 255–263.
28) T. DebRoy et al. Physical processes in fusion welding. Rev. Mod. Phys. 67 (1995) 85.
29) B. Keene. Review of data for the surface tension of pure metals. Int. Mater. Rev. 38 (1993) 157-92.
30) W. Pitscheneder et al. Role of Sulfur and Processing Variables on the Temporal Evolution of Weld Pool Geometry during Multi-Kilowatt Laser Welding of Steels. Weld. J. 75 (1996) 71s-80s.
31) P. Sahoo et al. Surface-tension of binary metal - surface-active solute systems under conditions relevant to welding metallurgy. Metal. Trans. B 19 (1988) 483–91.
32) H.L. Wei et al. Asymmetry in steel welds with dissimilar amounts of sulfur. Scripta Mater. 108 (2015) 88-91.
33) A. Arora et al. Unusual wavy weld pool boundary from dimensional analysis. Scripta Mater. 60 (2009) 68-71.
34) P.J. Withers et al. Residual stress. Part 2 – Nature and origins. Mater. Sci. Technol. 17 (2001) 366-75.
35) P. Ferro et al. The influence of phase transformations on residual stresses induced by the welding process—3D and 2D numerical models. Model. Simul. Mater. Sci. Eng. 14 (2006) 117-36.
36) N.S. Bailey et al. Laser direct deposition of AISI H13 tool steel powder with numerical modeling of solid phase transformation, hardness, and residual stresses. J Mater. Process. Technol. 247 (2017) 223-33.

37) E.R. Denlinger et al. Residual stress and distortion modeling of electron beam direct manufacturing Ti-6Al-4V. Proceed. Inst. Mech. Eng. B: J Eng. Manuf. 229 (2015) 1803-13.
38) P. Prabhakar et al. Computational modeling of residual stress formation during the electron beam melting process for Inconel 718. Add. Manufac. 7 (2015) 83-91.
39) K. Kempen et al. Producing crack-free, high density M2 HSS parts by selective laser melting: preheating the baseplate. Proceed. 24th Int. Solid Freeform Fab. Symp. Austin (TX). (2013) 131–139.
40) S. Leuders et al. On the mechanical behaviour of titanium alloy TiAl6V4 manufactured by selective laser melting: fatigue resistance and crack growth performance, Int. J. Fatigue. 48 (2013) 300–307.
41) P. Edwards et al. Electron beam additive manufacturing of titanium components: properties and performance, J. Manuf. Sci. Eng. 135 (2013) 061016.
42) A.G. Gavras et al. Effects of microstructure on the fatigue crack growth behavior of light metals and design considerations, Matéria (Rio de Janeiro) 15 (2010) 319–329.
43) M. Collur et al. Mechanism of alloying element vaporization during laser welding. Metal. Trans. B 18 (1987) 733-740.
44) H. Zhao et al. Weld metal composition change during conduction mode laser welding of aluminum alloy 5182. Metal. Mater. Trans. B-Proc. Metal. Mater. Proc. Sci. 32 (2001) 163-72.
45) S.M. Gaytan et al. Advanced metal powder based manufacturing of complex components by electron beam melting. Mater. Technol. 24 (2009) 180–90.
46) K. Taminger. Electron beam additive manufacturing: state-of-the-technology, challenges & opportunities. Direct digital manufacturing workshop. Solomons (MD) (2010).
47) V. Juechter et al. Processing window and evaporation phenomena for Ti–6Al–4V produced by selective electron beam melting. Acta Mater. 76 (2014) 252-258.
48) L. Thijs et al. A study of the microstructural evolution during selective laser melting of Ti–6Al–4V. Acta Mater. 58 (2010) 3303-3312.
49) M. Xia et al. Porosity evolution and its thermodynamic mechanism of randomly packed powder-bed during selective laser melting of Inconel 718 alloy. Int. J Machine Tool. Manuf. 116 (2017) 96-106.

50) N.T. Aboulkhair et al. Reducing porosity in AlSi10Mg parts processed by selective laser melting. Add. Manuf. 1 (2014) 77–86.
51) A. Bauereiss et al. Defect generation and propagation mechanism during additive manufacturing by selective beam melting. J Mater. Process. Technol. 214 (2014) 2522–8.
52) A.E. Wilson-Heid et al. Characterization of the Effects of Internal Pores on Tensile Properties of Additively Manufactured Austenitic Stainless Steel 316L. Exp. Mech. (2018) 1-12.
53) Y. Huang et al. A comprehensive analytical model for laser powder-fed additive manufacturing, Add.. Manuf. 12 (2016) 90–99.
54) X. He et al. Transport phenomena during direct metal deposition, J Appl. Phys. 101 (2007).
55) S.A. Khairallah et al. Laser powder-bed fusion additive manufacturing: physics of complex melt flow and formation mechanisms of pores, spatter, and denudation zones, Acta Mater. 108 (2016) 36–45.
56) Q. Wu et al. Residual stresses and distortion in the patterned printing of titanium and nickel alloys. Add. Manuf. (2019) 100808.
57) J. Ibarra-Medina et al. Transient Modelling of Laser Deposited Coatings. 26th Int. Conf. Surf. Mod. Technol. Ecully, FR (2012).
58) M. Jamshidinia et al. Numerical modeling of heat distribution in the electron beam melting® of Ti-6Al-4V. J Manuf. Sci. Eng. 135 (2013) 061010.
59) Z. Nie et al. Experimental study and modeling of H13 steel deposition using laser hot-wire additive manufacturing. J Mater. Process. Technol. 235 (2016) 171-86.
60) E. Salvati et al. Eigenstrain reconstruction of residual strains in an additively manufactured and shot peened nickel superalloy compressor blade. Comput. Method. Appl. Mech. Eng. 320 (2017) 335-51.
61) G. Yu et al. On the role of processing parameters in thermal behavior, surface morphology and accuracy during laser 3D printing of aluminum alloy. J Phys. D: Appl. Phys. 49 (2016) 135501.
62) E. Kundakcioglu et al. Transient thermal modeling of laser-based additive manufacturing for 3D freeform structures. Int. J Adv. Manuf. Technol. 85 (2016) 493-501.
63) N. Hodge et al. Experimental comparison of residual stresses for a thermomechanical model for the simulation of selective laser melting. Add. Manuf. 12 (2016) 159-68.

64) J. Ding et al. Thermo-mechanical analysis of Wire and Arc Additive Layer Manufacturing process on large multi-layer parts. Comp. Mater. Sci. 50 (2011) 3315-22.
65) B. Cheng et al. Stress and deformation evaluations of scanning strategy effect in selective laser melting. Add. Manuf. 12 (2016) 240-51.
66) S. Jayanath et al. A Computationally Efficient Finite Element Framework to Simulate Additive Manufacturing Processes. J Manuf. Sci. Eng. 140 (2018) 041009.
67) J. Ding et al. A computationally efficient finite element model of wire and arc additive manufacture. Int. J Adv. Manuf. Technol. 70 (2014) 227-36.
68) K. Mundra et al. Calculation of weld metal composition change in high-power conduction mode carbon dioxide laser-welded stainless steels. Metal. Trans. B 24 (1993) 145-155.
69) T. DebRoy et al. Probing laser induced metal vaporization by gas dynamics and liquid pool transport phenomena. J Appl. Phys. 70 (1991) 1313-9.
70) S. Anisimov et al. The dynamics of the expansion of a vapor when evaporated into a vacuum. Soviet J Exp. Theoretic. Phys. 37 (1973) 441-4.
71) C.J. Knight. Theoretical modeling of rapid surface vaporization with back pressure. AIAA J. 17 (1979) 519-23.
72) M. Tang et al. Prediction of lack-of-fusion porosity for powder bed fusion. Add. Manuf. 14 (2017) 39-48.
73) A.M. Rausch et al. Predictive Simulation of Process Windows for Powder Bed Fusion Additive Manufacturing: Influence of the Powder Bulk Density. Materials. 10 (2017) 1117.
74) H.G. Fan et al. Dynamic analysis of globular metal transfer in gas metal arc welding - a comparison of numerical and experimental results. J Phys. D: Appl. Phys. 31 (1998) 2929.
75) G. Xu et al. Three-dimensional modeling of arc plasma and metal transfer in gas metal arc welding. Int. J Heat Mass Trans. 52 (2009) 1709-24.

Chapter 3

HEAT TRANSFER AND FLUID FLOW CALCULATIONS FOR MULTI-LAYER, MULTI-HATCH COMPONENTS

In this chapter, the calculations of temperature and velocity fields and deposit geometries using 3D, transient heat transfer and fluid flow models for PBF-L, DED-L and DED-GMA are described. The models for three AM processes are modified starting from the fusion welding model developed at Penn State. The core engine of these models solves the equations of conservations of mass, momentum and energy. It is adapted from the original fusion welding model. However, depending on the different AM processes, modeling of heat sources, implementing boundary conditions, providing alloy properties, defining solution domain are the unique contributions of this thesis work and are described in detail in this chapter. In addition, this chapter also describes how a novel travelling grid approach is developed to enhance the computational efficiency of multi-layer, multi-hatch calculations. Estimations of residual stresses, distortion, composition change and lack of fusion defects using the results of the heat transfer and fluid flow models for three AM processes are described in subsequent chapters.

3.1 Mathematical formulation

The AM process is transient and the temperature and velocity fields are spatially variable in three dimensions [1]. Therefore, the mathematical formulation used here in the heat transfer and fluid flow model are in 3D. This sub-section summarizes the assumptions made in this model and provides the governing equations, heat sources and boundary conditions. Figure 3.1 shows a typical solution domain for PBF-L, as an example, consisting of the build, powder bed and substrate. The build shown in the Figure 3.1 may be printed using multiple layers and hatches.

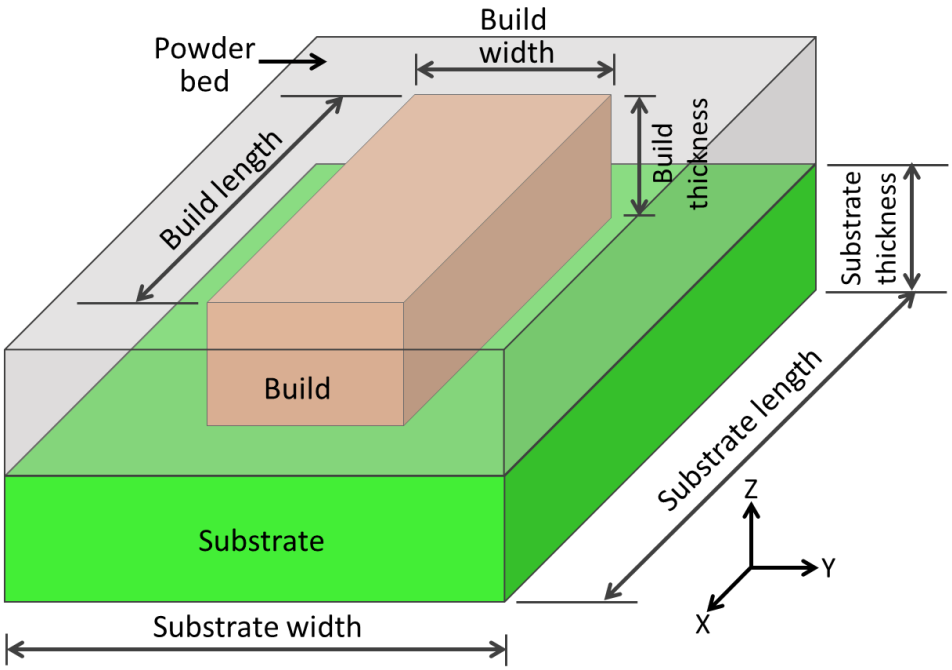

Figure 3.1. Schematic of a typical solution domain for PBF-L.

3.1.1 Assumptions

Several simplified assumptions are made in the heat transfer and fluid flow model to make the calculations tractable.

(a) Densities of powder, solid and liquid alloys in all three AM processes are assumed to be temperature independent except for the calculations of the buoyance force inside the molten pool. This assumption is known as the Boussinesq approximation and is commonly used in the calculations of buoyancy driven flow [2].

(b) The molten metal flow is assumed to be incompressible and Newtonian. The turbulence in the flow of liquid metal is considered through the use of the enhanced viscosity and thermal conductivity of the molten metal [3].

(c) The heat loss due to vaporization of alloying elements [1] is not considered in the calculations. The heat loss due to vaporization is estimated to be small compared to the heat input from the heat sources.

(d) The arc current in the DED-GMA is generally higher than 100 A. Therefore, metal transfer mode is assumed to be globular-type [4]. Droplet temperature is calculated based on net heat balance [5]. The droplet velocity is calculated based on arc plasma effect using the formula by Kumar and Bhaduri [6].

3.1.2 Governing equations

The heat transfer and fluid flow analysis in the molten pool and its surroundings commonly follows the equations of conservations of mass, momentum and energy in transient form in 3D Cartesian coordinate as [1]:

$$\frac{\partial(\rho u_i)}{\partial x_i} = 0 \tag{3-1}$$

$$\frac{\partial(\rho u_j)}{\partial t} + \frac{\partial(\rho u_j u_i)}{\partial x_i} = \frac{\partial}{\partial x_i}\left(\mu \frac{\partial u_j}{\partial x_i}\right) + S_{uj} - K_P \frac{(1-f_L)^2}{{f_L}^3 + B_N} u_j \tag{3-2}$$

$$\rho \frac{\partial h}{\partial t} + \frac{\partial(\rho u_i h)}{\partial x_i} = \frac{\partial}{\partial x_i}\left(\frac{k}{C_p}\frac{\partial h}{\partial x_i}\right) - \rho \frac{\partial \Delta H}{\partial t} - \rho \frac{\partial(u_i \Delta H)}{\partial x_i} + S_h \tag{3-3}$$

where ρ is the density, u_i and u_j are the velocity components along the i and j directions, respectively, x_i is the distance along the i direction, t is the time, μ is the viscosity, S_{uj} is the source term for the momentum equation that includes the driving forces for fluid motion, h is the sensible heat, C_p is the specific heat, k is the thermal conductivity, ΔH is the latent heat content, and S_h is the source term for the energy transfer that includes the volumetric heat sources.

The total enthalpy is the summation of the sensible heat (h) and the latent heat content (ΔH). The temperature values are calculated from this enthalpy by using the specific heat of the alloy. The last term on the right-hand side of Equation (3-2) is obtained from the Carman-Kozeny equation [7] that accounts for the frictional dissipation of flow velocity in the mushy region. The term f_L refers to the liquid fraction, K_P is a permeability coefficient, and B_N is a small numerical constant introduced to avoid division by zero when $f_L = 0$. The liquid fraction is assigned following the computed local temperature (T). For instance, $f_L = 1$ when $T \geq T_L$, and $f_L = 0$ when $T \leq T_S$, and, f_L varies linearly from 0 to 1 as T increases from T_S to T_L. The enthalpy-porosity formulation has the advantage that it does not require an explicit tracking of the location of liquid/solid interface nor does it require imposing any boundary condition at such interface.

3.1.3 Modeling of heat sources

In a powder bed, the absorption of a focused laser beam is not limited to its surface because of the multiple reflections of the beam within the bed. In powder feeding systems such as DED-L, the powders are preheated as they travel through the beam and the preheat of the

powders needs to be considered for accurate thermal simulation. Mechanistic modeling of the heat source requires consideration of the important physical processes that are specific to the individual AM processes, which is presented below.

PBF-L

In PBF-L process, the absorption of laser energy is significantly enhanced due to the multiple reflections and absorptions inside the powder bed [8]. Therefore, the heat input is approximated as a volumetric heat source which is axisymmetric about the laser beam axis. The power density distribution of the heat source can be expressed by the following equation which considers the laser power (P_L), laser beam radius (r_b) and a power distribution factor (d) [1]:

$$S_v = \frac{d \in P}{\pi r_b^2 \lambda} \exp\left(-\frac{d (x_b^2 + y_b^2)}{r_b^2}\right) \tag{3-4}$$

where x_b and y_b are the x and y distances to the axis of the laser beam, respectively, λ is the powder layer thickness and $\in$ represents absorptivity. The distribution of the laser power is practically uniform along the depth of the powder layer which is typically between 30 and 200 micrometers [1]. For PBF-L, the laser absorptivity is high inside the powder layer due to the multiple reflections of the laser beam prior to melting. However, as the powder melts the absorptivity drops to the Fresnel absorptivity [9].

DED-L

In DED-L, the metal particles are heated during flight prior to their impingement to the depositing surface. The extent of heating of the particles depends on the residence time of the particles, particle size, gas velocity, material properties and laser power density. The temperature rise of the particles during their flight can be estimated from the approximate heat balance [1]:

$$\Delta T = \frac{\eta_m \eta_s \frac{P}{\pi r_b^2} (2\pi r_p^2)\tau}{(\frac{4}{3}\pi r_p^3) C_P \rho_p} \tag{3-5}$$

where ΔT is the average in-flight temperature rise of the powder particles, P is the laser power, r_b and r_p are the laser beam radius and the average radius of the particles, respectively, C_P is the specific heat, η_m is an interference factor to account for shielding of some particles from the laser beam by other particles, η_s is the fraction of available laser power absorbed by the solid particles, τ is the time of flight, and ρ_P is the density of the particles. The expression

assumes that the absorption of the laser beam occurs on half of the total surface area $(2\pi r_p^2)$ which is exposed to the heat source during flight. The calculation of the energy absorbed by the powders should further consider the latent heat of fusion if the heated powder particles are melted during flight.

A significant portion of the heat energy that remains after heating the powder particles impinges directly on the melting bed. The extent of energy absorbed by the deposit surface depends on beam characteristics, nature of the deposit and the shielding gas. The total amount of heat absorbed by the depositing surface, P_s, is given by:

$$P_s = \eta_l \, (1-\eta_p) \, P \tag{3-6}$$

where η_p and η_l are the fractions of the laser power absorbed by the powder and the growing layer, respectively. As a result, the value of η_l depends on both time and local temperature of the bed. The energy absorbed by the powder and the depositing layer is considered as a spatially dependent volumetric heat flux as follows:

$$q_{VL} = \frac{Pd}{\pi r_b^2 t}\left[\eta_p + \eta_l(1-\eta_p)\right] \exp\left(-d\,\frac{r^2}{r_b^2}\right) \tag{3-7}$$

where η_p is the fraction of laser energy absorbed by the powder during flight, P is laser power, d is laser energy distribution factor, t is layer thickness, and r is radial distance from laser beam axis. The two terms within the square bracket represent the fraction of laser energy transferred to the particles during their flight and the direct heating by the beam on the growth surface, respectively. The exponential term represents the spatial variation of heat source energy at various distance from the axis of the beam.

DED-GMA

In the DED-GMA process, the filler wire absorbs heat in a manner like that for a consumable electrode in fusion welding processes. A volumetric heat source is also used for the DED-GMA process. In DED-GMA, the energy from the hot metal droplets is distributed inside the fusion zone. This energy from the droplets can be assumed to uniformly distribute in a small cylindrical region underneath the melting filler wire [6]. The magnitude of the volumetric heat source, q_{VA}, is calculated from the following equation:

$$q_{VA} = \frac{H_d}{\pi h_e r_e^2} \tag{3-8}$$

where H_d is the heat content of the droplet, h_e and r_e are the effective height and radius of the cylindrical cavity, and the heat content of the droplets is calculated from the temperature of the droplet [10].

$$H_d = \rho \pi r_w^2 w_f \left[C_P \left(T_d - T_a \right) + \Delta H \right] \quad (3\text{-}9)$$

where ρ is the density of the material, r_w is the wire radius, w_f is the wire feed rate, C_P is the specific heat, T_d is the droplet temperature, T_a is the ambient temperature, and ΔH is latent heat. The dimensions of the cylindrical cavity are estimated by equating the total work done in creating the cavity and the kinetic energy of droplets. The effective height (h_e) and radius (r_e) of the cylindrical cavity are expressed as [6]:

$$r_e = a \quad (3\text{-}10)$$

$$\mathrm{h}_e = \mathrm{h}_c - x + a \quad (3\text{-}11)$$

where x is the distance traveled by the center of mass of the cylinder, a is the droplet diameter and h_c is the height of the cavity. The droplet diameter (a) depends on the electrode diameter and arc current [10].

The height of the cavity (h_c) is calculated by equating the total work done in creating the cavity (W) and the kinetic energy of drop (KE). The total work done in creating the cavity (W) is represented as [6]:

$$\mathrm{W} = \int_0^{h_c} (pdV + 2\pi a \gamma dH) \quad (3\text{-}12)$$

where γ is the coefficient surface tension, H denotes the height, V and p denote the volume and the hydrostatic pressure of the cylindrical cavity, respectively. The volume and hydrostatic pressure are represented as [6]:

$$\mathrm{V} = \pi a^2 h_c \quad (3\text{-}13)$$

$$p = \rho \mathrm{g} h_c \quad (3\text{-}14)$$

Therefore, the total work done in creating the cavity, W, can be obtained as:

$$\mathrm{W} = \pi a \left(\frac{1}{2} a \rho g h_c^2 + 2\gamma h_c \right) \quad (3\text{-}15)$$

The kinetic energy of drop is expressed as:

$$\mathrm{KE} = \frac{1}{2} m v_d^2 \quad (3\text{-}16)$$

where m is the droplet mass depends on droplet diameter (a) and density (ρ) and v_d is the velocity of droplets. Therefore, by equating the total work done in creating the cavity (W) and the kinetic energy of drop (KE), the cavity height (h_c) can be calculated as:

$$h_c = \left(-\frac{2\gamma}{a\rho g} + \sqrt{\left[\left(\frac{2\gamma}{a\rho g} \right)^2 + \frac{a v_d^2}{6g} \right]} \right) \quad (3\text{-}17)$$

The distance traveled by the center of mass of the cylinder (x) is calculated by solving the acceleration equation of droplets:

$$\frac{d^2x}{dt^2} = \left(g + \frac{2\gamma}{a\rho h_c} \right) - \frac{g}{h_c} x \quad (3\text{-}18)$$

where g is the acceleration due to gravity. By solving this equation,

$$x = \left(h_c + \frac{2\gamma}{a\rho g} \right) \left\{ 1 - cos \left[\left(\frac{g}{h_c} \right)^{1/2} t \right] \right\} \quad (3\text{-}19)$$

where t is the time that is inverse to the droplet frequency (D). The droplet frequency (D) depends on wire feed rate (w_f), wire radius (r_w) and droplet diameter (a) and is represented as:

$$D = \frac{\pi {r_w}^2 w_f}{\frac{1}{6}\pi a^3} \quad (3\text{-}20)$$

3.1.4 Boundary conditions

The surface heat flux and the heat losses can be implemented on the surfaces of the deposit and substrate as boundary conditions of the energy conservation equation as:

$$k \frac{\partial T}{\partial \vec{n}} = q_{in} - q_{conv} - q_{rad} - q_{vapor} \quad (3\text{-}21)$$

where k is the thermal conductivity, $\frac{\partial T}{\partial \vec{n}}$ is the temperature gradient along the surface normal direction ($\vec{n}$), q_{in} is the heat input from the heat source and q_{conv}, q_{rad} and q_{vapor} are the heat loss by convection, radiation and vaporization, respectively. The heat loss due to radiation is given as:

$$q_{rad} = \sigma\varepsilon(T^4 - T_A^4) \quad (3\text{-}22)$$

where, σ is the Stefan-Boltzmann constant (5.67×10^{-8} Wm^{-2} K^{-4}), ε is the emissivity, T_A is the ambient temperature. The heat loss to surrounding due to shielding gas flow is given as [1]:

$$q_{conv} = h_c(T - T_A) \quad (3\text{-}23)$$

where h_c is the convective heat transfer coefficient. The heat loss due to vaporization is given as [11]:

$$q_{vapor} = \sum_{i=1}^{n} J_i \Delta H_i \quad (3\text{-}24)$$

where n is the number of the alloying elements, J_i is the vaporization flux of element i, ΔH_i is the enthalpy of vaporization of the element i. Volumetric heating due to viscous friction of liquid metal flow and Joule heating due to electric current flow in DED-GMA are typically much smaller than the heat input from the heat sources and are thus ignored.

Marangoni shear stresses on the top surface of the molten pool are applied as the boundary conditions in the fluid flow calculations. For PBF-L, the top surface of the molten pool is flat. Therefore, the temperature gradient has two components along X and Y directions i.e. G_x and G_y respectively. The Marangoni shear stresses along X and Y directions on the top surface of the molten pool can be written as,

$$\tau_x = \mu \frac{du}{dz} = -\frac{d\gamma}{dT} G_x \quad (3\text{-}25)$$

$$\tau_y = \mu \frac{dv}{dz} = -\frac{d\gamma}{dT} G_y \quad (3\text{-}26)$$

where μ is the viscosity of the liquid metal. The surface tension of the liquid metal (γ) depends both on temperature and alloy composition. However, deposit with curved surfaces are typically observed in DED-L and DED-GMA processes. Therefore, the boundary conditions depend on the temperature gradient along the 3D curved surface along the x-, y-, and z-directions (G_x, G_y, G_z, respectively) as shown in Figure 3.2. The Marangoni stresses at any point on the curved surface along the x-, y-, and z-directions are obtained from the following relations:

$$\tau_x = \mu \frac{du}{dz} = -\frac{d\gamma}{dT} G_x \quad (3\text{-}27)$$

$$\tau_y = \mu \frac{dv}{dz} = -\frac{d\gamma}{dT} G_y \quad (3\text{-}28)$$

$$\tau_z = \mu \frac{du}{dr} = -\frac{d\gamma}{dT} G_z \quad (3\text{-}29)$$

where r is the radial distance from the central axis of the heat source, and u, v, and w are the velocities of the liquid metal along the x-, y-, and z-directions, respectively.

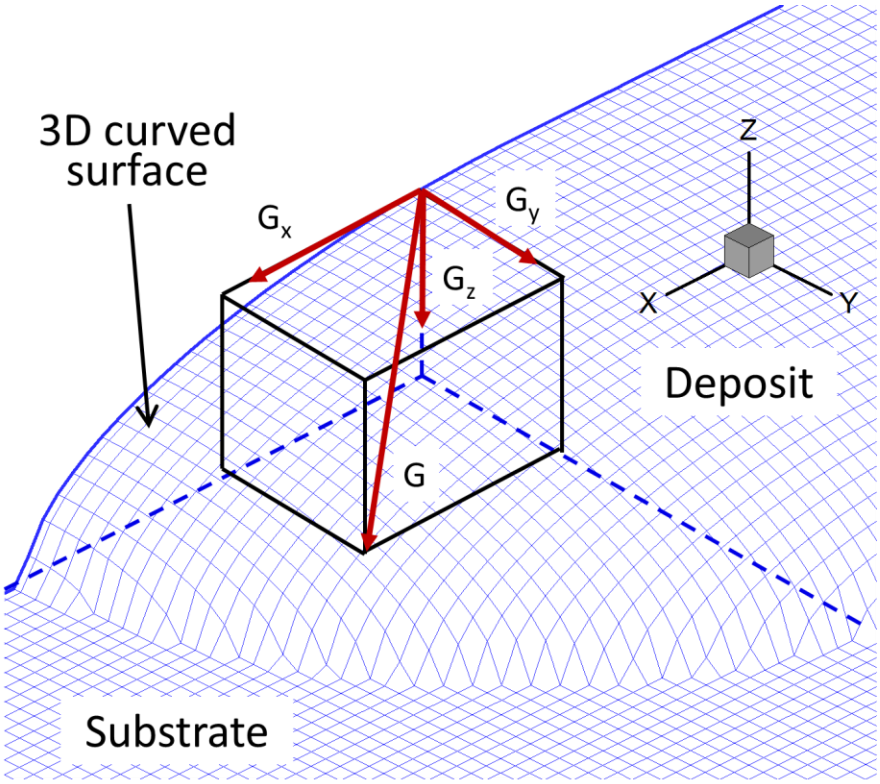

Figure 3.2. Three components of temperature gradient on a curved deposit surface in DED.

3.2 Temperature dependent thermo-physical properties of alloys

Calculations of heat, mass, and momentum transfer during AM processes require thermophysical properties of alloys such as thermal conductivity, specific heat, density, latent heat, viscosity and liquidus and solidus temperatures [1]. Properties responsible for the heat transport such as thermal conductivity and specific heat vary significantly with temperature. Therefore, assumption of constant values of these properties may result in errors in the calculated results. In this sub-section, implementation process of temperature dependent alloy properties for three AM processes are described. In addition, thermodynamic calculations of properties of graded alloys with varying compositions are also explained.

3.2.1 Implementation of single alloy properties

In AM, the most commonly used alloys are stainless and tool steels, titanium alloys, nickel based super alloys and aluminum alloys. Table 3.1 summarizes temperature dependent thermo-physical properties [1] of commonly used alloys that are used in the calculations.

Table 3.1. Thermo-physical properties of commonly used alloys in additive manufacturing. 'T' denotes the temperature in K varies between room temperature to solidus temperature [1].

Properties	SS 316	Ti-6Al-4V	IN 718	H 13	800 H	AlSi10Mg
Liquidus temperature (K)	1733	1928	1609	1725	1675	867
Solidus temperature (K)	1693	1878	1533	1585	1608	831
Thermal conductivity (W/m K)	$11.82 + 0.0106\ T$	$1.57 + 1.6 \times 10^{-2}\ T - 1 \times 10^{-6}\ T^2$	$0.56 + 2.9 \times 10^{-2}\ T - 7 \times 10^{-6}\ T^2$	$18.29 + 7.5 \times 10^{-3}\ T$	$0.51 + 2.0 \times 10^{-2}\ T - 6 \times 10^{-6}\ T^2$	$113 + 1.06 \times 10^{-5}\ T$
Specific heat (J/ kg K)	$330.9 + 0.563\ T - 4.015 \times 10^{-4}\ T^2 + 9.465 \times 10^{-8}\ T^3$	$492.4 + 0.025\ T - 4.18 \times 10^{-6}\ T^2$	$360.4 + 0.026\ T - 4 \times 10^{-6}\ T^2$	$341.9 + 0.601\ T - 4.04 \times 10^{-4}\ T^2$	$352.3 + 0.028\ T - 3.7 \times 10^{-6}\ T^2$	$536.2 + 0.035\ T$
Density (kg/m^3)	7800	4000	8100	7900	7270	2670
Viscosity (kg/m s)	7×10^{-3}	4×10^{-3}	5×10^{-3}	7×10^{-3}	7.5×10^{-3}	1.3×10^{-3}
$d\gamma/dT$ (N/m K)	-0.40×10^{-3}	-0.26×10^{-3}	-0.37×10^{-3}	-0.43×10^{-3}	-0.40×10^{-3}	-0.35×10^{-3}

PBF-L

In the PBF-L process, the effective thermo-physical properties of the packed powder bed depend on the shielding gas entrapped among the powder particles and the packing efficiency of the powder bed [1]. Table 3.2 provides the thermo-physical properties [12-14] of shielding gases commonly used in AM processes. The effective density (ρ_e) and specific heat (Cp_e) of the powder bed are written as [15]:

$$\rho_e = \rho_s \eta + \rho_g (1-\eta) \tag{3-30}$$

$$Cp_e = \frac{\rho_s \eta Cp_s + \rho_g (1-\eta) Cp_g}{\rho_s \eta + \rho_g (1-\eta)} \tag{3-31}$$

where η is the powder packing density of the powder bed, ρ_s and ρ_g are densities of the solid and gas, respectively and Cp_s and Cp_g are specific heat of the solid and the gas, respectively. The effective density of the powder bed is not strongly affected by the nature of the gas, since the density of the solid is significantly higher than the density of the gas. Therefore, for a given

powder bed, the effective density is proportional to the powder packing density. However, the effective specific heat of the powder bed depends significantly on the specific heat of the shielding gas.

Table 3.2. Thermo-physical properties of common shielding gases, Argon [13], Nitrogen [12, 13] and air [14]. Here 'T' represents temperature in K.

Properties	Argon	Nitrogen	Air
Density (Kg/m^3) at ambient temperature	0.97	1.25	1.20
Specific heat (J/kgK)	519 at ambient temperature	1040 at ambient temperature	$1034.09 - 0.285\ T + 0.782 \times 10^{-3}\ T^2 - 0.497 \times 10^{-6}\ T^3$
Thermal conductivity (W/mK)	$\frac{-0.1125}{\sqrt{T}} + 1.35 \times 10^{-3}\sqrt{T} + 1.453 \times 10^{-7}\ T^{1.5}$	$\frac{-0.0924}{\sqrt{T}} + 1.65 \times 10^{-3}\sqrt{T} + 5.255 \times 10^{-7}\ T^{1.5}$	$-2.276 + 0.126\ T - 1.481 \times 10^{-4}\ T^2 + 1.735 \times 10^{-7}\ T^3$
Range of temperature 'T' (K)	300-4500	300-2200	300-1050

Effective thermal conductivity of the powder bed is significantly affected by the powder particle shape and size and inter-particle distance. Therefore, a simplified formula [16] considering both these factors is used to represent the effective thermal conductivity of the powder bed (k_e):

$$k_e = k_g \frac{\eta N}{2}\left[0.5\ln(1+L) + \ln\left(1+\sqrt{L}\right) + \frac{1}{1+\sqrt{L}} - 1\right] \qquad (3\text{-}32)$$

where k_g is the thermal conductivity of the gas in W/mK, N is the coordination number and L is a ratio of a constant and powder particle diameter. The value of the constant depends on the shielding gas type and for Ar its value is 5.4×10^{-4} m^{-1} [16].

Figure 3.3 shows the variations in effective thermal conductivity of the powder bed (stainless steel 316 powder + Ar gas) with temperature. For higher packing density, it is easier to transfer heat from one particle to another due to increased area of contact. Therefore,

effective thermal conductivity of powder bed increases with packing efficiency as shown in Figure 3.3 (a). The interparticle space decreases with reduction in particle size. Therefore, the effective thermal conductivity of the powder bed increases with smaller powder particles as shown in Figure 3.3 (b).

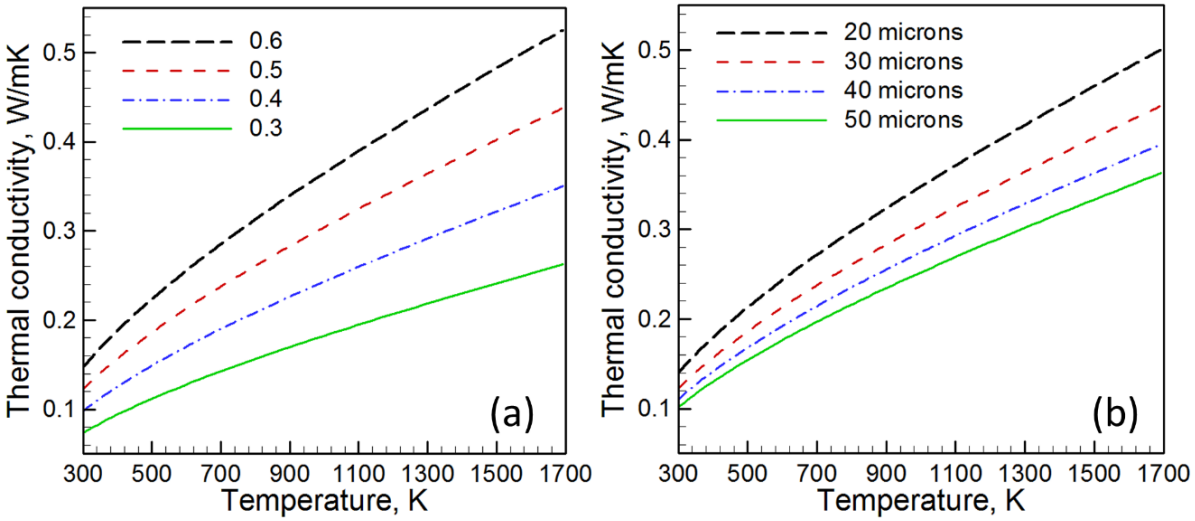

Figure 3.3. Variation of the computed effective thermal conductivity using Equation (3-32) of the powder bed (stainless steel 316 powder + Ar gas) with respect to temperature for different (a) packing efficiency of the powder bed and (b) powder particle diameter. In figure (a), packing efficiency is defined by the ratio of the net volume of powders to the total volume of the bed.

Figure 3.4 (a-b) show the temporal variations in temperature, thermal conductivity and specific heat for a location on the top surface of a stainless steel 316 part. The initial temperature at that location is room temperature (300 K). The thermal conductivity and specific heat at this location are assigned as effective values, k_e and Cp_e respectively. When the laser beam reaches the location at time t_1, the temperature at the location exceeds the liquidus temperature of the alloy (1693 K) and the thermophysical properties of the liquid are assigned there. When the temperature is between the solidus and liquidus temperatures, the thermophysical properties are linearly interpolated between the two temperatures. As the laser beam moves away from the location, the temperature drops to the solidus temperature of the alloy at time t_2 and the location solidifies. Therefore, after time t_2, thermal conductivity and specific heat of the solid alloy are applied at that location. As the location cools both thermal conductivity and specific heat of the location decreases with the temperature. Using this method, temperature dependent thermo-physical properties are assigned to all grid points in the solution domain. This process continues until the printing process is done and the deposit cools down to the room temperature.

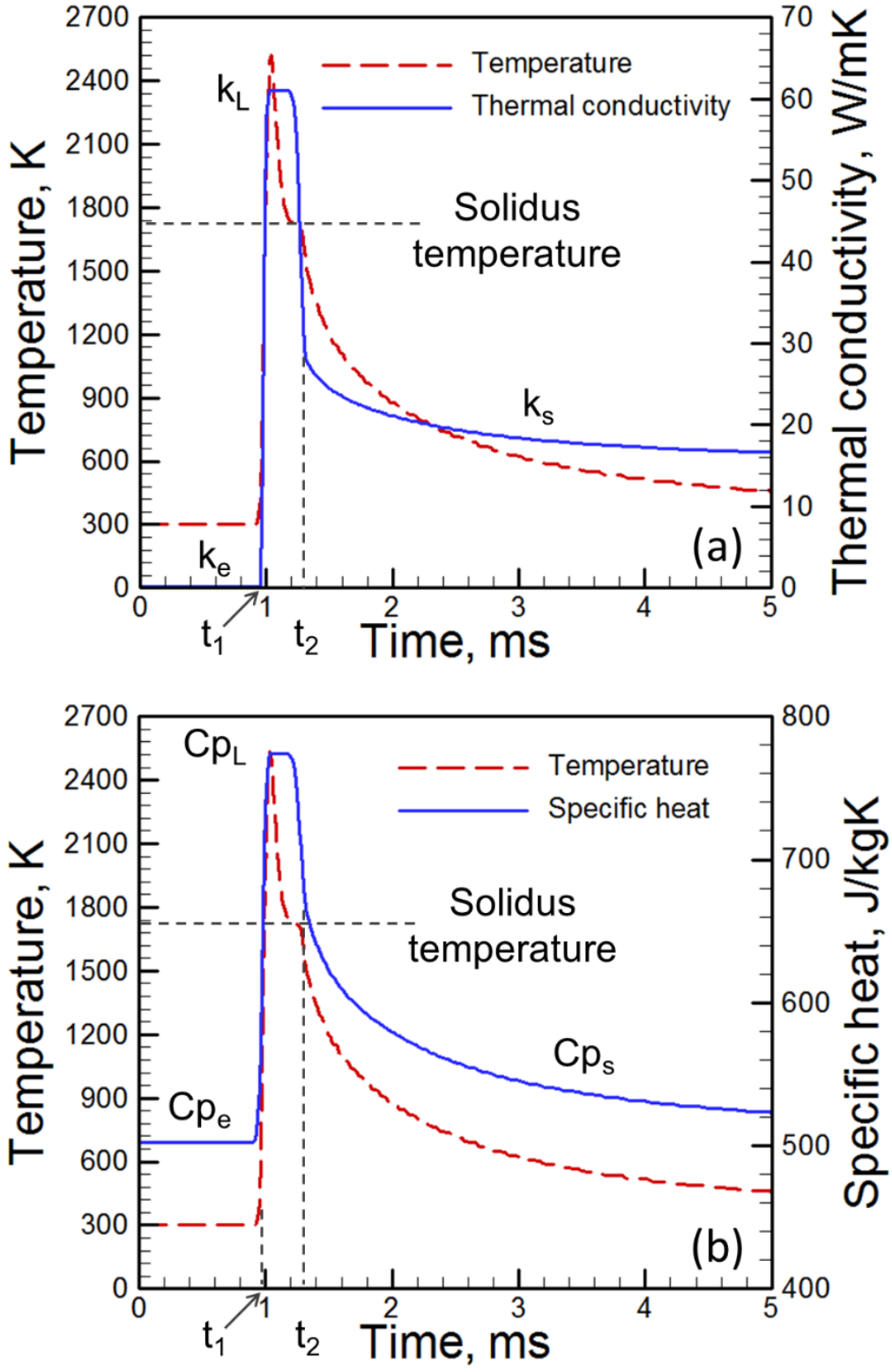

Figure 3.4. Variation of temperature and (a) thermal conductivity (k) and (b) specific heat (Cp) with time for a particular location on the top surface of a stainless steel 316 build using 60 W laser power and 1000 mm/s scanning speed. The suffix 'e', 'L' and 's' denote the effective properties of powder bed, properties of liquid and powder (or solid) respectively.

DED-L and DED-GMA

Unlike the PBF processes where feedstock materials are supplied as powders, in DED, the assignment of properties of the feedstock depends on the type of the materials such as wire in DED-GMA and powder in DED-L. Generally, the properties of the wire feedstock are the same as the alloy as provided in Table 3.1. However, in the DED-GMA processes with preheating of the wire, the properties are updated based on the preheating temperature as expressed in Table 3.1. However, in the DED-L process, the powder feedstock has high surface to volume ratio and different heat transfer and heat absorption characteristics compared to the solid alloy.

Assignment of the thermophysical properties to the substrate, deposited track and molten pool are identical for both DED-L and DED-GMA processes. At the beginning of the process, the substrate is assigned with the properties at room temperature or at a specified preheat temperature. During the process, the properties of the substrate and already deposited tracks are updated based on the temperature field as provided in Table 3.1. Inside the molten pool where the temperature is higher than the liquidus temperature of the alloy, properties of the liquid alloy are assigned. Inside the solid-liquid two phase region where the temperature is between the solidus and liquidus temperatures of the alloy, the thermophysical properties are updated based on both the temperature and the liquid fraction. Properties at every grid point are updated when new values of temperatures are obtained by iteration.

3.2.2 Thermodynamic calculations of properties for graded alloys

During the fabrication of compositionally graded joints, local chemical compositions can extend into regions where experimental property data are not available and approximations such as simplified phase diagrams, stress-strain plots and dilute alloy properties are not applicable. An alternative for determining important material properties is through numerical modeling based on interactions among elements. JMatPro® is a thermodynamic program designed for materials processing applications that models important alloy properties such as equilibrium phases, phase transformations, thermo-physical properties and mechanical behavior [17].

The prediction of thermo-physical properties using CALPHAD involves the following steps. First, the equilibrium fractions of phases are determined by minimizing the total Gibbs energy using thermodynamic excess functions. The property, *PR*, for a particular phase is expressed as [18],

$$PR = \sum_i MF_i\, PR_i + \sum_i \sum_{j>1} MF_i MF_j \sum_v \Omega_{ij}^v\, (MF_i - MF_j)^v \qquad (3\text{-}33)$$

where, PR_i is the property of the phase in the pure element, Ω_{ij}^v is a binary interaction parameter between elements *i* and *j* dependent on an integer, *v*. MF_i and MF_j are the mole fractions of *i* and *j* in the phase, respectively. Both PR_i and Ω_{ij}^v are temperature-dependent to incorporate the effects of temperature on alloy properties. The total property of the graded alloy is then determined from the mass fractions and properties of each phase using the law of mixtures [19]. Calculated thermo-physical properties of two graded alloys between 2.25Cr-1Mo steel and alloy 800 H and Ti-6Al-4V and alloy 800 H are provided in Table 3.3 and 3.4 respectively. These thermodynamically calculated property values for the graded alloys are used for the simulations of graded joints printed using DED-L between 2.25Cr-1Mo steel and alloy 800 H as well as between Ti-6Al-4V and 800 H, as described in Section 4.4.

Table 3.3. Thermo-physical properties of the transition joint between 2.25Cr-1Mo steel and alloy 800 H. Here 'T' represents temperature in K.

Composition of the joint (wt.% of 800H)	Liquidus temperature (K)	Solidus temperature (K)	Thermal conductivity (W/m K)	Specific heat (J/ kg K)	Density (kg/m^3)	dγ/dT (N/m K)
10%	1770	1746	12.25 + 0.0125 T	413.4 + 0.1672 T	7840	-0.38×10^{-3}
20%	1758	1736	11.16 + 0.0125 T	407.6 + 0.1672 T	7890	-0.35×10^{-3}
30%	1746	1707	10.20 + 0.0125 T	322.3 + 0.2508 T	7940	-0.34×10^{-3}
40%	1736	1689	9.53 + 0.0125 T	319.4 + 0.2508 T	7970	-0.33×10^{-3}
50%	1727	1671	9.03 + 0.0125 T	324.0 + 0.2508 T	7940	-0.31×10^{-3}
60%	1713	1650	8.65 + 0.0125 T	327.3 + 0.2508 T	7920	-0.30×10^{-3}
70%	1704	1634	8.44 + 0.0125 T	326.9 + 0.2508 T	7910	-0.28×10^{-3}
80%	1694	1626	8.32 + 0.0125 T	321.0 + 0.2508 T	7900	-0.27×10^{-3}
90%	1684	1617	8.36 + 0.0167 T	314.3 + 0.2508 T	7880	-0.25×10^{-3}

Table 3.4. Thermo-physical properties of the transition joint between Ti-6Al-4V and alloy 800 H. Here 'T' represents temperature in K.

Composition of the joint (wt.% of 800H)	Liquidus temperature (K)	Solidus temperature (K)	Thermal conductivity (W/m K)	Specific heat (J/ kg K)	Density (kg/m^3)	$d\gamma/dT$ (N/m K)
10%	1903	1851	$1.47 + 0.017\ T - 2 \times 10^{-6}\ T^2$	$478.8 + 0.2519\ T$	4330	-0.27×10^{-3}
20%	1877	1824	$1.37 + 0.019\ T - 2 \times 10^{-6}\ T^2$	$465.6 + 0.2530\ T$	4650	-0.29×10^{-3}
30%	1852	1797	$1.27 + 0.020\ T - 3 \times 10^{-6}\ T^2$	$452.4 + 0.2541\ T$	4980	-0.30×10^{-3}
40%	1827	1770	$1.16 + 0.021\ T - 3 \times 10^{-6}\ T^2$	$439.2 + 0.2552\ T$	5310	-0.32×10^{-3}
50%	1802	1743	$1.06 + 0.023\ T - 4 \times 10^{-6}\ T^2$	$425.9 + 0.2563\ T$	5640	-0.33×10^{-3}
60%	1776	1716	$0.96 + 0.024\ T - 5 \times 10^{-6}\ T^2$	$412.7 + 0.2574\ T$	5960	-0.34×10^{-3}
70%	1751	1689	$0.86 + 0.025\ T - 5 \times 10^{-6}\ T^2$	$399.5 + 0.2584\ T$	6290	-0.36×10^{-3}
80%	1726	1662	$0.76 + 0.027\ T - 6 \times 10^{-6}\ T^2$	$386.3 + 0.2595\ T$	6620	-0.37×10^{-3}
90%	1700	1635	$0.66 + 0.028\ T - 6 \times 10^{-6}\ T^2$	$373.1 + 0.2606\ T$	6940	-0.39×10^{-3}

3.3 Traveling grid system to enhance computational efficiency

Simulation of large components printed using multiple hatches and layers requires a large number of grid points and high computation time. A conventional fixed grid system where grids are specified at the beginning of the calculations and remain fixed throughout the entire process is not very efficient because a large number of fine grids are needed throughout

the calculation domain during the entire simulation process. In this research, an adaptive travelling grid system is developed and used to avoid that problem. A fine grid region near the moving heat source that travels with the heat source, is used. Figure 3.5 (a) shows the grid system on the XY plane at the beginning of the printing process. The grid is very fine near the heat source axis so that the entire molten pool is contained inside this fine grid region. The grids are coarser elsewhere. The size of the x-grids increase gradually away from the fine grid region. The x-coordinate of a particular x-grid (i) can be written as,

$$x = L_t \left(\frac{i}{N_g}\right)^m \qquad \text{for m>0} \qquad (3\text{-}34)$$

$$x = L_t \left[1 - \left(1 - \frac{i}{N_g}\right)^{-m}\right] \qquad \text{for m<0} \qquad (3\text{-}35)$$

where L_t and N_g are the total length of the solution domain and total numbers of grid points, respectively. The grid size changes along the length of the solution domain depending on the value of the constant m. The fine grid region travels with the heat source along the scanning direction (positive x-axis). The number of x-grids ahead and behind the fine grid region are adjusted to keep the total number of x-grids constant. Figure 3.5 (b) shows the grids at the end of a hatch in a particular layer. For a new hatch, the fine grid region moves back to its initial position same as that shown in Figure 3.5 (a). However, all calculated variables are to be remapped from the previous grids to the current grids. Figure 3.5 (c) shows that the grid shifts from its previous position A′B′C′D′ to its current position ABCD. Therefore, a variable, Φ for the grid point A, $\Phi(A)$ can be interpolated from the values at the previous step as,

$$\Phi(A) = \Phi'(A') + \frac{[\Phi'(D') - \Phi'(A')]\ \ [x(A) - x(A')]}{x\ (D') - x(A')} \qquad (3\text{-}36)$$

where x denotes the x-coordinate of a particular grid point and the dash in the superscript represents the values of the previous step. Similarly, the values of the variables are calculated for all grid points. Therefore, for a particular grid point (i), the equation can be written as,

$$\Phi(i) = \Phi'(i') + \frac{[\Phi'\{(i+1)'\} - \Phi'(i')]\ \ [x(i) - x(i')]}{x\ \{(i+1)'\} - x(i')} \qquad (3\text{-}37)$$

After the variables are interpolated and remapped from the previous to the current grid system, the iterative calculations for that particular location of the heat source are started. Similar process continues until the simulations of all layers and hatches are finished.

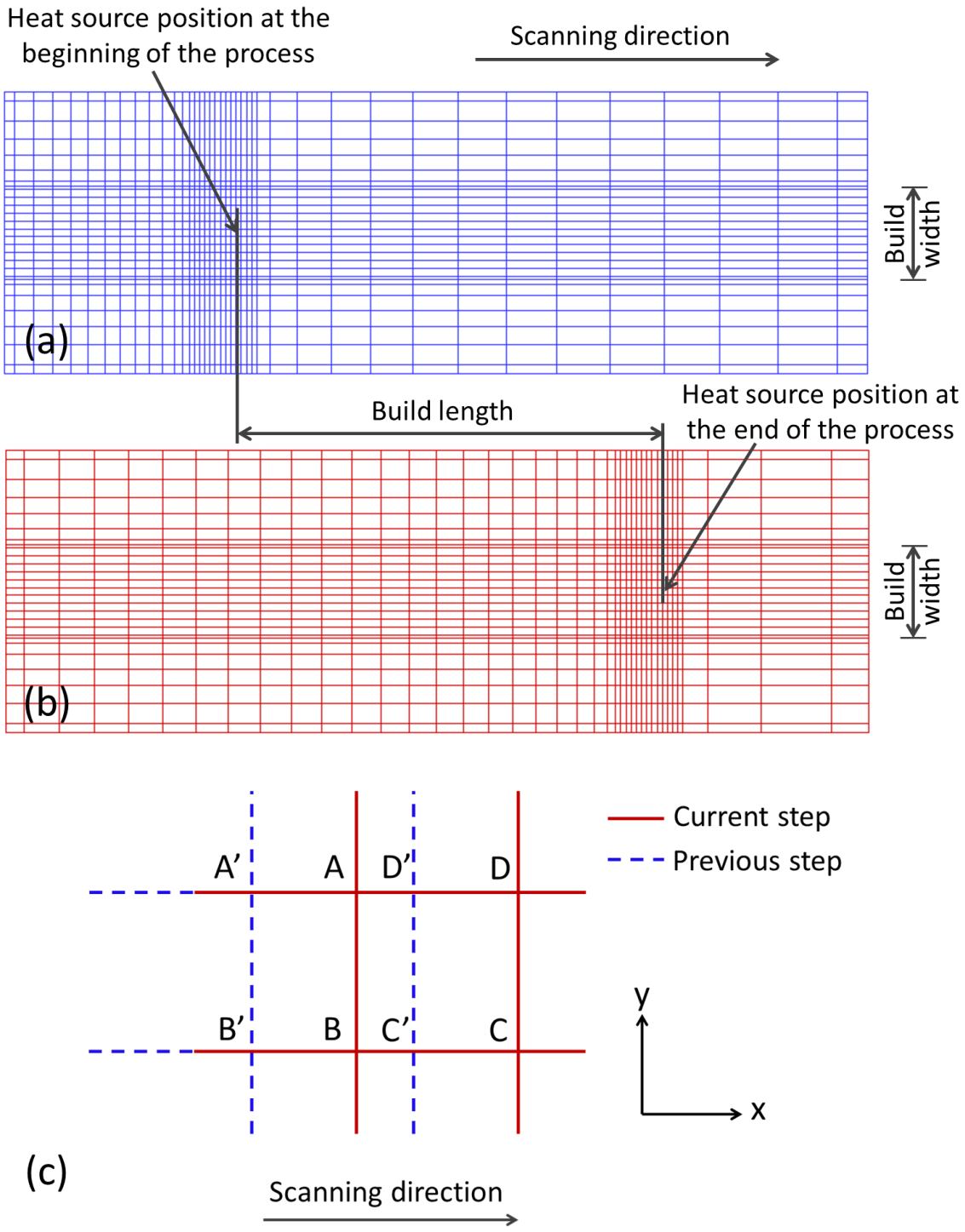

Figure 3.5. Schematic representation of the grid system on the top surface of the solution domain at the (a) beginning and (b) end of the process. (c) Schematic representation of the travelling grid where the grid shifts from its previous position A'B'C'D' to its current position ABCD.

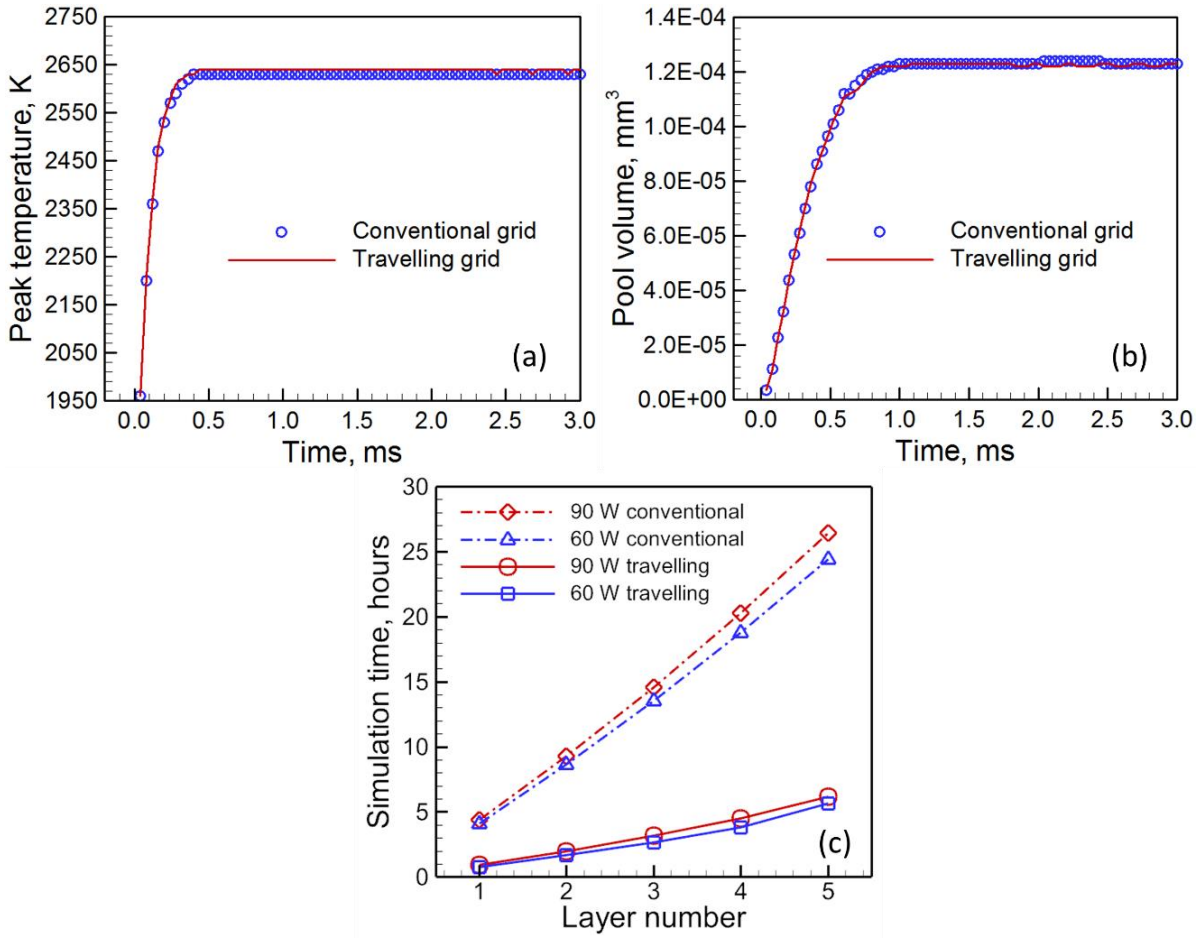

Figure 3.6. Comparison of the calculated (a) peak temperature and (b) pool volume with the progress of the building process using traveling grid and conventional fixed grid. Both the plots are for a stainless steel 316 build printed by PBF-L using 60 W laser power and 250 mm/s scanning speed. (c) Simulation time for different layers for PBF-L of a 5 layers 5 hatches stainless steel 316 build with 1000 mm/s scanning speed and 60 W and 90 W laser powers using traveling and conventional fixed grid systems.

Variations of calculated peak temperature and pool volume with building time using both conventional and traveling grid systems are shown in Figure 3.6 (a) and (b) respectively. Both peak temperature and pool volume continue to increase with the progress of the process for a particular hatch and reach steady state after a certain time. The calculated values of both the peak temperature and pool volume using the traveling grids match exactly with the results obtained using the conventional fixed grid for the same processing conditions. Figure 3.6 (c) shows the simulation time needed for different layers in a 20 mm long 5 layers, 5 hatches stainless steel 316 build. Since total number of grids increases with number of layers, the simulation time is higher for the upper layers. Higher laser power results in larger molten pool that increases the size of the solution domain for the fluid flow calculations. Therefore, the

simulation time for the deposition with a 90 W laser power is higher than that that required for a 60 W power. In conventional fixed grid system, fine grids are required for the entire component. As a result, the total number of grids for the conventional fixed grid system is much more than that required for the travelling grid system. Therefore, the simulation time can be significantly reduced by using the traveling grid system. These aforementioned results provide confidence of using the traveling grid system to achieve better computational efficiency without sacrificing any calculation accuracy.

3.4 Estimation of free surface of the molten pool

While modeling of fluid flow in the molten pool, the profile of the pool surface is not known *a priori* and varies with time. The molten pool surface geometry must be determined explicitly to apply appropriate boundary conditions. The surface profile of the fusion zone can be estimated by minimizing the total energy on the top surface of the molten pool. The total energy includes the surface energy due to the change in area of the pool surface, the potential energy and the recoil force and the work performed by the arc pressure displacing the pool surface.

The arc pressure (P_a) depends on the total arc force on the top surface of the molten pool [20]. Average droplet impact force on the top surface of the molten pool depends on droplet mass, velocity and transfer frequency [21]. The pressure due to the droplet impact (P_d) is essentially the impact force per unit area and is assumed to have Gaussian distribution on the top surface of the molten pool. The following two equations are solved to obtain the fusion zone surface profile [21]:

$$\gamma\left\{\frac{(1+\phi_y{}^2)\phi_{xx}-2\phi_x\phi_y\phi_{xy}+(1+\phi_x{}^2)\phi_{yy}}{(1+\phi_x{}^2+\phi_y{}^2)^{3/2}}\right\}=\rho g\phi+P_a+\lambda \tag{3-38}$$

$$\int(\phi_s-z_0)dy-\frac{\pi r_w^2 w_f}{U_w}=0 \tag{3-39}$$

Subscripts x and y in Equation (3-38) represent partial derivative with respect to x and y, respectively, γ is the surface tension, and λ is the Lagrange multiplier. In Equation (3-39), r_w, w_f and U_w are the wire radius, wire feeding rate and the welding speed, respectively, and ϕ_s is the solidified surface profile, z_0 is the z location of the specimen top surface. Equation (3-38) represents the static force balance at the fusion zone surface, while Equation (3-39) defines

mass conservation where the deposited area, A_{FW}, at a solidified cross section of the fusion zone is equal to the amount of feedstock per unit length as shown in Figure 3.7. To obtain the free surface profile, both equations need to be solved. These equations are discretized using the finite difference method. It is then solved using the Gauss-Seidel point-by-point method for an assumed λ with appropriate boundary conditions. The resulting free surface profile is applied to the mass conservation equation, and the residual (defined as the left hand side of Equation (3-38)) is evaluated. The value of λ is determined iteratively using the bisection method until both Equation (3-38) and (3-39) are satisfied.

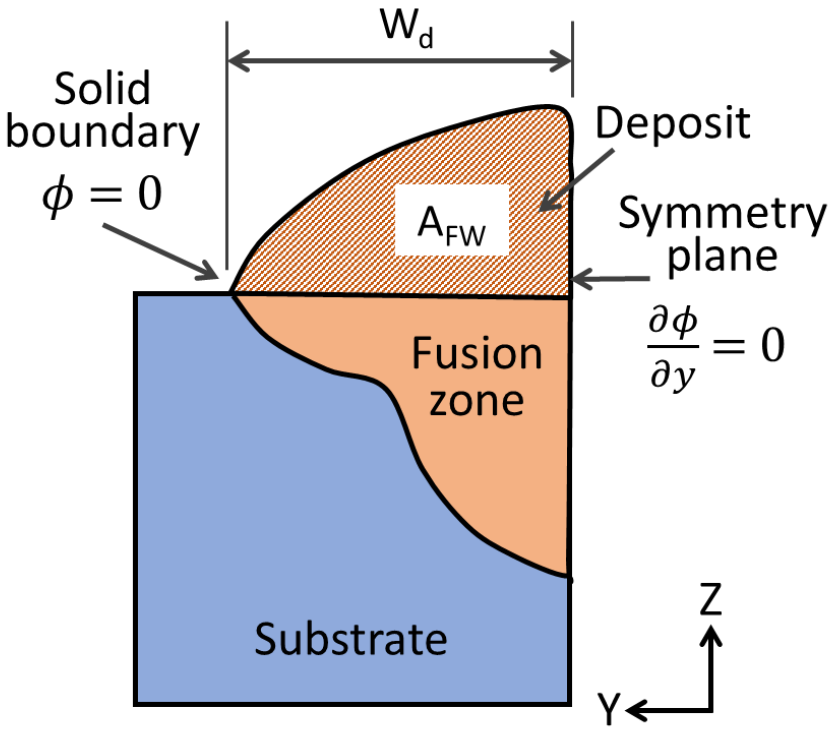

Figure 3.7. Schematic representation of the calculations of free surface.

3.5 Numerical solution approach

Transient equations of conservation of mass, momentum and energy in 3D are very challenging to solve analytically. Therefore, a control volume based finite difference method is used to numerically solve these equations in a 3D solution domain. This sub-section describes the method of discretizing the equations into small control volumes and the step by step solution procedure. In addition, the numerical stability and convergence criteria of the model are also discussed.

3.5.1 Discretization of the governing equations

The solution domain is divided into small rectangular control volumes, as shown in Figure 3.8. The three components of velocity along X, Y and Z directions are represented as u, v and w, respectively. The dashed lines represent control volume's interfaces and solid dots indicate the scalar grid points. A scalar grid point is located at the center of each control volume, storing the values of scalar quantities such as pressure and enthalpy. Grid points w, e, s, n, b, t are of east, west, south, north, bottom, and top neighbors of the grid point P, respectively. The positions of the velocity components are at the control volume faces, staggered with respect to the scalar locations. For example, velocities v_s and v_n are placed at the south and north faces of the scalar control volume of the grid point P. Therefore, the discretized governing equation of a variable, Φ (enthalpy, velocity or pressure) for a control volume with grid point P is formulated by integrating the equation as [22],

$$a_P \Phi_P = a_n \Phi_n + a_s \Phi_s + a_e \Phi_e + a_w \Phi_w + a_t \Phi_t + a_b \Phi_b + f \qquad (3\text{-}40)$$

where 'a' denotes the convection-diffusion co-efficients and 'f' includes the source terms.

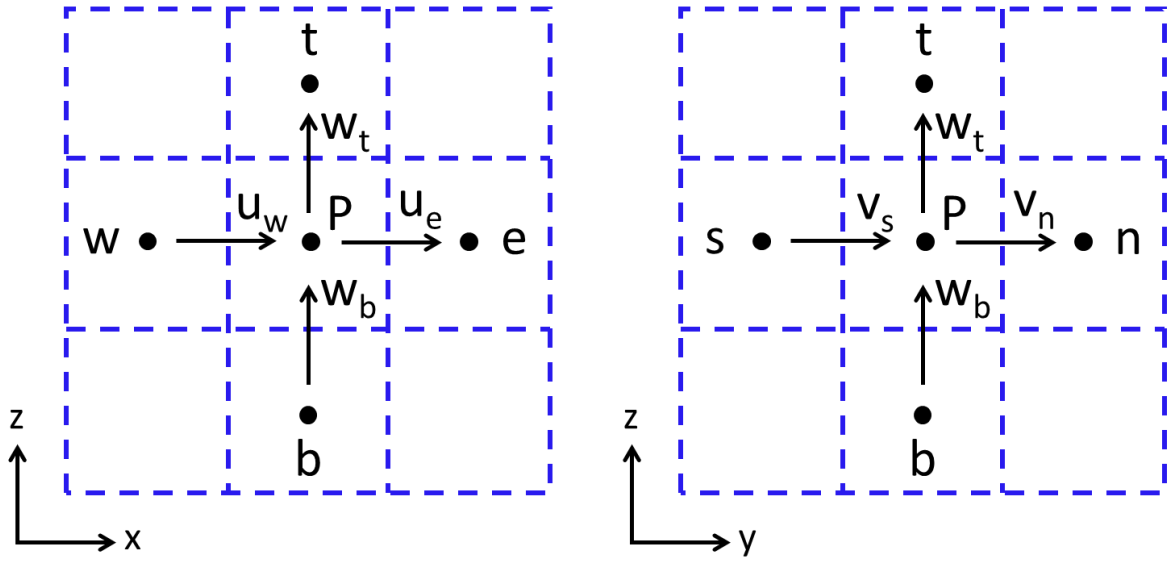

Figure 3.8. Grid system using control volume method on (a) XZ and (b) YZ planes of the solution domain. The dashed lines indicate the control volume's interfaces and solid dots represent the scaler grid points. The symbols w, e, s, n, b, t are for east, west, south, north, bottom, and top neighbors of the grid point P, respectively.

3.5.2 Solution procedure

Figure 3.9 is a flow chart showing the step by step computational procedure used in the heat transfer and fluid flow model. For a particular layer, the y-location of the heat source is decided based on the specific hatch and the hatch spacing. The continuous movement of the heat source is simulated by progressively shifting the axis by a very short distance equal to a small fraction of the heat source spot diameter. The time step for the calculation is decided based on that incremental distance and the scanning speed. For a particular step (at a specified x-location) the x-grid is updated and all the variables are interpolated from the grid system of the previous beam location. Based on the updated grids, the governing equations are discretized and the volumetric heat source and boundary conditions are applied. Depending on the continuously varying temperature field, thermo-physical properties are assigned to all grid points.

All discretized equations are simultaneously solved using a Gaussian elimination technique known as the tri-diagonal matrix algorithm (TDMA) [22] to calculate enthalpy, velocity and pressure fields. The temperature field is obtained from the enthalpy values by using temperature dependent specific heat of the alloy. The iterative calculations for solving the governing equations continue until they converge for all the hatches and layers are finished. These calculations are performed using a Fortran code developed in Penn State and compiled using an Intel Fortran compiler.

Here is an example of a sample calculation for PBF-L of stainless steel 316. For a 20 mm long, 5 layers, 5 hatches build, the size of the solution domain is 22 mm × 5mm × 3.5 mm (length × width × height). This domain is divided into 385000 grid points, where, the number of grids along X, Y and Z directions are 110, 50 and 70, respectively. Among these 110 X-grids, 50 grids are fine travelling grids that cover a region of 0.5 mm and move with the laser beam. The remaining 60 grids are distributed in the coarse X-grid region. Five main variables, temperature, pressure and three velocity components are calculated at each grid points for 2000 small time steps. At each step, about 30 iterations are found to be sufficient to achieve good convergence. Therefore, the total number of linear equations being solved for the 20 mm long build with 5 hatches and 5 layers is around 385000 × 5 × 2000 × 30 × 5 × 5 (number of grids × variables × time steps × iterations per step × layers × hatches) = 3×10^{12}. The calculation time is approximately 5 hours for a 5 layers, 5 hatches build in a personal computer with a 3.40GHz i7 processor and 8 GB RAM.

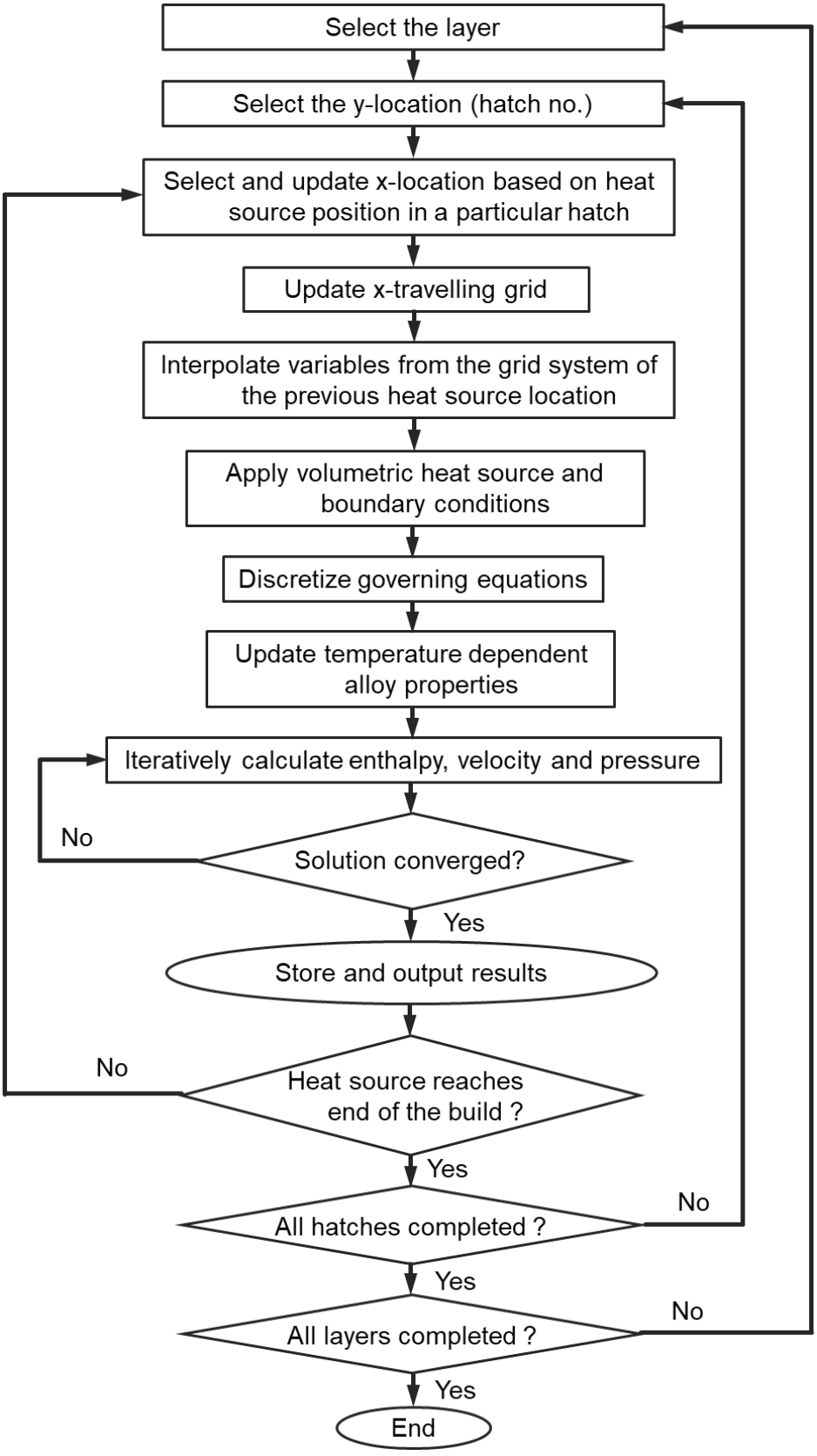

Figure 3.9. Schematic diagram showing the overall algorithm of the heat transfer and fluid flow model.

3.5.3 Stability and convergence of solution

The stability of the heat transfer and fluid flow numerical scheme is evaluated based on the fluctuation of the output variables such as temperature, velocity and pool dimensions with processing time. Figure 3.10 (a) shows the variation of the pool volume during PBF-L of stainless steel 316 with time for two linear heat inputs (laser power / scanning speed). Higher heat input can melt more materials and form bigger molten pool. With the progress of the printing process, the molten pool becomes bigger and after a certain time it reaches steady state. After it reaches the steady state, it does not fluctuate with time indicating it as a stable solution.

The convergence of the heat transfer and fluid flow calculations is defined based on an error or residue value. The solution is recognized as converged when the residue is smaller than a specified value. In this numerical method described here, residue for enthalpy calculations (R_h) is defined as:

$$R_h = \frac{\sum\left[\frac{1}{a_P}(a_n\, h_n + a_s\, h_s + a_e\, h_e + a_w\, h_w + a_t\, h_t + a_b\, h_b + f) - h_P\right]}{\sum h_P} \qquad (3\text{-}41)$$

where the coefficients a and f are defined in Equation (3-40), h is the corresponding enthalpy and Σ denotes the summation over all grid points of the solution domain. The residue for the calculations of u-velocity (R_u) is defined as:

$$R_u = \frac{[\,\sum(a_n\, u_n + a_s\, u_s + a_e\, u_e + a_w\, u_w + a_t\, u_t + a_b\, u_b + f - a_P\, u_P)]/\xi}{M_{ref}} \qquad (3\text{-}42)$$

where u is the corresponding u-velocity and Σ denotes the summation over all grid points (ξ) inside the liquid pool. Since, the three components of velocity are calculated by solving the momentum conservation equation, a reference momentum, M_{ref} is used to calculate the velocity residues, as given below:

$$M_{ref} = -\frac{d\gamma}{dT}\,\frac{\rho_L}{\mu}\,(T_P - T_S)\,(\lambda\, r_b) \qquad (3\text{-}43)$$

where $d\gamma/dT$, ρ_L and μ are the surface tension gradient, density and viscosity of the liquid alloy, respectively, T_P and T_S are the peak temperature and the solidus temperature of the alloy, respectively and λ and r_b are the layer thickness and heat source radius, respectively. The calculation of residues for v and w velocities are also performed in the same way. When these calculated residues are below a pre-defined value (typically ± 0.1 %), the solution is considered to be converged. The calculations are done iteratively to obtain lower residues and good convergence as shown in Figure 3.10 (b).

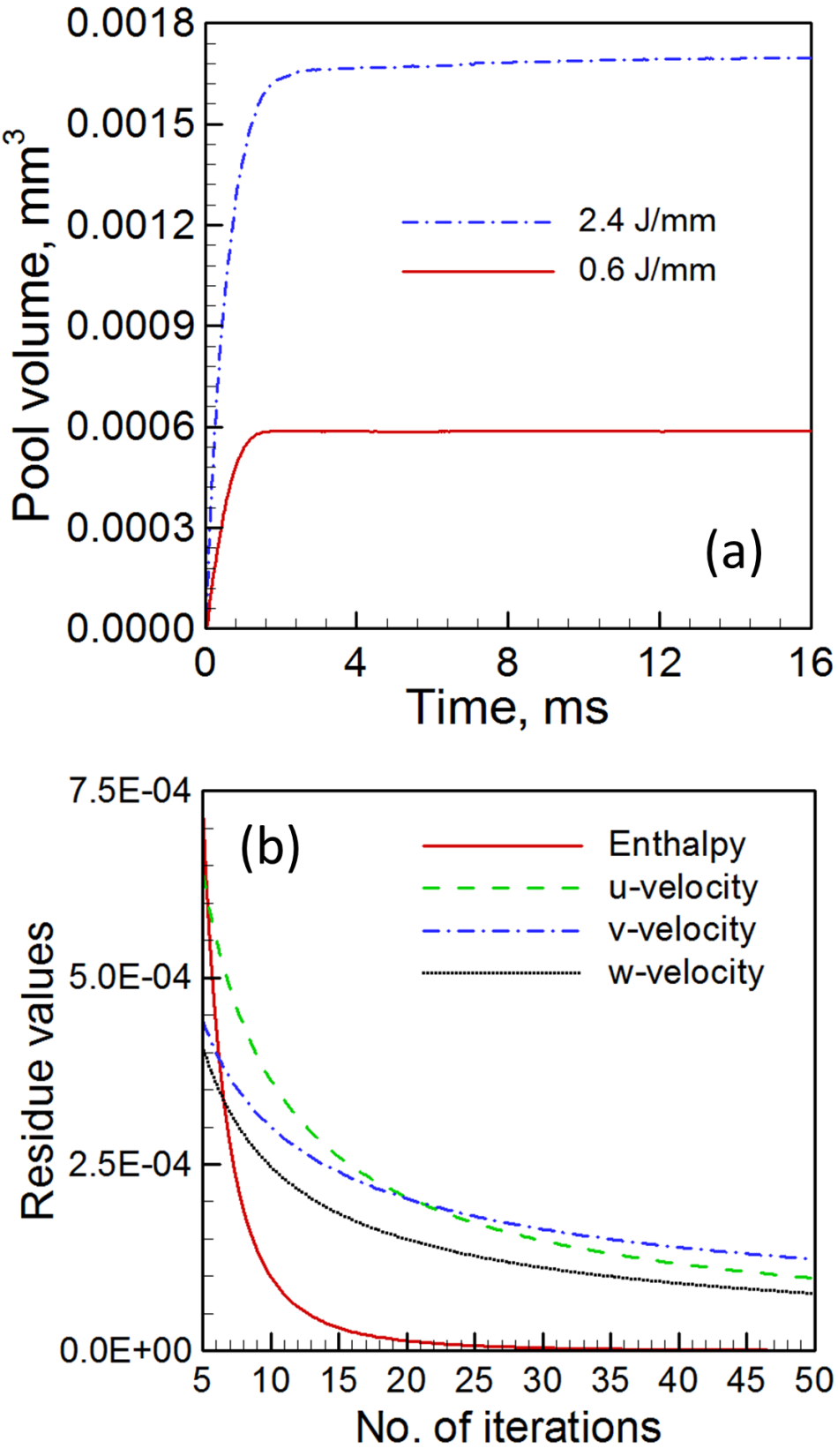

Figure 3.10. (a) Variation of pool volume with time for a single layer single hatch stainless steel build using PBF-L at two heat inputs. (b) Variations of calculated residues or error values with iterations for enthalpy and three components of velocity.

3.6 Transient temperature and velocity fields

In this sub-sections, 3D transient temperature and velocity fields calculated using the heat transfer and fluid flow models for three AM processes are described. The results shown in this section are for the process parameters provided in Table 3.5.

Table 3.5. Process parameters used for the calculations in Section 3.6.

Process parameters	PBF-L	DED-L	DED-GMA
Laser power, W	60	2500	
Arc current, A			200
Arc voltage, V			22.0
Heat source power, W	60	2500	
Scanning speed, mm/s	250-1000	10.6	5
Layer thickness, mm	0.03	0.8	3.0
Wire radius, mm			0.6
Wire feed rate, m/min			4.98
Catchment efficiency		0.3	
Packing efficiency	0.5		
Deposition rate, g/s		0.2	0.5
Heat source radius, mm	0.05	2.0	4.0
Substrate thickness, mm	2	12.7	17.0

3.6.1 Results for PBF-L

Figure 3.11 (a) shows the three-dimensional temperature and velocity fields calculated using the heat transfer and fluid flow model during the building of first layer first hatch of a SS 316 build. The temperature and velocity fields on top (XY), transverse (YZ) and longitudinal (XZ) planes are shown in Figure 3.11 (b), (c) and (d) respectively. The region bounded by the liquidus temperature isotherm (1733 K) of SS 316 represents the molten pool. The light blue region within the liquidus and the solidus temperature (1693 K) isotherms represents the two-phase solid liquid region or mushy zone. The velocity vectors are represented by the black arrows whose magnitude can be determined by comparing their length with the reference vector provided. The velocity vectors are radially outwards because molten metal flows from the high temperature to the low temperature. The laser beam travels in the direction of positive X-axis. The molten pool is elongated in the opposite to the scanning direction. The track width is determined from the solidus isotherms on the transverse sections as shown in Figure 3.11 (d).

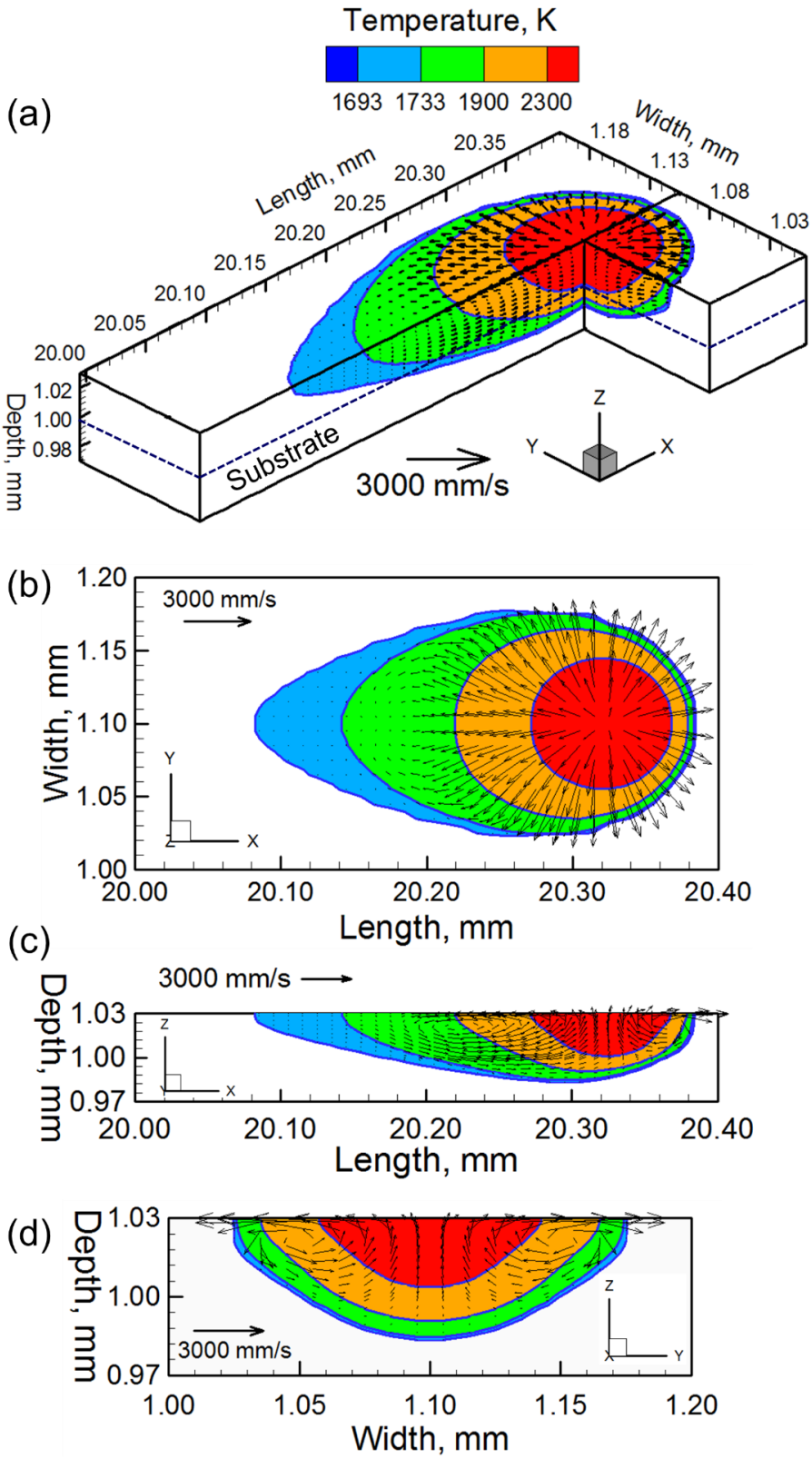

Figure 3.11. Temperature and velocity distributions for 1st hatch and 1st layer of a 20 mm long SS 316 build on a 24 mm long SS 316 substrate using 60 W laser power and 500 mm/s scanning speed on (a) 3D isometric section (b) top (c) longitudinal and (c) transverse planes. The length of the build is from x = 2.0 mm to 22.0 mm. Scanning direction of the laser beam is along the positive x-axis. All other process parameters are given in Table 3.5.

Figure 3.12 (a-d) show the calculated temperature and velocity fields for first layer, first hatch of SS 316 build at four different scanning speeds. The size of the fusion zone decreases with increase in scanning speed because of the lower heat input at faster scanning speeds. Figure 3.13 (a-d) show the computed temperature and velocity fields for four alloy powders. The velocity vectors are radially outward from the laser beam axis as the liquid metal flows in the direction of positive temperature gradient. For a given processing condition, AlSi10Mg exhibits the largest molten pool due to its lowest density and liquidus temperature. The build with IN 718 results in largest mushy zone due to the maximum difference between the liquidus and solidus temperatures.

Figure 3.14 (a) describes the effects of scanning speed on pool volume during PBF-L using four alloy powders. Reduction in pool volume with higher scanning speed is attributed to lower heat input at faster scanning speeds. AlSi10Mg exhibits the largest pool size due to its lowest density and liquidus temperature as shown in Figure 3.14 (a). Thermo-physical properties of SS 316 and IN 718 are almost similar. However, smaller latent heat of fusion of IN 718 results in slightly larger pool for IN 718 than SS 316. Smaller density of Ti-6Al-4V than SS 316 causes larger melt pool size for Ti-6Al-4V compared to that for SS 316. Laser scanning speeds in PBF processes are often very high. At very high scanning speeds, the heat transfer is primarily influenced by the scanning speed in the direction of travel of the laser beam. As a result, the differences in the molten pool size for different alloys are less pronounced at higher scanning speeds as observed in Figure 3.14 (a).

Heat transfer patterns from the molten pool continuously vary during the deposition of different layers and hatches. These variations in heat transfer result in changing volume of the liquid pool in different layers and hatches as shown in Figure 3.14 (b). In AM, most of the heat transfer occurs from the molten pool through the substrate. For upper layers, the molten pool volume increases because of reduced rate of heat transfer further away from the substrate. However, after a few layers the molten pool reaches steady state and after that the pool volume remains constant. During the building of the second hatch, one side of the pool faces the solidified build which has a higher thermal conductivity. As a result, the volume of the liquid pool in the second hatch is smaller than that of the first hatch. In the subsequent hatches, the liquid pool volume does not significantly change because the heat transfer pattern remains the same in the subsequent hatches.

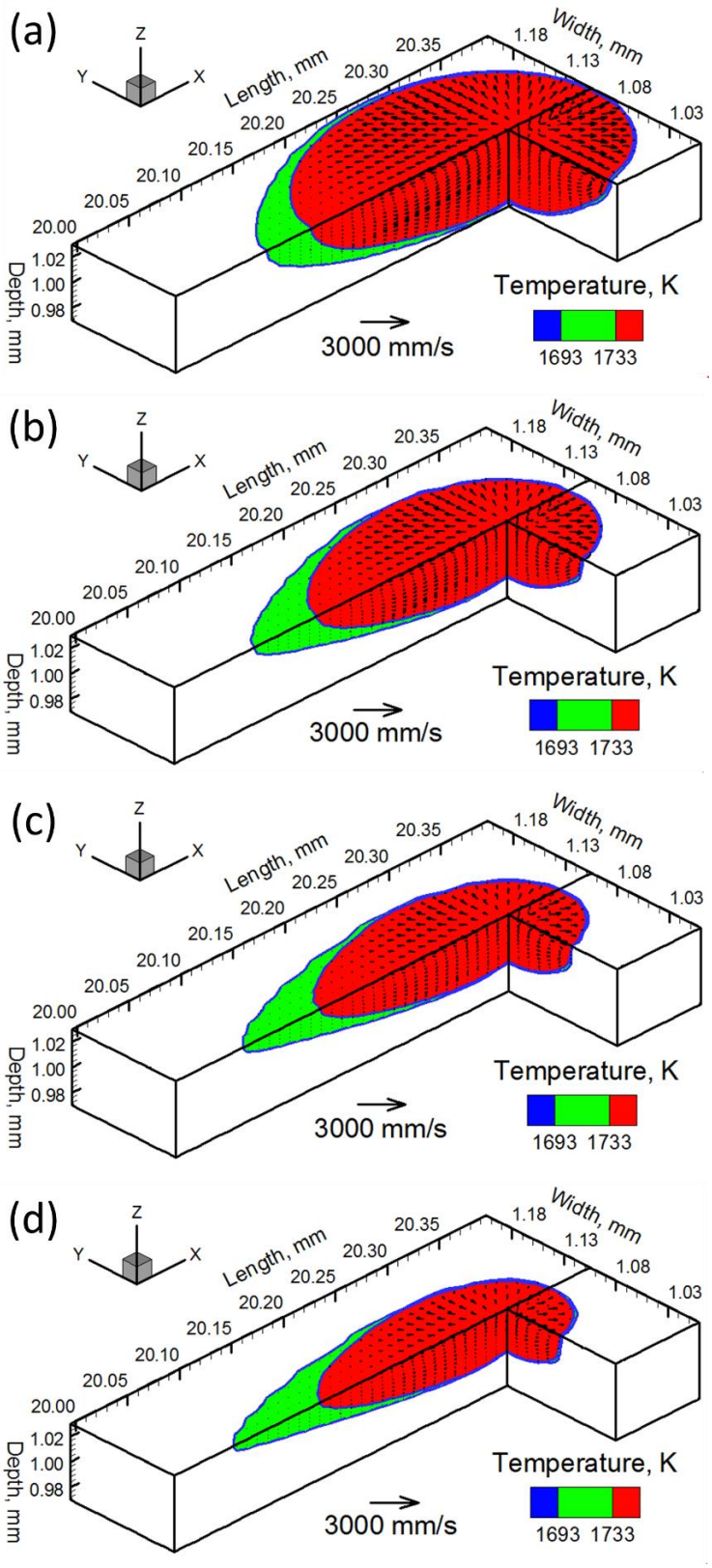

Figure 3.12. Three-dimensional temperature and velocity distributions in the 1st layer 1st hatch of 20 mm long build of SS 316 using laser scanning speed of (a) 250 (b) 500 (c) 750 and (d) 1000 mm/s. For all the cases laser power is 60 W. Scanning direction of the laser beam is along the positive x-axis. All other process parameters are given in Table 3.5.

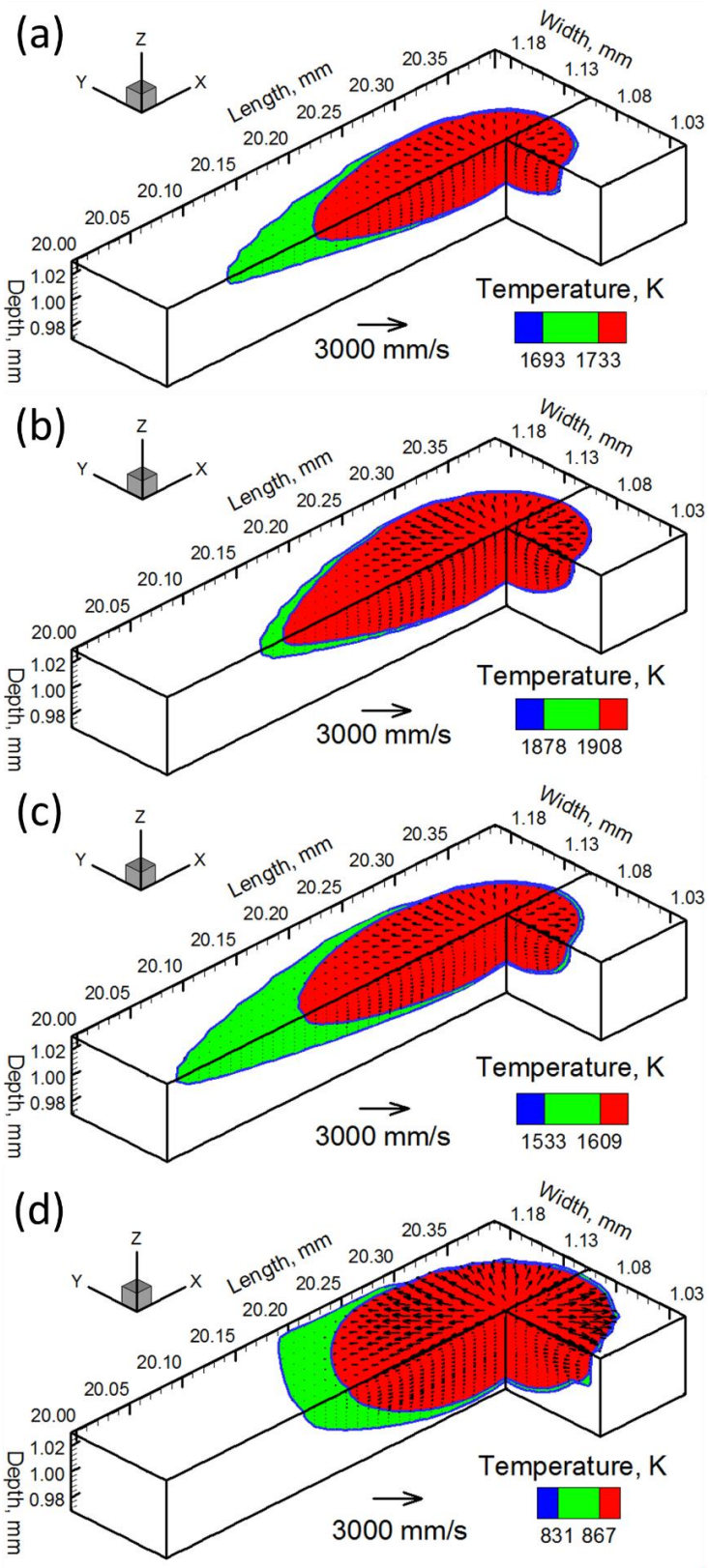

Figure 3.13. Three-dimensional temperature and velocity distributions in the 1st layer 1st hatch of 20 mm long build of (a) SS 316 (b) Ti-6Al-4V (c) IN 718 and (d) AlSi10Mg using 60 W laser power and 1000 mm/s scanning speed. Scanning direction of the laser beam is along the positive x-axis. All other process parameters are given in Table 3.5.

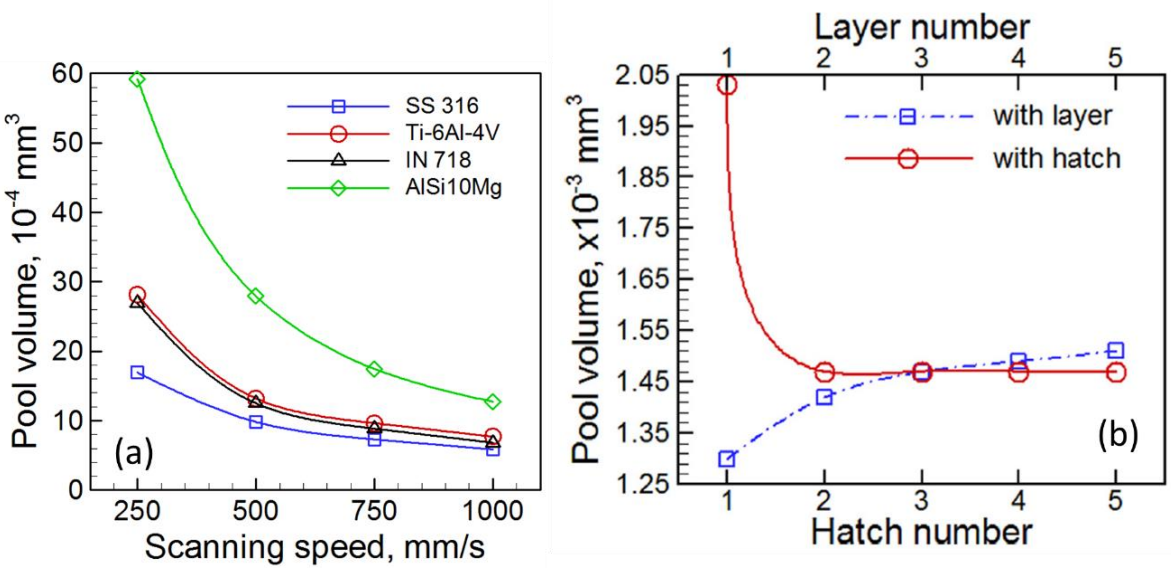

Figure 3.14. (a) Effect of scanning speed on pool volume calculated at the mid-length of 1st layer 1st hatch for 4 different alloys. (b) Variation of molten pool volume with layer number at 3rd hatch and with hatch number for 3rd layer for a 5 layers 5 hatches SS 316 build using 1000 mm/s scanning speed. Pool volumes are calculated at the mid-length of a particular track. Both the plots are for laser power of 60 W. All other process parameters are given in Table 3.5.

Figure 3.15 (a) shows the variation in temperature with time (thermal cycle) for a location at mid-length and on the top surface of first layer, first hatch of the builds of four alloy powders using the same process parameters. The peak temperature is attained at a time of 2 ms when the laser beam reaches on the top of the location. The small knee, observed in the thermal cycle between the liquidus and solidus temperatures for all alloys, are due to the liquid to solid phase transformation during the solidification. The highest peak temperature for the Ti-6Al-4V build is because of its lowest density. However, the AlSi10Mg build exhibits the lowest peak temperature among the four alloys because of its highest thermal diffusivity. Alloy with high thermal diffusivity dissipates heat rapidly that reduces the peak temperature. The influence of laser scanning speed on thermal cycle during the fabrication of the first layer, first hatch of a SS 316 build is explained in Figure 3.15 (b). Different scanning speeds allow the laser beam to reach to the same location at different time instants. Therefore, the peak temperature is attained at different time for different scanning speeds. Faster scanning reduces the net amount of heat input resulting in a lower peak temperature. These transient variations in the temperature fields significantly affect the evolution of residual stresses and distortion as will be discussed in chapter 4.

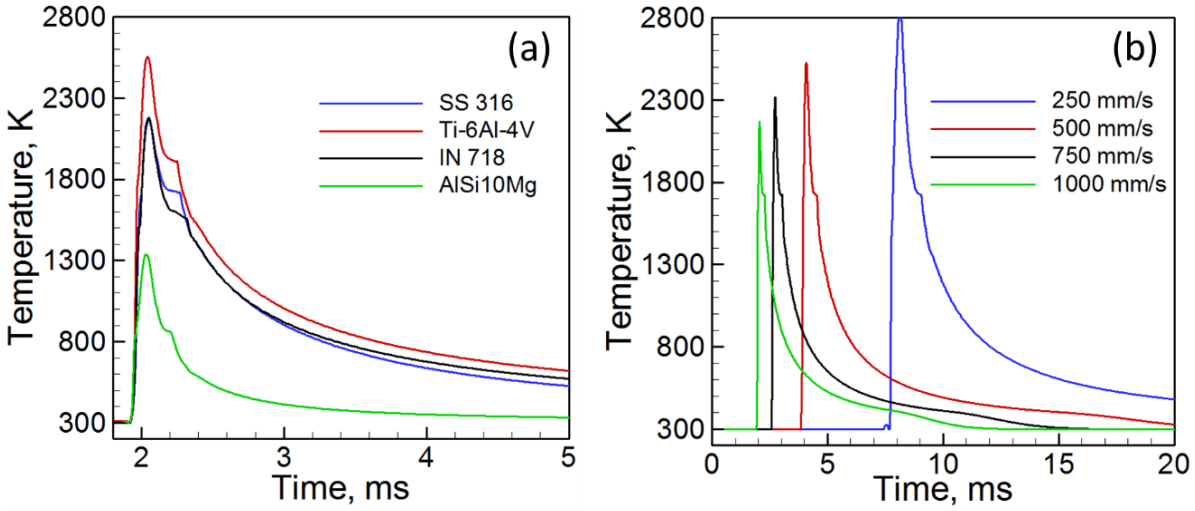

Figure 3.15. Temperature variation with time for a location on the top surface and at the mid length of first layer, first hatch of the build (a) of four different alloys using 1000 mm/s scanning speed and (b) of SS 316 using four different scanning speeds. Both the plots are for a laser power of 60 W. All other process parameters are given in Table 3.5.

3.6.2 Results for DED-L

Figures 3.16 (a) and (b) show the calculated temperature and the velocity fields on the 3D curved surface and along the longitudinal section (XZ plane) of the stainless steel 316 deposit, respectively. The color contours represent the temperature ranges corresponding to the figure legend. The laser beam scanning direction is along the positive x-axis. Because of the rapid scanning of the laser beam along the positive x-axis, the isotherms behind the beam axis are elongated while the isotherms ahead of the beam are compressed. The black arrows represent the velocity vectors of the molten metal inside the pool. A reference vector is shown by an arrow and a comparison of the length of this arrow with the vectors in the plots represents the magnitudes of the computed velocities. As described before, the convective flow of liquid metal is primarily driven by the Marangoni stresses due to the temperature difference on the surface of the molten pool. Therefore, on the top surface of the deposit the liquid metal flows from the high temperature near the beam axis to the low temperature region along the curved surface as shown in the figures. Figure 3.16 (b) shows that the pool is deep just near the laser beam axis. In addition, the molten pool has higher temperature and velocities towards the front part of it. As velocity diverges from the location of the heat source, separate convective loops are formed, as seen in the front, side, and back of the pool in Figure 3.17 (a-d). The difference in fluid flow at different vertical plane (YZ) away from the beam axis significantly affects the shape of the fusion zone near the trailing edge of the molten pool.

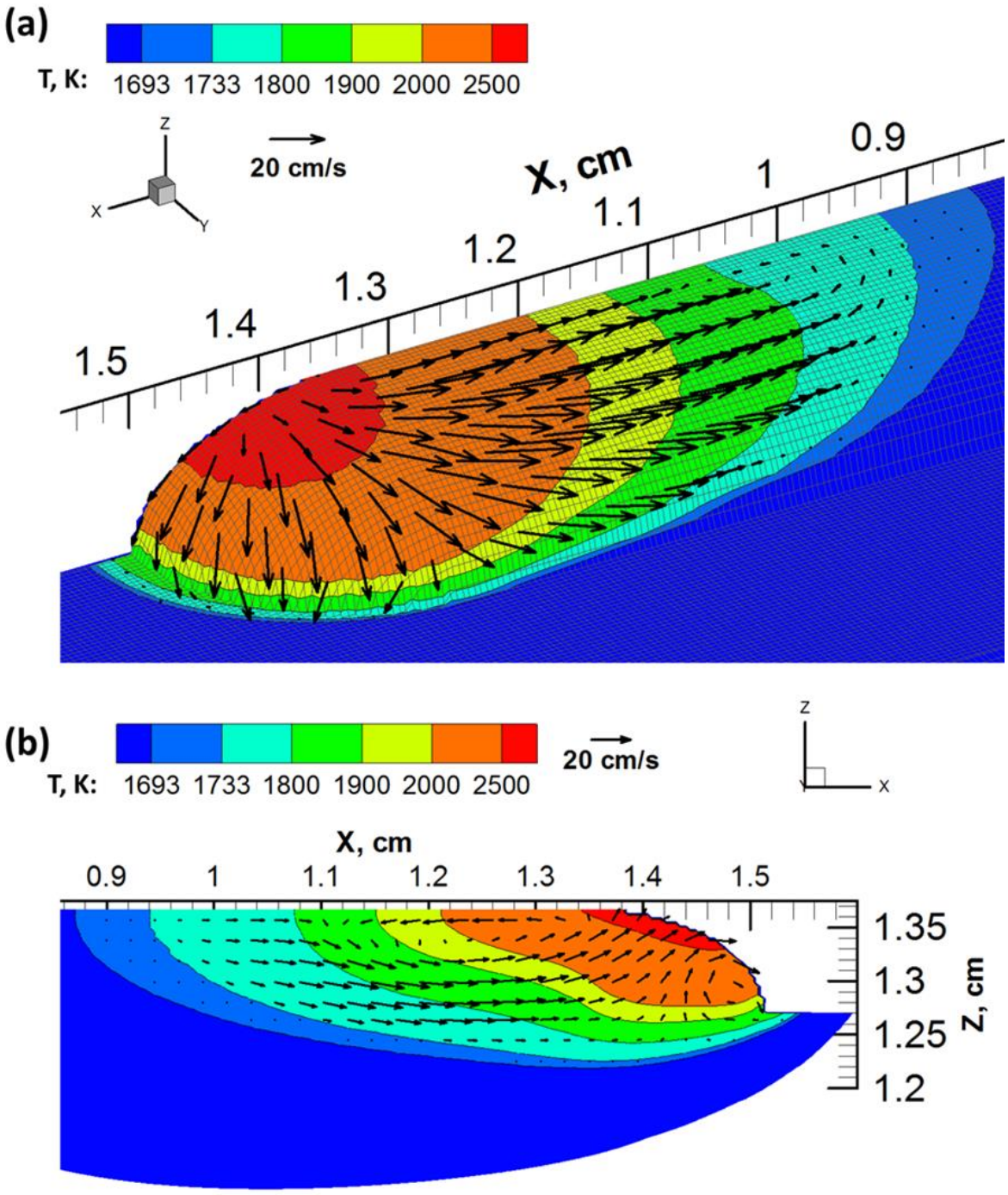

Figure 3.16. Temperature and velocity distributions on the curved shaped deposit for stainless steel 316 at 2500 W laser power and 10.6 mm/s scanning speed (a) 3D isometric view and (b) longitudinal sectional view, where the scanning direction is along the positive x-axis. All other process parameters are given in Table 3.5.

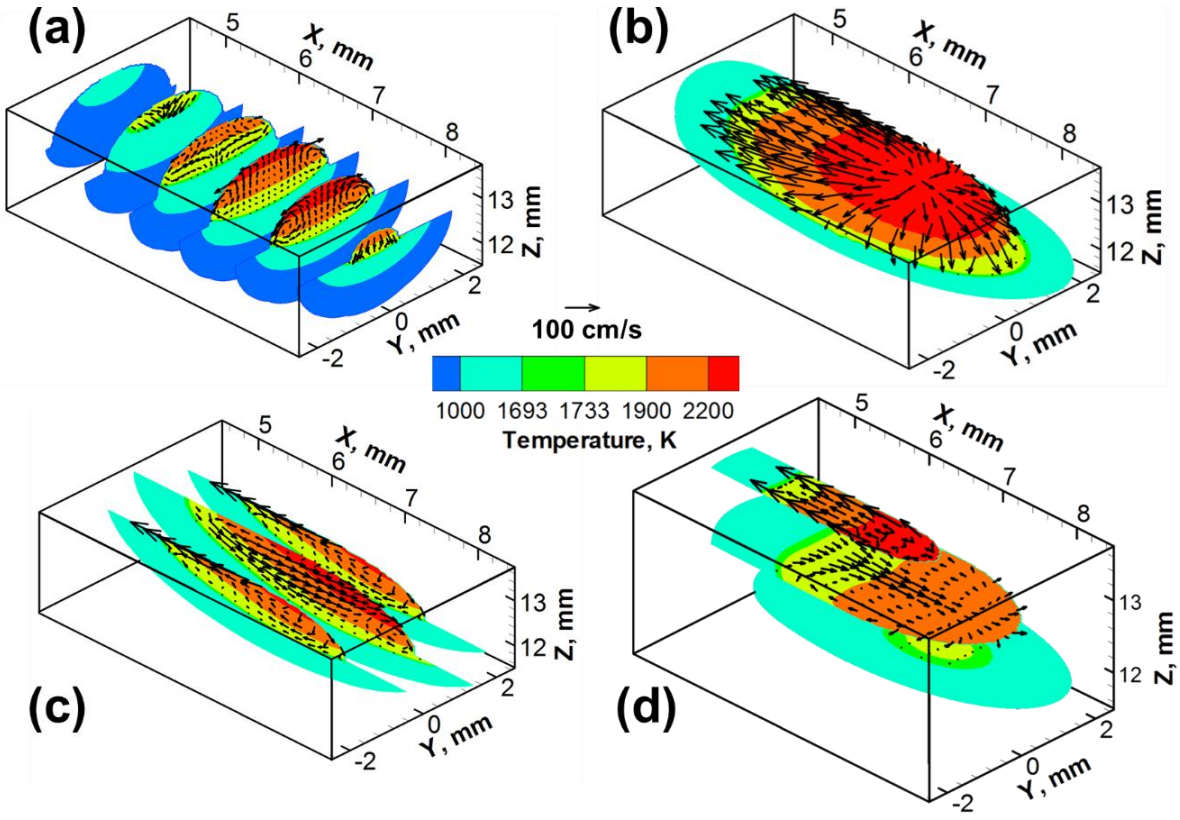

Figure 3.17. An instantaneous view of multiple sections through the deposit from simulated stainless steel 316 at 2500W laser power and 10.6 mm/s scanning speed: (a) horizontal sections, (b) top-surface, (c) longitudinal sections, and (d) transverse sections. The leading edge of the bead is at x = 8.5mm. All other process parameters are given in Table 3.5.

Figure 3.18 shows the calculated variation of the temperature with respect to time, monitored at the mid height and mid width of the deposit while fabricating 1.0 cm long SS 316 and alloy 800 H parts. Alloy 800H has higher thermal diffusivity than that of SS 316. The alloy with low thermal diffusivity retains the heat in the component for longer time which results in high peak temperature. Therefore, the peak temperature in the SS 316 deposit is higher than that for alloy 800H. From this figure, it can be noted that the rate of heating is much faster than the rate of cooling. During the cooling, there is a sudden change in the slope of the curve due to the solid-to-liquid phase transformation during the solidification.

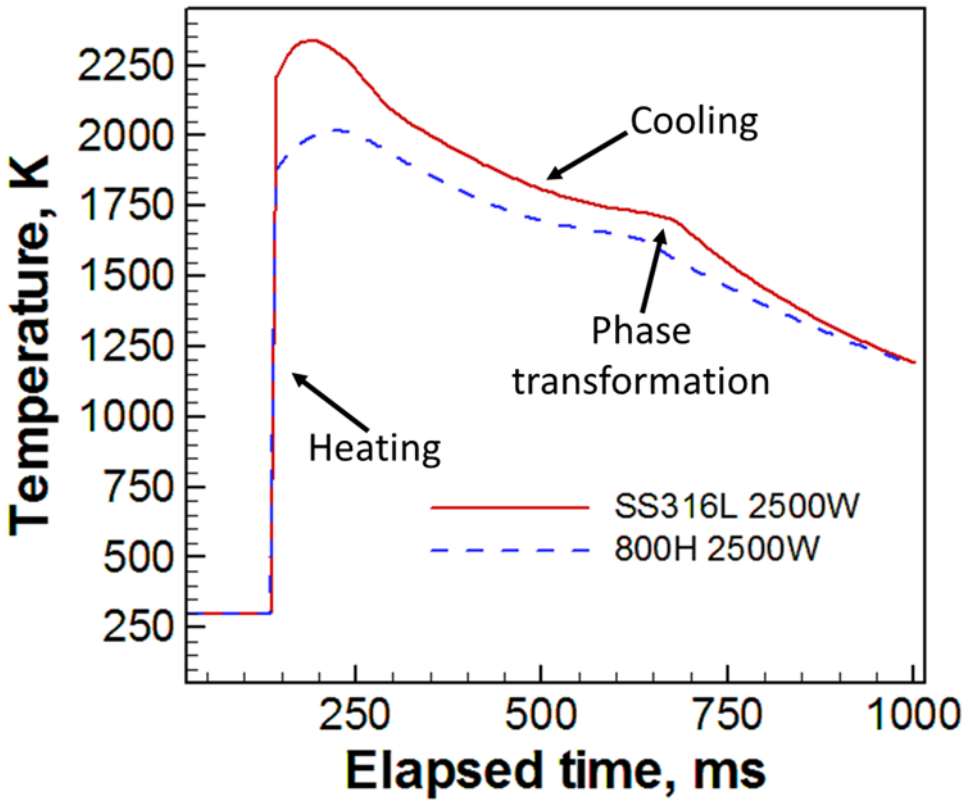

Figure 3.18. Simulated thermal history for a location approximately a fifth of the way along the 1.0 cm long deposit length of stainless 316 and alloy 800 H at 2500W laser power and 10.6 mm/s scanning speed. All other process parameters are given in Table 3.5.

3.6.3 Results for DED-GMA

Figure 3.19 (a) shows the 3D temperature and velocity fields during the deposition of a H13 steel track. Similar to DED-L, the isotherms at the trailing edge of the molten pool are elongated due to the rapid scanning of the arc source. Figure 3.19 (b) shows the magnified view of the temperature and velocity fields near the molten pool. The two-phase region containing both liquid and solid, commonly called the mushy zone, is bounded by the solidus temperature (1585 K) and liquidus temperature (1725 K) isotherms. The area bound by the liquidus isotherm is called the fusion zone. Molten metal velocities are shown by black arrows whose magnitude can be predicted by comparing their lengths with the reference vector provided. Due to the negative value of the temperature gradient of surface tension for H13 steel, the liquid metal flows from the center to the periphery on the top surface of the molten pool. The molten metal is depressed in the middle of the pool under the arc source due to the strong arc pressure and droplet impinging force. This flow pattern allows more heat transfer from the heat source to the bottom of the fusion zone and results in deep penetration. Because

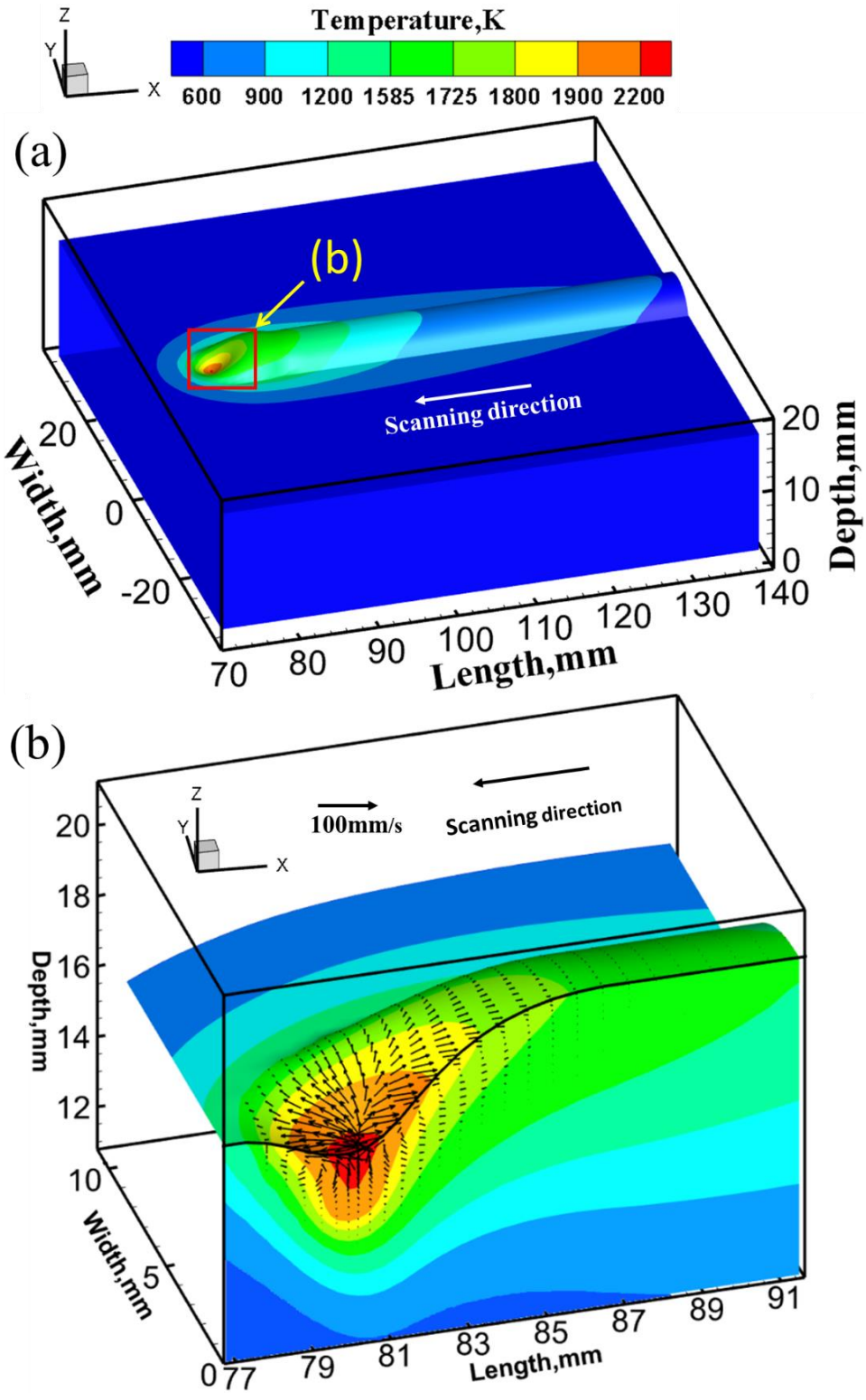

Figure 3.19. (a) Calculated temperature and velocity fields for a single track DED-GMA of H13 using 5 mm/s scanning speed. (b) Magnified views of temperature fields in (a). All other process parameters are given in Table 3.5.

of the depression at the center of the molten pool, the liquid metal is pushed to the rear part of the fusion zone and forms the curved surface as it solidifies.

Figure 3.20 (a) shows the temperature and velocity fields at different transverse sections of the deposit. Near the leading edge of the deposit, the molten pool is depressed due to arc and droplet forces and the fusion zone has finger-like (i.e. deep and narrow) penetration in to the substrate. Towards the rear end of the molten pool, the arc and droplet forces acting on the surface decrease, resulting in a crown geometry determined largely by surface tension forces. Figures 3.20 (b) and (c) show the stream traces on two transverse planes at two different distances along the distance of the arc travel. Under the arc, the surface depression combined with surface tension gradients leads to two separate convection loops, as shown by the stream traces in section 1 of Figure 3.20 (b). Behind the arc, the circulation of the molten metal is slower due to the reduced temperature gradients, as shown in section 2 of Figure 3.20 (c).

Temperature and velocity fields for longitudinal sections at different distances from the arc center are shown in Figure 3.21 (a). Comparing the two sections in Figures 3.21 (b) and (c), there little difference in the distribution of temperatures and velocities. Stream traces for both sections reveal a small convection loop in the front of the molten pool and a larger convection loop in the rear of the pool. Because the pool is longer than it is wide, the temperature gradient from the peak temperature at the center of the pool to the liquidus isotherm at the edge of the pool is larger in the width direction than the length direction. This results in a higher surface tension gradient near the front of the pool and lower surface tension gradient in the rear, correlating to the magnitude of the velocities.

Figure 3.22 shows the temperature variation with time monitored at the mid-height and mid-length of the deposit center while fabricating a single track H13 deposit. The peak temperature corresponds with the time the arc source reaches the monitoring location. At 11.7 mm/s scanning speed, the peak temperature is observed at around 2.6 s. However, at a slower traveling speed of 5 mm/s the peak temperature is observed at about 6 s, because the arc source takes a longer time to reach the monitoring location. Heating takes place rapidly as the arc approaches the monitoring location. However, once heated, cooling is comparatively slower because of the time needed for the transport of heat throughout the molten pool and into the substrate. During cooling, there is a sudden change in slope between the liquidus (1725 K) and solidus (1585 K) temperatures because of the liquid-to-solid phase transformation and the release of latent heat during solidification.

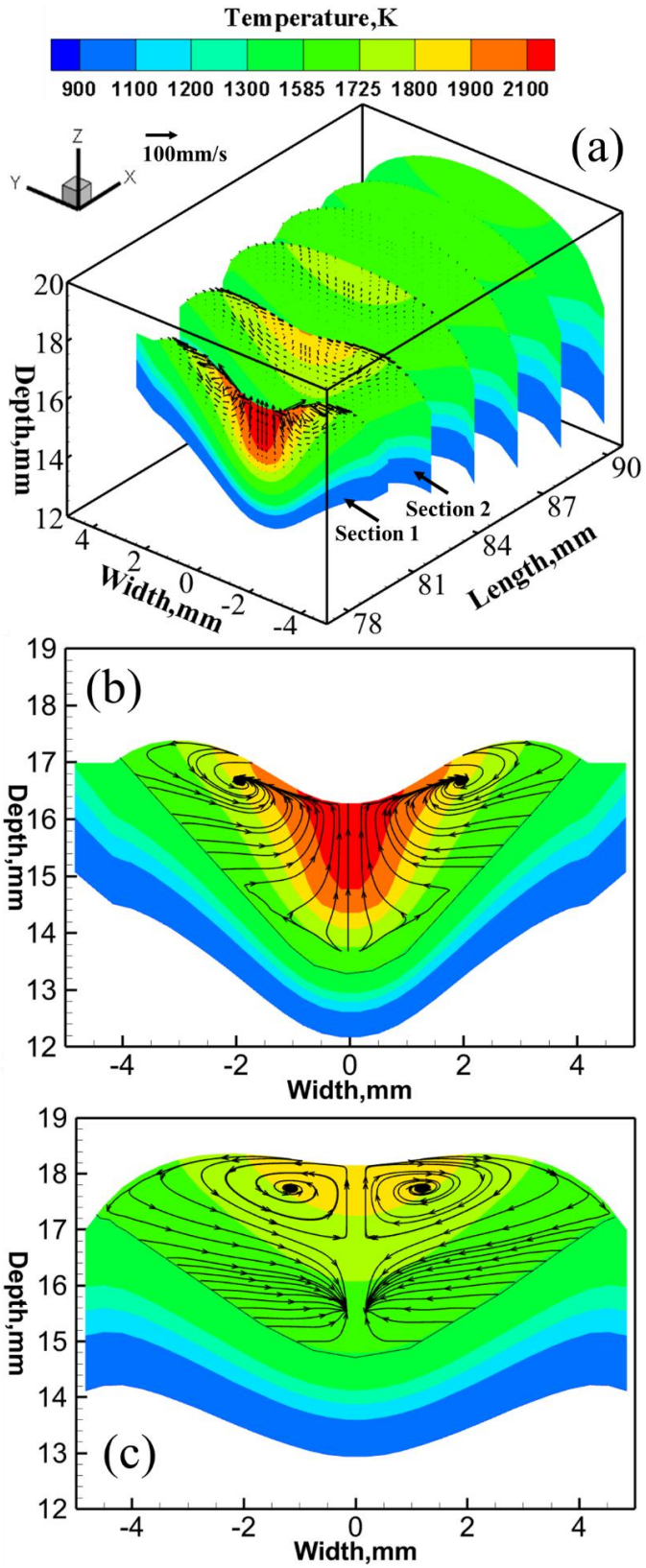

Figure 3.20. (a) Temperature and velocity fields during DED-GMA of H13 steel at different transverse planes. Temperature fields and stream traces of molten metal flow at two transverse sections (b) section 1 (under the arc) and (c) section 2 (behind the arc) shown in figure (a). All plots are for 5 mm/s scanning speed. All other process parameters are given in Table 3.5.

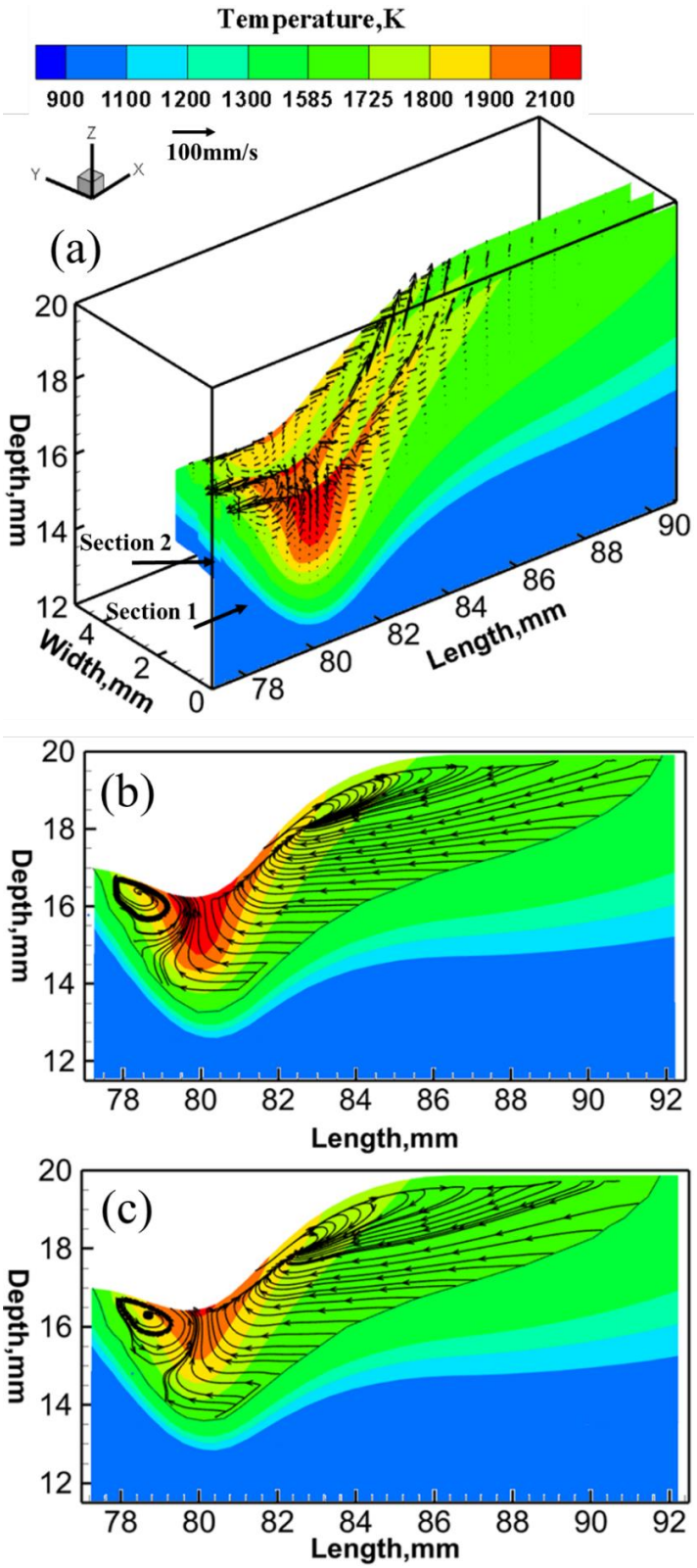

Figure 3.21. (a) Temperature and velocity fields during DED-GMA of H13 steel at different longitudinal planes. Temperature fields and stream traces of molten metal flow at two longitudinal sections (b) section 1 (under the arc) and (c) section 2 (right side of the arc) shown in figure (a). All plots are for 5 mm/s scanning speed. All other process parameters are given in Table 3.5.

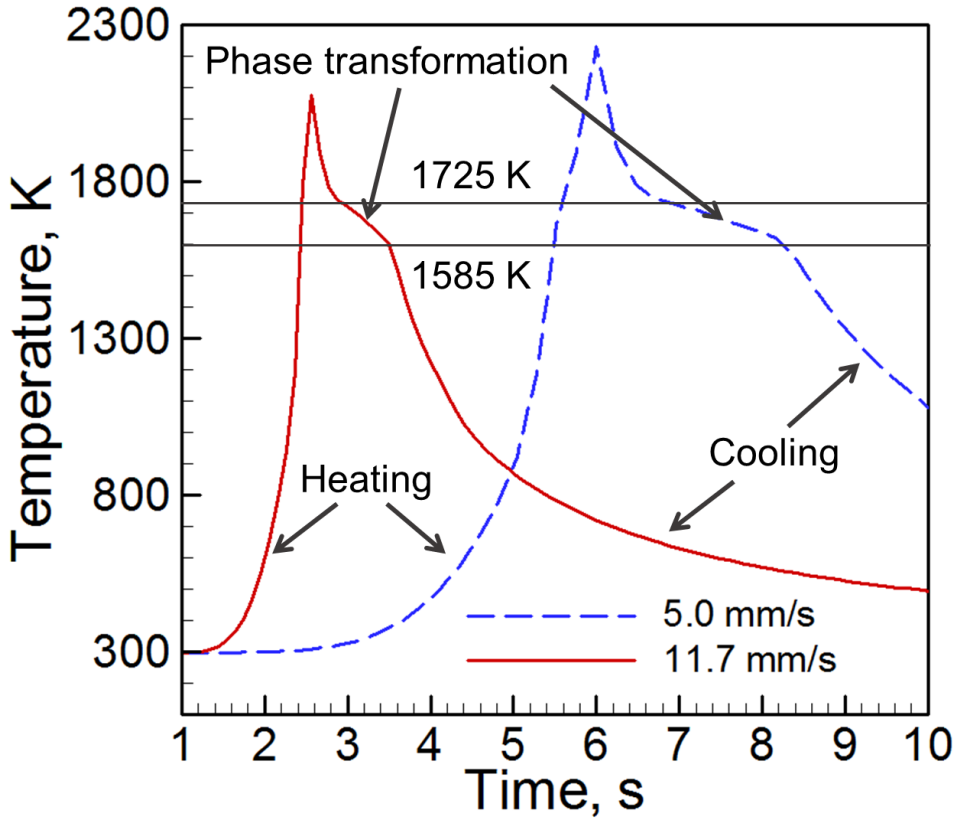

Figure 3.22. Temperature variation with time monitored at the mid height and mid-length of the deposit center while fabricating a single track H13 deposit using DED-GMA at two different scanning speeds. All other process parameters are given in Table 3.5.

3.6.4 Comparison among the three processes

Figure 3.23 compares the shape and size of the molten pools during printing of SS 316 components using DED-GMA, DED-L and PBF-L. The figure shows the transient temperature and velocity fields on the longitudinal (XZ) plane. The color bands represent the temperature range corresponding to the figure legend. The molten pool is bounded by the solidus temperature (1693 K) isotherm of stainless steel 316. The velocity vectors for the convective flow inside the molten pool are shown by black arrows. These results are for the typical processing conditions used for DED-GMA [23], DED-L [24] and PBF-L [25] which are mentioned in Table 3.6. Two important observations can be made from these figures.

(1) The shape of the molten pool remarkably varies for the three printing processes because of the unique features of each process. For example, in DED-GMA, the molten metal near the arc axis is depressed by the arc pressure and the impact force of the impinging droplets, as indicated by an arrow. The liquid metal is pushed to the rear part of the molten pool and forms the curved deposit as it solidifies. The impinging effect of the droplets also result in deep

penetration in DED-GMA. However, in DED-L the curved pool surface is formed immediately under the laser beam axis due to the accumulation of the powder particles. In contrast, the figure shows that the top surface of the molten pool in PBF-L is flat because of the addition of thin flat layers of powders while printing the component using a fairly low heat input.

(2) The size of the molten pool in the three printing processes widely varies depending on the heat sources and heat input. The linear heat input (power/speed) in PBF-L is in the order of 0.1 J/mm that results in very small pool whose dimensions are in micrometers. However, linear heat inputs in DED-L and DED-GMA are in the order of 10 J/mm and 100 J/mm, respectively. Therefore, the molten pool width in DED-GMA is the largest followed by that in DED-L. The pool dimensions in PBF-L are around 10% and 30% of those for DED-GMA and DED-L respectively for the conditions considered in Figure 3.23.

Table 3.6. Process parameters used for DED-GMA [23], DED-L [24] and PBF-L [25].

Process parameters	DED-GMA	DED-L	PBF-L
Laser power, W		1500	110
Arc current, A	150		
Arc voltage, V	14.2		
Heat source power, W	2130	1500	110
Scanning speed, mm/s	10	10.6	100
Layer thickness, mm	1.0	0.8	0.25
Wire radius, mm	0.5		
Wire feed rate, m/min	8.0		
Catchment efficiency		0.3	
Packing efficiency			0.5
Deposition rate, g/s	0.5	0.2	
Heat source radius, mm	4.0	2.0	0.3
Substrate thickness, mm	10.0	12.7	0.75

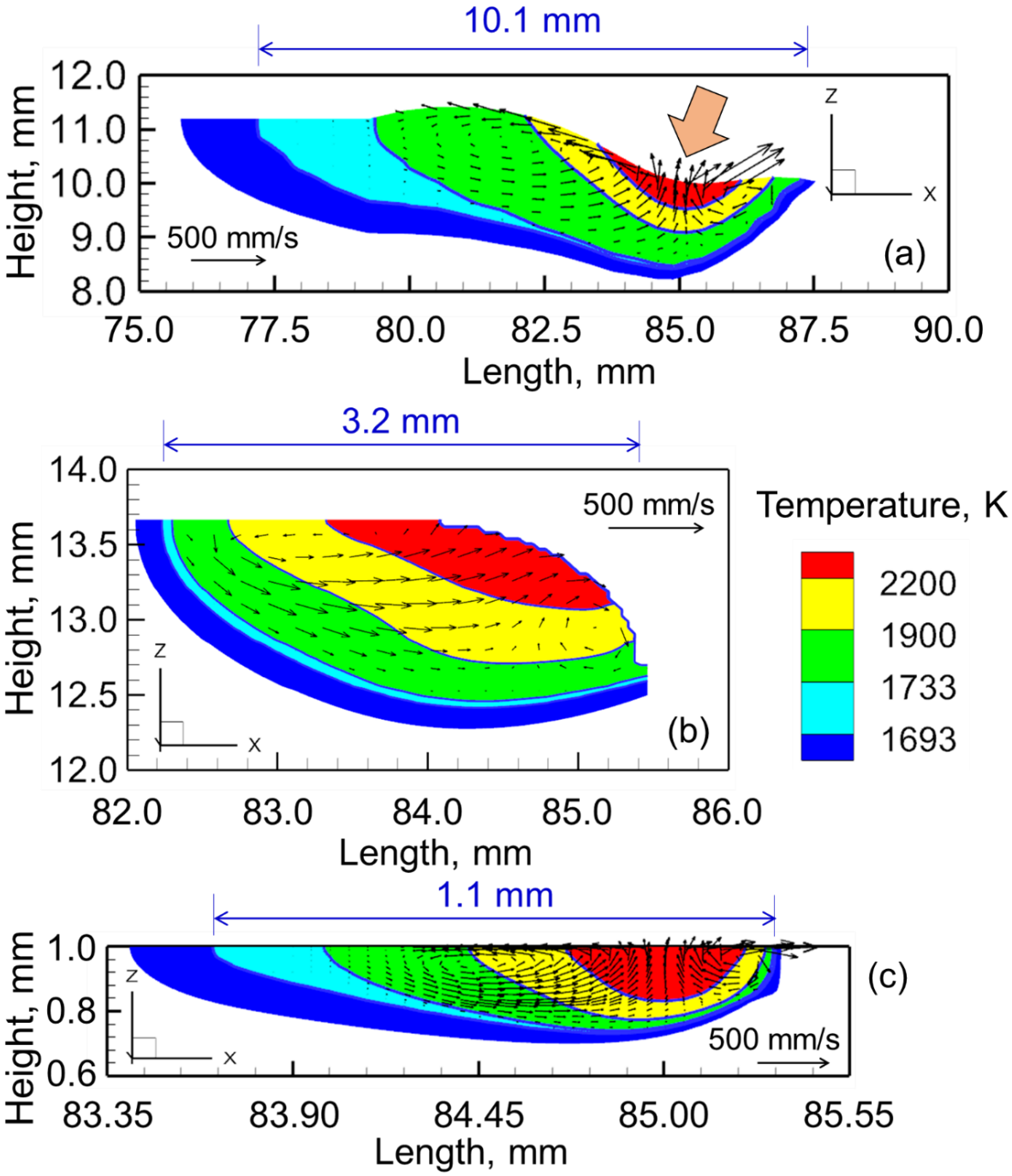

Figure 3.23. Comparison between calculated longitudinal sections of the deposit for (a) DED-GMA (b) DED-L and (c) PBF-L. The process conditions are given in Table 3.6. Scanning direction is along the positive x-axis. For all three cases, the axis of the heat source is at x = 85.0 mm.

3.7 Validation of the models

Validation of the heat transfer and fluid flow model is needed to gain confidence to use the results to estimate the defect formation. Therefore, the calculated temperature fields and deposit geometry for the three AM processes are rigorously tested and selected validation results are provided below.

PBF-L

The depth and width of the fusion zone for a particular hatch during PBF-L can be found from the largest transverse cross-section (in YZ-plane) of the three-dimensional pool. Figure 3.24 shows reasonably good agreement between the computed and the corresponding measured [25] build shapes and sizes for two consecutive hatches of a single layer SS 316 build. Figure 3.25 (a) and (b) show that the calculated molten pool width and depth, respectively, and their variations with linear heat input (laser power/scanning speed) agree well with the corresponding independent experimental observations [26-30] for single layer single hatch builds of SS 316, Ti-6Al-4V and AlSi10Mg. Figure 3.26 shows the variation of temperature with the y-distance (width direction) from the laser beam axis for a Ti-6Al-4V build agrees well with the experimental result by Roberts et al. [31]. Slight mismatch between the computed and measured results can be due to the complexity of temperature measurement for a rapidly moving laser beam as well as several simplified assumptions used in the model.

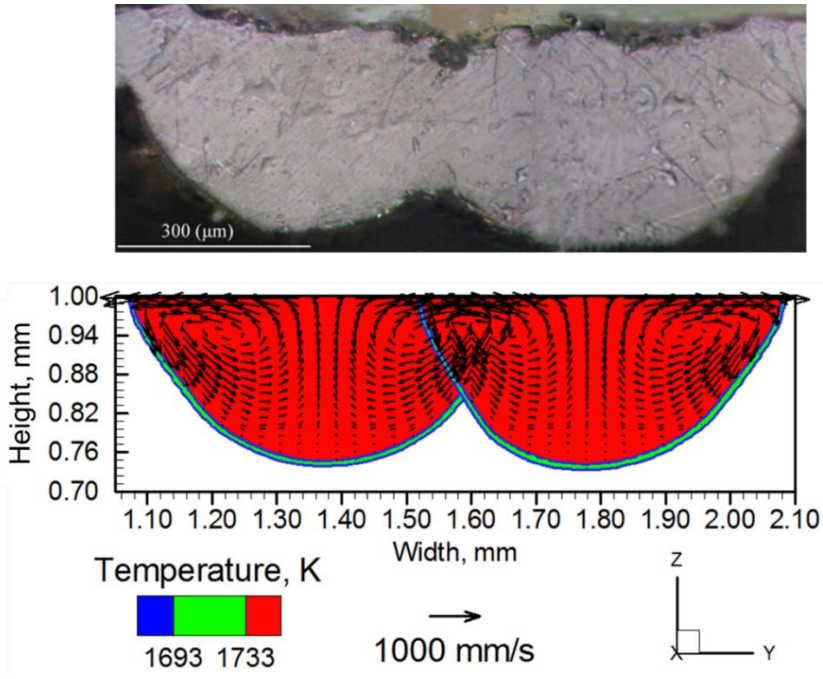

Figure 3.24. Comparison between the calculated and experimentally [25] observed transverse section of the SS 316 single layer multi-hatch build fabricated by PBF-L using 110 W laser power, 100 mm/s scanning speed, 300 microns layer thickness and 300 microns hatch spacing.

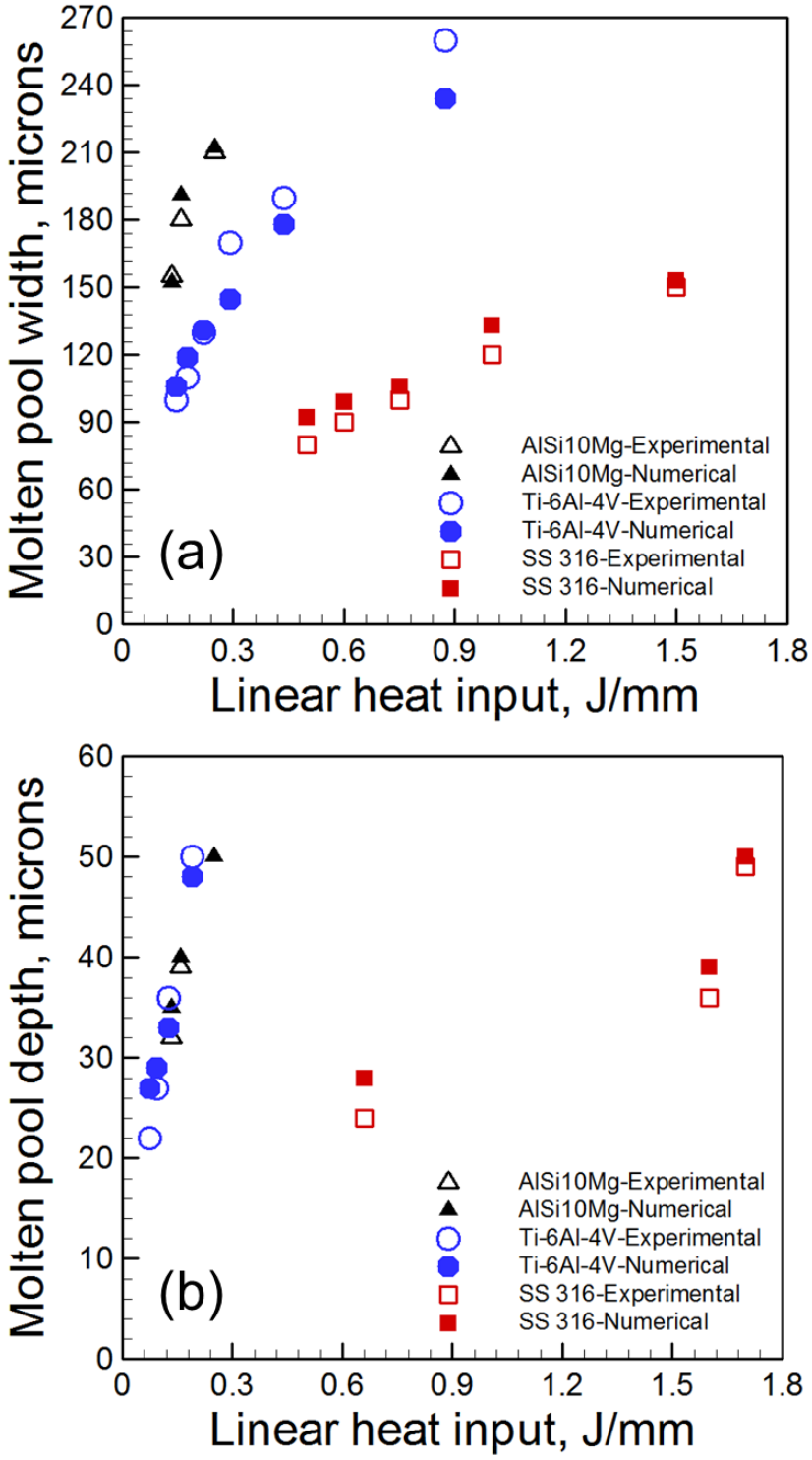

Figure 3.25. Comparison between the calculated and experimentally observed (a) width and (b) depth of the molten pool of a single layer single hatch builds of SS 316, Ti-6Al-4V and AlSi10Mg at different linear heat inputs. The experimentally measured width and depth for SS 316 are adapted from Di et al. [26] and Li et al. [30], respectively. The experimental results for Ti-6Al-4V and AlSi10Mg are taken from Gong et al. [27] and Kempen et al. [29], respectively. Gong et al. [27] and Kempen et al. [29] provided the macrograph from which Tang et al. [28] measured the dimensions. Process conditions used in the model are same as what used in the experiments.

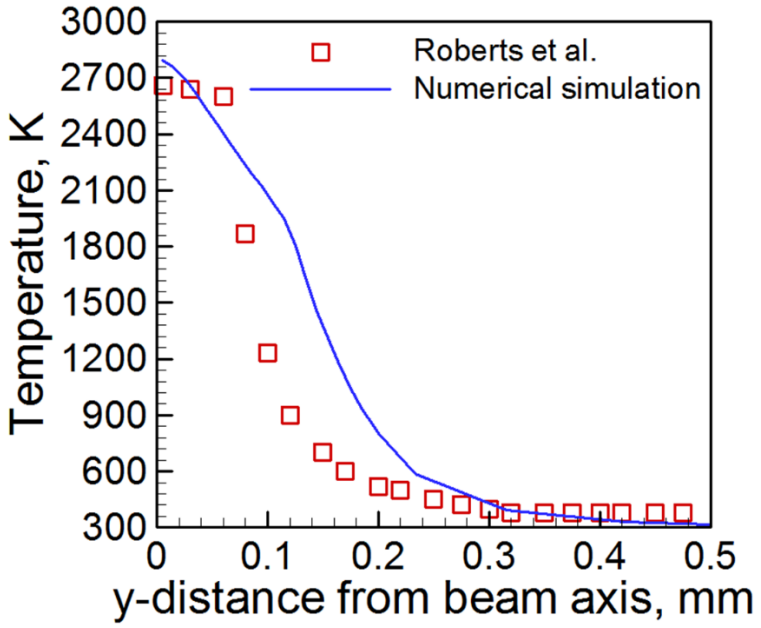

Figure 3.26. Comparison between numerically calculated and experimentally measured [31] temperature variation with y-distance (width direction) from the laser beam axis for a Ti-6Al-4V build printed by PBF-L using 120 W laser power and 220 mm/s scanning speed.

DED-L

Figures 3.27 (a) and (b) compare the calculated transverse section of the deposit with the corresponding experimentally measured macrograph of SS 316 deposits [24] for 1500 W and 2500 W laser powers, respectively. Both figures show good agreement between the computed and the measured results. Since the temperature at the center of the deposit is higher than that of the sides, molten metal flows from the center to the sides along the curved top surface, as shown in the figure. In addition, higher laser power can melt more material. Therefore, the deposit fabricated using 2500 W laser power is larger than that produced with 1500 W. Similarly, Figures 3.28 (a) and (b) also show the comparisons between the computed transverse section of the deposit with the corresponding macrograph for alloy 800H deposits fabricated using 1500 W and 2500 W laser powers, respectively. Alloy 800 H has a lower liquidus temperature than that of SS 316. Therefore, for the same heat input, more of alloy 800H melts, resulting in a larger deposit for alloy 800H. The agreement between the measured and calculated deposit geometries for both SS 316 and alloy 800H indicates that the computed transient results can be used for the calculations of residual stresses, distortion, composition change and lack of fusion defects with confidence.

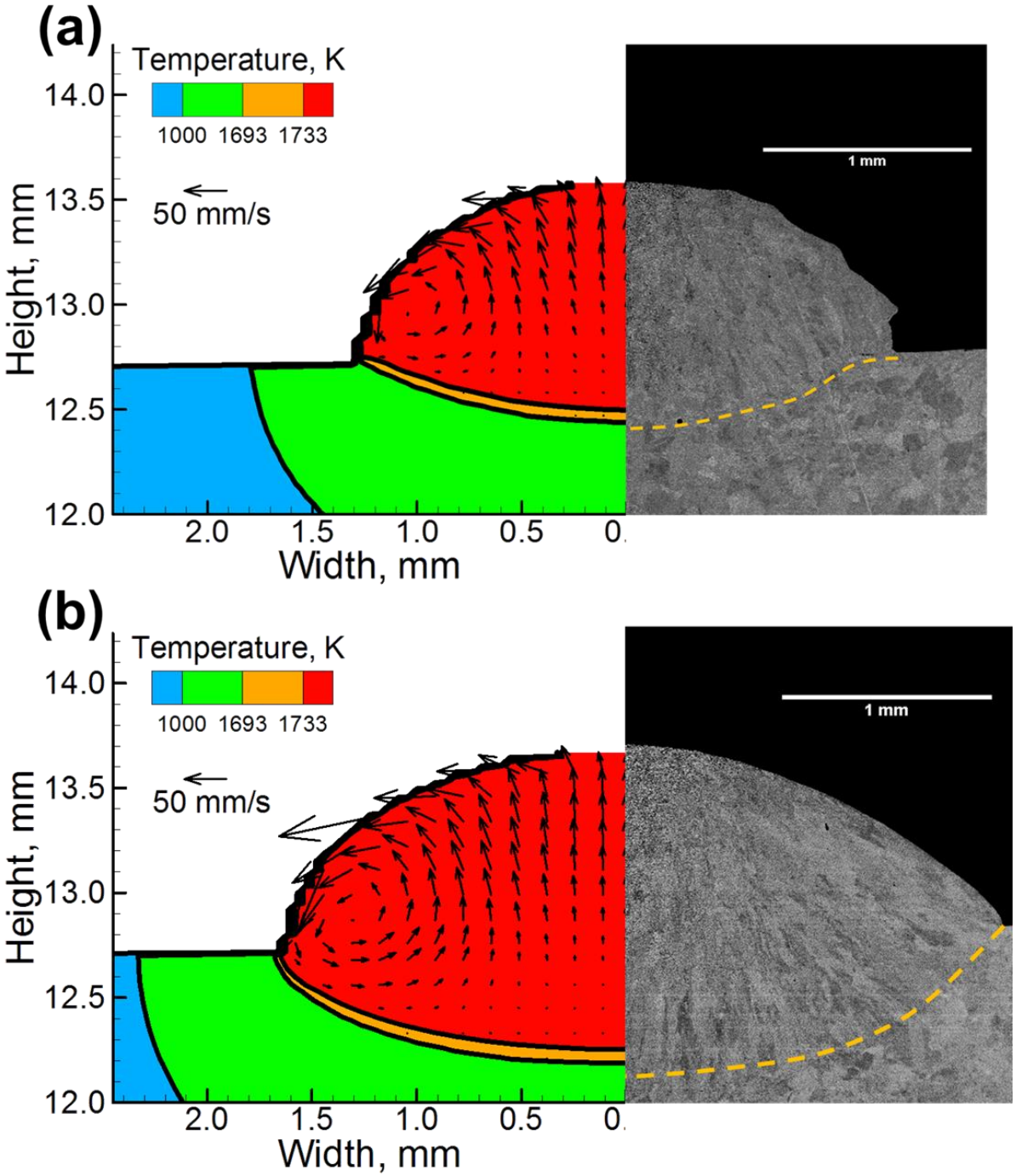

Figure 3.27. Comparison of the calculated deposit shape and size with experimental macrograph [24] at the transverse cross section of the build for stainless steel 316L at (a) 1500 W and (b) 2500 W laser power. The dotted lines indicate the edge of the dilution region.

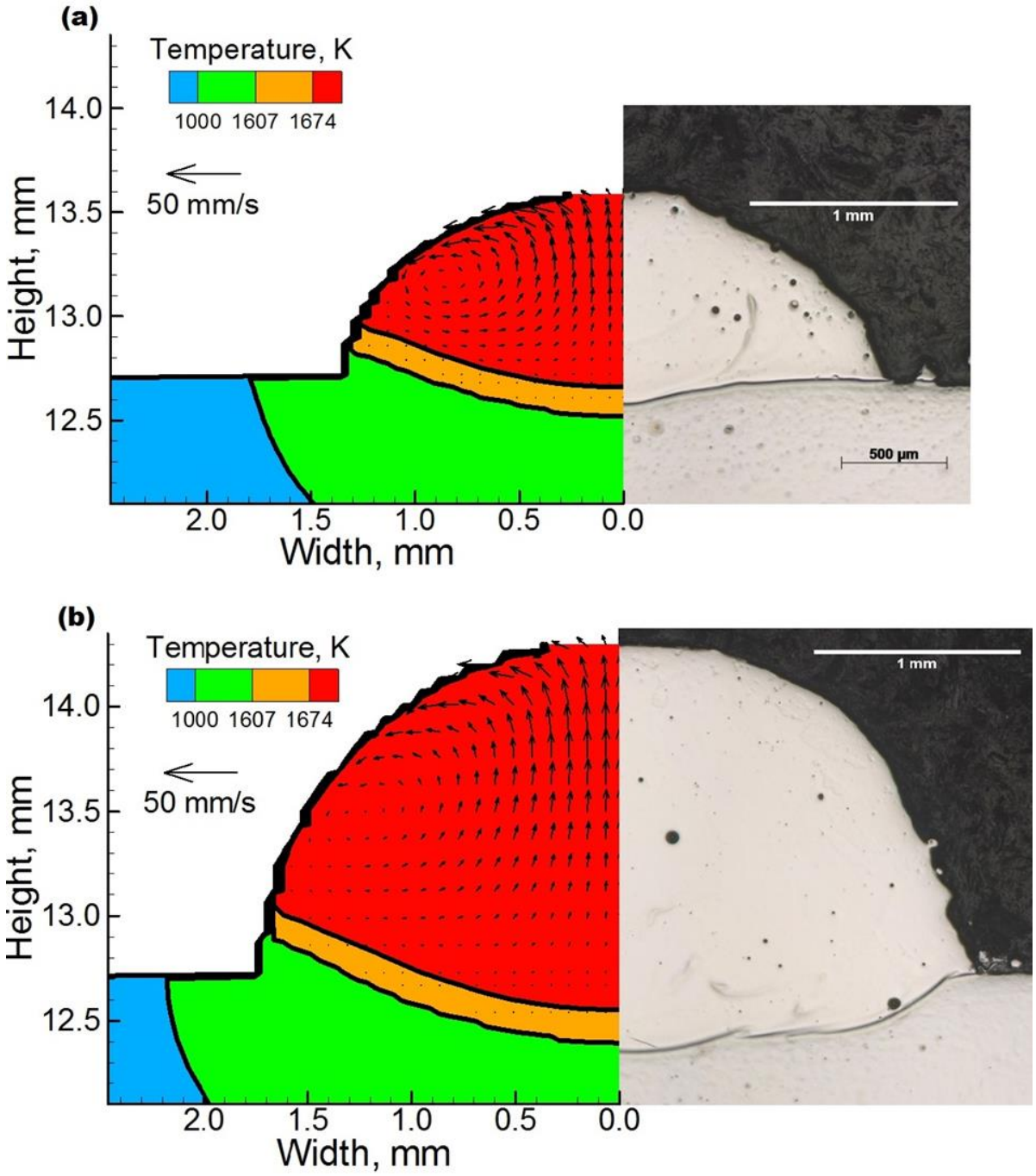

Figure 3.28. Comparison of the calculated deposit shape and size with experimental macrograph [24] at the transverse cross section of the build for alloy 800H at (a) 1500 W and (b) 2500 W laser power.

Figure 3.29 (a) shows a good agreement between the calculated and the corresponding experimentally measured [32] widths of deposits for different layers in a seven layers SS 316 build. Both the calculated and the measured results show progressively larger melt pools as the deposition moves to upper layers because heat loss from the melt pool to the substrate decreases as more layers are deposited. A slight mismatch between the measured and computed results is probably because of the uncertainty in the actual rates of heat input and heat loss in the presence of a stream of alloy powder.

Figure 3.29 (b) shows that the calculated variations in temperature with respect to time agree well with the experimentally measured values [33] for a 5 layer deposition of a 150 mm long Ti-6Al-4V build. The temperature was measured using a thermocouple located on the top of the substrate at the mid length of the deposit. The temperature variations are calculated at the same location of the thermocouple. Thermal cycles are simulated for the entire component using a corresponding solution domain of 150 mm length. The agreement between the experimental and theoretical calculations indicates that the computed transient temperature field can be used for the residual stress and strain calculations with confidence.

DED-GMA

Two most influential and easily adjustable parameters in DED-GMA are the arc power and travel speed. Calculated variations in the fusion zone geometries with respect to these two variables agree well with the corresponding experimental results [34] as shown in Figures 3.30 and 3.31. Figures 3.30 (a-c) show the effects of varying travel speed. Since the heat input per unit length reduces at faster scanning speed, the cross-section of the fusion zone decreases in size with increasing travel speed in both the calculated and measured results. Figures 3.31 (a-c) show that the deposit sizes and fusion zone dimensions increase with arc power attributed to an increase in the heat input per unit length for higher power.

Figure 3.32 compares the calculated temperature variation with time during the deposition of a single track of ER70S-6 steel to the corresponding experimental data adapted from Bai et al. [35]. Temperatures were measured with an infrared camera during the deposition process. The slight mismatch between the experimental and calculated results is probably due to the difficulties in the temperature measurement during deposition, as well as several assumptions in the model.

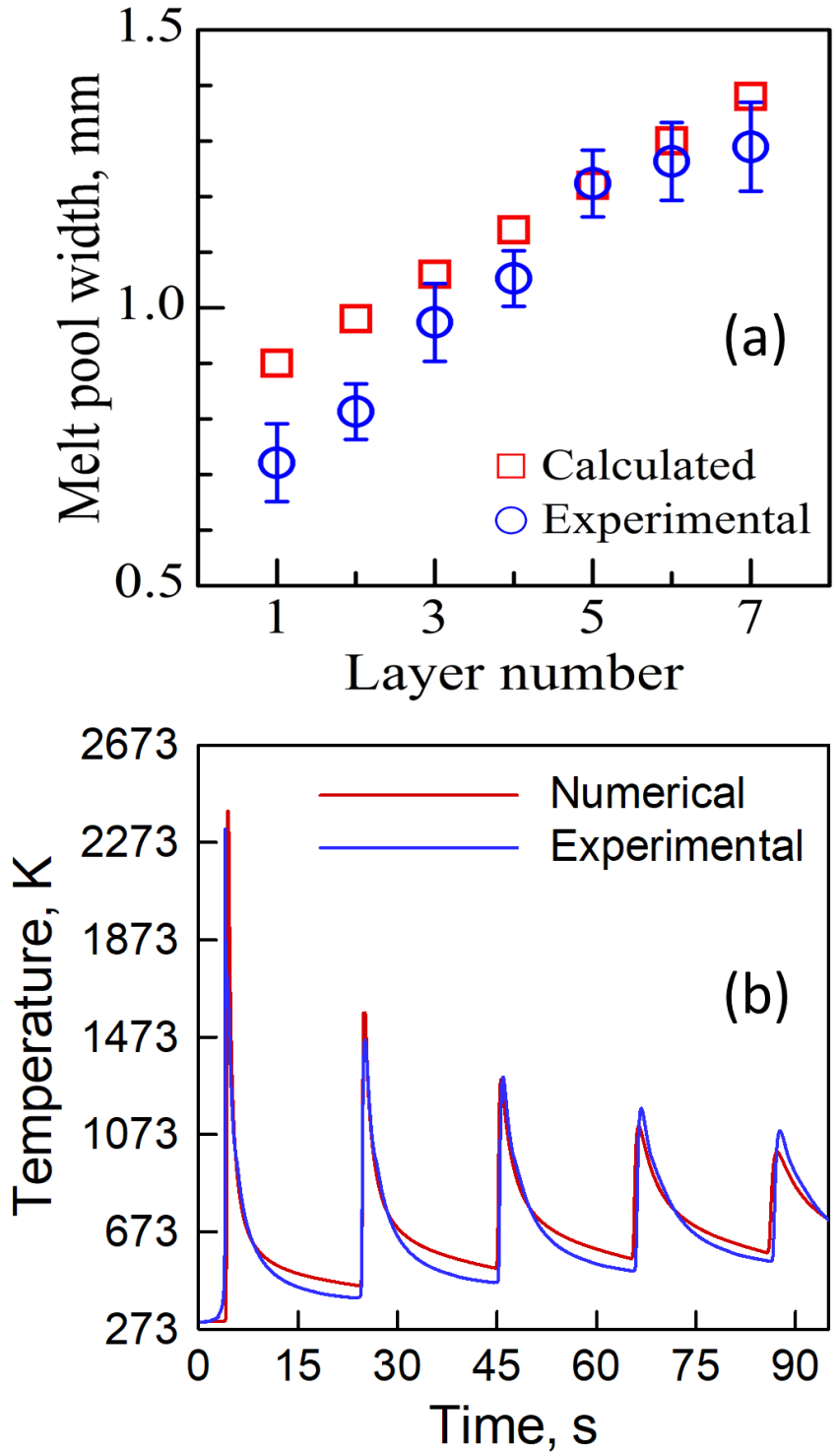

Figure 3.29. (a) Comparison of calculated and experimentally measured [32] pool width for a 7 layers deposition of SS 316 made using DED-L for 210 W laser power, 12.5 mm/s scanning speed and 0.5 mm beam radius. The errors in the experimental measurements are estimated from several readings taken along the layer thickness. (b) Comparison of experimentally measured [33] and numerically computed thermal cycle for a 5 layers DED-L of 150 mm long Ti-6Al-4V deposit on Ti-6Al-4V substrate using 2000 W laser power, 10.5 mm/s scanning speed and 1.5 mm beam radius. The monitoring location is at the mid length of the deposit on the top surface of the substrate.

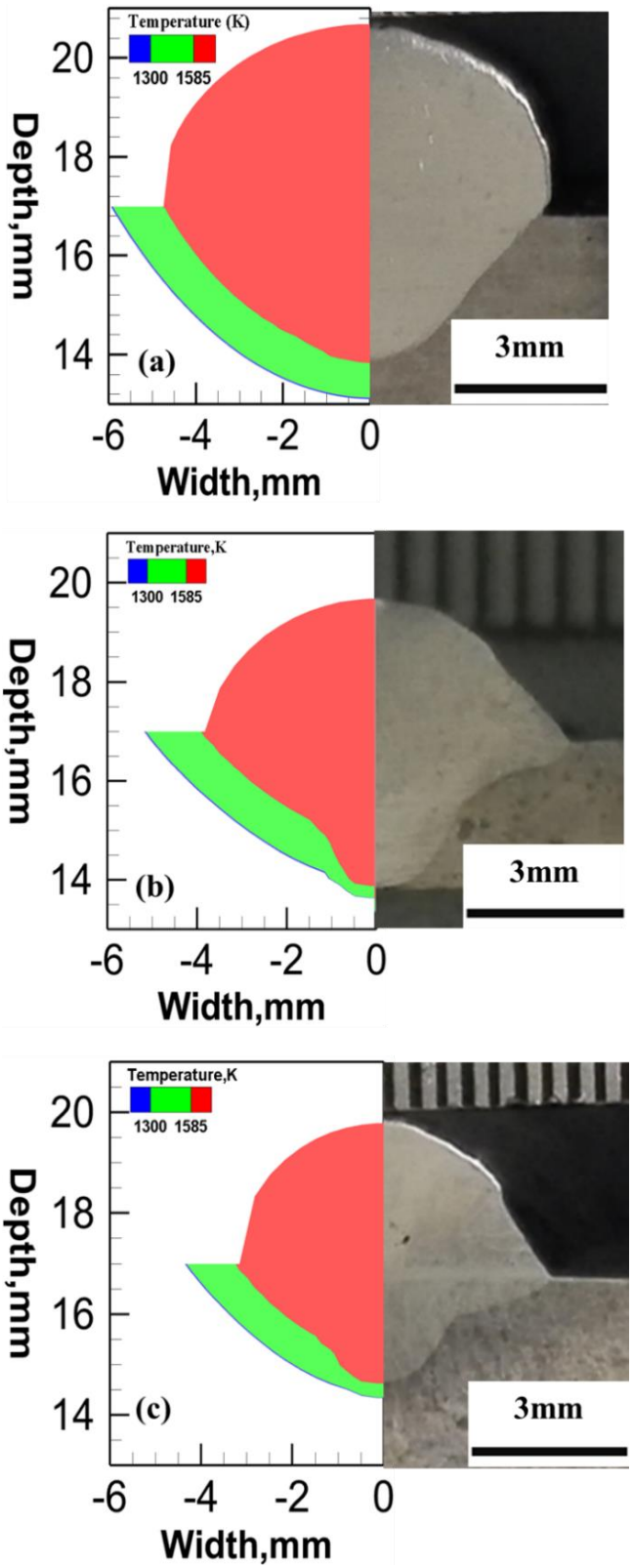

Figure 3.30. Comparison between the calculated transverse sections of the H13 DED-GMA deposit with the corresponding experimentally measured [34] macrograph using (a) 5 mm/s (b) 8.3 mm/s and (c) 11.7 mm/s scanning speed and 200 A arc current, 22 V voltage, 133 mm/s wire feed rate and 1.2 mm wire diameter. The red region bounded by the solidus temperature (1585 K) isotherm represents the transverse section of the deposit.

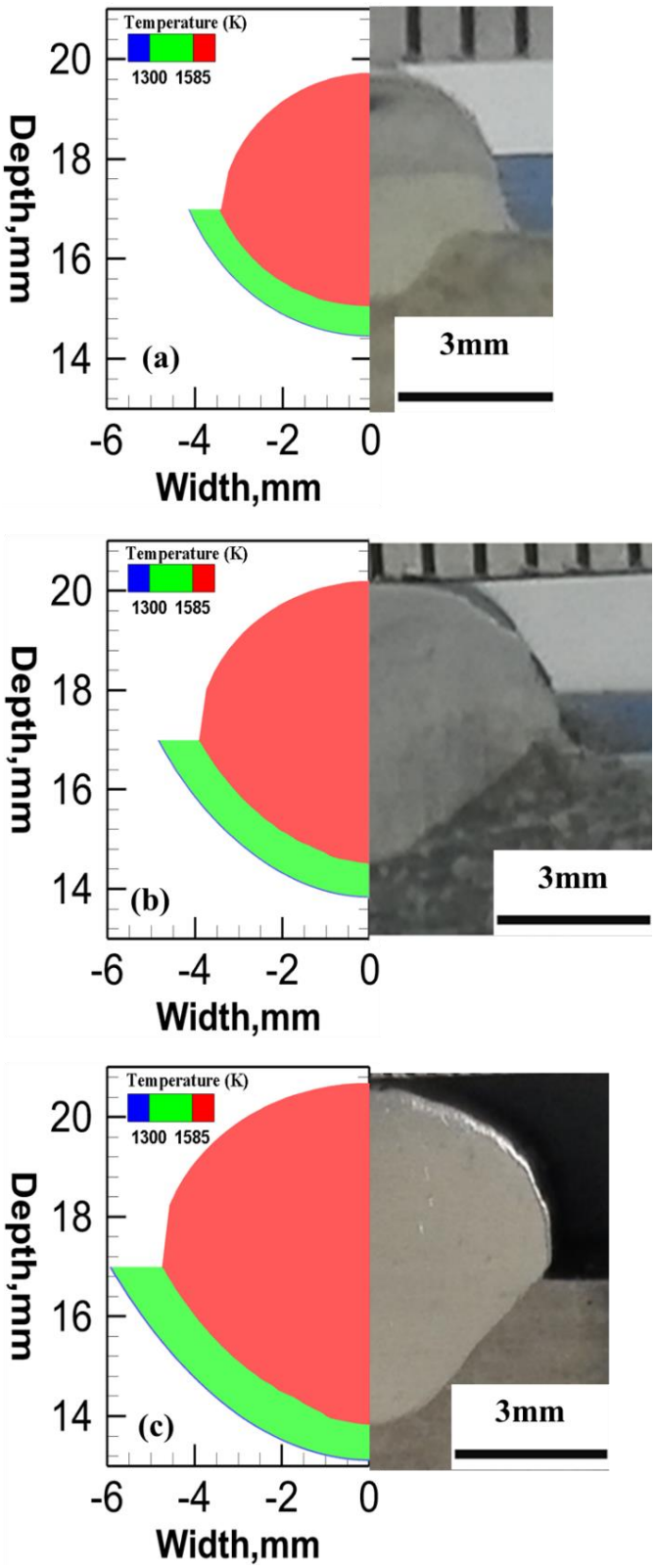

Figure 3.31. Comparison between the calculated transverse sections of the H13 DED-GMA deposit with the corresponding experimentally measured [34] macrograph using (a) 1800 W (b) 3000 W and (b) 4400 W arc power and 5 mm/s scanning speed, 63 mm/s wire feed rate and 1.2 mm wire diameter.. The red region bounded by the solidus temperature (1585 K) isotherm represents the transverse section of the deposit.

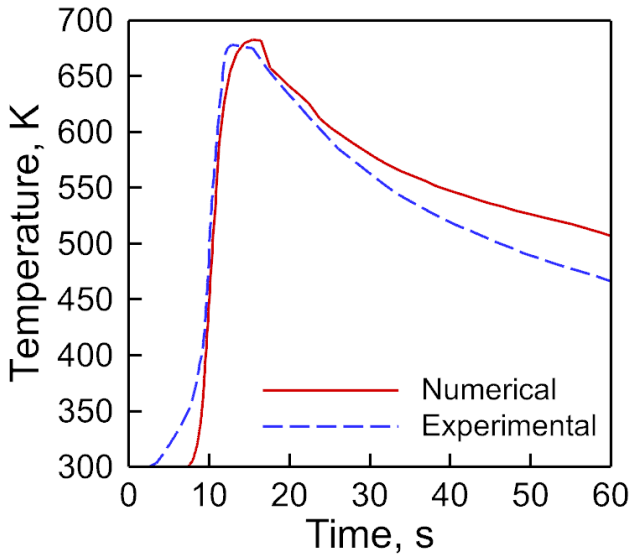

Figure 3.32. Comparison between the calculated and the measured [35] thermal cycles during DED-GMA of a carbon steel using 250 A arc current, 30 V voltage, 10 mm/s scanning speed, 60 mm/s wire feed rate and 1.6 mm wire diameter.

3.8 Importance of fluid flow calculations

The velocity of liquid metal flow is on the order of 50-100 mm/s during AM depending on the value of the temperature coefficient of surface tension, $d\gamma/dt$ and local temperature gradient. This flow influences the pool geometry, heat transfer mechanism inside the pool and temperature field. Therefore, calculations using heat conduction models that ignore the effects of molten metal convection are often erroneous. For example, the peak temperature in PBF-L estimated by heat conduction model is overestimated by approximately 400 K, as shown in Figure 3.33 (a). Since molten metal convection mixes hot and cold liquid and reduces the peak temperature, the temperature values predicted by heat conduction models are overestimated. In the absence of surface active elements like sulfur and oxygen, liquid metal flows from the center to the periphery of the molten pool, resulting in a wide and shallow deposit. In contrast, heat conduction calculations, where convective flow is neglected, predict narrower and deeper molten pool geometries that often do not agree well with the experimental measurements [34], as shown in Figure 3.33 (b). However, under some processing conditions fluid flow calculations provide limited advantage. For example, Figure 3.33 (c-d) show that the effects of molten metal convection on peak temperature and pool width during PBF-L become less significant at high scanning speeds. At higher scanning speed, the molten pool solidifies rapidly even before the convective flow can mix the hot and cold liquids. Therefore, inclusions of molten metal convection in the modeling for very high speed AM processes often provides limited advantage.

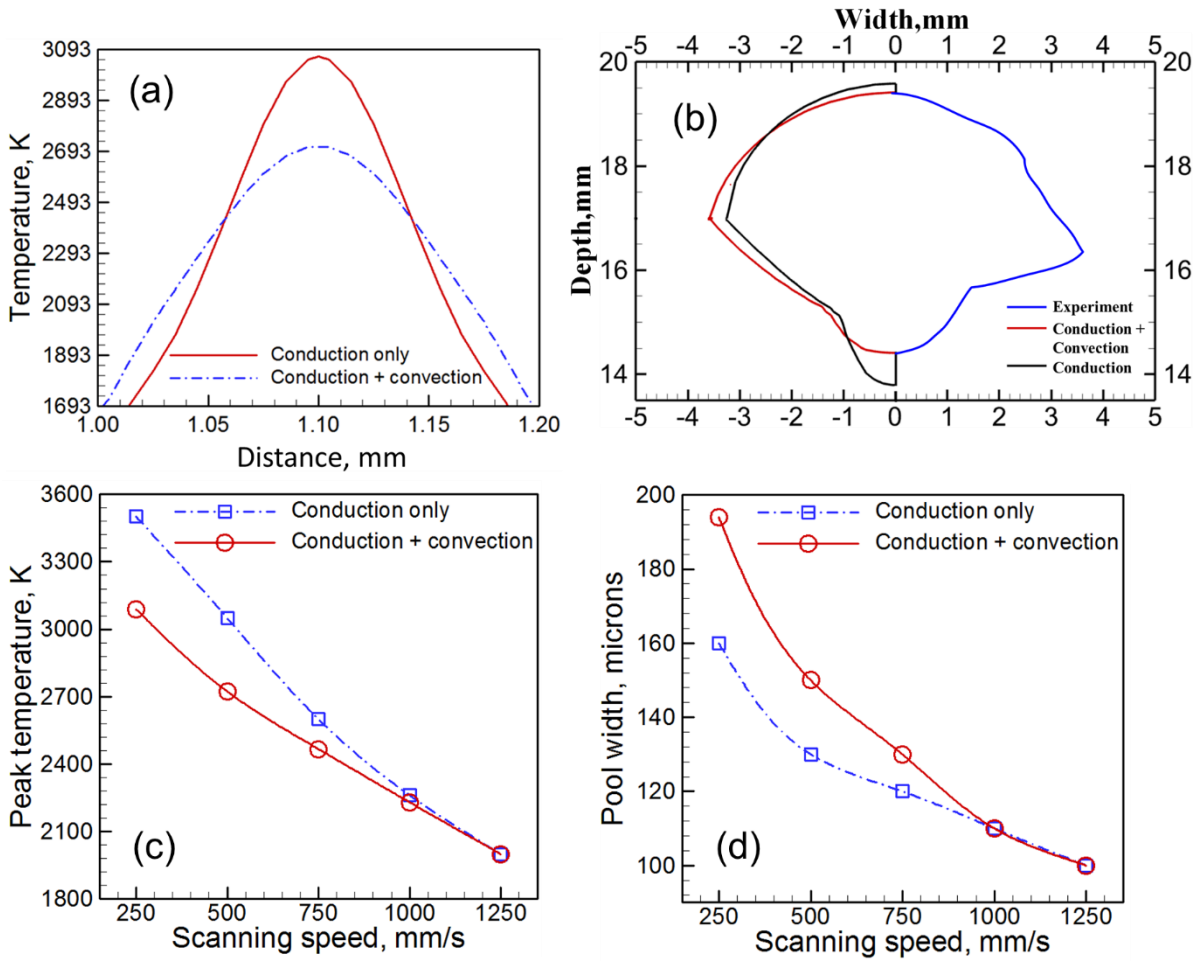

Figure 3.33. Comparisons between conduction only and conduction + convection calculations of (a) spatial distribution of temperature field in PBF-L of SS 316 using 60W laser power, 250 mm/s scanning speed, 50 microns beam radius and 30 microns layer thickness (b) build geometry for DED-GMA of H13 steel with comparison with corresponding experimental result for 200 A arc current, 22 V voltage, 133 mm/s wire feed rate and 1.2 mm wire diameter [34]. Comparison of (c) peak temperature and (d) pool width at different scanning speeds during PBF-L of SS 316 calculated both considering and neglecting the effects of molten metal convection using 60W laser power, 250 mm/s scanning speed, 50 microns beam radius and 30 microns layer thickness.

3.9 Summary and conclusions

3D, transient heat transfer and fluid flow models of three AM processes are developed and used to calculate temperature and velocity fields and deposit and fusion zone geometries. The calculated temperature distribution and deposit geometries are tested using independent experimental data. Several conclusions can be drawn from these results as described below.

(1) The first hatch produces larger liquid pool than the other hatches in PBF-L process because heat transfer from the liquid pool to its surroundings improves slightly from the first to the

subsequent hatches. This is because in the first hatch the liquid pool is surrounded by the powder bed on both sides while in subsequent hatches one side of the liquid pool interfaces with already deposited dense metal.

(2) For all three AM processes, since heat transfer from the molten pool to the substrate becomes progressively slower in the upper layers, molten pool size increases and cooling rate decreases.

(3) Droplet impact force and arc pressure resulted in deep finger penetration under the arc during DED-GMA. The liquid metal depressed under the arc was displaced to the rear end of the molten pool and formed a crown. The wide and deep deposits facilitate high deposition rates that make the DED-GMA process a practical choice for rapid production of large components at low cost.

(4) Higher heat input achieved by slow scanning or higher arc power resulted in larger deposits in DED-GMA. Use of thicker wire and rapid wire feeding also increased deposit size because of higher amount of material deposition under those conditions.

(5) A travelling fine grid-system is capable of providing good convergence, stability and accuracy of the computed transient three-dimensional temperature and velocity fields for large problems with high computational efficiency and limited memory requirement. For example, a 20 mm long SS 316 component fabricated using PBF-L with 5 layers and 5 hatches is simulated within about 5 hours where the conventional fixed grid model takes around 25 hours to simulate component of similar dimensions in an i7 PC with 8GB RAM.

(6) In PBF-L process, the type of shielding gas plays a more important role than the type of metal powder in determining the thermal conductivity of the powder bed. Because of the high temperature sensitivity of the thermo-physical properties, temperature dependent properties are critical for effective simulation of heat transfer and fluid flow in AM.

3.10 References

1) T. DebRoy et al. Additive manufacturing of metallic components - Process, structure and properties. Prog. Mater. Sci. 92 (2018) 112-224.
2) J.S. Turner, Buoyancy Effects in Fluids, Cambridge University Press (1979).
3) A. De et al. A smart model to estimate effective thermal conductivity and viscosity in the weld pool. J Appl. Phys. 95 (2004) 5230-5240.
4) J.F. Lancaster, The Physics of Welding, International Institute of Welding, Pergamon, Oxford (1986).
5) Z. Yang et al. Modeling macro-and microstructures of gas-metal-arc welded HSLA-100 steel. Metall. Mater. Trans. B 30 (1999) 483–493.
6) S. Kumar et al. Theoretical investigation of penetration characteristics in gas metal-arc welding using finite element method, Metall. Mater. Trans. B 26 (1995) 611–624.
7) F.O. Alpak et al. Validation of a modified Carman-Kozeny equation to model two-phase relative permeabilities. SPE Ann. Tech. Conf. Exhibit. (1999).
8) X. Wang et al. Direct selective laser sintering of hard metal powders: experimental study and simulation. Int. J Adv. Manuf. Technol. 19 (2002) 351-357.
9) P. Farahmand et al. An experimental–numerical investigation of heat distribution and stress field in single-and multi-track laser cladding by a high-power direct diode laser. Opt. Laser Technol. 63 (2014) 154-68.
10) Z. Yang et al. Modeling macro-and microstructures of gas-metal-arc welded HSLA-100 steel. Metal. Mater. Trans. B 30 (1999) 483-93.
11) K. Mundra et al. Toward understanding alloying element vaporization during laser beam welding of stainless steel. Weld. J. 72 (1993) 1-s.
12) W. Giauque et al. The Heat Capacity and Entropy of Nitrogen. Heat of Vaporization. Vapor Pressures of Solid and Liquid. The Reaction 1/2 N2+ 1/2 O2= NO from Spectroscopic Data. J American Chem. Soc. 55 (1933) 4875-89.
13) T. Hoshino et al. Determination of the thermal conductivity of argon and nitrogen over a wide temperature range through data evaluation and shock-tube experiments. Int. J Thermophys. 7 (1986) 647-62.
14) P. Tsilingiris. Thermophysical and transport properties of humid air at temperature range between 0 and 100 C. Energy Conv. Manage. 49 (2008) 1098-110.

15) Y. Zhang et al. Melting and resolidification of a subcooled mixed powder bed with moving Gaussian heat source. J Heat Trans. 120 (1998) 883-91.
16) M. Rombouts et al. Photopyroelectric measurement of thermal conductivity of metallic powders. J Appl. Phys. 97 (2005) 024905.
17) N. Saunders et al. Using JMatPro to model materials properties and behavior. JOM 55 (2003) 60–65.
18) N. Saunders et al. Modelling the material properties and behaviour of Ni-based superalloys. Superalloys. 2004 (2004) 849-58.
19) Z. Fan et al. A generalized law of mixtures. J Mater. Sci. 29 (1994) 141-50.
20) Z.N. Cao et al. Modeling of GMA weld pools with consideration of droplet impact. J Eng. Mater. Technol. 120 (1998) 313-20.
21) W. Zhang et al. Heat and fluid flow in complex joints during gas metal arc welding—part I: numerical model of fillet welding. J Appl. Phys. 95 (2004) 5210-9.
22) S.V. Patankar. Numerical Heat Transfer and Fluid Flow, McGraw-Hill, New York (1982).
23) N. Rodriguez et al. Wire and arc additive manufacturing: a comparison between CMT and TopTIG processes applied to stainless steel. Weld. World 62 (2018) 1083-1096.
24) G.L. Knapp et al. Building blocks for a digital twin of additive manufacturing. Acta Mater. 135 (2017) 390-399.
25) A. Foroozmehr et al. Finite element simulation of selective laser melting process considering optical penetration depth of laser in powder bed. Mater. Des. 89 (2016) 255–263.
26) W. Di et al. Study on energy input and its influences on singletrack, multi-track, and multi-layer in SLM. Int. J Adv. Manuf. Technol. 58 (2012) 1189-99.
27) H. Gong et al. Melt pool characterization for selective laser melting of Ti-6Al-4V pre-alloyed powder. Solid Freeform Fab. Symp. (2014) 256–67.
28) M. Tang et al. Prediction of lack-of-fusion porosity for powder bed fusion. Add. Manuf. 14 (2017) 39–48.
29) K. Kempen et al. Processing AlSi10Mg by selective laser melting: parameter optimisation and material characterisation. Mater. Sci. Technol. 31 (2015) 917–23.
30) R. Li et al. Densification behavior of gas and water atomized 316L stainless steel powder during selective laser melting. Appl. Surf. Sci. 256 (2010) 4350–6.

31) I.A. Roberts et al. A three-dimensional finite element analysis of the temperature field during laser melting of metal powders in additive layer manufacturing. Int. J. Machine Tools. Manuf. 49 (2009) 916–923.
32) V.D. Manvatkar et al. Estimation of melt pool dimensions, thermal cycle, and hardness distribution in the laser-engineered net shaping process of austenitic stainless steel. Metall. Mater. Trans. A 42 (2011) 4080-87.
33) F. Lia et al. Process and microstructural validation of the laser-based directed energy deposition process for Ti-6Al-4V and Inconel 625 material. Mater. Sci. Technol. Columbus, OH, USA (2015).
34) W. Ou et al. Fusion zone geometries, cooling rates and solidification parameters during wire arc additive manufacturing. Int. J Heat Mass Trans. 127 (2018) 1084-1094.
35) X. Bai et al. Improving prediction accuracy of thermal analysis for weld-based additive manufacturing by calibrating input parameters using IR imaging, Int. J. Adv. Manuf. Technol. 69 (2013) 1087–1095.

Chapter 4

RESIDUAL STRESSES AND DISTORTION IN ADDITIVE MANUFACTURING OF ALLOYS

It is evident from the previous chapters in this thesis that AM of alloys involves rapid heating, melting, solidification and cooling of the part. As a result, different regions of the component experience repeated heating and cooling. The spatially varied thermal cycles result in residual stresses and distortion in the AM parts [1]. High residual stresses may cause macroscopic defects such as delamination, buckling and warping of components [1] and degrade the fatigue properties of AM parts [1]. The dimensions of the printed part may deviate significantly from the designed specifications due to distortion which may lead to part rejection in extreme cases. To avoid these difficulties, a better understanding of the accumulation of residual stresses and distortion in AM parts is needed. Therefore, in this thesis research, transport phenomena based modeling is used to explain the evolution and spatial variations of residual stresses and distortion during AM of metallic components.

In this chapter, the calculations of residual stresses and distortion using a finite element based thermomechanical model are described. This model calculates the residual stresses and distortion based on the 3D, transient temperature fields estimated using the heat transfer and fluid flow model as described in Chapter 3. The methodology for the calculations of residual stresses and distortion described in this chapter are applicable for all three AM processes, DED-GMA, DED-L and PBF-L. However, in this chapter, results are presented for DED-L of Inconel 718 and Ti-6Al-4V as examples. In addition, based on the modeling results, it was explained how the sharp gradients in residual stresses and distortion in the dissimilar joints between 2.25Cr-1Mo steel and alloy 800H as well as Ti-6Al-4V and 800H can be alleviated using graded joints made by DED-L between those alloys. Finally, a novel, dimensionless strain parameter was proposed for shop floor usage in order to guide engineers to find suitable conditions to mitigate distortion in AM parts.

4.1 Thermomechanical model to calculate residual stresses and distortion in AM

In this thesis research, a thermomechanical model is used to calculate residual stresses and distortion in AM of metallic components. The mathematical formulation including the governing equations and boundary conditions as well as the numerical solution technique of the model are described in this sub-section. Results on model validation using independent experimental data from the literature are also provided.

4.1.1 Mathematical formulation of residual stresses and distortion

The thermomechanical model calculates residual stresses based on the total strain increment ($\Delta\varepsilon_{lm}^{tot}$) with respect to time during the AM process [2]. The total strain increment is

$$\Delta\varepsilon_{lm}^{tot} = \Delta\varepsilon_{lm}^{E} + \Delta\varepsilon_{lm}^{P} + \Delta\varepsilon_{lm}^{Th} + \Delta\varepsilon_{lm}^{V} \quad (4\text{-}1)$$

where $\Delta\varepsilon_{lm}^{E}$, $\Delta\varepsilon_{lm}^{P}$ and $\Delta\varepsilon_{lm}^{Th}$ are the elastic, plastic and thermal strain increments respectively. $\Delta\varepsilon_{lm}^{V}$ is the strain induced due to the solid state phase transformation and creep, which is assumed to be zero. The resulting stress increment estimated from the elastic strain as [3]:

$$\Delta\sigma_{ij}^{E} = D_{ijlm} \cdot \Delta\varepsilon_{lm}^{E} \quad (4\text{-}2)$$

where D_{ijlm} is stiffness matrix calculated from Young's modulus (E) and Poisson's ratio (υ) [4],

$$D_{ijlm} = \frac{E}{1+\nu}\left[\frac{1}{2}\left(\delta_{ij}\,\delta_{lm} + \delta_{il}\,\delta_{jm}\right) + \frac{\nu}{1-2\nu}\delta_{ij}\,\delta_{lm}\right] \quad (4\text{-}3)$$

where δ is a Dirac delta function [4] whose value is one only for $i=j$ and $l=m$, and is zero otherwise. Temperature-dependent plasticity with the von Mises yield criterion [3] is utilized to model the flow stress and plastic strain. The thermal strain increment is calculated as [2]:

$$\Delta\varepsilon_{lm}^{Th} = \beta\,\delta_{lm}\,\Delta T \quad (4\text{-}4)$$

where, β is the volumetric thermal expansion coefficient and ΔT is the temperature increment with respect to time. The temperature increment is calculated from the transient temperature distribution estimated using the heat transfer and fluid flow model. It is evident from Equations (4-2) to (4-4) that the thermomechanical calculations require temperature dependent mechanical properties of alloys. Since, in this chapter, evolution (Section 4.2) and spatial distribution (Section 4.3) of residual stresses and distortion are explained by considering DED-L of Inconel 718 and Ti-6Al-4V as examples, mechanical properties of these two alloys used in the calculations are provided in Table 4.1 and 4.2. These property data are taken from the literature [5-7]. Figure 4.1 shows that alpha volume fraction does not have significant effect on yield strength of Ti-6Al-4V compared to temperature [8]. Therefore, effect of alpha and beta fractions on mechanical properties in thermomechanical model are not considered.

Table 4.1. Temperature dependent mechanical properties of Inconel 718 [5]

Temperature (K)	Young's Modulus (GPa)	Temperature (K)	Volumetric expansion co-efficient (/K)	Temperature (K)	Yield stress (MPa)
300	156.3	300	1.17E-05	300	308.9
366.5	151.8	477.6	1.28E-05	588.7	246.3
477.6	144.9	588.7	1.34E-05	810.9	226.1
588.7	138	922	1.46E-05	1033.2	207.7
699.8	131.4	1033.2	1.51E-05	1255.4	114
810.9	124.7	1144.3	1.57E-05		
922	124	1366.5	1.66E-05		
1033.2	123.4	1672	1.66E-05		
1144.3	107.7	1900	1.42E-05		
1255.4	92.05	2400	1.08E-05		
1366.5	68.95	2700	9.47E-06		
1672	23.79	3200	7.84E-06		

Table 4.2. Temperature dependent mechanical properties of Ti-6Al-4V [6-7]

Temperature (K)	Young's Modulus (GPa)	Temperature (K)	Volumetric expansion co-efficient (/K)	Temperature (K)	Yield stress (MPa)
300	125	300	8.78E-06	300	955
533	110	533	9.83E-06	573	836
589	100	589	1.00E-05	773	732
700	93	700	1.07E-05	1023	581
755	80	755	1.11E-05	1073	547
811	74	811	1.12E-05	1173	480
923	55	923	1.17E-05	1273	405
1073	27	1073	1.22E-05	1373	330
1098	22	1098	1.23E-05		
1123	18	1123	1.24E-05		
1573	12	1573	1.30E-05		
1873	9	1873	1.63E-05		

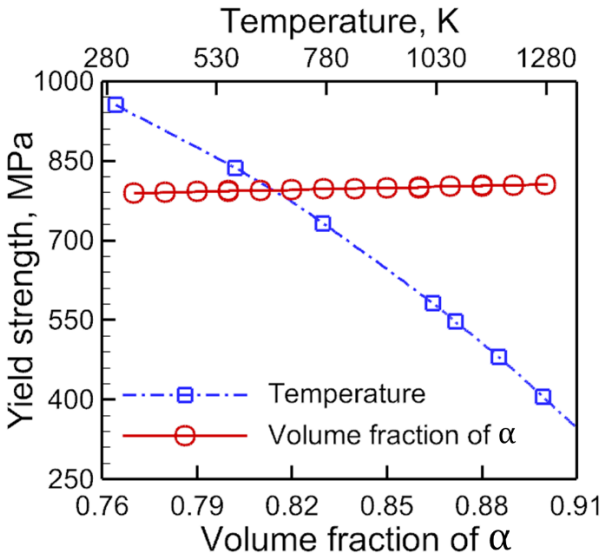

Figure 4.1. Variations in yield strength of Ti-6Al-4V with volume fraction of alpha phase (room temperature) and temperature. The data are taken from the literature [7-8]. Insignificant effect of volume fraction of alpha justifies the assumption of ignoring phase transformation effect on mechanical properties.

The thermomechanical model is developed based on Abaqus®, a commercial finite element analysis (FEA) code [2]. All results presented in this chapter are for single hatch, multi-layer DED-L deposits. The surfaces of the deposited layers are considered to be flat to make calculations tractable. Half of the solution domain is considered by taking the advantage of the symmetry to enhance the computational efficiency. The boundary conditions for the calculations include fixed bottom surface, i.e. the displacements of all nodes of the bottom surface are zero. These conditions are consistent with the large substrate typically used in AM.

4.1.2 Numerical solution technique of the model

The step-by-step procedure for calculating the residual stresses and distortion is illustrated in Table 4.3. A Python script is developed to facilitate mapping the transient temperature fields from the heat transfer and fluid flow model to the Abaqus-based FEA model. The script uses the Abaqus Scripting Interface, an application programming interface (API), to create an ODB file that contains the transient temperature fields. Compared to the other option using Abaqus user subroutine UTEMP to load temperature fields into the stress model, the ODB file has the advantage of more easily handling large dataset of temperature fields. In this chapter, the stresses along scanning, hatching and building directions are called as longitudinal, transverse and through-thickness residual stresses, respectively.

4.1.3 Model validation

Residual stresses calculated using the thermomechanical model are tested against independent experimental data. Figure 4.2 shows a fair agreement between the calculated residual stresses with the corresponding experimentally measured values taken from the literature [9] for DED-L of IN 718 on a Ti-6Al-4V substrate. Figures 4.2 (a) and (b) represent the longitudinal and through-thickness components of the residual stresses, respectively. The stresses were measured at different locations along the substrate deposit interface. Several measurements were taken at the same position to estimate the error bars [9]. The reasons for the slight mismatch between the experimental and calculated values could be caused both by the measurement difficulties and the assumptions made in numerical calculations. However, reasonably good agreement between the calculated and measured values provides the confidence to use this model to explain the temporal evolution and spatial distribution of residual stresses and distortion as discussed in the next section.

Table 4.3. Outline of the sequentially-coupled model combining the heat transfer and fluid flow model with the FEA model.

Computational model	Inputs	Outputs	Description
3D transient heat transfer and fluid flow model	Process parameters and temperature dependent thermo-physical properties of the alloys	Temperature and velocity fields	The model solves the equations of conservation of mass, momentum and energy in a 3D discretized solution domain consisted of the substrate, and deposited layers.
Importing the nodes, elements and temperature data to the FEA model	Nodes, elements and temperature data from the heat transfer and fluid flow model	A temperature field data file (ODB) that can be imported in the FEA solver for mechanical analysis	A Python script that combines all nodes, elements and corresponding transient temperature data and generates an ODB file that can be directly used in the Abaqus-based FEA solver to calculate stress and strain fields.
Abaqus-based FEA model for stress and strain calculations	Nodes, elements, boundary conditions, transient temperature data, and temperature-dependent mechanical properties of the alloys	Transient stress and strain fields	Finite element solution of static force equilibrium equations in the discretized solution domain for the temperature data calculated using the heat transfer and fluid flow model.

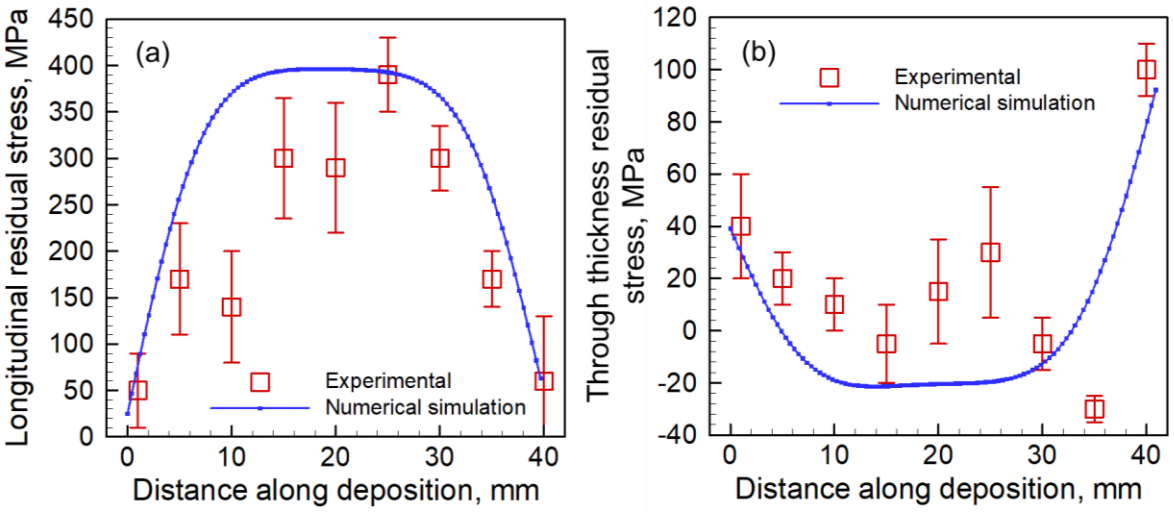

Figure 4.2. Comparison of experimentally measured [9] and numerically computed (a) longitudinal residual stress and (b) through-thickness residual stress during single-track DED-L of IN 718 powder on a Ti-6Al-4V substrate using 600 W laser power, 4 mm/s scanning speed, 0.8 mm beam radius, 0.358 g/s powder mass flow rate and 11 mm substrate thickness. The stress values are measured at the substrate deposit interface at mid-width of the track.

4.2 Evolution of residual stresses and distortion during AM

Evolution of residual stresses and distortion during AM of metallic components depends on the transient temperature distribution during both deposition and cooling of the deposit. The stresses and distortion experienced by components during deposition significantly contribute to the final residual stresses fields. In other words, the evolution of stresses and distortion during cooling starts from their distributions during deposition. Therefore, to provide a detailed understanding of the residual stresses and distortion in AM parts, their evolution both during the deposition process as well as when the parts cools down to the room temperature at the end of the deposition are examined.

In this subsection, the temporal evolution of residual stresses and distortion is explained based on the transient temperature distributions during single track, multi-layer DED-L of IN 718 and Ti-6Al-4V. The parameters used in the calculations are summarized in Table 4.4. Figure 4.3 to 4.6 show the evolution of vertical deformation and longitudinal, transverse and through-thickness components of residual stresses during deposition. Figure 4.3 shows that during the deposition process temperature of the component increases which results in an enhancement in deformation. In contrast, deposition of a new layer softens the component because of reheating which partially alleviates the residual stresses already accumulated in the component. Figure 4.7 to 4.10 show the evolution of vertical deformation and stress components during cooling. During the deposition of a particular layer the heating effect partially alleviate the residual stresses that accumulated while depositing the previous layer. The stresses are accumulated during cooling starting from the stress field already evolved during deposition. It is evident from the figures that deformation is reduced during the cooling process. As a result, stresses are accumulated in the component during the cooling. Since the top edge of the component cools down to the room temperature at the end, high tensile stresses accumulate in that region as shown in figures (f) in Figure 4.7 to 4.10. The stresses that remain at the end of the cooling when the component reaches the ambient temperature are the residual stresses as shown in Figure 4.11.

Table 4.4. Process parameters corresponding to the results in Sections 4.2 and 4.3.

Laser power (W)	Beam radius (mm)	Scanning speed (mm/s)	Layer thickness (mm)	Substrate thickness (mm)	Powder flow rate (gm/s)
200-400	0.5	15	0.4-0.8	4	0.416

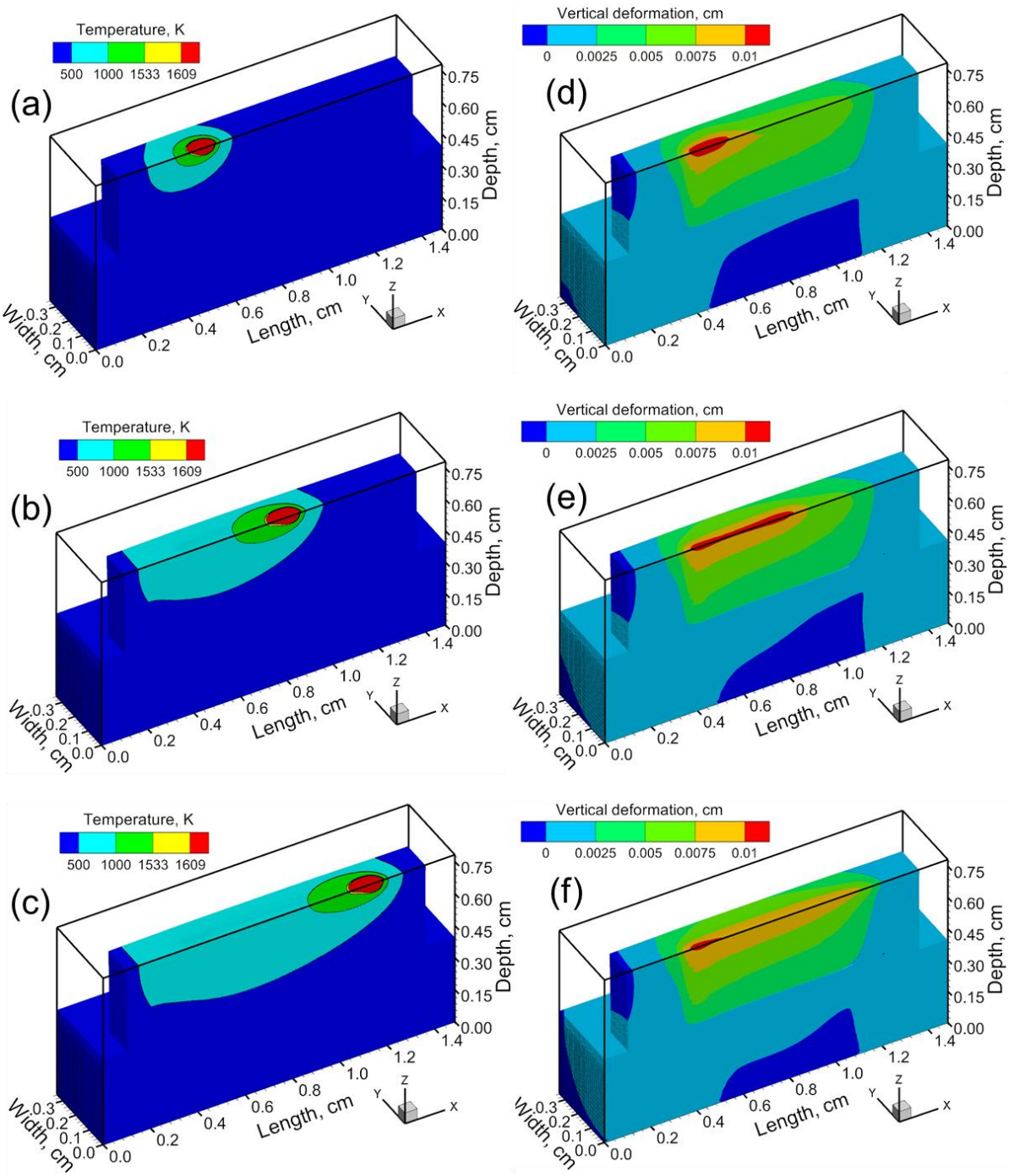

Figure 4.3. Temperature fields at (a) beginning (b) middle and (c) end of deposition of 10th layer. Vertical deformation at (a) beginning (b) middle and (c) end of deposition of 10th layer. All results are for a 10 layers deposit of IN 718 powder printed using DED-L on a IN 718 substrate. Laser beam scanning direction is along the positive x-axis. This simulation is done for 300 W laser power and 15 mm/s scanning speed. Other parameters are provided in Table 4.4. Half of the solution domain is shown because of the symmetry with respect to XZ plane.

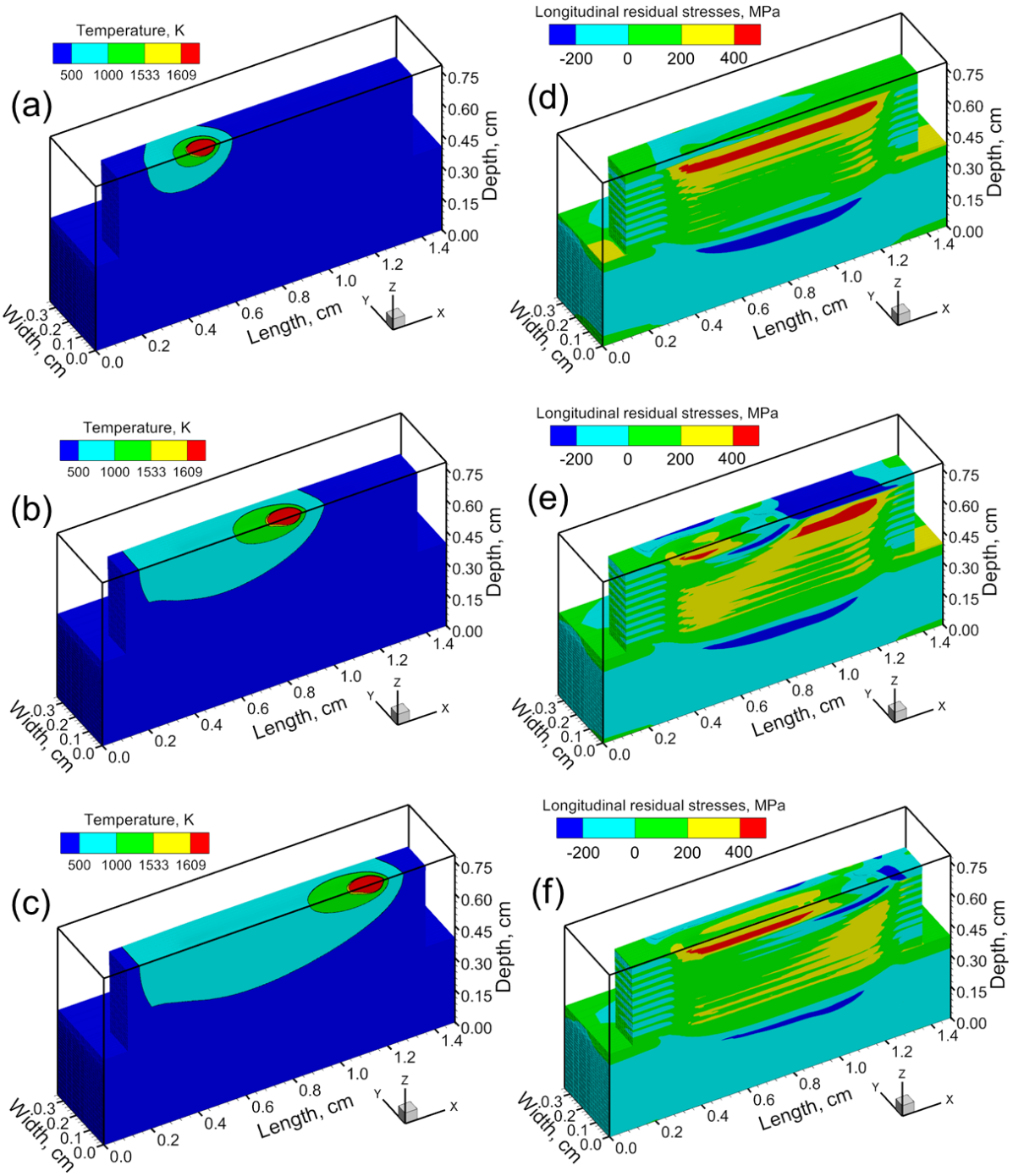

Figure 4.4. Temperature fields at (a) beginning (b) middle and (c) end of deposition of 10th layer. Longitudinal residual stresses at (a) beginning (b) middle and (c) end of deposition of 10th layer. All results are for a 10 layers deposit of IN 718 powder printed using DED-L on a IN 718 substrate. Laser beam scanning direction is along the positive x-axis. This simulation is done for 300 W laser power and 15 mm/s scanning speed. Other parameters are provided in Table 4.4. Half of the solution domain is shown because of the symmetry with respect to XZ plane.

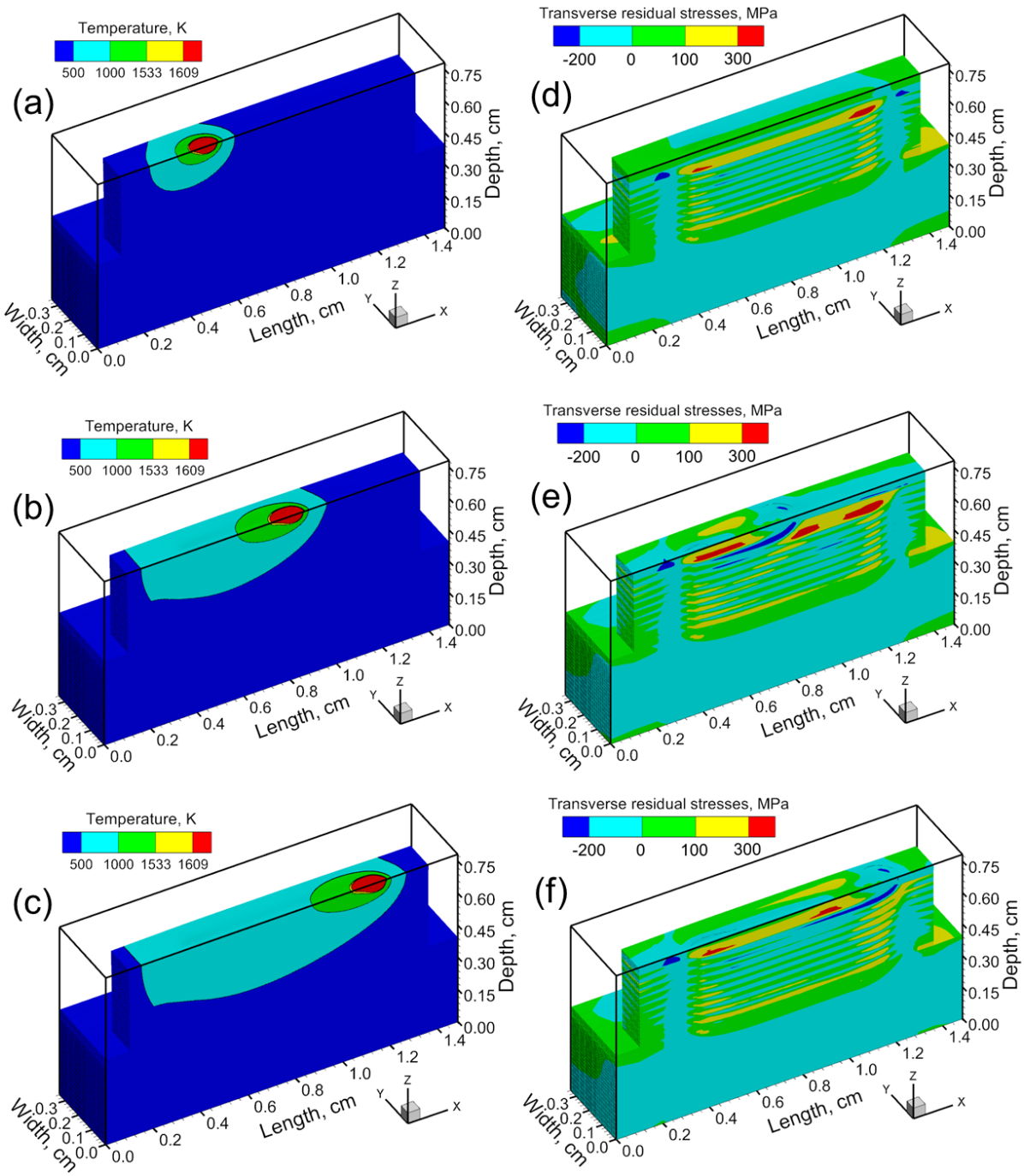

Figure 4.5. Temperature fields at (a) beginning (b) middle and (c) end of deposition of 10th layer. Transverse residual stresses at (a) beginning (b) middle and (c) end of deposition of 10th layer. All results are for a 10 layers deposit of IN 718 powder printed using DED-L on a IN 718 substrate. Laser beam scanning direction is along the positive x-axis. This simulation is done for 300 W laser power and 15 mm/s scanning speed. Other parameters are provided in Table 4.4. Half of the solution domain is shown because of the symmetry with respect to XZ plane.

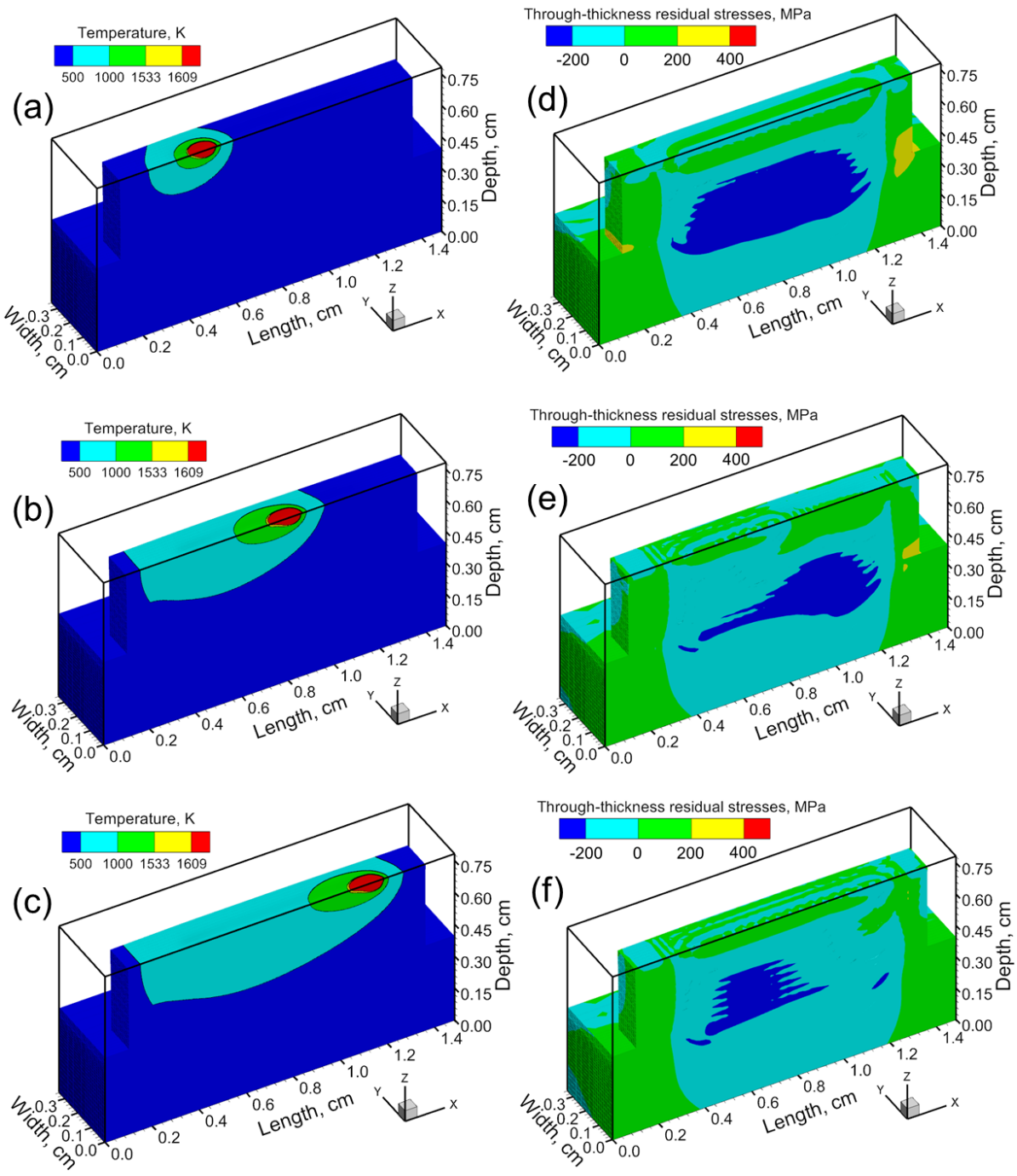

Figure 4.6. Temperature fields at (a) beginning (b) middle and (c) end of deposition of 10th layer. Through-thickness residual stresses at (a) beginning (b) middle and (c) end of deposition of 10th layer. All results are for a 10 layers deposit of IN 718 powder printed using DED-L on a IN 718 substrate. Laser beam scanning direction is along the positive x-axis. This simulation is done for 300 W laser power and 15 mm/s scanning speed. Other parameters are provided in Table 4.4. Half of the solution domain is shown because of the symmetry with respect to XZ plane.

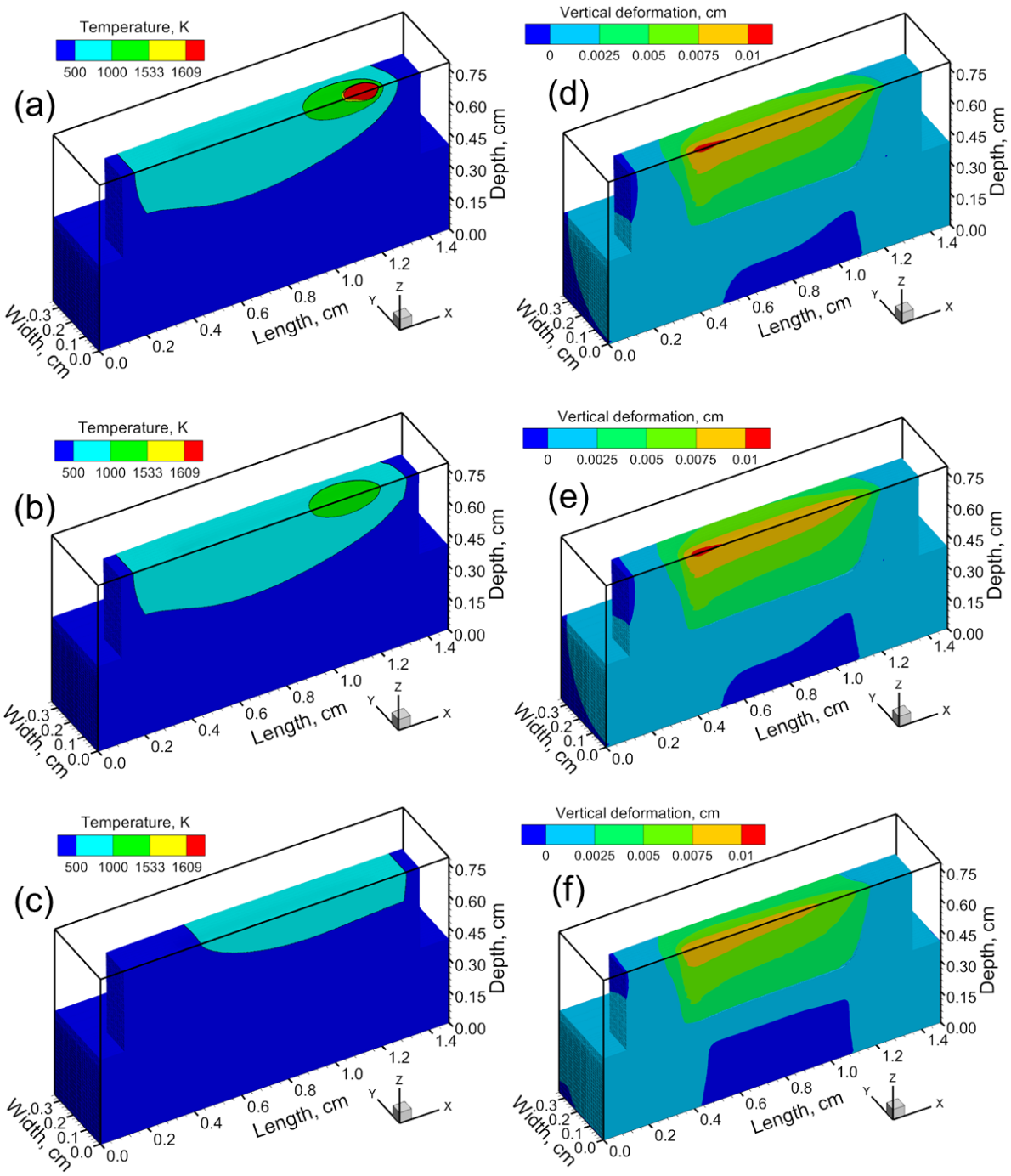

Figure 4.7. Temperature fields at (a) beginning (b) middle and (c) end of cooling after the deposition of 10th layer. Vertical deformation at (a) beginning (b) middle and (c) end of cooling after the deposition of 10th layer. All results are for a 10 layers deposit of IN 718 powder printed using DED-L on a IN 718 substrate. Laser beam scanning direction is along the positive x-axis. This simulation is done for 300 W laser power and 15 mm/s scanning speed. Other parameters are provided in Table 4.4. Half of the solution domain is shown because of the symmetry with respect to XZ plane.

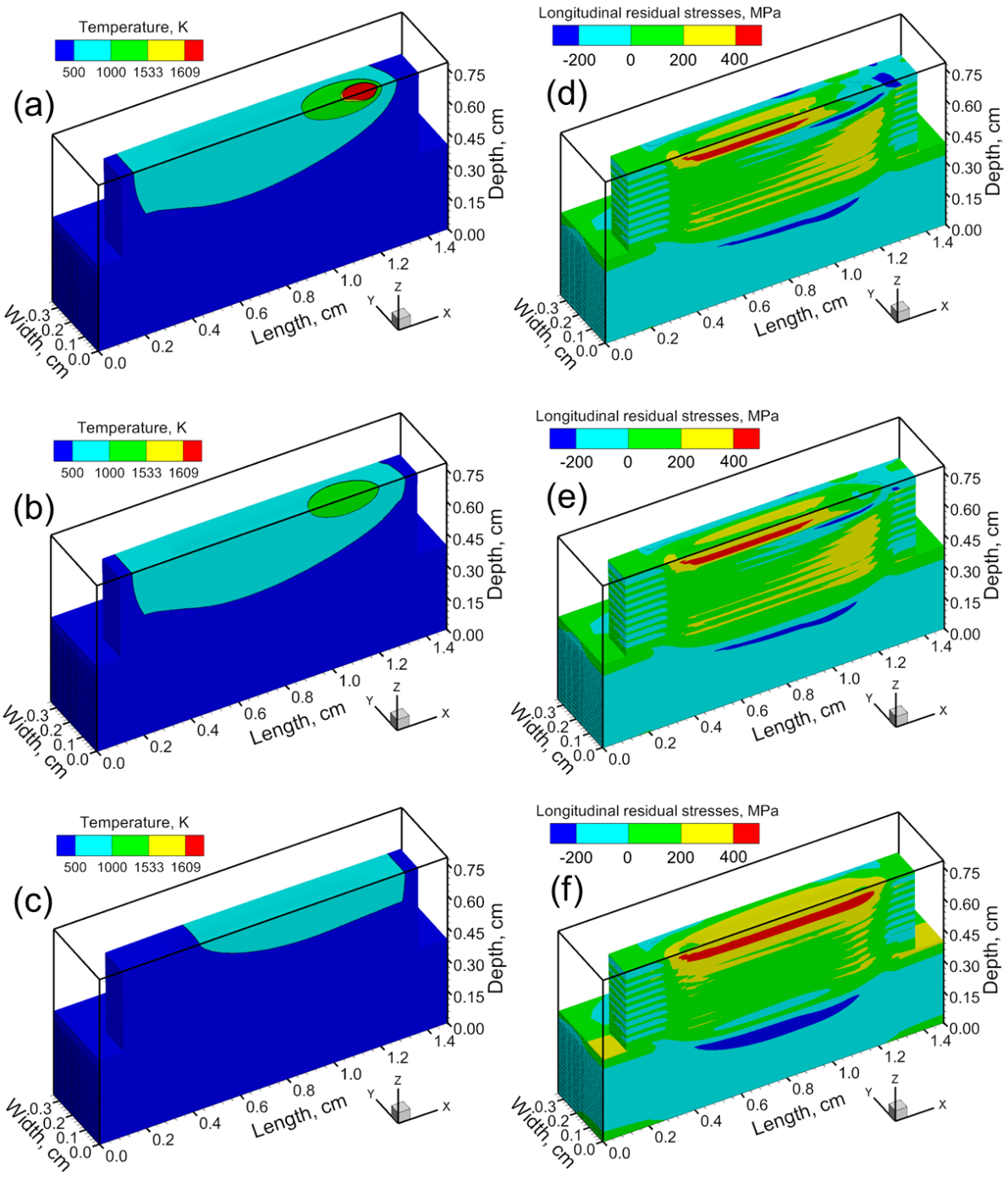

Figure 4.8. Temperature fields at (a) beginning (b) middle and (c) end of cooling after the deposition of 10th layer. Longitudinal residual stresses at (a) beginning (b) middle and (c) end of cooling after the deposition of 10th layer. All results are for a 10 layers deposit of IN 718 powder printed using DED-L on a IN 718 substrate. Laser beam scanning direction is along the positive x-axis. This simulation is done for 300 W laser power and 15 mm/s scanning speed. Other parameters are provided in Table 4.4. Half of the solution domain is shown because of the symmetry with respect to XZ plane.

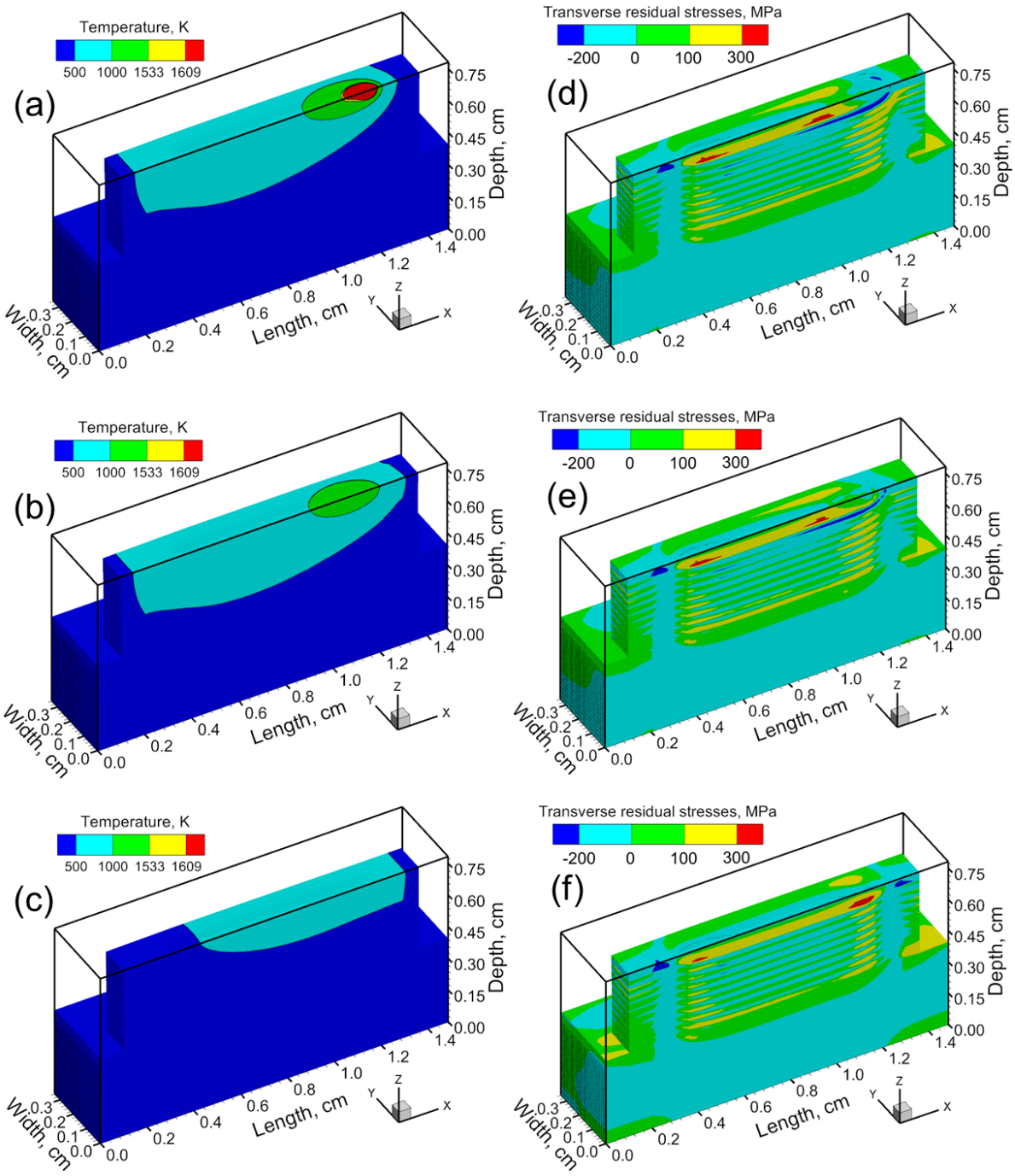

Figure 4.9. Temperature fields at (a) beginning (b) middle and (c) end of cooling after the deposition of 10th layer. Transverse residual stresses at (a) beginning (b) middle and (c) end of cooling after the deposition of 10th layer. All results are for a 10 layers deposit of IN 718 powder printed using DED-L on a IN 718 substrate. Laser beam scanning direction is along the positive x-axis. This simulation is done for 300 W laser power and 15 mm/s scanning speed. Other parameters are provided in Table 4.4. Half of the solution domain is shown because of the symmetry with respect to XZ plane.

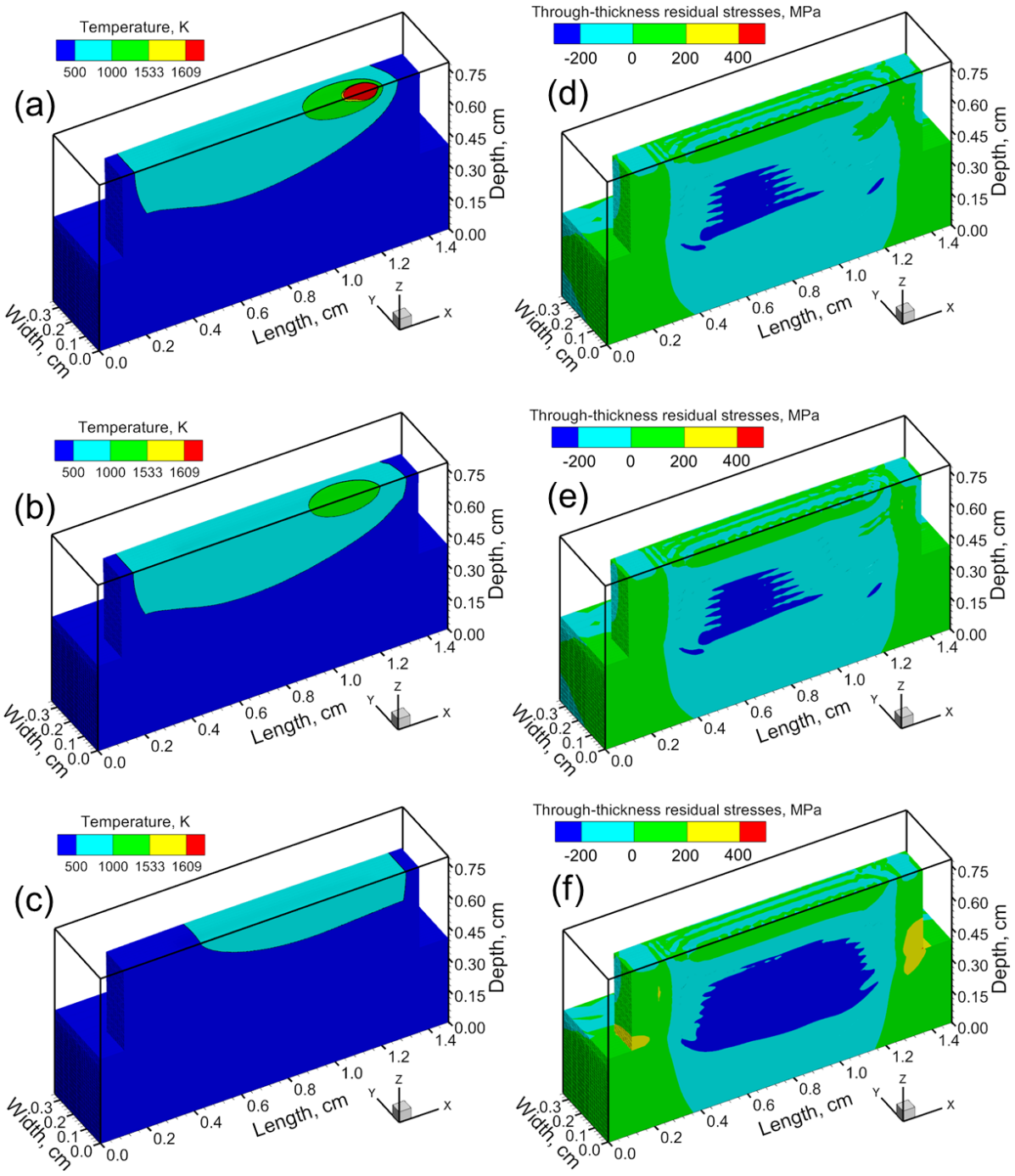

Figure 4.10. Temperature fields at (a) beginning (b) middle and (c) end of cooling after the deposition of 10th layer. Through-thickness residual stresses at (a) beginning (b) middle and (c) end of cooling after the deposition of 10th layer. All results are for a 10 layers deposit of IN 718 powder printed using DED-L on a IN 718 substrate. Laser beam scanning direction is along the positive x-axis. This simulation is done for 300 W laser power and 15 mm/s scanning speed. Other parameters are provided in Table 4.4. Half of the solution domain is shown because of the symmetry with respect to XZ plane.

Evolution of stresses depending on transient temperature field is explained in Figure 4.12 by analyzing the temperature and stress variations during cooling along the substrate deposit interface. Figure 4.12 (a) shows the temperature distribution along the substrate deposit interface during cooling of the build. Figure 4.12 (b) represents the corresponding longitudinal stress profile developed along the same line. At t = 0 s, i.e., just after the laser beam traverses the entire length and is switched off temporarily to prepare for the deposition of the next layer, the peak temperature of the deposit along the substrate-deposit interface is about 950 K. This high temperature softens the material locally. Therefore, the magnitude of the stress is relatively low as it is limited by the yield strength at the high temperature. The stress field evolves as the deposit continues to cool down further. After 50 seconds, the temperature of the deposit almost cools down to the room temperature and the longitudinal stress is highly tensile, as shown in Figure 4.12 (b). If there was no additional layer deposited, the stress field at the end of cooling would not change further, corresponding to the residual stress field in the part.

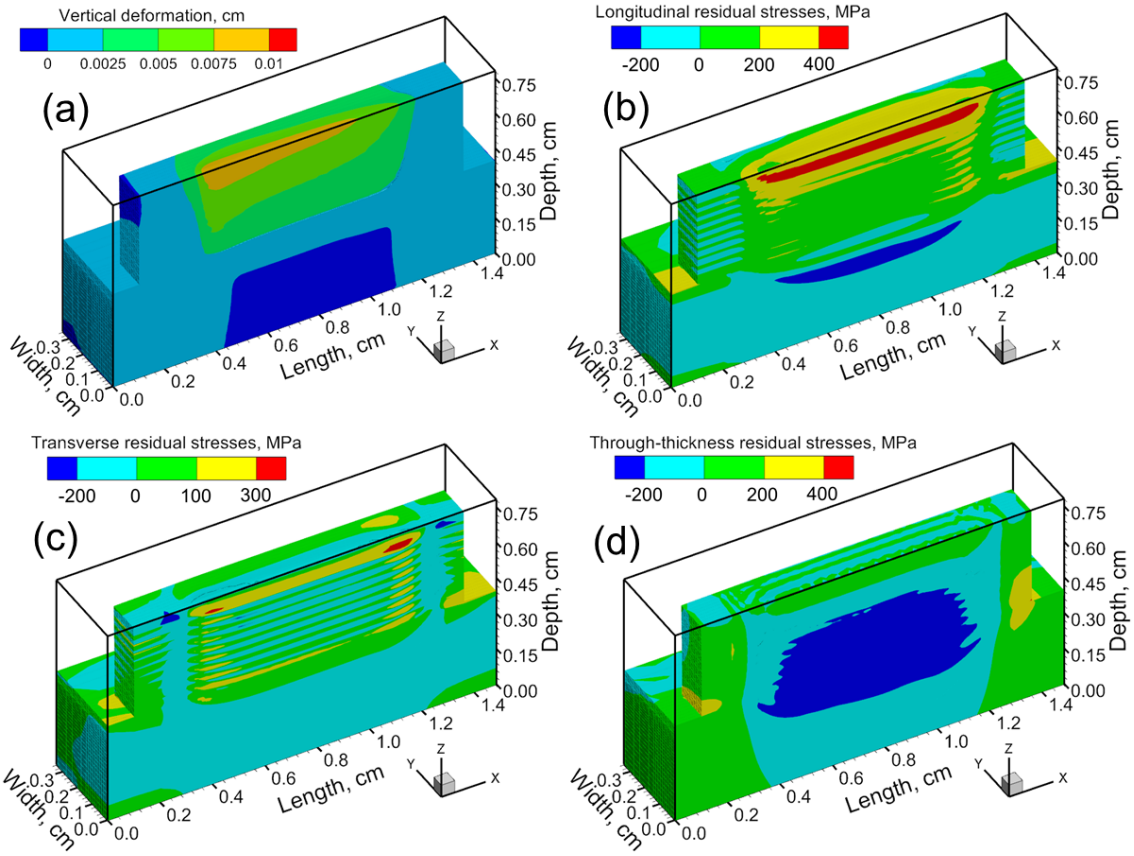

Figure 4.11. (a) Vertical deformation and (b) longitudinal (c) transverse and (d) through-thickness residual stresses in a 10 layers IN 718 deposit printed using DED-L. Laser beam scanning direction is along the positive x-axis. This simulation is done for 300 W laser power and 15 mm/s scanning speed. Other parameters are provided in Table 4.4. Half of the solution domain is shown because of the symmetry with respect to XZ plane.

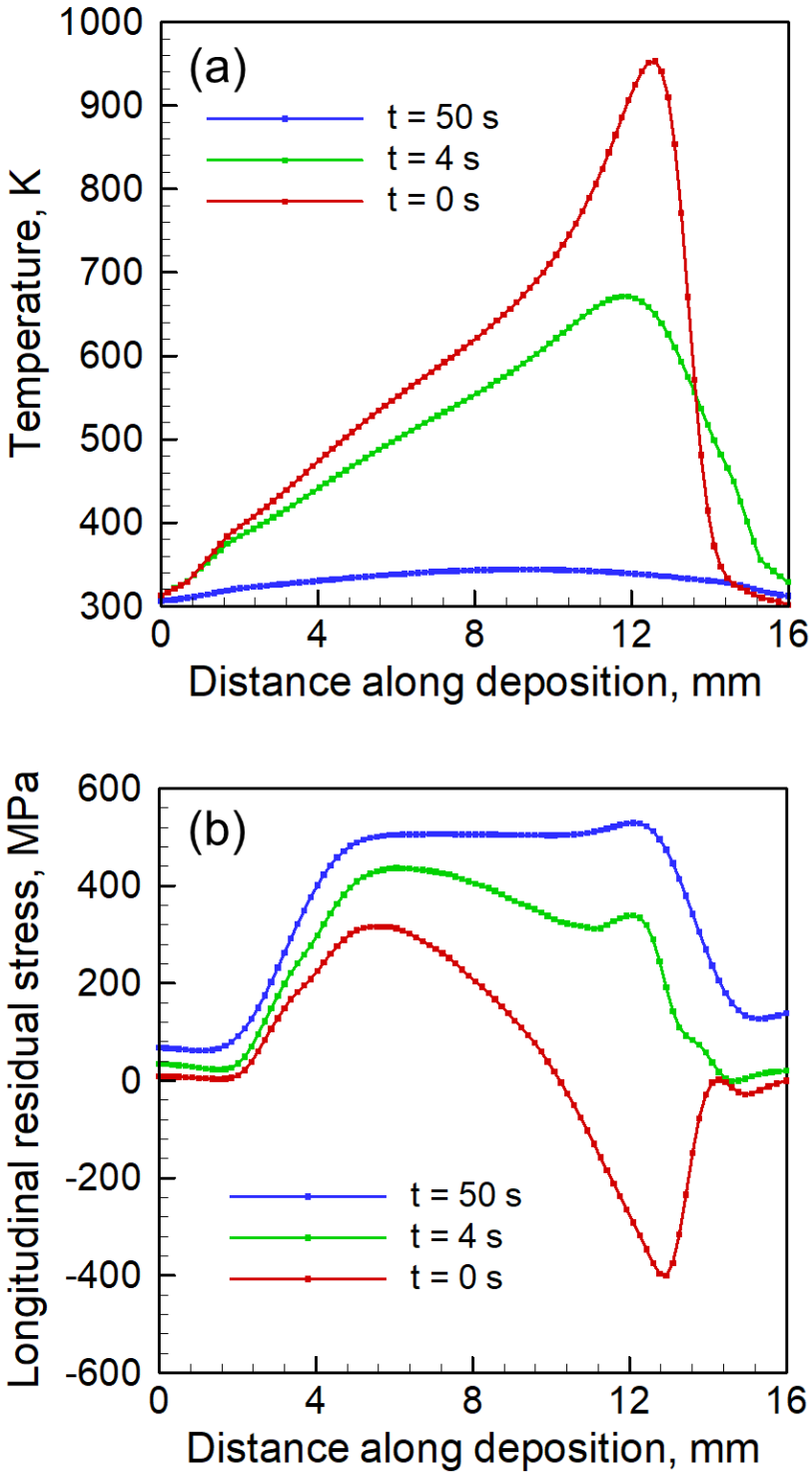

Figure 4.12. Variation in (a) temperature distribution and (b) longitudinal stress distribution along substrate deposit interface with time after the laser beam extinguishes. This simulation is done for IN 718 deposit printed using DED-L with 300 W laser power and 15 mm/s scanning speed. "t" represents the time after the laser beam extinguishes at the end of the deposition. Other parameters are provided in Table 4.4.

4.3 Spatial variation of residual stresses and distortion in AM parts

In AM parts, residual stresses and distortion are spatially non-uniform depending on the transient temperature field, geometric constraints and temperature dependent mechanical properties of the alloy. Stresses can sharply change from tensile to compressive which may cause delamination. In addition, high residual stresses accumulated at a particular region of the part may cause local warping of the component. Since spatial distribution of residual stresses and distortion may result in defects in AM parts, calculated 3D distributions of stresses and strains in AM parts are discussed in this sub-section. For example, Figure 4.13 shows the evolution of the longitudinal strain field during DED-L of IN 718. With the progress of the deposition process, more heat accumulates in the work piece. High heat accumulation increases the local temperature and the thermal strain. Therefore, the strain value increases continuously for the upper layers as shown in Figure 4.13 (a-f). The results indicate that thin-walled, taller structures are more susceptible to deformation than the shorter ones.

Figures 4.14 to 4.16 show the distribution of the residual stresses along x (longitudinal), y (transverse) and z (through-thickness) directions, respectively. The location of the maximum longitudinal and transverse (tensile) residual stresses are near the top of the deposit. For example, after the deposition of the 2^{nd} layer the maximum stress accumulation is observed near the 2^{nd} layer. However, this stress is relieved partially because of the reheating and cooling effects while depositing the upper layers. Therefore, after the deposition of the 4^{th} layer the maximum stress accumulates near layer 4. Similar observations can be made after the depositions of 6^{th}, 8^{th} and 10^{th} layers. In addition, in both Figures 4.14 and 4.15, the residual stresses change from tensile to compressive at the interfaces of the two successive layers as indicated in the figures. The through-thickness stress in Figure 4.16 is compressive in the center of the deposit and tensile near the start and stop at the substrate deposit interface.

To understand the variations in residual stresses distributions for different alloys under same processing conditions, Figure 4.17 compares the distribution of the residual stress components along x, y and z directions at the end of the cooling of 2^{nd} layer of IN 718 and Ti-6Al-4V deposits. All three residual stress components are highly non-uniform, as expected. The residual stresses in the substrate are mostly compressive. There also exists a sharp gradient of stresses at the substrate-deposit interface. For both alloys the longitudinal stress (x-direction) reaches the maximum at the mid length of the deposit and exhibits a sharp decrease toward both ends (free surfaces). A high gradient in through-thickness residual stress (z-direction) at

substrate-deposit interface can potentially cause the separation of the component from the substrate (i.e., delamination). The yield strength of Ti-6Al-4V at room temperature is much higher than that of IN 718. Therefore, the residual stresses are much higher for Ti-6Al-4V as shown in Figure 4.17.

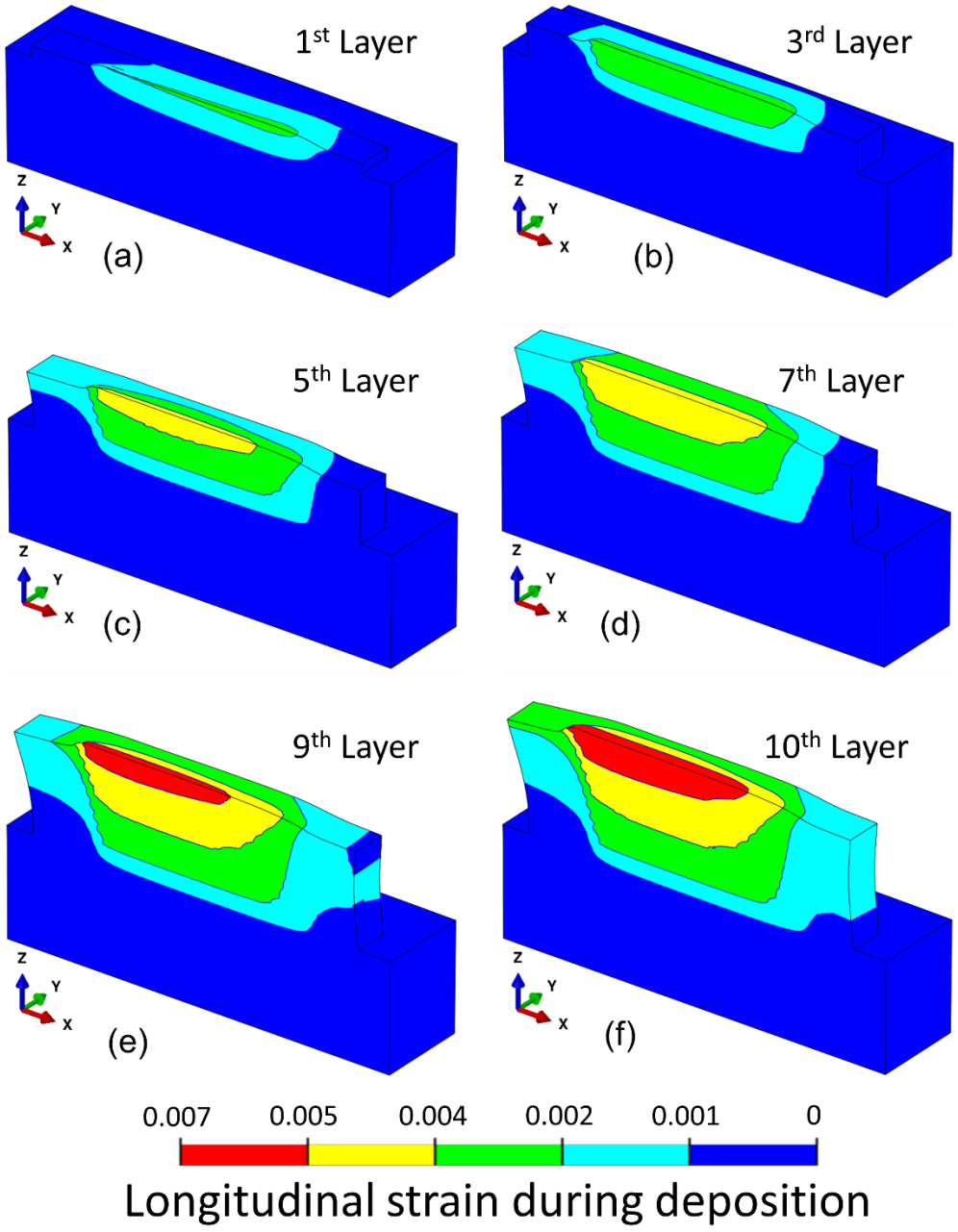

Figure 4.13. Longitudinal strain field at the end of depositing (a) 1st (b) 3rd (c) 5th (d) 7th (e) 9th and (f) 10th layer DED-L of IN 718 powder on IN 718 substrate. Laser beam scanning direction is along the positive x-axis. This simulation is done for 300 W laser power and 15 mm/s scanning speed. Other parameters are provided in Table 4.4. Deformation is magnified by 10x. Half of the solution domain is shown because of the symmetry with respect to XZ plane.

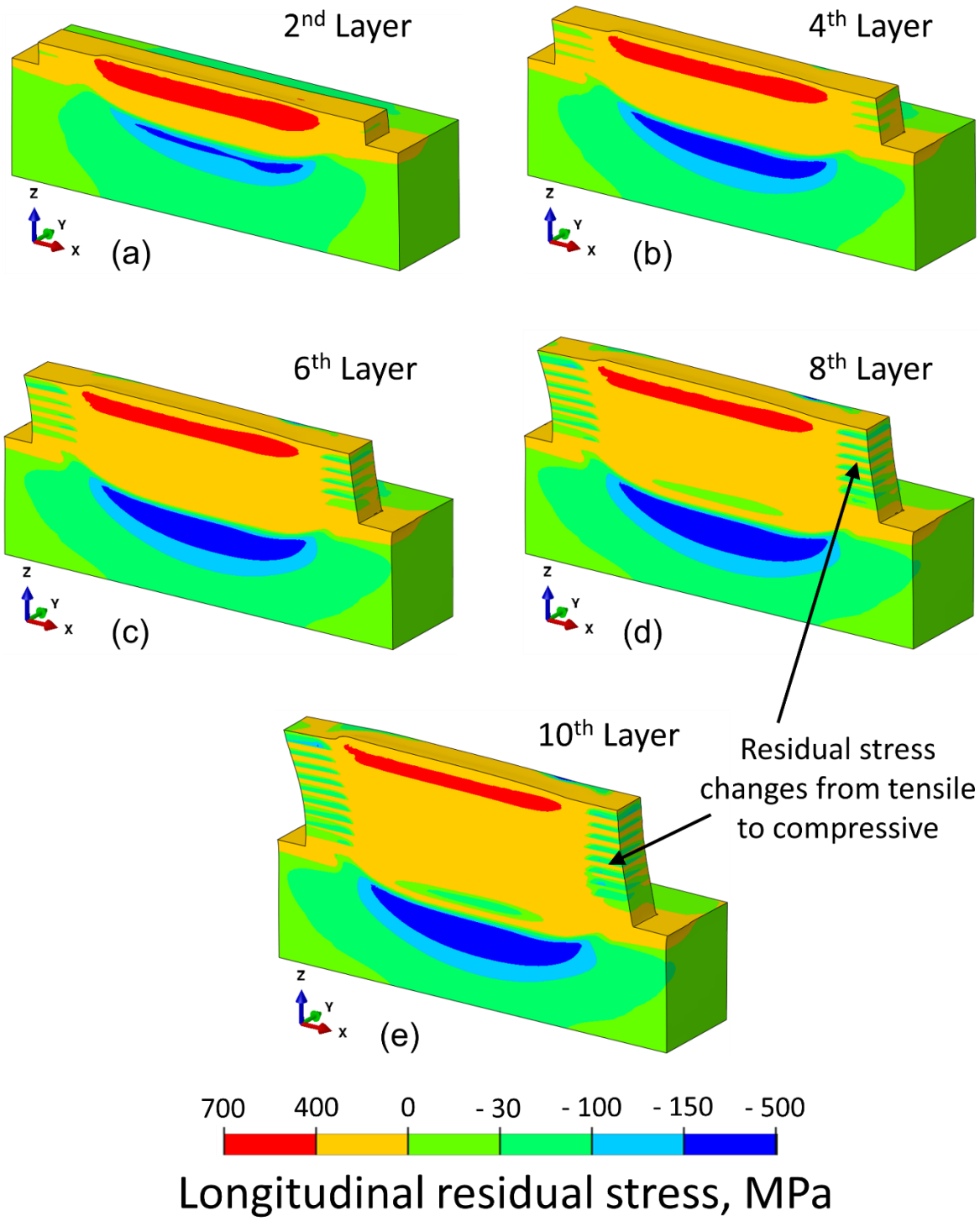

Figure 4.14. Residual stress along x-direction (longitudinal) at the end of the deposition of (a) 2nd (b) 4th (c) 6th (d) 8th and (e) 10th layer of IN 718 powder on IN 718 substrate using DED-L. Laser beam scanning direction is along the positive x-axis. This simulation is done for 300 W laser power and 15 mm/s scanning speed. Other parameters are provided in Table 4.4. Deformation is magnified by 10x. Half of the solution domain is shown because of the symmetry with respect to XZ plane.

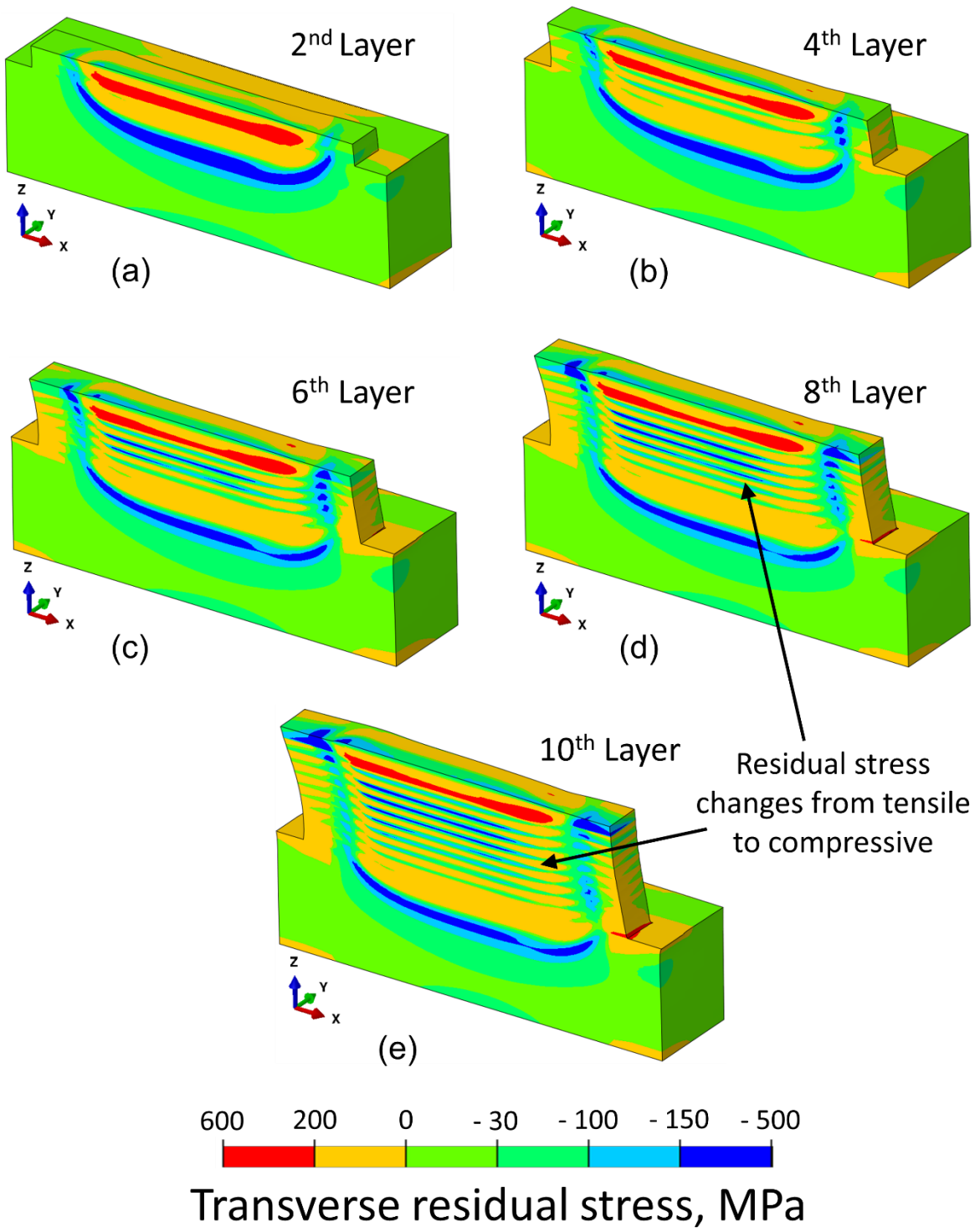

Figure 4.15. Residual stress along y-direction (transverse) at the end of the deposition of (a) 2nd (b) 4th (c) 6th (d) 8th and (e) 10th layer of IN 718 powder on IN 718 substrate using DED-L. Laser beam scanning direction is along the positive x-axis. This simulation is done for 300 W laser power and 15 mm/s scanning speed. Other parameters are provided in Table 4.4. Deformation is magnified by 10x. Half of the solution domain is shown because of the symmetry with respect to XZ plane.

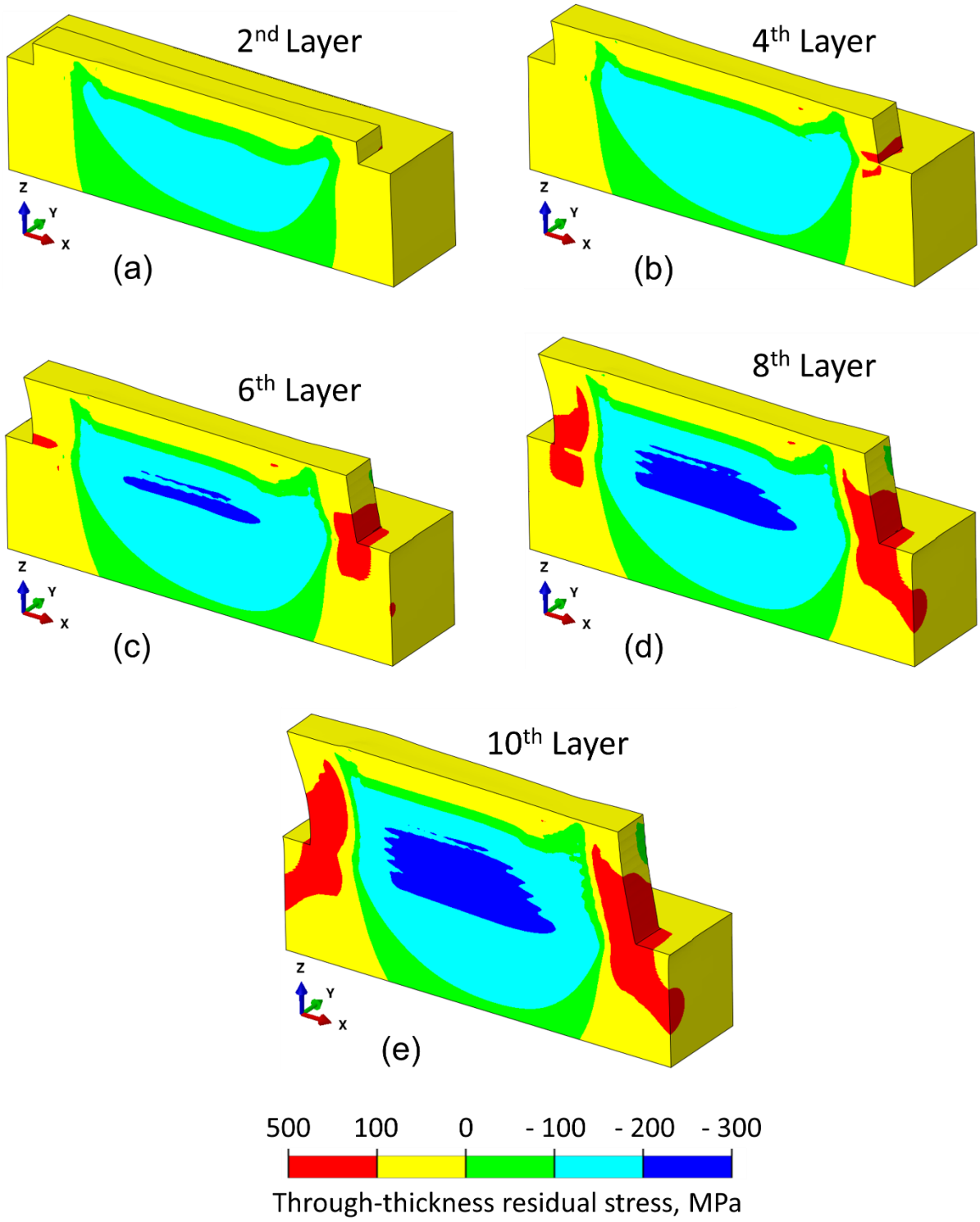

Figure 4.16. Residual stress along z-direction (through-thickness) at the end of the deposition of (a) 2nd (b) 4th (c) 6th (d) 8th and (e) 10th layer of IN 718 powder on IN 718 substrate using DED-L. Laser beam scanning direction is along the positive x-axis. This simulation is done for 300 W laser power and 15 mm/s scanning speed. Other parameters are provided in Table 4.4. Deformation is magnified by 10x. Half of the solution domain is shown because of the symmetry with respect to XZ plane.

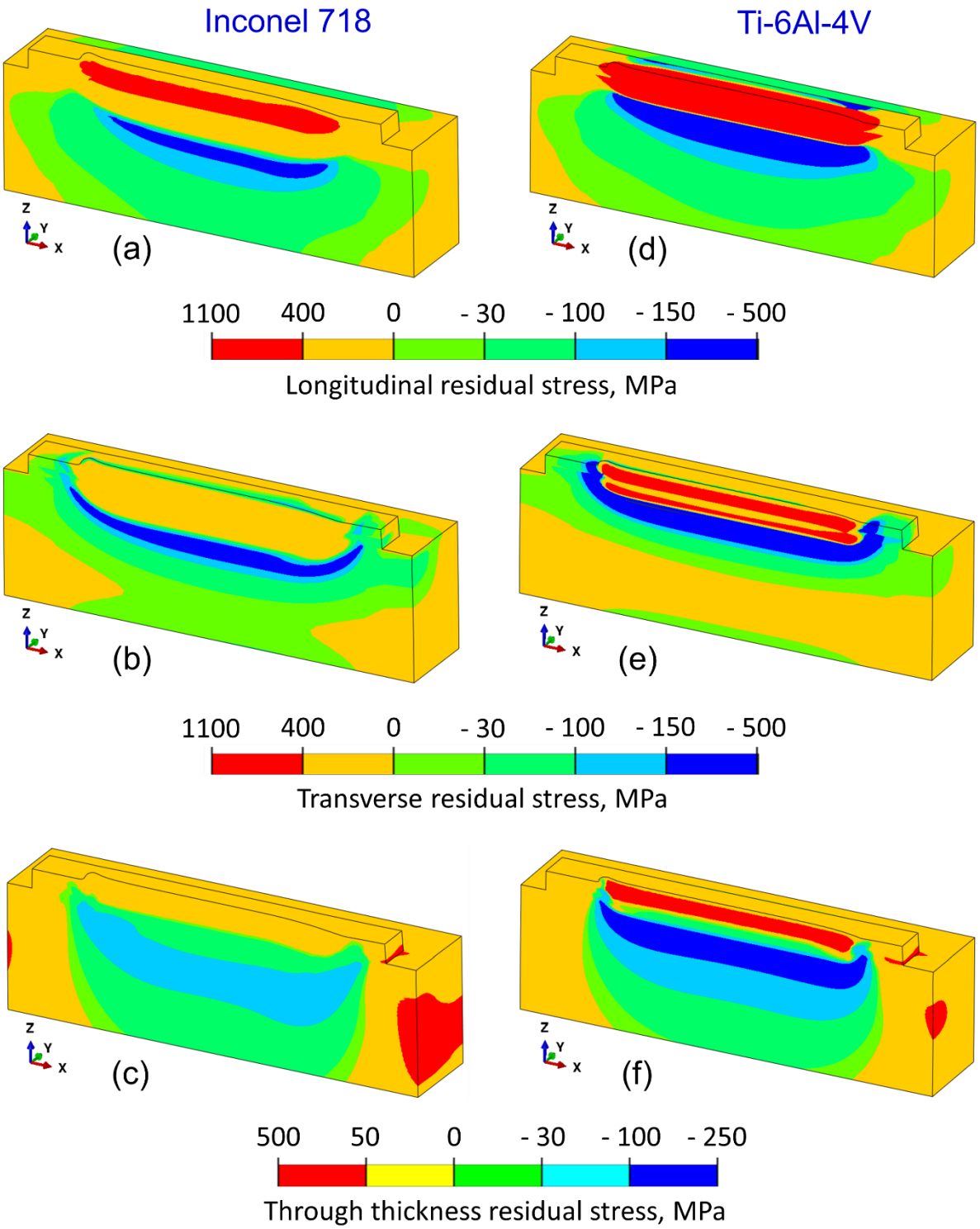

Figure 4.17. Residual stress distribution for IN 718 along (a) x (b) y and (c) z directions, and for Ti-6Al-4V along (d) x (e) y and (f) z directions of the 2 layers deposit using DED-L. Laser beam scanning direction is along the positive x-axis. The simulations are done for 250 W laser power and 15 mm/s scanning speed. Other parameters are provided in Table 4.4. Deformation is magnified by 10x. Half of the solution domain is shown because of the symmetry with respect to XZ plane.

Figure 4.18 (a) also shows that the longitudinal stress along the substrate deposit interface for Ti-6Al-4V is higher than that for IN 718. However, susceptibility to warping and delamination depends not only on the magnitude of the residual stresses but also the yield strength of the alloy. Therefore, a normalized residual stress [10] expressed as the ratio of the longitudinal residual stress along the substrate deposit interface to the room-temperature yield strength of the alloy is used for assessment of such problems. Figure 4.18 (b) shows that the normalized stress along the substrate deposit interface is higher for IN 718 than that of Ti-6Al-4V. This is because of the lower yield strength of IN 718 than Ti-6Al-4V. Therefore, under the same processing conditions, IN 718 is more susceptible to warping and delamination from the perspective of residual stresses. The high susceptibility to warping and delamination of additively manufactured Inconel 718 components is also reported by Prabhakar et al. [11].

In many AM builds, residual stresses are minimized by printing the component using thinner layers. Therefore, effects of layer thickness on residuals stresses are investigated for DED-L. Figure 4.19 (a) and (b) show the longitudinal and through-thickness residual stress distributions, respectively, during the deposition of a 0.8-mm-high wall using 2 and 4 layers. Building the same height using more layers requires a lower layer thickness. For the same laser power and scanning speed, a lower layer thickness increases the volumetric heat flux intensity and hence the peak temperature. At the same time, it takes longer time to build the same height using thinner layers. Therefore, the total deposition time increases. Both the higher peak temperature and more exposure time tend to increase the distortion. However, the deformation can reduce the residual stresses in the deposit. Therefore, both the longitudinal and the through-thickness residual stresses decrease with an increasing number of layers as shown in the figures. For the deposition conditions studied here, the maximum longitudinal and through-thickness residual stresses can be reduced by about 20% and 30%, respectively by using 4 layers to build the same height instead of 2 layers.

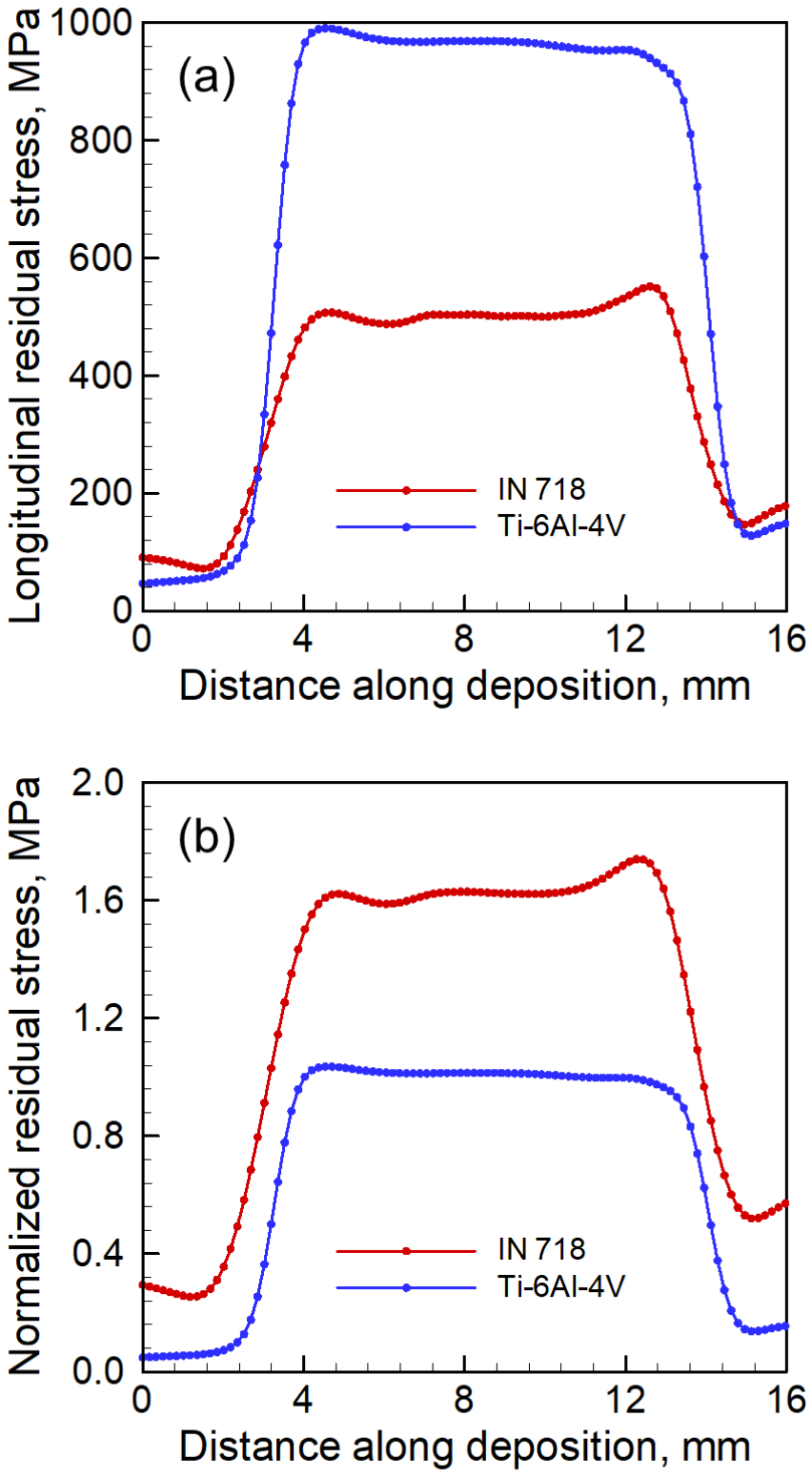

Figure 4.18. (a) The longitudinal and (b) the normalized residual stress (longitudinal residual stress/yield strength) distributions along substrate deposit interface for DED-L of IN 718 and Ti-6Al-4V using 250 W laser power and 15 mm/s scanning speed. Other parameters are provided in Table 4.4.

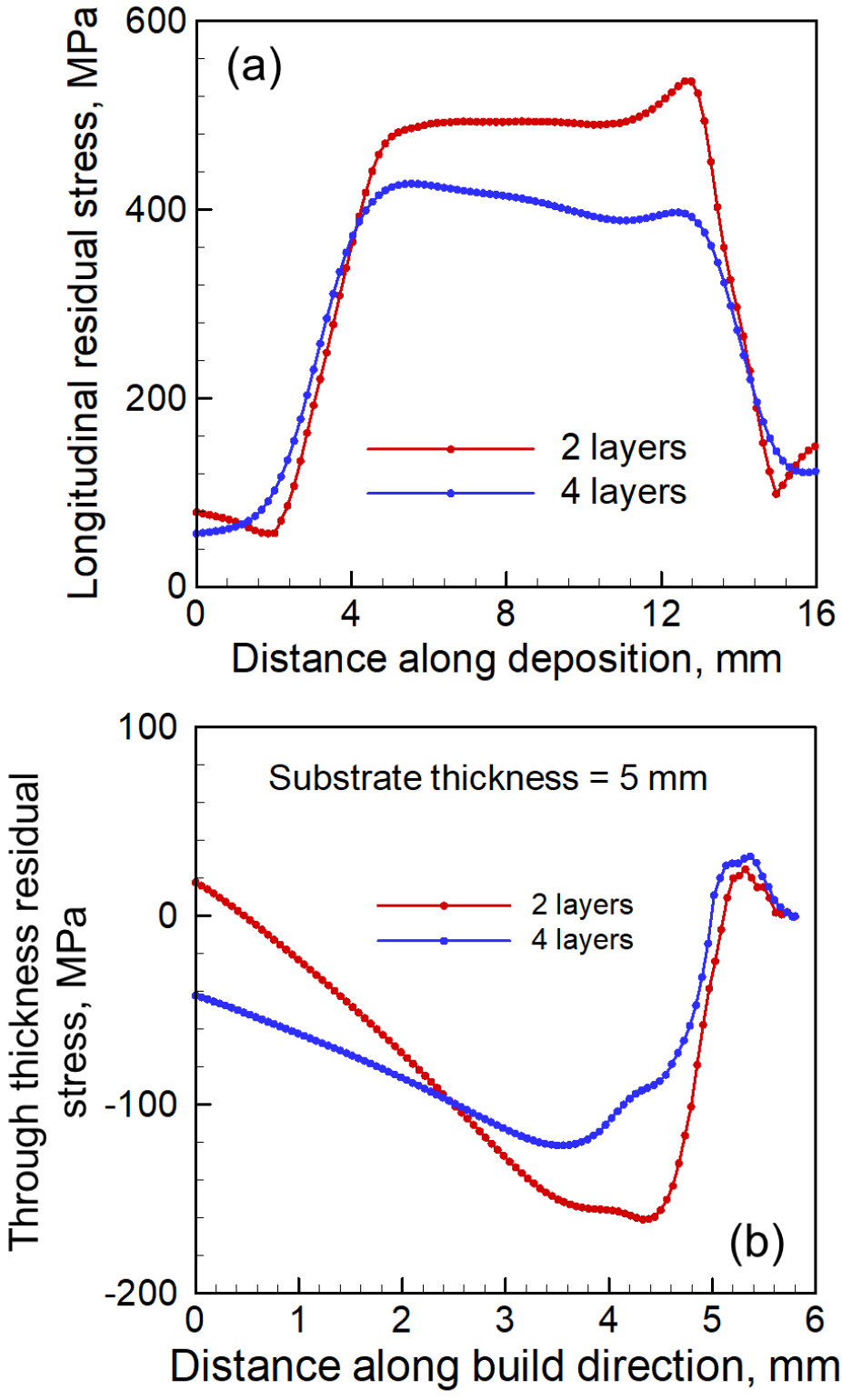

Figure 4.19. (a) The longitudinal and (b) the through-thickness residual stress distributions of IN 718 deposit on IN 718 substrate using 2 and 4 layers DED-L to build a 0.8-mm-high wall. The simulations are done for 250 W laser power and 15 mm/s scanning speed. Other parameters are provided in Table 4.4.

Figure 4.20 shows that doubling the heat input (laser power/speed) increases the maximum strain in the component by almost 2.5 times in DED-L of IN 718 deposit. However, the maximum longitudinal residual stresses can be reduced significantly by increasing the heat input. Distortion is often a crucial issue in AM as it affects the dimensional accuracy of the fabricated part. On the other hand, the residual stresses can be reduced by post process heat treatment or by reducing the layer thickness. Therefore, an appropriate processing condition must be carefully selected considering both the distortion and residual stresses. In Figure 4.20, for example, a heat input of 20 J/mm seems to provide a strain of 0.0057 and a longitudinal residual stress of 540 MPa. This figure is useful to select a heat input considering both the maximum longitudinal residual stress and strain. In practice lower heat input can be achieved by low laser power and faster scanning speed. In addition, from Figure 4.19 it is evident that the residual stresses may also be reduced by depositing thinner layers. This finding is consistent with the current industrial practice. For example, General Electric uses low heat input (100-500 W and 2000 mm/s) and low layer thickness of 40-100 microns to fabricate aero-engine fuel nozzles using PBF-L [12].

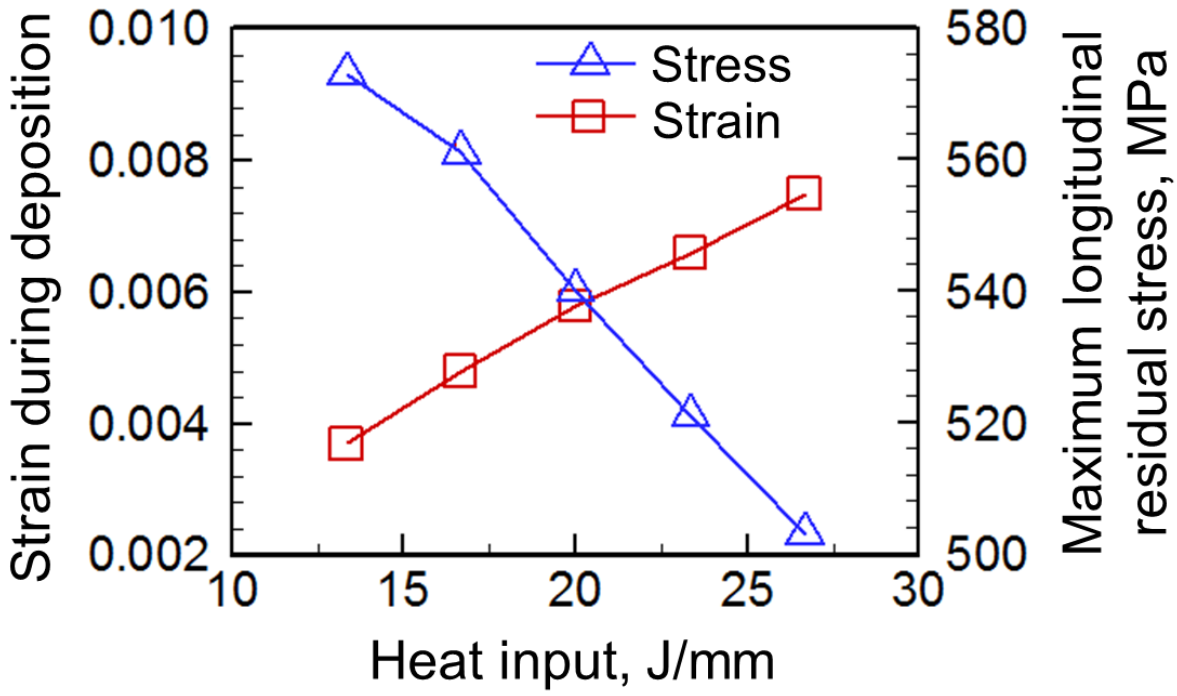

Figure 4.20. Effect of heat input (laser power/scanning speed) on maximum longitudinal stress and strain. Both the plots are drawn for 2 layers DED-L of IN 718 part on IN 718 substrate. Process parameters are provided in Table 4.4. Heat input is varied by changing the laser power at a constant scanning speed.

4.4 Residual stresses and distortion in additively manufactured compositionally graded joints

Dissimilar metal joints are used in various engineering applications. Failures of dissimilar metal joints have been attributed to the very sharp changes in chemical composition and microstructure along the joint interface [13]. Such failures are minimized or eliminated by the development of compositionally graded joints where the variation of chemical composition occurs smoothly across the joint over a large distance [13]. DED-L has been proved to be a practical choice to fabricate graded joints [13].

Unlike a single alloy component, in a compositionally graded joint, differences in thermal expansion coefficients can lead to the development of unique residual stresses and distortion patterns. Variations in thermo-physical properties can also lead to different cooling rates and temperature gradients during cooling, further influencing the development of residual stresses. In addition, the yield strength varies spatially in many graded components, so two regions with the same magnitude of residual stresses can have different susceptibilities to delamination, buckling and warping. Therefore, in this sub-section a detailed investigation of the residual stresses and distortion in graded joints is provided. The calculation methods of residual stresses and distortion for graded joints using the thermomechanical model are same as that for single alloy parts as described in Section 4.1.

4.4.1 Calculated residual stresses and distortion in two graded joints

In this research, two types of graded joints are considered, 2.25Cr-1Mo steel to 800H joint and Ti-6Al-4V to 800H joint both of which are printed using DED-L. Substrates for these two graded joints are 2.25Cr-1Mo steel and Ti-6Al-4V, respectively. For both joints, the 10^{th} layer is made by 100% alloy 800H. From the 1^{st} layer to the 9^{th} layer, the composition is changed linearly with an increment of 10 wt.% of 800H. For instance, the composition of the 1^{st} layer is 10% 800H and 90% Ti-6Al-4V or 2.25Cr-1Mo steel and composition of the 9^{th} layer is 90% 800H and 10% Ti-6Al-4V or 2.25Cr-1Mo steel. For the dissimilar joints, substrate and layer 1 to 5 are made of Ti-6Al-4V or 2.25Cr-1Mo steel and 6^{th} to 10^{th} layer are made of 800H. Therefore, a sharp change in composition occurs at the interface of 5^{th} and 6^{th} layer of the dissimilar joints. Schematic representations of both graded and dissimilar joints are given in Figure 4.21. The temperature dependent mechanical properties of the graded compositions are thermodynamically calculated as described in Section 3.2.2 and are provided in Tables 4.5 to 4.12. Residual stresses and distortion are calculated for the process conditions in Table 4.13.

Table 4.5. Temperature dependent mechanical properties of 2.25%Cr-1%Mo steel

Temperature (K)	Young's Modulus (GPa)	Temperature (K)	Volumetric expansion co-efficient (/K)	Temperature (K)	Yield stress (MPa)
300	211.3	300	12.39E-06	300	312.5
400	206.4	400	12.76E-06	700	156.9
500	200.0	500	13.12E-06	1100	88.1
600	191.5	600	13.49E-06	1300	57.7
700	181.0	700	13.85E-06	1500	42.4
800	168.8	800	14.22E-06		
900	155.2	900	14.59E-06		
1000	140.4	1000	14.98E-06		
1100	124.2	1500	15.22E-06		
1200	109.1	1600	16.01E-06		
1300	98.3	1700	17.13E-06		
1400	81.36				
1500	61.31				
1600	34.12				
1700	8.79				

Table 4.6. Temperature dependent mechanical properties of 800H

Temperature (K)	Young's Modulus (GPa)	Temperature (K)	Volumetric expansion co-efficient (/K)	Temperature (K)	Yield stress (MPa)
300	200.7	300	15.68E-06	300	272.3
400	194.5	400	16.01E-06	500	157.7
500	188.0	500	16.34E-06	700	139.3
600	181.3	600	16.68E-06	1500	50.8
700	174.4	700	17.02E-06		
800	167.3	800	17.35E-06		
900	158.8	900	17.71E-06		
1000	148.4	1000	18.18E-06		
1100	139.1	1100	19.10E-06		
1200	131.2	1200	19.47E-06		
1300	113.1	1300	19.85E-06		
1400	94.7	1400	20.24E-06		
1500	76.0	1500	20.65E-06		
1600	37.1	1600	21.05E-06		

Table 4.7. Temperature dependent Young's modulus (GPa) of the graded joint between 2.25Cr-1Mo steel and alloy 800 H

Temperature (K)	Composition of the transition joint (wt.% of 800H)								
	10%	20%	30%	40%	50%	60%	70%	80%	90%
300	210.9	207.7	202.9	198.2	197.6	197.1	197.1	196.9	198.7
400	205.8	201.8	196.1	190.8	190.4	190.2	190.5	190.5	192.4
500	199.2	194.8	188.7	183.3	183.2	183.2	183.7	183.9	185.8
600	190.8	186.5	180.6	175.5	175.7	176	176.8	177.2	179.1
700	180.6	177.0	172	167.6	168.1	168.6	169.6	170.2	172.2
800	168.9	166.4	162.8	159.6	160.3	161.8	162.2	162.9	165
900	155.4	153.5	150.2	151.2	152.2	153	154.2	155.3	156.6
1000	138.8	139.1	141.1	142.7	144	145	145.8	146.3	147.4
1100	126.2	129.4	131.9	133.9	135.5	136.8	137.8	138.4	138.9
1200	112.2	119.9	122.7	124.9	126.8	128.3	129.5	128.4	127.9
1300	95.70	105.7	106.5	110.9	112.9	115.7	115	112.1	112.7
1400	70.00	91.3	88.1	92.7	93.9	95.8	96.3	97.5	94.3
1500	40.19	71.69	64.4	67.19	69.62	71.7	73.3	74.6	71.5
1640	20.24	40.98	34.89	37.72	30.17	32.29	34.11	35.52	36.52

Table 4.8. Temperature dependent volumetric expansion coefficient (10^{-6} /K) of the graded joint between 2.25Cr-1Mo steel and alloy 800 H

Temperature (K)	Composition of the transition joint (wt.% of 800H)								
	10%	20%	30%	40%	50%	60%	70%	80%	90%
300	12.81	15.29	16.28	17.25	17.35	17.54	17.78	17.07	16.35
400	13.17	15.58	16.49	17.41	17.55	17.77	18.04	17.35	16.66
500	13.53	15.88	16.7	17.59	17.75	18.0	18.29	17.64	16.97
600	13.89	16.17	16.92	17.75	17.96	18.23	18.56	17.93	17.28
700	14.24	16.46	17.14	17.93	18.17	18.47	18.82	18.23	17.6
800	14.6	16.75	17.36	18.11	18.39	18.72	19.09	18.53	17.92
1200	14.75	17.16	17.66	18.31	18.61	19.09	19.54	18.88	18.22
1300	15.46	17.83	18.12	18.5	18.83	19.33	20.03	19.65	18.84
1400	16.26	18.42	18.54	18.73	19.08	19.59	20.29	19.94	19.44
1500	16.95	18.94	18.93	18.96	19.34	19.87	20.58	20.24	19.78
1640	17.57	19.42	19.27	19.18	19.59	20.15	20.87	20.55	20.13

Table 4.9. Temperature dependent yield strength (MPa) of the graded joint between 2.25Cr-1Mo steel and alloy 800 H

Temperature (K)	Composition of the transition joint (wt.% of 800H)								
	10%	20%	30%	40%	50%	60%	70%	80%	90%
300	298.1	302.2	310.3	319.1	309.9	192.1	204.2	216.6	229.3
500	192.9	198.7	207.6	216.5	170.9	116.6	126.3	136.3	146.8
700	163.5	169.9	179.0	187.9	142.6	100.4	109.4	118.9	128.9
1300	66.84	76.31	89.44	100.6	112.1	52.08	53.48	65.80	101.3
1500	50.78	47.89	39.84	39.53	39.69	15.27	15.90	19.79	30.76

Table 4.10. Temperature dependent yield strength (MPa) of the graded joint between Ti-6Al-4V and alloy 800 H

Temperature (K)	Composition of the transition joint (wt.% of 800H)								
	10%	20%	30%	40%	50%	60%	70%	80%	90%
300	883.73	812.46	741.19	669.92	598.65	527.38	456.11	384.84	313.57
500	768.17	700.34	632.51	564.68	496.85	429.02	361.19	293.36	225.53
700	672.73	613.46	554.19	494.92	435.65	376.38	317.11	257.84	198.57
1500	203.07	186.15	169.22	152.30	135.38	118.45	101.53	84.608	67.684

Table 4.11. Temperature dependent Young's modulus (GPa) of the graded joint between Ti-6Al-4V and alloy 800 H

Temperature (K)	Composition of the transition joint (wt.% of 800H)								
	10%	20%	30%	40%	50%	60%	70%	80%	90%
300	132.57	140.14	147.71	155.28	162.85	170.42	177.99	185.56	193.13
533	117.6	125.2	132.8	140.4	148	155.6	163.2	170.8	178.4
589	108.3	116.6	124.9	133.2	141.5	149.8	158.1	166.4	174.7
700	101.14	109.28	117.42	125.56	133.7	141.84	149.98	158.12	166.26
755	89.14	98.28	107.42	116.56	125.7	134.84	143.98	153.12	162.26
811	83.33	92.66	101.99	111.32	120.65	129.98	139.31	148.64	157.97
923	65.13	75.26	85.39	95.52	105.65	115.78	125.91	136.04	146.17
1073	38.61	50.22	61.83	73.44	85.05	96.66	108.27	119.88	131.49
1098	33.71	45.42	57.13	68.84	80.55	92.26	103.97	115.68	127.39
1123	29.81	41.62	53.43	65.24	77.05	88.86	100.67	112.48	124.29
1573	15.511	19.022	22.533	26.044	29.555	33.066	36.577	40.088	43.599
1643	12.711	15.422	18.133	20.844	23.555	26.266	28.977	31.688	34.399

Table 4.12. Temperature dependent volumetric expansion co-efficient (10^{-6} /K) of the graded joint between Ti-6Al-4V and alloy 800 H

Temperature (K)	Composition of the transition joint (wt.% of 800H)								
	10%	20%	30%	40%	50%	60%	70%	80%	90%
300	9.47	10.16	10.85	11.54	12.23	12.92	13.61	14.3	14.99
533	10.492	11.154	11.816	12.478	13.14	13.802	14.464	15.126	15.788
589	10.677	11.344	12.011	12.678	13.345	14.012	14.679	15.346	16.013
700	11.341	11.972	12.603	13.234	13.865	14.496	15.127	15.758	16.389
755	11.707	12.314	12.921	13.528	14.135	14.742	15.349	15.956	16.563
811	11.833	12.446	13.059	13.672	14.285	14.898	15.511	16.124	16.737
923	12.283	12.886	13.489	14.092	14.695	15.298	15.901	16.504	17.107
1073	12.899	13.588	14.277	14.966	15.655	16.344	17.033	17.722	18.411
1098	12.991	13.692	14.393	15.094	15.795	16.496	17.197	17.898	18.599
1123	13.08	13.79	14.5	15.21	15.92	16.63	17.34	18.05	18.76
1573	13.765	14.53	15.295	16.06	16.825	17.59	18.355	19.12	19.885
1643	16.055	16.61	17.165	17.72	18.275	18.83	19.385	19.94	20.495

Table 4.13. AM parameters used to calculate residual stresses and distortion in Section 4.4.

Laser power (W)	Beam radius (mm)	Scanning speed (mm/s)	Layer thickness (mm)	Substrate thickness (mm)	Powder flow rate (gm/s)
300	0.5	10	0.38	4	0.416

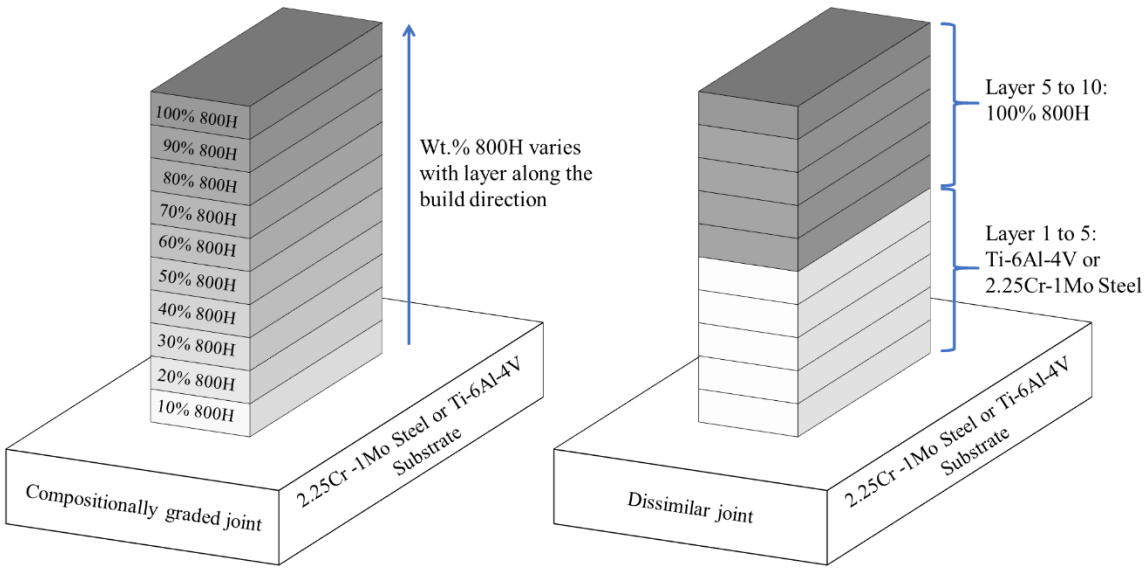

Figure 4.21. Schematic representation of the compositionally graded and the dissimilar joints fabricated using DED-L studied in this research.

Figure 4.22 shows the longitudinal stress distribution at the end of 2nd and 10th layer depositions. Longitudinal stress is the component of the residual stress along the scanning direction (x-direction). The positive and the negative values of the stresses in the figures represent the tensile and the compressive residual stresses, respectively. Magnitudes of the residual stresses vary with the progress of the deposition process. For example, at the end of the deposition of the 2nd layer, the highest magnitude of the longitudinal residual stress is observed near the 2nd layer. However, with the progress of the deposition process this high residual stress near the 2nd layer is partially alleviated. The residual stresses are spatially non-uniform depending on the varying material properties of the graded joints. For example, after deposition of all 10 layers, the maximum value of the longitudinal stress is near the top of the deposit for both types of joints. However, in Ti-6Al-4V to 800H joint, a high accumulation of tensile residual stress is also observed near the substrate deposit interface.

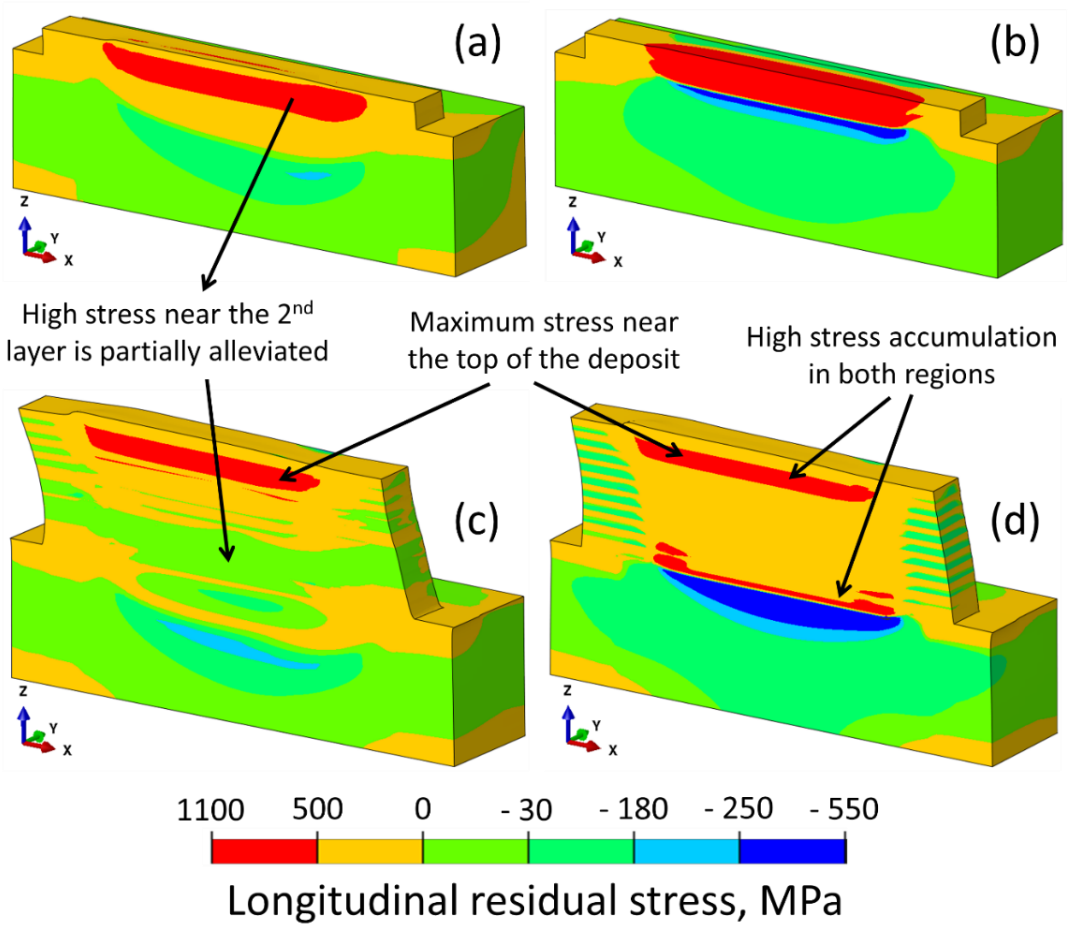

Figure 4.22. Longitudinal residual stresses at the end of 2nd layer for (a) 2.25Cr-1Mo steel to 800H and (b) Ti-6Al-4V to 800H joints and at the end of 10th layer for (c) 2.25Cr-1Mo steel to 800H and (d) Ti-6Al-4V to 800H joints. Both the graded joints are using DED-L for the process conditions provided in Table 4.13. Scanning direction is along the positive x-axis. Half of the solution domain is shown because of the symmetry with respect to XZ plane.

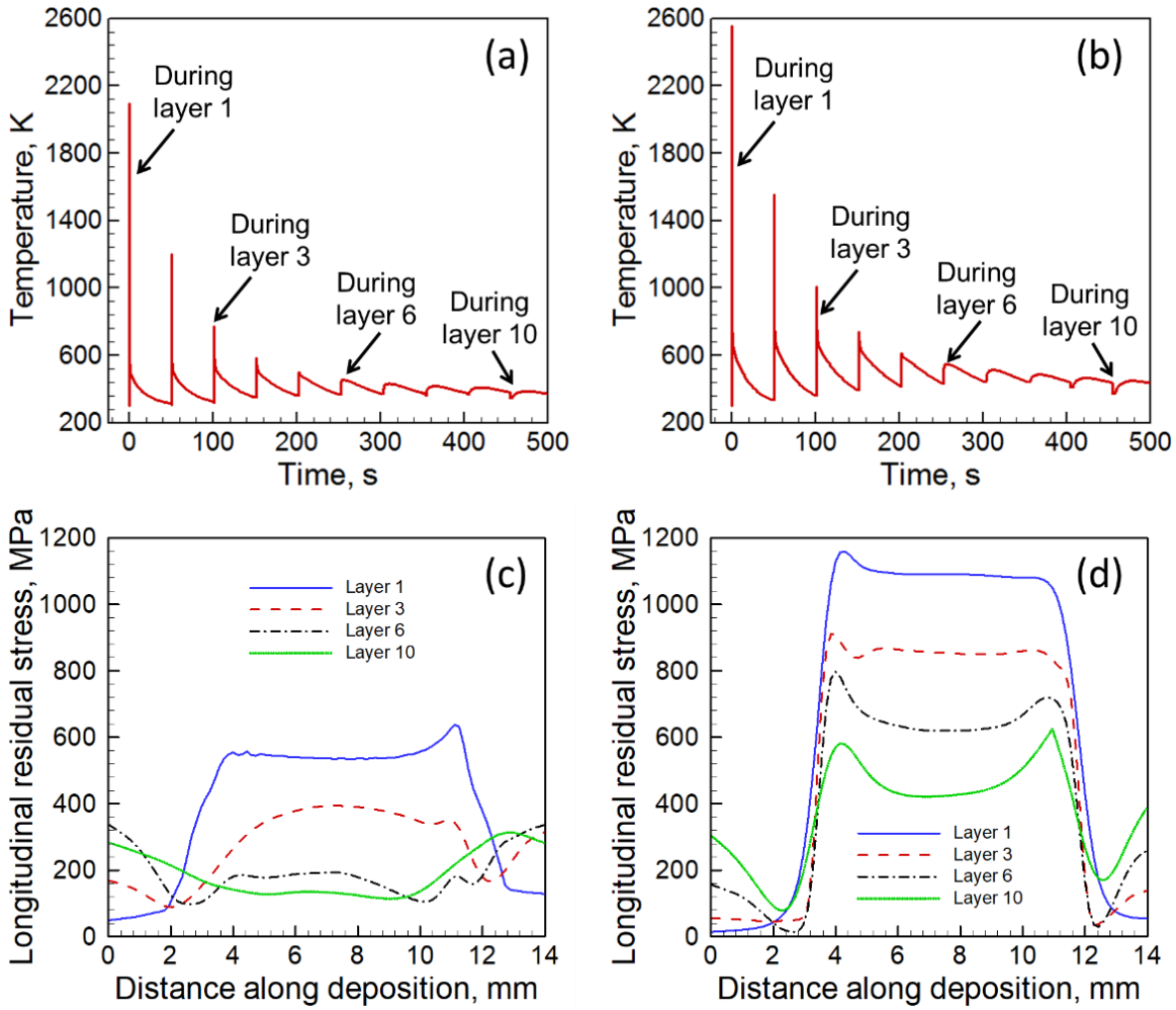

Figure 4.23. Variation of the temperature with time monitored at mid length of substrate deposit interface for (a) 2.25Cr-1Mo steel to 800H and (b) Ti-6Al-4V to 800H joints. Longitudinal residual stress distribution along substrate deposit interface for (c) 2.25Cr-1Mo steel to 800H and (d) Ti-6Al-4V to 800H joints after 1st, 3rd, 6th and 10th layer. Both the graded joints are deposited using DED-L for the process conditions provided in Table 4.13.

During AM, the previously deposited layers experience reheating and cooling during the deposition of upper layers. Figure 4.23 (a) and (b) show the temperature variation with time at mid-length and mid-width of substrate deposit interface during the fabrication of 2.25Cr-1Mo to 800H joint and Ti-6Al-4V to 800H joint, respectively. Ti-6Al-4V substrate has lower thermal conductivity than 2.25Cr-1Mo steel substrate. Therefore, in Ti-6Al-4V to 800 H joint, less heat can be transferred through the Ti-6Al-4V substrate. That is why the peak temperatures monitored in Figure 4.23 (b) are higher than those in Figure 4.23 (a) for the same layer. This repetitive heating and cooling partially alleviate the residual stresses for both types of the joints. Figures 4.23 (c-d) show the longitudinal stress distribution along the substrate deposit

interface after the deposition of 1st, 3rd, 6th and 10th layers, for 2.25Cr-1Mo to 800H joint and Ti-6Al-4V to 800 H joint, respectively. For both types of the joints, the magnitude of the residual stress near the center along the substrate deposit interface decreases with the progress of the deposition process due to the repetitive heating and cooling. However, longitudinal residual stress along that interface in Ti-6Al-4V to 800 H joint is always higher than that in 2.25Cr-1Mo to 800H joint, due to higher room temperature yield strength and lower thermal expansion coefficient of Ti-6Al-4V substrate compared to those of 2.25Cr-1Mo steel substrate.

4.4.2 Comparison between graded and dissimilar joints

Figure 4.24 explains the benefits of fabricating graded joints over dissimilar joints for minimizing residual stresses and distortion. The results for 2.25Cr-1Mo to 800H joint and Ti-6Al-4V to 800H joint are shown in Figures 4.24 (a-c) and Figures 4.24 (d-f), respectively. In graded joints, the substrate is Ti-6Al-4V or 2.25Cr-1Mo steel and the 10th layer is 800 H. From the 1st to 9th layer the composition changes with a step of 10 wt.% of 800H. On the other hand, for the dissimilar joints, substrate and layer 1 to layer 5 are made of Ti-6Al-4V or 2.25Cr-1Mo steel and 6th to 10th layer are made of 800H, as shown in Figure 4.20. Therefore, sharp change in composition occurs at the interface of 5th and 6th layer of the dissimilar joints. Longitudinal residual stresses are plotted along the substrate deposit interface and through-thickness residual stress and strain are plotted along the build direction at mid length of the deposit. The mechanical properties of 2.25Cr-1Mo steel and alloy 800H are similar. As a result, no sharp changes in residual stresses and strain at the joint interface are observed. Therefore, a graded joint between these two alloys provides marginal benefit over the dissimilar alloy joint for minimizing residual stress and distortion in this pair. However, mechanical properties of Ti-6Al-4V are significantly different from those of alloy 800H. For example, room temperature yield strength of Ti-6Al-4V is about four times higher than that of 800 H. However, room temperature Young's modulus and volumetric expansion coefficient of Ti-6Al-4V are almost half of 800 H. Sharp changes in residual stresses and strain in the dissimilar joints due to these differences in mechanical properties can be minimized by fabrication of compositionally graded joints between these two alloys.

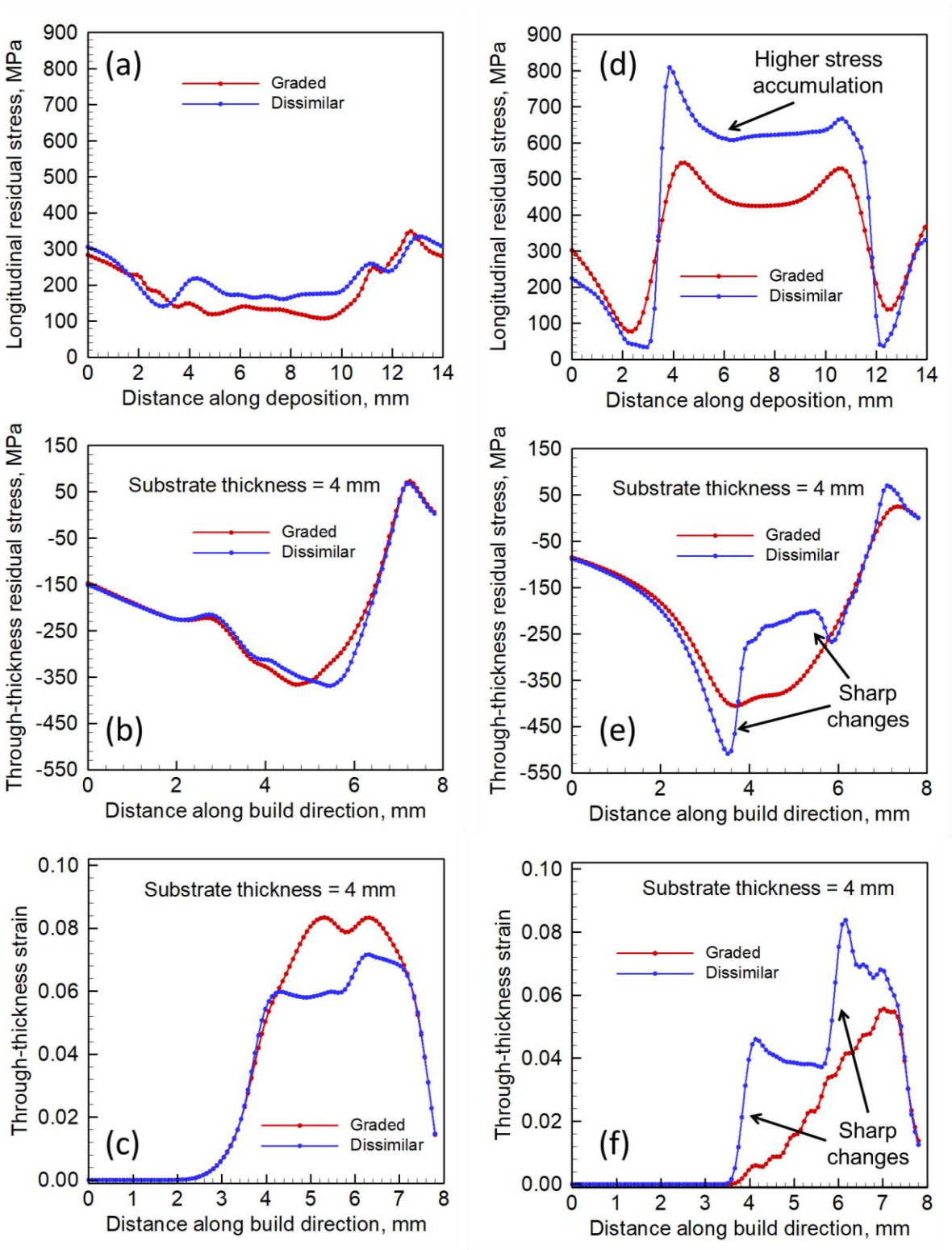

Figure 4.24. (a) Longitudinal residual stress along substrate deposit interface, through-thickness (b) stress and (c) strain along the build direction at mid length of the deposit for 2.25Cr-1Mo steel to 800H joint and (d) longitudinal residual stress along substrate deposit interface, through-thickness (e) stress and (f) strain along the build direction at mid length of the deposit Ti-6Al-4V to 800H joints. All joints are made using DED-L for the process conditions provided in Table 4.13.

4.5 Back-of-the-envelope calculations of distortion in AM parts

The detailed thermomechanical calculations using numerical model, as described in the previous sections of this chapter, are helpful to provide detailed understanding of the evolution mechanism and spatial non-uniformity of residual stresses and distortion in AM parts. However, it is often impractical to use these models for real time prediction of part distortion in shop floor because of the time constraints and unavailability of proper computational resources. Back-of-the-envelope calculations are often beneficial for real time predictions. Therefore, in this section, a dimensionless strain parameter is proposed, derived using back of the envelope calculations and used to quantify distortion during AM. Although, this strain parameter can be applied for all three AM processes studied in this thesis research, results are provided here for DED-L as an example. The computed results uncover the effects of both the key process variables such as power, scanning speed and transport phenomena related non-dimensional parameters such as Marangoni and Fourier numbers and non-dimensional peak temperature on thermal strain.

4.5.1 Mathematical derivation of strain parameter

A relation between the strain parameter (ε^*) and the AM variables is developed based on the Buckingham π-theorem [14]. The meanings of the various symbols are explained in Table 4.14. The table also provides their dimensions in MLTθ system. Since there are 4 fundamental dimensions and 8 variables, there are four (8 – 4 = 4) π terms. Non-repeating variables are chosen to be ρV, h, ΔT and k/C_P. Applying Buckingham π-theorem, the final four π terms can be written as

$$\pi_1 = \varepsilon^* \tag{4-5}$$

$$\pi_2 = \beta \Delta T \tag{4-6}$$

$$\pi_3 = \frac{\rho V H}{h^3 (k/C_P)^2} \tag{4-7}$$

$$\pi_4 = \frac{\rho V E I}{h^5 (k/C_P)^2} \tag{4-8}$$

From the above relationships, the thermal strain parameter can be expressed as a function of the AM variables as:

$$\varepsilon^* = \pi_1 = \frac{\pi_2 \pi_3^{3/2}}{\pi_4} = \frac{\beta \Delta T}{EI} \frac{\sqrt{h(\rho V)}}{(k/C_P)} H^{3/2} = \frac{\beta \Delta T}{EI} \frac{\sqrt{Vh}}{\alpha \sqrt{\rho}} H^{3/2} \tag{4-9}$$

The heat transfer in AM processes is transient in nature which is best characterized by the Fourier number (F) given as $\alpha\tau/w^2$ where α, τ and w refer to thermal diffusivity, characteristic time scale and length through which the heat conduction occurs, respectively. The Fourier number (F) can be rewritten as α/vw considering v as the beam scanning speed and w as the length of the molten pool. The term $\sqrt{Vh}$ in the equation is dimensionally equivalent to w^2. Therefore, the parameter, ε^*, can be expressed in terms of Fourier number as

$$\varepsilon^* = \frac{\beta\Delta T}{EI}\frac{t}{F\sqrt{\rho}}H^{3/2} \tag{4-10}$$

Equation (4-10) indicates that high strains result from large volumetric change ($\beta\Delta T$), long deposition time (t) and high rates of heat input per unit length (H). In contrast, terms in the denominator of Equation (4-10) indicate factors that are helpful to reduce thermal strain. For example, a high flexural rigidity (EI) of a structure resists deformation. Similarly, a high Fourier number (F) indicates faster diffusive heat transfer relative to heat accumulation and a high rate of heat transfer reduces the peak temperature and thus, the thermal strain.

Figure 4.25 shows the maximum thermal strains (ε) obtained from the experimentally measured thermal distortions reported in the literature [15-19] as a function of the thermal strain parameter (ε^*), which is estimated using Equation (4-10). Figure 4.25 indicates that the maximum thermal strain (ε) for an AM part can be expressed as a linear function of the thermal strain parameter (ε*). Based on the trend of the data points presented in the figure, the maximum thermal strain (ε) can be expressed as

$$\varepsilon = \frac{0.9081\ \beta\Delta T}{EI}\frac{t}{F\sqrt{\rho}}H^{3/2} + 0.0009 \tag{4-11}$$

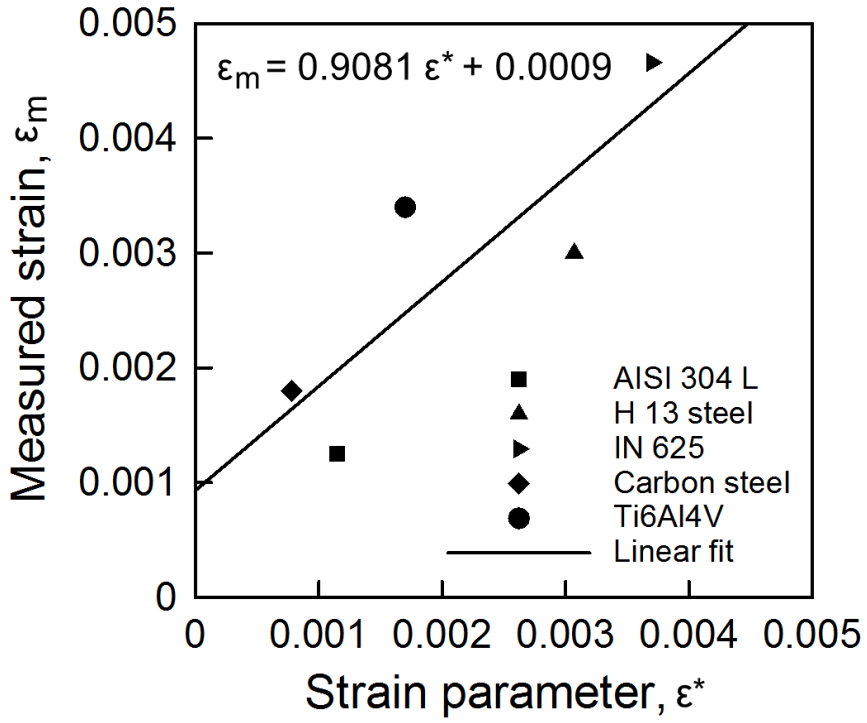

Figure 4.25. Values of measured maximum thermal strain as a function of the thermal strain parameter for five alloys [15-19] showing a linear relationship.

Table 4.14. Variables used in dimensional analysis in the MLTθ system

Variable	Dimension
Volumetric thermal expansion coefficient, β	θ^{-1}
Temperature gradient, $\Delta T = T_P - T_S$, where T_P and T_S refer respectively to peak and surrounding temperature	θ
Deposition layer thickness, h	L
Thermal diffusivity, $\alpha = k/\rho C_P$, where k, ρ and C_P are thermal conductivity, density and specific heat, respectively of deposit material	L^2T^{-1}
Heat input per unit length, $H = \eta P/v$, where η, P, and v refer to absorption coefficient, beam power and scanning speed, respectively	MLT^{-2}
Melt pool volume, V	L^3
Flexural rigidity of the substrate plate, EI, where E and I refer respectively to elastic modulus and second moment of inertia	ML^3T^{-2}
Thermal strain parameter, ε^*	$M^0L^0T^0\theta^0$

4.5.2 Mitigation of distortion in AM parts based on strain parameter

The dimensionless strain parameter can be used to predict the relative susceptibilities to distortion for different alloy and process condition combinations. For example, Figures 4.26 (a) and (b) show that the strain parameter, ε^*, rises with increase in laser power and decrease in scanning speed. The peak temperature during AM increases with increasing laser power and decreasing scanning speed. The ratio of laser power to scanning speed is the heat input per unit length and higher heat input results in a larger melt pool and greater distortion on solidification. The higher peak temperature, in turn, enhances the thermal strain. The peak temperature also rises as the deposition moves to the upper layers away from the substrate and the rate of heat loss through the substrate reduces. Hence, the thermal strain increases during the deposition of upper layers as indicated in Figure 4.26 (c). However, depending on the deposition conditions, the build may attain a steady state after many layers of deposition and the thermal strain may become almost constant, particularly for longer track lengths. For example, the thermal strain in a multi-layer build of SS 316 becomes almost constant after fifteen layers as shown in Figure 4.26 (c). The number of layers to attain a steady state when no further appreciable increase in thermal strain takes place depends on process parameters, build geometry and alloy properties.

Figure 4.26 shows that in addition to laser power and scanning speed other factors such as the alloy properties, the number of deposited layers and processing conditions affect thermal strain significantly. In order to understand these effects, the thermal strain parameter is correlated with three important non-dimensional numbers, (1) Fourier number, (2) Marangoni number and (3) non-dimensional temperature. The Fourier number is the ratio of heat dissipation rate to heat storage rate. Marangoni number represents the strength of the convective transport of heat in melt pool and the non-dimensional temperature is an indicator of the extent of overheating of the melt pool.

Reduction of thermal strain and distortion requires efficient dissipation of heat to avoid localized accumulation of heat. A non-dimensional parameter that embodies both heat diffusion and accumulation of heat is the Fourier number (F):

$$F = \alpha \tau / w^2 \qquad (4\text{-}12)$$

where α, τ and w refer to thermal diffusivity, characteristic time scale and length, respectively. The characteristic time can be expressed as L/V, where, L and V are the pool length and

scanning speed respectively. Length of the molten pool is calculated using the heat transfer and fluid flow model. So, Equation (4-12) can be re-written as:

$$F = \alpha / V\ L \tag{4-13}$$

Both rapid heat dissipation and reduction of heat accumulation result in lower peak temperature, higher Fourier number and smaller molten pool length. Therefore, higher Fourier number results in lower thermal strain and distortion. In contrast, rigidity of the substrate can counter thermal distortion in AM. Figure 4.27 (a) shows the variation of the strain parameter, ε^* as function of Fourier number and rigidity of the substrate for three different heat inputs. The thermal strain parameter reduces with increase in both the Fourier number and the rigidity, *EI*, of the structure. For a set of process variables, the effects of Fourier number and rigidity of the structure on thermal strain follow nearly the same trend for all three alloys, which is expected. The figure shows that the thermal strain increases with heat input. This behavior is attributed to more pronounced heat accumulation and decrease in Fourier number when the heat input is increased. Since decrease in laser power and smaller layer heights can reduce the rate of heat accumulation and thus, increase the Fourier number, they are practical means to control the thermal distortion in AM.

Convection is often the primary mechanism of heat transfer in the molten pool during AM. The convective transport of heat within the molten pool is driven primarily by the spatial variation of interfacial tension, also referred to as the Marangoni stress. The shape and size of the molten pool is affected by the magnitude of the convective velocity of liquid metal that is expressed by the Marangoni number, *Ma*:

$$Ma = -\frac{d\gamma}{dT}\frac{L\Delta T}{\eta\ \alpha} \tag{4-14}$$

where η is the viscosity, α is the thermal diffusivity of the alloy, *L* is the characteristic length of the molten pool, which is taken as the width of the molten pool, ΔT is the difference between the maximum temperature inside the pool and the solidus temperature of an alloy, and $\frac{d\gamma}{dT}$ is the sensitivity of surface tension with respect to temperature. For most alloys without any surface-active elements, this quantity is negative. The overall molten pool volume is also affected significantly by the density of an alloy powder for a particular heat input. Lighter alloys tend to form larger molten pools and undergo greater volume contraction and thermal

distortion. Therefore, the combined effect of density of alloy powder and Marangoni number on the thermal strain parameter is examined.

Figure 4.27 (b) shows an increase in thermal strain with rise in Marangoni number and decrease in density of alloy powder for a particular set of process variables. The effect of Marangoni number and powder density follows a nearly similar trend for all the three alloys considered here for a particular processing condition. Increase in heat input leads to both higher peak temperature and Marangoni number, and higher thermal strain. Thus, reducing heat input by selecting either a lower laser power or a higher scanning speed or both, when possible, is a practical method to reduce thermal strain.

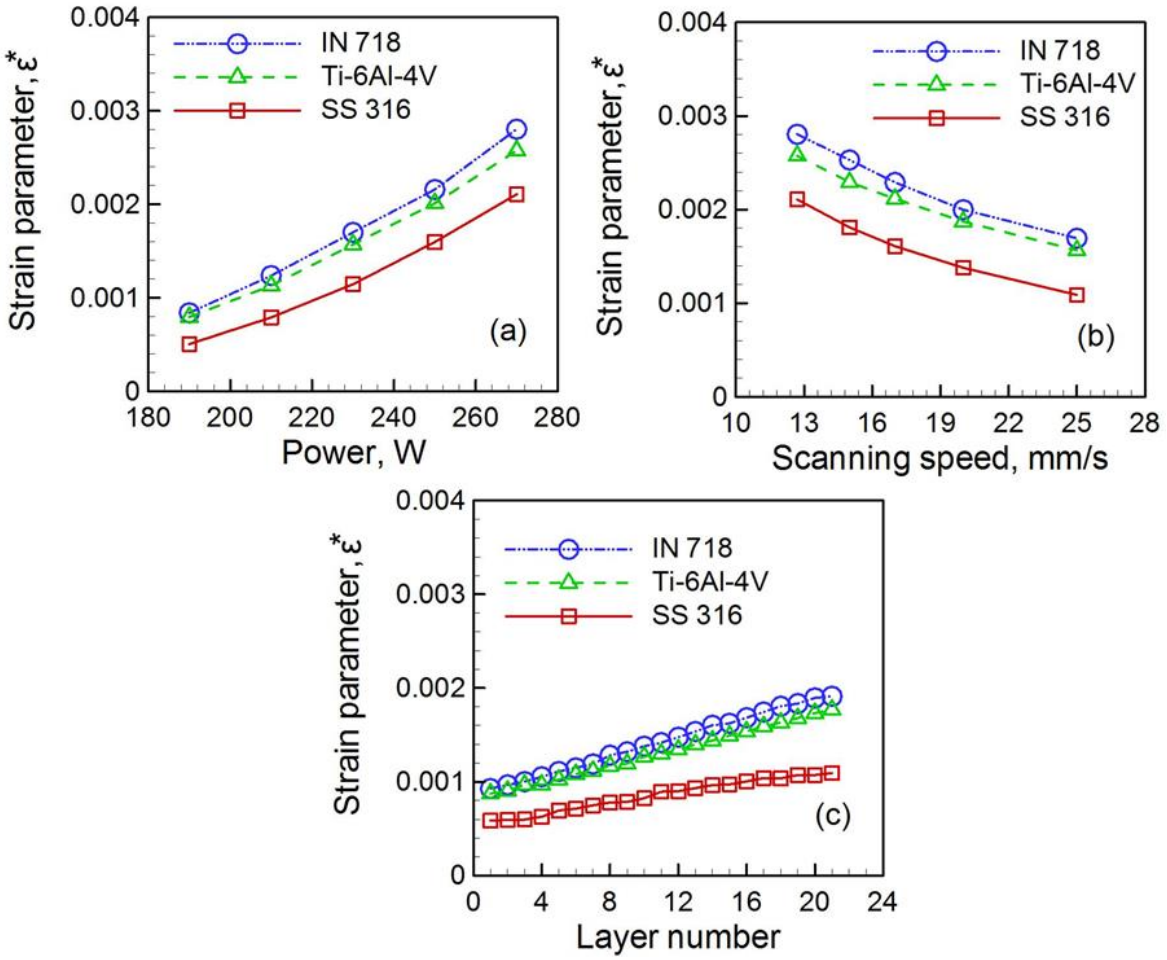

Figure 4.26. Variation of non-dimensional strain during DED-L as function of (a) laser power for a constant scanning speed of 12.7 mm/s and (b) scanning speed for a constant laser power of 270 W (c) layer number for a constant laser power of 230 W and scanning speed of 20 mm/s.

The strain parameter, ε^*, increases with rise in peak temperature and ΔT. In particular, higher peak temperature, T_P, results in greater volume shrinkage during solidification. A non-dimensional temperature T^* can reveal the effect of process variables on thermal strain due to rise in peak temperature:

$$T^* = \frac{T_P - T_A}{T_L - T_A} \tag{4-15}$$

where T_A and T_L are the ambient temperature and liquidus temperature, respectively. The term βT^* is a measure of the volumetric contraction. Since a lighter alloy and a larger liquid pool is more susceptible to thermal distortion, a combined effect of βT^*, pool length and alloy density on strain parameter is examined in Figure 4.27 (c). It is clear that the thermal strain increases with βT^* and pool length and decreases with density, as expected. Low heat input and rapid heat dissipation can effectively reduce the peak temperature and pool dimension and reduce strain.

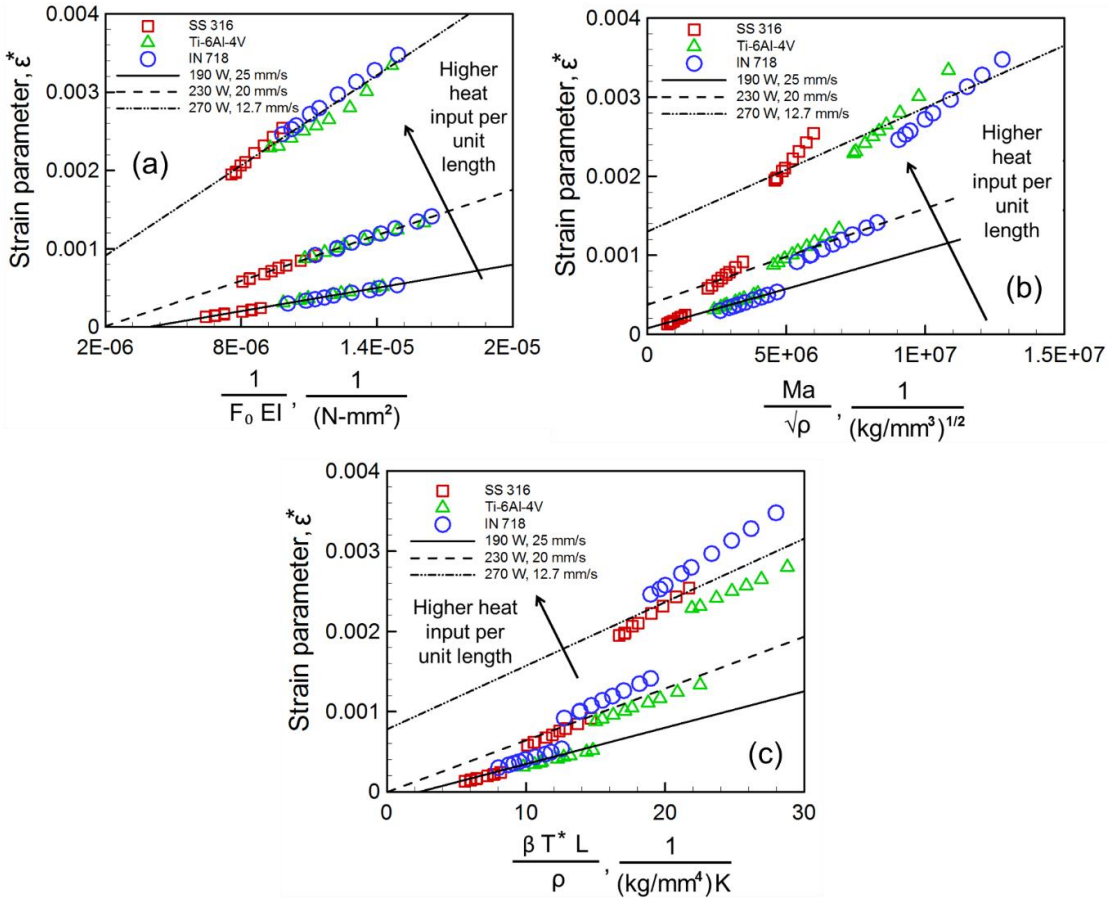

Figure 4.27. Variation of non-dimensional strain during DED-L as function of (a) Fourier number (b) Marangoni number, and (c) non-dimensional temperature, for three heat inputs per unit length.

4.6 Summary and conclusions

Evolution mechanism and spatial non-uniformity of residual stresses and distortion in additively manufactured components are discussed based on the results calculated using a finite element based thermomechanical model. The results shown here are for DED-L of a nickel alloy IN 718 and a titanium alloy Ti-6Al-4V. In addition, it was explained how the sharp gradients in residual stresses and strains in the dissimilar alloy joints between 2.25Cr-1Mo steel and alloy 800H as well as Ti-6Al-4V and alloy 800H can be alleviated using graded joints between the alloys made using DED-L. A novel, dimensionless strain parameter was proposed for shop floor usage in order to guide engineers to find suitable conditions to mitigate distortion. Below are some important findings.

1) For both IN 718 and Ti-6Al-4V components printed using DED-L, the longitudinal residual stress exhibits a steep gradient at both ends of the deposit that makes the parts susceptible to buckling and warping. The through-thickness stress that is responsible for the possible delamination of a component changes sharply at the substrate deposit interface. The residual stress changes from tensile to compressive at the layer interfaces. In extreme cases, this behavior may result in the separation of layers. Ti-6Al-4V components suffer higher residual stresses than IN 718 when printed using DED-L under the same processing conditions. However, IN 718 parts are more susceptible to warping, delamination and buckling because of their higher residual stress to yield strength ratio.

2) Heat input and layer thickness are found to be critical in controlling residual stresses and distortion. The parts fabricated using thin layers encounter a high peak temperature and long exposure time under the laser beam and thus suffer from low residual stresses. For example, the residual stresses in IN 718 parts printed using DED-L can be decreased as much as 30% by reducing the thickness of each layer to fabricate the component for the process conditions studied here. Increasing the heat input can significantly reduce the residual stresses for IN 718 parts printed using DED-L. However, the same condition enhances the thermal distortion by about 2.5 times. Therefore, an appropriate heat input selected by trading off both distortion and residual stresses will be helpful to fabricate a dimensionally accurate part with good mechanical properties.

3) Since, the mechanical properties of Ti-6Al-4V and 800H are significantly different, dissimilar joints between these two alloys exhibited sharp changes in residual stresses and strains at the interface between the two alloys. These sharp changes in residual stresses and

strains can be avoided by fabricating a graded joint between these two alloys made using DED-L. In contrast, because of the similar mechanical properties of 2.25Cr-1Mo steel and 800H, graded joints between these two alloys fabricated using DED-L provided relatively smaller benefits for minimizing residual stresses and distortion compared to the dissimilar joints between them.

4) Low heat input sufficient for maintaining adequate interlayer bonding is beneficial for the control of thermal strain. A decrease in laser power and layer height can also result in higher Fourier number and lower thermal strain. A reduction in laser power and an increase in scanning speed can reduce Marangoni number and non-dimensional temperature and decrease thermal strain. Likewise, alloys with lower heat capacity and higher thermal diffusivity will be susceptible to higher peak temperature, larger pool volume and higher thermal strain.

4.7 References

1) T. DebRoy et al. Additive manufacturing of metallic components - Process, structure and properties. Prog. Mater. Sci. 92 (2018) 112-224.
2) Abaqus Documentation, Version 6.14, Dassault Systems (2015).
3) D. Deng et al. Numerical simulation of temperature field and residual stress in multi-pass welds in stainless steel pipe and comparison with experimental measurements. Comput. Mater. Sci. 37 (2006) 269–277.
4) A. Kamara et al. A numerical investigation into residual stress characteristics in laser deposited multiple layer waspaloy parts. Trans. ASME-B – J. Manuf. Sci. Eng. 133 (2011) 1–9.
5) P. Scott et al. The Battelle Integrity of Nuclear Piping (BINP), Program Final Report, Columbus, OH (2005).
6) T. Seshacharyulu et al. Microstructural mechanisms during hot working of commercial grade Ti–6Al–4V with lamellar starting structure. Mater. Sci. Eng. A 325 (2002) 112–125.
7) P. Rangaswamy et al. High temperature stress assessment in SCS-6/Ti-6Al-4V composite using neutron diffraction and finite element modeling. Int. Conf. Process. Manuf. Adv. Mater. Las Vegas, NV, USA (2000).
8) S.K. Kar. Modeling of mechanical properties in alpha/beta-titanium alloys. PhD diss., The Ohio State University (2005) 152.

9) K. Shah et al. Experimental study of direct laser deposition of Ti-6Al-4V and Inconel 718 by using pulsed parameters. Sci. World J. 2014 (2014).
10) A.M. Al-Mukhtar. Residual stresses and stress intensity factor calculations in T-welded joints. J. Fail. Anal. Prevent. 13 (2013) 619–623.
11) P. Prabhakar et al. Computational modeling of residual stress formation during the electron beam melting process for Inconel 718. Additive Manuf. 7 (2015) 83–91.
12) P.M. Kenney et al. General Electric Company, U.S. Patent Application 14/440 (2013) 154.
13) J.S. Zuback et al. Additive manufacturing of functionally graded transition joints between ferritic and austenitic alloys. J Alloy Compound. 770 (2019) 995-1003.
14) R.B. Bird et al. Transport phenomena. John Wiley & Sons, New York (2002).
15) J. Grum et al. Microstructure, microhardness, and residual stress analysis of laser surface cladding of low-carbon steel. Mater. Manuf. Process. 19 (2004) 243–258.
16) J.C. Heigel et al. In situ monitoring and characterization of distortion during laser cladding of Inconel® 625. J. Mater. Process. Tech. 220 (2015) 135–145.
17) P. Farahmand et al. An experimental–numerical investigation of heat distribution and stress field in single- and multitrack laser cladding by a high-power direct diode laser. Opt. Laser Technol. 63 (2014) 154–168.
18) S. Okano et al. Effect of welding conditions on reduction in angular distortion by welding with trailing heat sink. Sci. Technol. Weld. Joi. 17 (2012) 264–268.
19) Y.P. Yang et al. Material strength effect on weld shrinkage and distortion. Weld. J. 93 (2014) 421s-430s.

Chapter 5

COMPOSITION CHANGE DUE TO EVAPORATIVE LOSS AND LACK OF FUSION DEFECTS IN AM PARTS

It is evident from the previous chapters of this thesis that during additive manufacturing (AM) of alloys, the peak temperature inside the molten pool can be between the liquidus temperature and boiling point of the alloy. At this very high temperature, alloying elements may vaporize significantly depending on the equilibrium vapor pressure above the molten pool [1]. All elements do not vaporize at the same rate because of the difference in vapor pressures of elements. Such selective vaporization of alloying elements often results in a significant change in the composition of the part from that of the original feedstock. This change in composition affects the microstructure as well as mechanical and chemical properties of AM parts [1]. In Chapter 3 of this thesis, it is shown that the fusion zone shape and size can vary significantly depending on the AM process, process conditions and alloy used. The shape and size of the fusion zone control the overlap between neighboring tracks of deposits and an insufficient overlap may result in lack of fusion defect [1]. Lack of fusion defect degrades the tensile properties of the printed parts and may lead to part rejection in extreme cases [1]. Therefore, to print sound metallic components with desired structure, properties and serviceability, composition change and lack of fusion defects should be mitigated. Both of these macroscopic defects are affected by temperature fields and fusion zone geometry and thus are impacted by heat transfer and fluid flow. Therefore, in this thesis research, transport phenomena based modeling is used to provide a better understanding of the evolution of these defects for different AM process and alloy combinations in order to minimize them.

In this chapter, composition change is computed using a well-tested vaporization model based on the transient temperature field and molten pool geometry calculated using the heat transfer and fluid flow model. Although the vaporization model can be applied for predicting composition change for all three AM processes considered in this thesis research, calculated

results are provided for DED-L and PBF-L of stainless steel 316 as examples. Lack of fusion defects are estimated from the fusion zone shape and size using a heat transfer fluid flow model. Calculated results for DED-L and PBF-L of various commonly used alloys are provided in this chapter as examples. The calculated results are validated against independent experimental data. In addition, a novel, dimensionless lack of fusion number was proposed for shop floor usage to mitigate lack of fusion defects in additively manufactured parts.

5.1 Calculation of composition change in AM using a vaporization model

Composition change in the printed alloy components is calculated based on mass balance during AM processes. The decrease in the concentration of an element i, due to evaporative loss, can be expressed as follows [2]:

$$\Delta\%C_i = 100 \sum(R_i \, dA_s)/(\rho \, V_m) \quad (5\text{-}1)$$

where $\Delta\%C_i$ is the decrease in the concentration of alloying elements, R_i is the local vaporization rate of i per unit top surface area of the molten pool, dA_s is the local top surface area of the molten pool, ρ is the density of the alloy, and V_m is the volume of the deposited material per unit time. The term $\sum(R_i \, dA_s)$ is the total rate of vaporization of element i per unit time from the top surface of the molten pool. The change in the concentration of an element depends on both the vaporization rate of the element and the volume of the molten pool. Since the vaporization rate depends on the top surface area and the elemental loss is distributed over the entire volume of the molten pool, the surface to volume ratio of the molten pool plays an important role in influencing the composition change, often being more important than the pool size. Heat transfer and fluid flow calculations are required to estimate alloying element loss from pools of molten metal, because the temperature distribution of the molten pool surface is needed to calculate the rate of vaporization.

Rate of vaporization is computed based on the vaporization model proposed by Knight [3]. The model solves the equations of conservation of mass, momentum and energy in a thin layer adjacent to the liquid-vapor interface known as the Knudsen layer. It considers the possibility that some atoms that leave the molten pool as vapor will not escape into the atmosphere, and instead will condense on the molten pool surface. To account for this condensation, the model considers the velocity distribution functions of the metal vapor molecules close to the molten pool. At the liquid pool surface, the velocity distribution, f_1, is half-Maxwellian because the vapor molecules can only move away from the pool surface, i.e. the velocity is positive. A portion of the vaporized material, f_2, condenses on the liquid surface.

The Knudsen layer which is a distance of several mean free paths length after which the velocity distribution, f_3, becomes fully Maxwellian and the velocity can vary between -∞ to +∞. It can be shown [3] that the temperature T_v, density ρ_v, pressure p_v and the mean velocity u_v of the vapor at the edge of the Knudsen layer can be related to temperature T_L, density ρ_L, and pressure p_L, of the vapor at the liquid surface by treating the Knudsen layer as a gas dynamic discontinuity. The derived relations across the Knudsen layer are given by:

$$\frac{T_v}{T_L} = \left[\sqrt{1 + \pi\left(\frac{\gamma_v - 1}{\gamma_v + 1}\,\frac{m}{2}\right)^2} - \sqrt{\pi}\,\frac{\gamma_v - 1}{\gamma_v + 1}\,\frac{m}{2}\right]^2 \tag{5-2}$$

$$\frac{\rho_v}{\rho_L} = \sqrt{\frac{T_L}{T_v}}\left[\left(m^2 + \frac{1}{2}\right)\, e^{m^2}\, erfc(m) - \frac{m}{\sqrt{\pi}}\right] + \frac{1}{2}\,\frac{T_L}{T_v}\left[1 - \sqrt{\pi} m\, e^{m^2}\, erfc(m)\right] \tag{5-3}$$

$$\beta = \left[(2m^2 + 1) - m\sqrt{\pi\frac{T_L}{T_v}}\right]\, e^{m^2}\,\frac{\rho_L}{\rho_v}\,\sqrt{\frac{T_L}{T_v}} \tag{5-4}$$

where $m = u_v/\sqrt{2\,R_v T_v/M_v}$, R_v is the constant for vapor, γ_v is the ratio of specific heats of the vapor which is treated as a monatomic gas, and β is the condensation factor. The equilibrium vapor pressure at the pool surface is obtained from the sum of the equilibrium vapor pressures of all alloying elements at the local temperature and M_v is the average molecular weight of the vapor. In order to compute the four unknowns in Equations (5-2) through (5-4), namely, T_v, ρ_v, β, and m, another independent equation is necessary. This relation is obtained by applying the Rankine-Hugoniot relation [3] to relate the pressure at the edge of the Knudsen layer to the ambient pressure.

$$\frac{p_L}{p_g}\,\frac{p_2}{p_1} = 1 + \gamma_g M\Gamma\left[\frac{\gamma_g + 1}{4} M\Gamma + \sqrt{1 + \left(\frac{\gamma_g + 1}{4} M\Gamma\right)^2}\right] \tag{5-5}$$

where p_1 and p_2 are the pressures in front of and behind the wavefront, respectively, and $\Gamma = \sqrt{\gamma_v R_v T_v}/\sqrt{\gamma_g R_g T_g}$ and M is the Mach number which is related to m by the relation:

$$m = M\sqrt{\frac{\gamma_v}{2}} \tag{5-6}$$

The Mach number M and the density ρ_v, obtained by solving the above equations, can be used to calculate the vaporization flux due to convection from the liquid pool surface corresponding to a local surface temperature T_L from:

$$J_P = \rho_v M S \tag{5-7}$$

where S is the speed of sound in vapor at temperature T_v. The vaporization flux of an alloying element i, J_i, is given by the product of the total vapor flux and the mole fraction of i in the gas.

$$J_i = a_i \frac{p_i^0}{p_L} \frac{M_i}{M_v} J_P \tag{5-8}$$

The total evaporative flux can be calculated by adding flux due to concentration gradient to the flux calculated from Equation (5-8). Calculations of equilibrium vapor pressure of elements (p_i^0) over their pure liquid were made using the data presented in Table 5.1 and 5.2 to examine the printability of alloys in terms of vaporization. The coefficients in Table 5.1 correspond to the equation from Gale [4] given by

$$\log (\mathrm{P_i^0} \times 760) = -\frac{\mathrm{A}}{\mathrm{T}} + \mathrm{B} + \mathrm{C} \log \mathrm{T} + 10^{-3}\,\mathrm{DT} \tag{5-9}$$

while the coefficients in Table 5.2 correspond to the equation from Yaws [5] and are given by

$$\log (P_i^0 \times 760) = A + \frac{B}{T} + C \log T + DT + ET^2 \tag{5-10}$$

In both Equations (5-9) and (5-10), P_i^0 is expressed in [atm] and T is expressed in [K].

Table 5.1. Coefficients used for calculating equilibrium vapor pressure

Element	A ($\times 10^4$)	B	C	D
Al	1.6450	12.36	–1.023	0
Cu	1.765	13.39	–1.273	0
Mg	0.7550	12.79	–1.41	0
Ni	2.24	16.95	–2.01	0
Si	2.09	10.84	–0.565	0
Ti	2.32	11.74	–0.66	0

Table 5.2. Coefficients used for calculating equilibrium vapor pressure over pure liquid

Element	A	B ($\times 10^4$)	C	D	E
Cr	–80.3456	–1.2221	2.9746	-6.84×10^{-3}	5.2454×10^{-7}
Fe	11.5549	–1.9538	–0.62549	-2.7182×10^{-9}	1.9086×10^{-13}
Mo	74.9735	–4.1955	–20.072	3.2166×10^{-3}	-2.2507×10^{-7}
Nb	–64.3485	–2.9438	23.622	-3.9155×10^{-3}	2.0660×10^{-7}
V	52.0677	–3.1989	–12.620	1.6179×10^{-3}	-1.0505×10^{-7}

Calculations from Equations (5-9) and (5-10) correspond to the equilibrium vapor pressure of elements over the pure liquid metal. Considering that the liquid alloy behaves ideally near its boiling point, the equilibrium vapor pressure P_i of element i over the liquid alloy is estimated as,

$$P_i = X_i \, P_i^0 \tag{5-11}$$

where X_i and P_i^0 are the mole fraction and the equilibrium vapor pressure of element i over its pure liquid, respectively. The compositions of the common alloys shown in Table 5.3 are used to calculate the mole fractions of each element. Figure 5.1 shows the equilibrium vapor pressure of the elements over liquid alloy for five different alloys as a function of temperature. The plot shows that the vapor pressure of the elements has a strong dependence on temperature.

Table 5.3. Alloy compositions showing the wt.% of different elements.

Alloy	Al	Cr	Cu	Fe	Mn	Mo	Nb	Ni	Si	Ti	V
IN 625	0.2	21.5	-	4	-	9	3.6	61.5	-	0.2	-
SS 316	-	17	-	68	2	-	-	12	1	-	-
800H	0.6	21	0.75	39.5	1.5	-	-	34.9	1	0.6	-
2.25Cr-1Mo Steel	0.6	2.25	-	95.6	0.5	1	-	0.04	0.5	0.6	-
Ti-6Al-4V	6	-	-	-	-	-	-	-	-	90	4

5.2 Controlling composition change in AM parts

The composition change of each constituting elements of stainless steel 316 is calculated using the vaporization model, as described above, during single-track PBF-L using the process conditions provided in Table 5.4. Vaporization flux of each elements depends on the equilibrium vapor pressure of that element and total vaporization flux from the top surface of the molten pool. Total vaporization flux depends on the temperature distribution on the top surface of the molten pool. Figure 5.2 (a) shows the temperature distribution on the top surface of the deposit. The corresponding total vapor flux is shown in Figure 5.2 (b). The vaporization flux of one of the constituting elements, manganese, is also shown in Figure 5.2 (c). Calculated changes in composition of four main constituting elements of stainless steel 316 are compared with the corresponding experimental data [6] for DED-L as shown in Figure 5.3 (a). Experimentally measured values of compositions in the alloy powders and the built specimens were reported. Composition change is estimated based on those reported values. The computed composition change values agree well with the corresponding experimental data. All elements vaporize from the molten pool with different rates, as shown in Figure 5.3 (b). The relative

susceptibility to vaporization is consistent with their equilibrium vapor pressures, as shown in Figure 5.1 (d). Depending on the initial weight percentage, compositions of some elements decreases and to maintain the balance, compositions of other elements increase, as evident from Figure 5.3 (a).

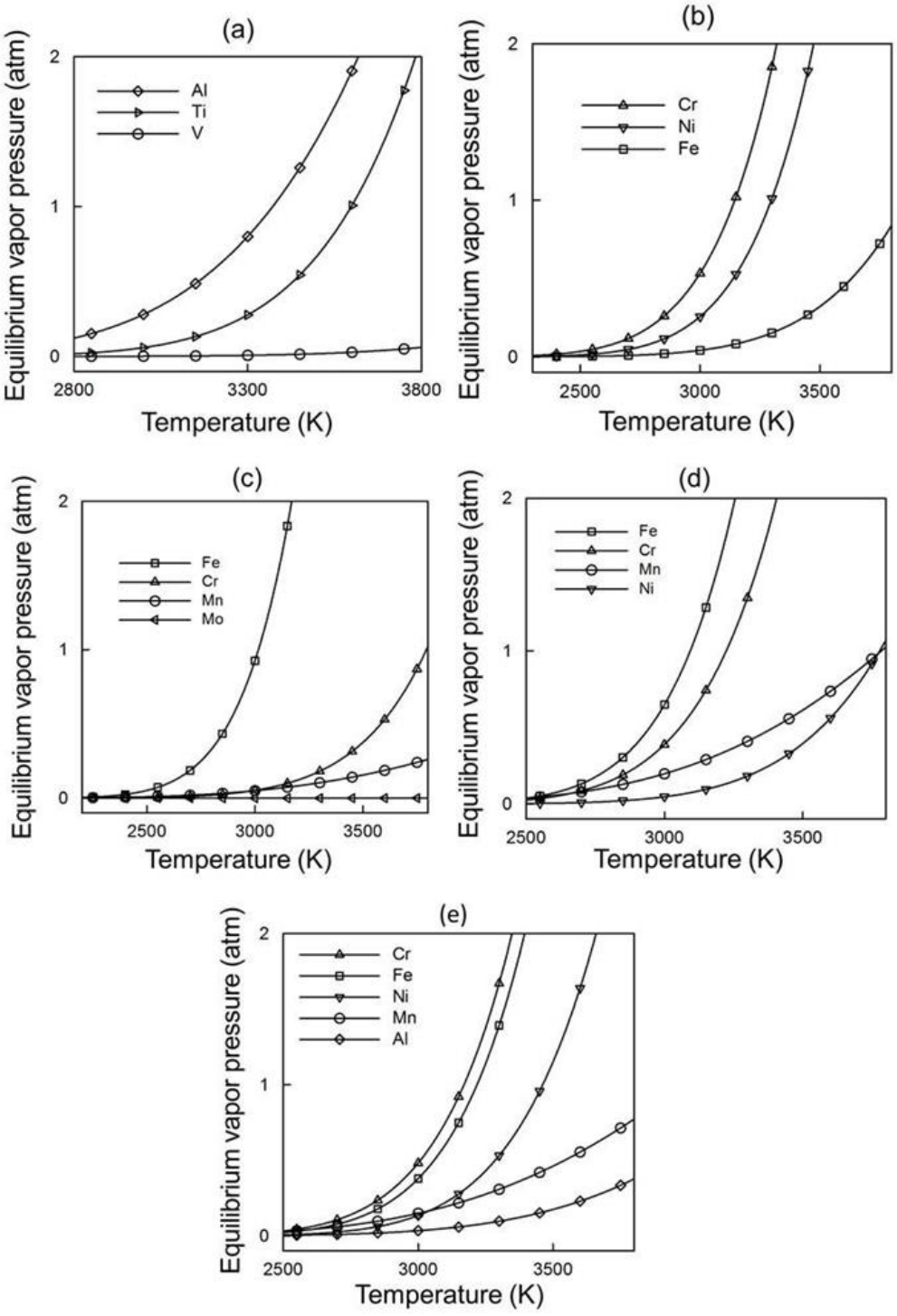

Figure 5.1. Equilibrium vapor pressures for alloying elements of different alloys as functions of temperature. (a) Ti-6Al-4V (b) IN625 (c) 2.25Cr-1Mo Steel (d) SS 316 (e) Alloy 800H.

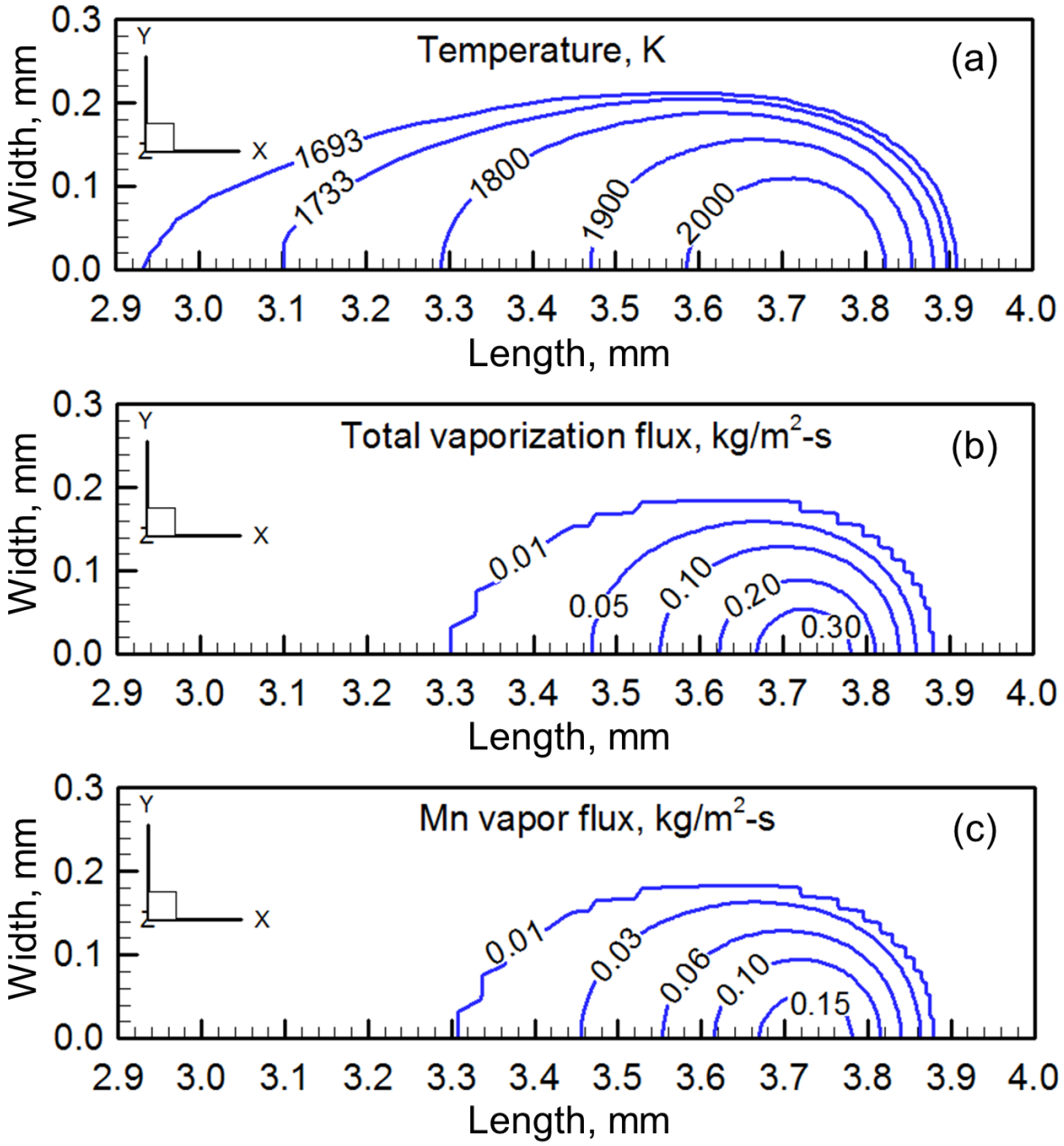

Figure 5.2. Distribution of (a) temperature, (b) total vaporization flux and (c) Mn vapor flux on the top surface during printing of SS 316 using PBF-L. The process conditions used in this calculation are given in Table 5.4.

Table 5.4. Process parameters used for the composition change calculation for Figure 5.2.

Laser power, W	110
Scanning speed, mm/s	100
Layer thickness, mm	0.25
Laser beam radius, mm	0.3
Substrate thickness, mm	0.75

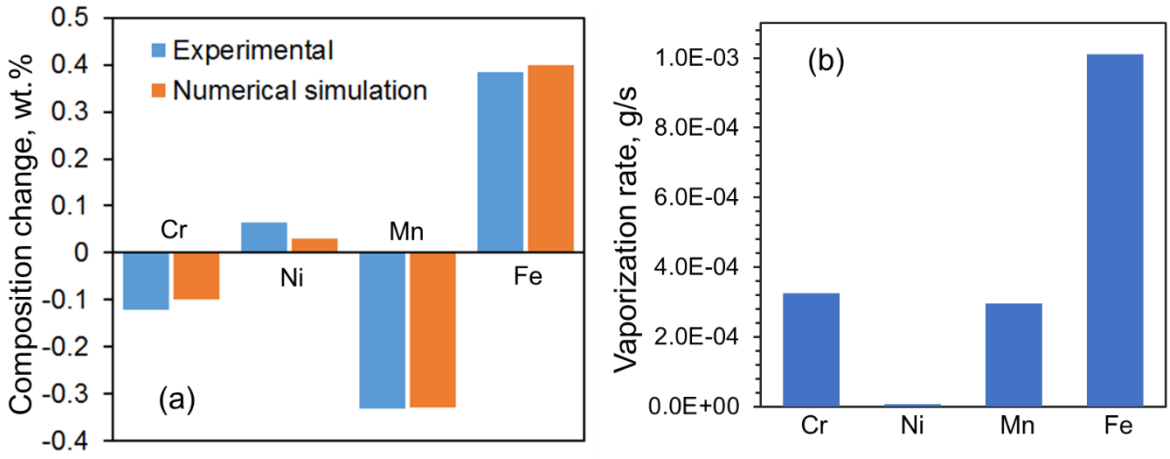

Figure 5.3. (a) Comparison between the experimentally measured [6] and numerically computed composition change and (b) vaporization rates for four main constituting elements of stainless steel 316 during DED-L. Processing conditions used in these calculations are given as: laser power = 2000 W, scanning velocity = 7 mm/s, powder feed rate = 0.12 g/s, laser spot diameter = 4 mm.

5.3 Prediction of lack of fusion defect in AM components

In AM, lack of fusion defects originate due to insufficient bonding between neighboring tracks. For a single track, multi-layer deposit, adequate fusion and inter-layer bonding for different alloys can be examined by the ratio of the penetration depth (d) of the molten pool to the thickness of a layer (h) of material deposited onto the substrate or previously deposited layer. The penetration depth (d) is calculated using the heat transfer and fluid flow model. In order for a deposited layer to bond properly with a previous layer, the penetration depth of the molten pool, d, should exceed the layer thickness, h, and adequately remelt the previously deposited layer. The minimum possible value of the ratio d/h for establishing contact between two successive layers is 1, indicating a penetration depth (d) equal to layer thickness (h). However, this contact is inadequate for good bonding. Carroll et al. [7] reported a 99.999% dense part for DED-L of Ti-6Al-4V, indicating proper inter-layer bonding. A corresponding value for d/h is estimated as 1.15. So, a penetration of 15% of the layer thickness into the previous layer signifies good interlayer bonding. Figure 5.4 shows an inverse relationship between the macro-porosity resulting from lack of fusion defects [8-12] and the corresponding estimated d/h values for DED-L of common AM alloys. The values of the ratio 'd/h' for different alloys are calculated using the corresponding process conditions taken from the literature [8-12]. For larger values of the ratio d/h, the molten pool penetrates deeper into the previously deposited layer to provide adequate inter-layer bonding. For alloys that are

highly susceptible to lack of fusion defects, AM variables like laser power, scanning speed and powder feed rate should be appropriately adjusted to attain an adequate depth of penetration.

For multi-layer, multi-hatch deposits, lack of fusion defects originate from improper fusional bonding between hatches and layers. Therefore, these defects depend on both width and depth of the molten pool as well as layer thickness and hatch spacing. Figure 5.5 (a) and (b) show the computed shapes and sizes of the molten pool transverse sections (YZ plane) for different hatches and layers of five hatches, five layers, PBF-L builds of SS 316 and Ti-6Al-4V, respectively using the process conditions in Table 5.4. For the SS 316, unmelted regions between the molten pools indicating improper fusional bonding among layers and hatches represent lack of fusion voids. For the same conditions, molten pools in Ti-6Al-4V build are much larger in size and prevent lack of fusion defects as observed in Figure 5.5 (b). Figures 5.6 (a-c) show the computed shapes and sizes of the molten pool transverse sections (YZ plane) for different hatches and layers of five hatches, three layers, PBF-L builds of SS 316 at different heat inputs. Lack of fusion voids observed in Figure 5.6 (a) are eliminated by increasing laser power and decreasing scanning speed, as shown in Figure 5.6 (b) and (c), respectively.

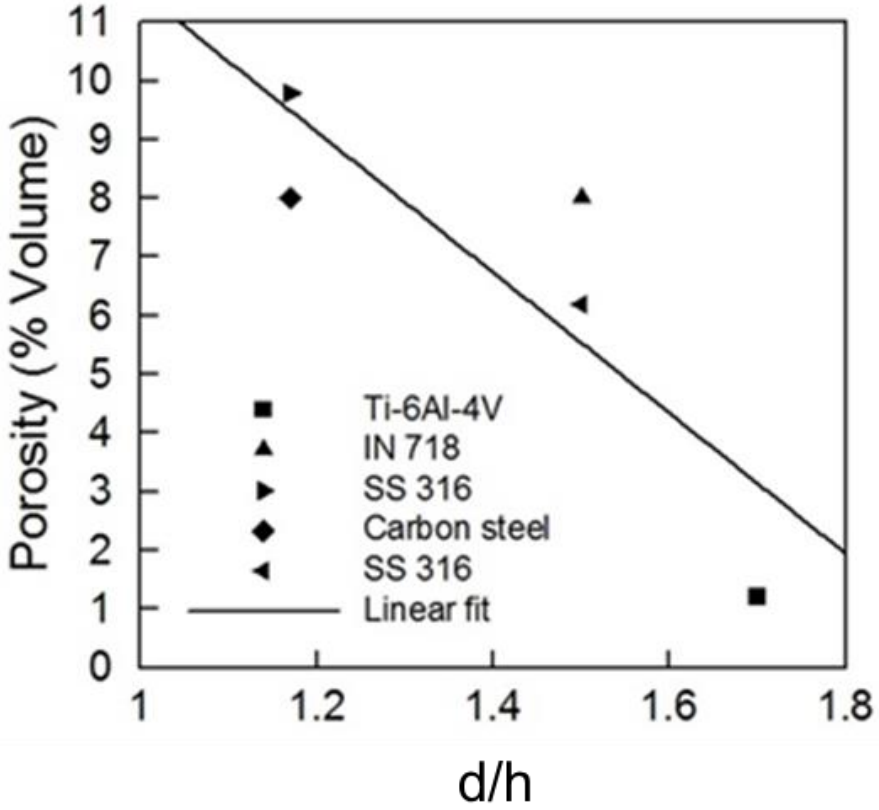

Figure 5.4. Correlation between the ratio between depth of penetration and layer thickness and macro-porosity due to lack of fusion during DED-L of Ti-6Al-4V [8], IN 718 [9], SS 316 [10], carbon steel [11] and SS 316 [12]. The values of the ratio 'd/h' for different alloys are calculated using the corresponding process conditions taken from the literature [8-12].

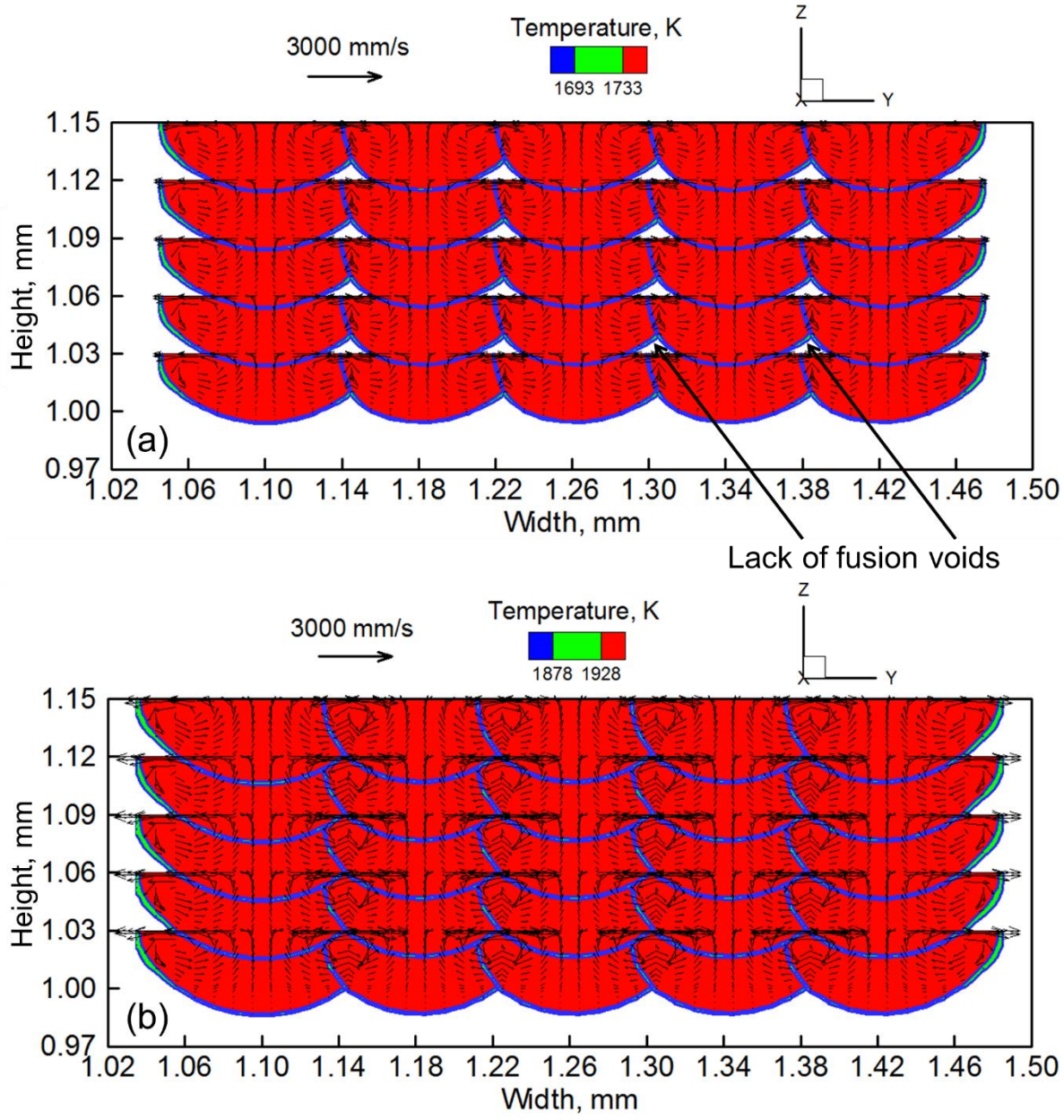

Figure 5.5. Transverse sectional view of the molten pools for 5 layers 5 hatches PBF-L build of (a) SS 316 (b) Ti-6Al-4V build using 1000 mm/s scanning speed and 80 microns hatch spacing. Other process conditions are same as Table 5.4. These results are for unidirectional scanning strategy where scanning directions of all hatches are the same.

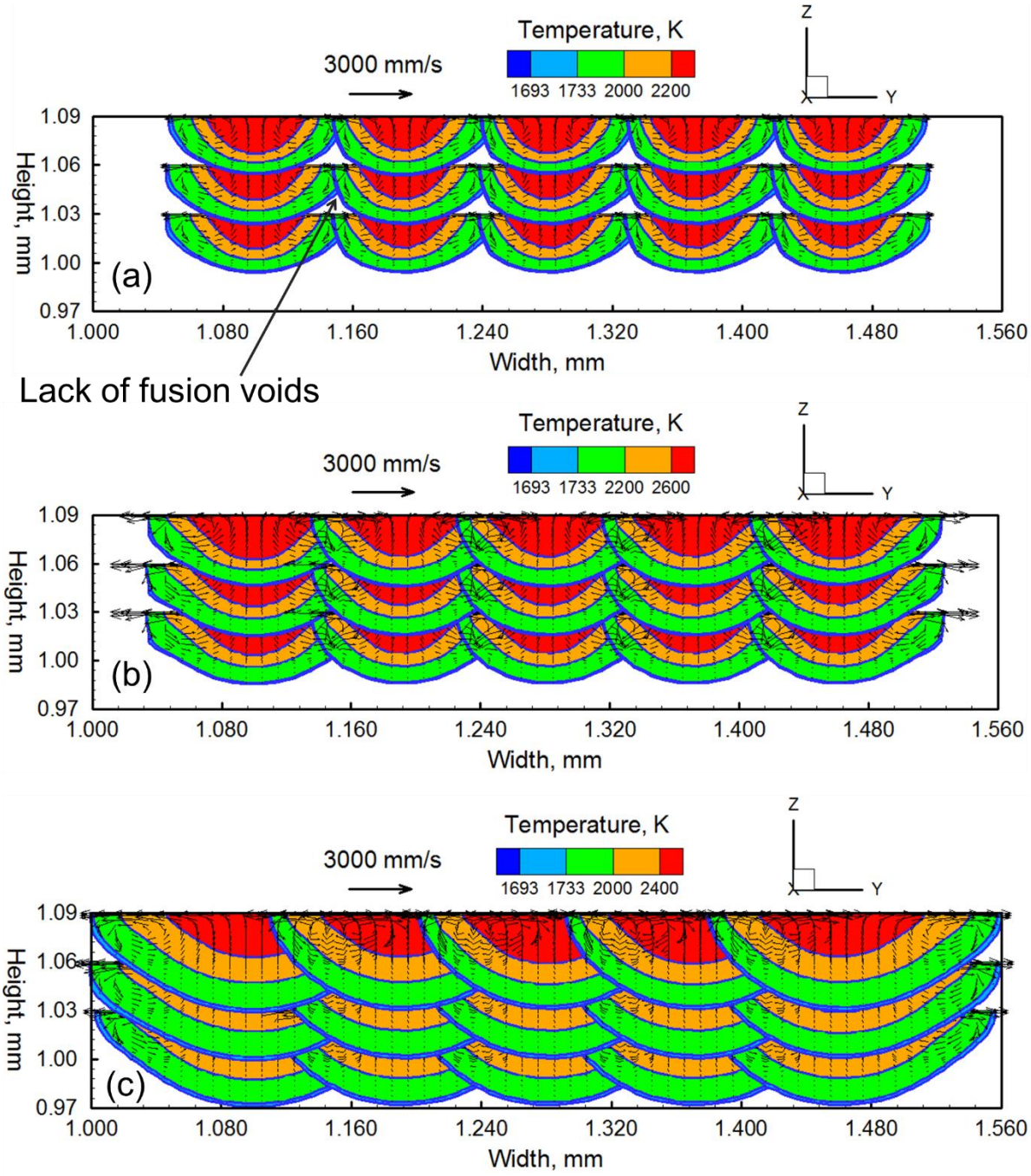

Figure 5.6. Transverse sectional view of the molten pools for 3 layers 5 hatches PBF-L builds of SS 316 using (a) 60 W power and 1000 mm/s speed (b) 100 W power and 1000 mm/s speed and (c) 60 W power and 250 mm/s speed. All three results are using 90 microns hatch spacing. Other process conditions are mentioned in Table 5.4. These results are for unidirectional scanning strategy where scanning directions of all hatches are the same.

Figures 5.7 shows the effect of hatch spacing on the lack of fusion voids during PBF-L of SS 316. The percentage of lack of fusion voids is calculated as a ratio of area in the unmelted region to the total area of cross section of the build expressed in percentage. Higher hatch spacing results in improper fusional bonding between two successive hatches and increases the lack of fusion voids. At a given hatch spacing, the lack of fusion voids can be minimized by increasing the overlapping of the fused regions. This can be accomplished by increasing the size of the molten pool at lower scanning speeds as shown in the figure. Therefore, for a particular alloy component the lack of fusion defects can be minimized by reducing the scanning speed and/or hatch spacing.

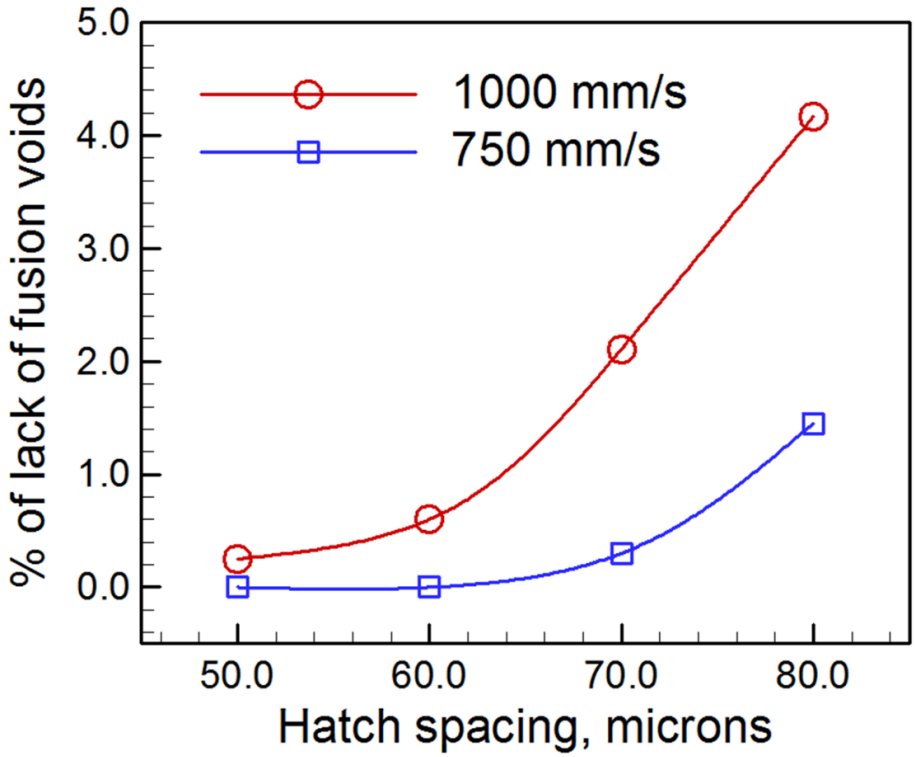

Figure 5.7. Variation of area percentage of lack of fusion voids with hatch spacing for 5 layers 5 hatches PBF-L build of SS 316 using 750 mm/s and 1000 mm/s scanning speeds and 60 W laser power. Other process conditions are same as Table 5.4.

5.4 Lack of fusion number for predicting defects in printed parts rapidly

The detailed heat transfer and fluid flow calculations using numerical model are helpful to provide detailed understanding of the evolution of lack of fusion defects in AM parts. However, it is often impractical to use these models for real time prediction of lack of fusion defects in shop floor because of the time constraints and unavailability of proper computational resources. Back-of-the-envelope calculations are often beneficial for real time predictions.

Therefore, in this section, a dimensionless lack of fusion number is proposed for back of the envelope calculations to predict lack of fusion defects in AM components.

Lack of fusion defect depends on process parameters such as laser power, scanning speed, layer thickness and hatch spacing. For example, Figures 5.8 (a) and (b) show the relation of experimentally measured [13, 14] lack of fusion void fraction with laser power and scanning speed, respectively. In these plots the experimental data are taken from the independent literature [13, 14]. It has been found that the amount of lack of fusion voids is inversely proportional to the laser power and directly proportional to the scanning speed. Apart from these two process conditions, layer thickness and hatch spacing also play important role in determining lack of fusion defect. Figures 5.8 (c) and (d) show the relation of experimentally measured [15, 16] lack of fusion void area fraction with layer thickness and hatch spacing, respectively. In these plots the experimental data are taken from the independent literature [15, 16]. It has been found that amount of the lack of fusion voids is directly proportional to both the layer thickness and hatch spacing. In addition, other process parameters such as laser spot radius, absorptivity of the laser beam at the powder bed, molten pool width and depth and rate of heat transfer also govern lack of fusion defect. Thermophysical properties of alloys also affect the susceptibility to lack of fusion defects. Therefore, to quantify and provide better understanding of the effects of these governing factors on the lack of fusion defect in multi-layer, multi-hatch AM builds, a non-dimensional lack of fusion number (L_F) is used here. This number, L_F consists of all important process parameters and alloy properties and is represented as:

$$L_F = \frac{\rho\,(C_P\,\Delta T + L)}{\frac{\eta\,P}{\pi\,r^2\,v}}\;\; F\;\frac{t}{d}\left(\frac{h}{w}\right)^2 \qquad (5\text{-}12)$$

All the symbols used in this equation are described along with their units and dimensions in Table 5.5. Equation (5-12) clearly indicates that the lack of fusion defect is directly proportional to scanning speed, layer thickness and hatch spacing and inversely to laser power. Molten pool width and depth and Fourier number used in this equation are calculated using the heat transfer and fluid flow model. The molten pool dimensions do not change significantly after the hatch and the layer where the temperature field reaches steady state, as described in Chapter 3 of this thesis. Therefore, molten pool dimensions used in Equation (5-12) are taken after they reach the steady state. Since wider and deeper molten pool ensures proper fusional bonding among successive layers and hatches, both pool width and depth are in the denominator of the equation. Other important material properties that affect pool dimensions

and thus the lack of fusion defect such as viscosity and coefficient of surface tension are considered by including their effects during pool depth and width predictions. Fourier number indicates faster diffusive heat transfer relative to heat accumulation. A high rate of heat transfer reduces the pool size and thus increases the lack of fusion defect. The term $\rho\ (C_P\ \Delta T + L)$ denotes the amount of heat needed to melt unit volume of material. For a given heat input, an alloy with high energy required for melting exhibits smaller molten pool that increases the susceptibility of lack of fusion defect.

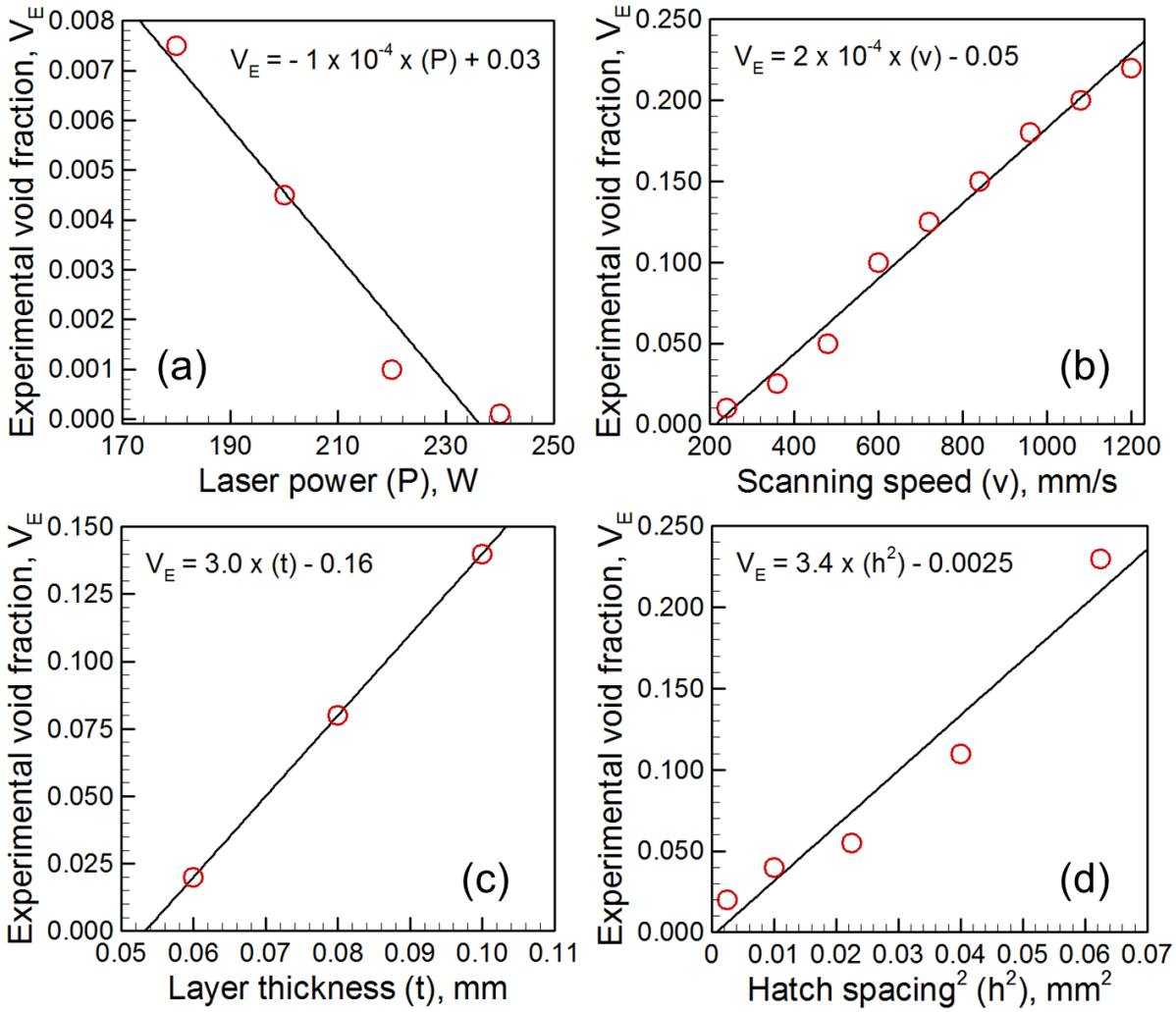

Figure 5.8. Relation of experimentally measured void fraction during PBF-L with (a) laser power, (b) scanning speed, (c) layer thickness and (d) hatch spacing. The data to plot the figures (a-d) are taken from Darvish et al. [14], Di et al. [13], Qiu et al. [15] and Aboulkhair et al. [16], respectively. The results at the figures (a-d) are for CoCrMo alloy, SS 316, Ti-6Al-4V and AlSi10Mg, respectively.

Table 5.5. Variables used in the lack of fusion number (L_F) in the MLTθ system

Variable	S.I. unit	Dimension
Density of alloy, ρ	kg/m^3	ML^{-3}
Specific heat of alloy, C_P	J/kg K	L^{2}T^{-2}θ^{-1}
Temperature gradient, $\Delta T = T_L - T_S$, where T_L and T_S refer respectively to liquidus and solidus temperature	K	θ
Latent heat of fusion of alloy, L	J/kg	L^{2}T^{-2}
Absorptivity of laser beam, η	--	M^{0}L^{0}T^{0}θ^0
Laser beam power, P	W	ML^{2}T^{-3}
Laser scanning speed, v	m/s	LT^{-1}
Laser beam radius, r	m	L
Fourier number, F denoted by $F = \alpha/v\,l$ where α is the thermal diffusivity of alloy and l is the molten pool length	--	M^{0}L^{0}T^{0}θ^0
Layer thickness, t	m	L
Hatch spacing, h	m	L
Molten pool depth, d	m	L
Molten pool half-width, w	m	L

Figure 5.9 shows that the experimentally measured [13, 16-18] lack of fusion void fraction (V_E) for three commonly used alloys during PBF-L follows a linear relationship with corresponding L_F, which is estimated using Equation (5-12). The molten pool dimensions used in this calculation are predicted using the heat transfer and fluid flow model of PBF-L using the process conditions taken from the corresponding literature [13, 16-18]. Based on the trend of data points presented in Figure 5.9, lack of fusion void fraction (V_E) can be expressed as:

$$V_E = 15.3\, L_F \qquad (5\text{-}13)$$

Equation (5-13) is valid for the heat input range of 0.05-1.00 J/mm, which is widely used for major L-PBF applications [1]. In this equation, when L_F is zero there are no lack of fusion voids observed. To include a new alloy, the correlation in Equation (5-13) needs to be updated by including new experimental data for that alloy in Figure 5.9. However, the lack of fusion number is applicable for any alloy for a wide range of processing conditions for both DED and PBF processes.

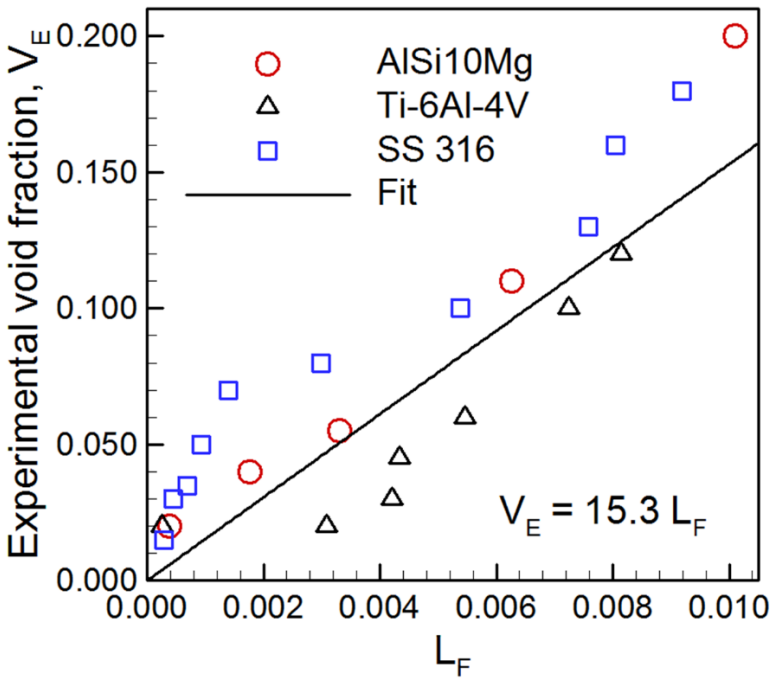

Figure 5.9. Values of experimental void fraction (V_E) during PBF-L as a function of the lack of fusion number (L_F) for AlSi10Mg [16], Ti-6Al-4V [17, 18] and SS 316 [13, 17] showing a linear relationship. Experimentally measured void fraction values are directly taken from the literature [13, 16-18]. L_F values are calculated using corresponding process parameters directly adapted from the literature [13, 16-18] and alloy properties.

5.5 Mitigation of lack of fusion voids in AM parts

The lack of fusion number, L_F, described in the previous section, provides a usable scale to estimate and compare the amount of lack of fusion void of different alloys for a given set of process conditions. Therefore, this dimensionless number is used to evaluate the susceptibility to lack of fusion defects for various alloys at different process conditions. The results obtained from this analysis can be helpful to find out a proper process condition to mitigate lack of fusion defects during AM of alloys.

Figure 5-10 compares three commonly used alloys based on their vulnerability to the lack of fusion defect at three different scanning speeds during PBF-L. SS 316 is the most susceptible to lack of fusion defects because of its smallest molten pool attributed to its relatively high density. Since rapid scanning reduces the pool size, the amount of lack of fusion voids enhances with increasing scanning speed as shown in the figure. Lack of fusion defects depend largely on the molten pool shape and size governed by the flow of liquid metal driven primarily by the spatial gradient of interfacial tension, also known as the Marangoni stress. Higher Marangoni number indicates vigorous flow of liquid metal inside the pool that increases the molten pool width and ensures proper fusional bonding among successive layers and

hatches. Therefore, lack of fusion defects decrease when hatch spacing and layer thickness are constant for processes with higher Marangoni number as shown in Figure 5-11.

Assuming a constant cross-section, hatch spacing, and layer thickness, higher molten pool peak temperature may indicate heat accumulation and consequentially a larger molten pool which facilitates better bonding of the depositing metal with the previously deposited metal. Therefore, monitoring of peak temperature during AM can be used as an indicator of the extent of lack of fusion defect. A non-dimensional temperature T* can reveal the change in the amount of lack of fusion voids due to a rise in peak temperature:

$$T^* = \frac{T_P}{T_L} \tag{5-14}$$

where T_P and T_L are the peak temperature and liquidus temperature of the alloy, respectively. The peak temperature required for the calculations may be estimated from the heat transfer and fluid flow model. Figure 5-12 shows that the lack of fusion defect decreases with an increase in peak temperature. The peak temperatures for the parameter range considered here are below the boiling point of the alloys and keyholes do not form during the process. However, instabilities in the keyholes formed at very high power density may result in porosity that are different from the lack of fusion voids described here [1]. Figures 5-11 and 5-12 show that the lack of fusion voids can be effectively minimized by enhancing Marangoni number and non-dimensional temperature during the process by adjusting different processing conditions.

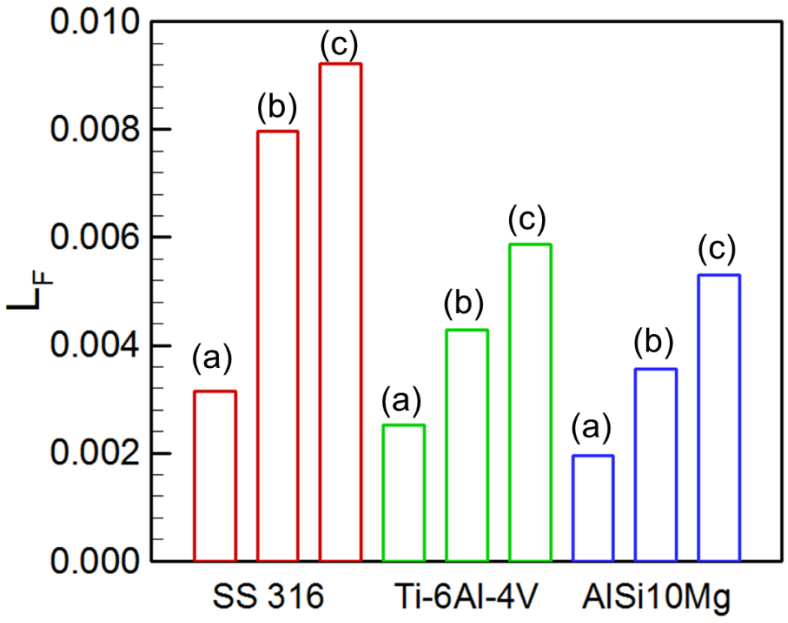

Figure 5.10. Values of the calculated lack of fusion number (L_F) for PBF-L calculated for SS 316, Ti6Al4V and AlSi10Mg builds. The symbol (a), (b) and (c) denote the scanning speed of 500 mm/s, 750 mm/s and 1000 mm/s scanning speed, respectively. Other process conditions are same as Table 5.4.

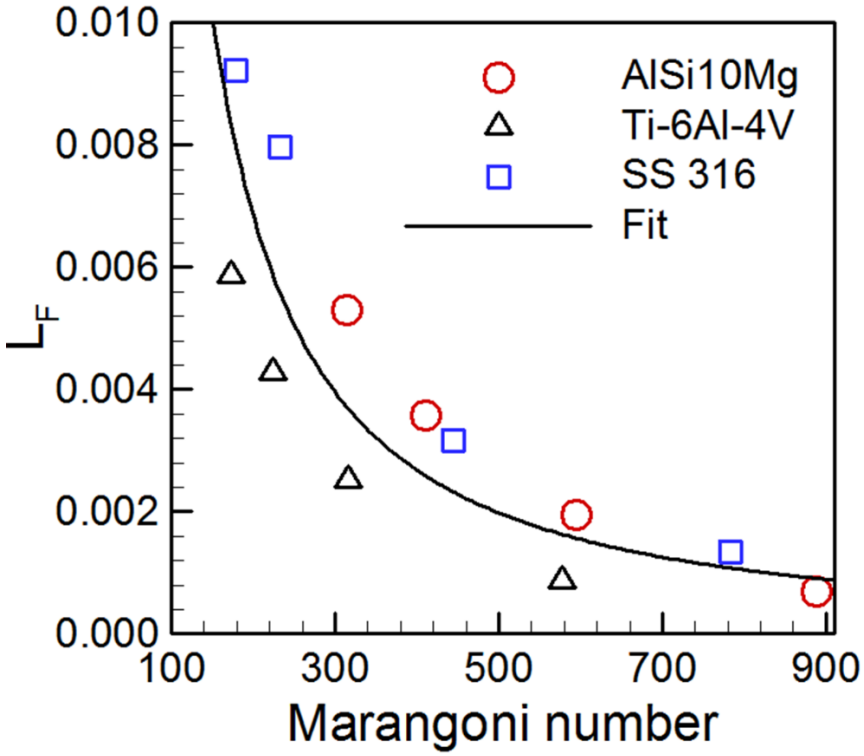

Figure 5.11. Variation of the calculated lack of fusion number (L_F) for PBF-L as a function of Marangoni number for different heat inputs per unit length. Other process conditions are same as Table 5.4.

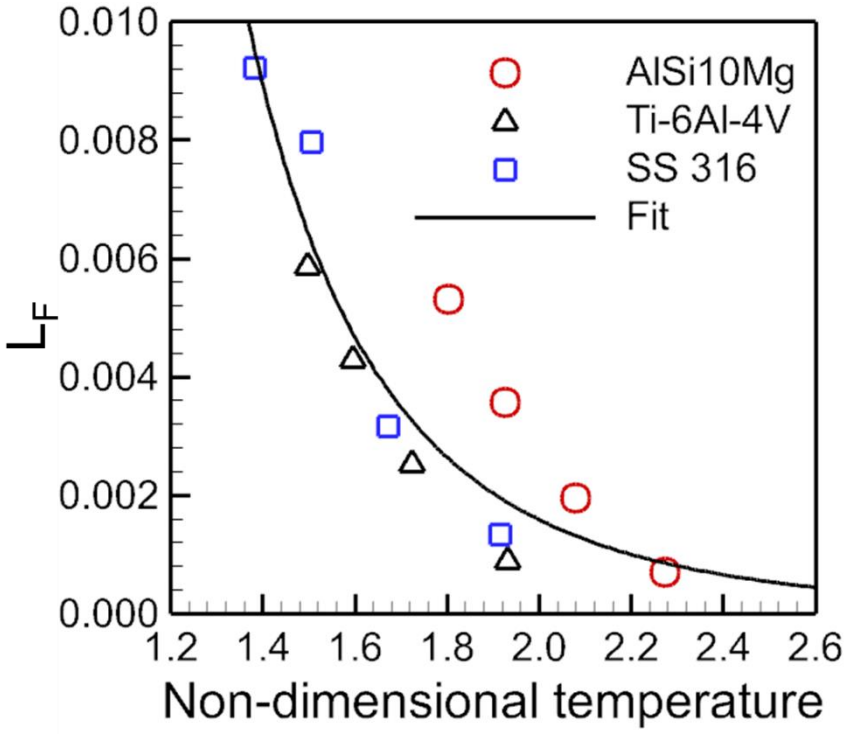

Figure 5.12. Variation of the calculated lack of fusion number (L_F) for PBF-L as a function of non-dimensional temperature for different heat inputs per unit length. Other process conditions are same as Table 5.4.

5.6 Summary and conclusions

In this chapter, composition change is computed using a well-tested vaporization model based on the transient temperature field and molten pool geometry calculated using the heat transfer and fluid flow model. Calculated results are provided for DED-L and PBF-L of stainless steel 316 as examples. Lack of fusion defects are estimated from the fusion zone shape and size calculated using the heat transfer fluid flow model. Calculated results for DED-L and PBF-L of various commonly used alloys are provided in this chapter as examples. In addition, a novel, dimensionless lack of fusion number was proposed for shop floor usage in order to guide engineers to find suitable conditions to mitigate that lack of fusion defect in additively manufactured parts. Below are the most important findings.

1) The vaporization model used here is proved to be efficient for accurate prediction of composition change due to evaporative loss during AM. For AM of SS 316, the alloying element that is the most susceptible for composition change is manganese.

2) A larger heat input per unit length obtained by reduction of scanning speed or an increase in laser power or both results is larger liquid pool and lower occurrence of lack of fusion defect during AM of alloys.

3) A high value of Marangoni number that indicates vigorous circulation of the liquid metal inside the molten pool during AM correlated well with the reduction of the lack of fusion defects.

4) High values of peak temperature encountered during AM of metallic components also correlated well with the reduction of the occurrence of lack of fusion defects. Since the temperature can be monitored during deposition, this correlation can be used to reduce lack of fusion defects.

5.7 References

1) T. DebRoy et al. Additive manufacturing of metallic components - Process, structure and properties. Prog. Mater. Sci. 92 (2018) 112-224.
2) T. DebRoy et al. Physical processes in fusion welding. Rev. Mod. Phys. 67 (1995) 85-112.
3) C.J. Knight. Theoretical modeling of rapid surface vaporization with back pressure. AIAA J. 17 (1979) 519-23.
4) W.F. Gale et al. Smithells Metals Reference Book, 8th edition, Butterworth-Heinemann, Burlington (2003).

5) C.L. Yaws. Handbook of Vapor Pressure, Gulf Pub. Co, Houston (1994).
6) H. Zhang et al. Effect of Ni content on stainless steel fabricated by laser melting deposition. Opt. Laser Technol. 101 (2018) 363–371.
7) B.E. Carroll et al. Anisotropic tensile behavior of Ti-6Al-4V components fabricated with directed energy deposition additive manufacturing. Acta Mater. 87 (2015) 309–320.
8) C.J. Kong et al. High density Ti6Al4V via SLM processing: microstructure and mechanical properties. Int. Solid Freeform Fab. Symp. 36 (2011) 475–483.
9) Q. Jia et al. Selective laser melting additive manufacturing of Inconel 718 superalloy parts: Densification, microstructure and properties. J. Alloy Compd. 585 (2014) 713–721.
10) A.B. Spierings et al. Comparison of density measurement techniques for additive manufactured metallic parts. Rapid Prototyping J. 17 (2011) 380–386.
11) M.A. Taha et al. On selective laser melting of ultra high carbon steel: Effect of scan speed and post heat treatment. Mat.-wiss.u. Werkstofftech. 43 (2012) 913–923.
12) A. Mertens et al. Microstructures and mechanical properties of stainless steel AISI 316L processed by selective laser melting. Mater. Sci. Forum. 783-786 (2014) 898–903.
13) W. Di et al. Study on energy input and its influences on singletrack, multi-track, and multi-layer in SLM. Int. J Adv. Manuf. Technol. 58 (2012) 1189-99.
14) K. Darvish et al. Reducing lack of fusion during selective laser melting of CoCrMo alloy: Effect of laser power on geometrical features of tracks. Mater. Des. 112 (2016) 357–66.
15) C. Qiu et al. On the role of melt flow into the surface structure and porosity development during selective laser melting. Acta Mater. 96 (2015) 72–79.
16) N.T. Aboulkhair et al. Reducing porosity in AlSi10Mg parts processed by selective laser melting. Additive Manuf. 1 (2014) 77–86.
17) M. Tang et al. Prediction of lack-of-fusion porosity for powder bed fusion. Additive Manuf. 14 (2017) 39–48.
18) H. Gong et al. Analysis of defect generation in Ti–6Al–4V parts made using powder bed fusion additive manufacturing processes. Additive Manuf. 1 (2014) 87–98.

Chapter 6

PRINTABILITY IN AM

In the practice of welding, the widely used database of weldability [1] indicates if a welding process is recommended, difficult or cannot be easily undertaken for a given alloy. In the field of 3D printing, a similar concept of printability is still developing and currently there is no universally accepted definition for this term [2]. In this chapter, the word printability is used to mean the ability of an alloy-AM process combination to resist common AM defects such as residual stresses and distortion, composition change due to evaporative losses and lack of fusion defects. Three commonly used AM processes, DED-GMA, DED-L and PBF-L are operated using a wide variety of heat source power, scanning speed, layer thickness and mass deposition rate. Based on the literature data [3-17] on printing of SS 316, Figure 6.1 (a) shows that the arc power in DED-GMA can be 5 to 10 times higher than that of the laser in DED-L and PBF-L. In contrast, the scanning speed in PBF-L can be 80-100 times faster than the other two processes. From Figure 6.1 (b), it is evident that the faster deposition rate in DED-GMA is contributed by depositing layers of higher thicknesses, often 2 to 3 times thicker than that in DED-L. The PBF-L components are printed with thin layers that are 10-50 times thinner than those used in DED-L and DED-GMA. These wide variations in processing conditions are responsible for varying ability to resist defects for the same alloy printed using different AM processes. In addition, different alloys have distinct ability to resist defects for same AM process and process conditions due to the differences in their thermo-physical properties. In this chapter, printability of different alloys is evaluated while printing them using the same AM process, DED-L and process conditions. In addition, printability of a particular alloy, SS 316 is evaluated while printing it using three AM processes, DED-L, DED-GMA and PBF-L. The calculations of residual stresses and distortion, composition change and lack of fusion defects are done as described in the previous chapters of this thesis.

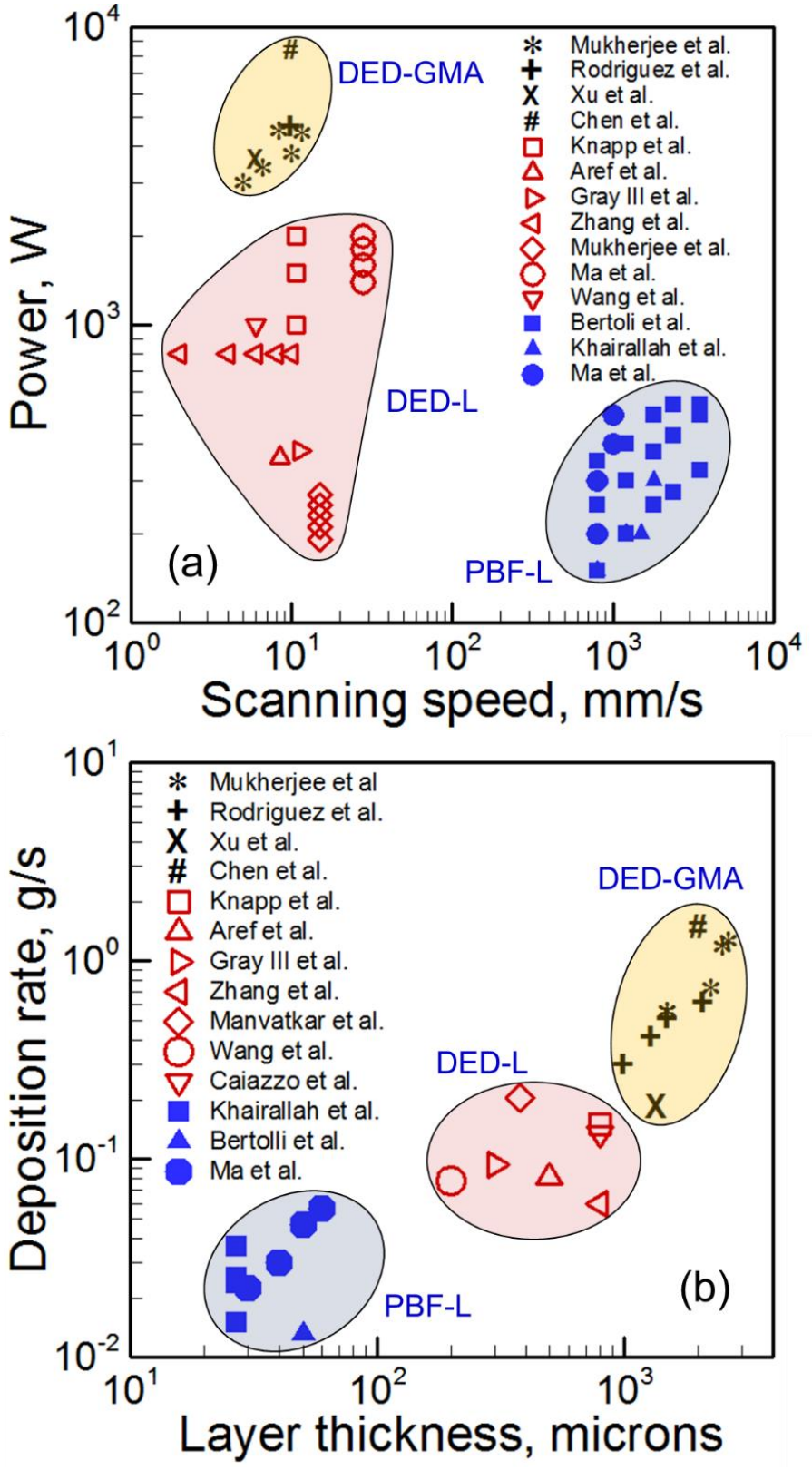

Figure 6.1. Variations of (a) heat source power and scanning speed and (b) mass deposition rate and layer thickness for PBF-L, DED-L and DED-GMA processes for stainless steel 316. The data are taken from the literature [3-17]. The curved lines for each process show regions that contain all data points.

6.1 Printability of different alloys for a particular AM process

In this section, printability of various AM alloys is evaluated during their deposition using DED-L. Figure 6.2 compares the distribution of the residual stress components along x, y and z directions at the end of the cooling of 2nd layer of IN 718 and Ti-6Al-4V deposits using DED-L. All three residual stress components are highly non-uniform, as expected. The residual stresses in the substrate are mostly compressive. There also exists a sharp gradient of stresses at the substrate-deposit interface. For both alloys the longitudinal stress (x-direction) reaches the maximum at the mid-length of the deposit and exhibits a sharp decrease toward both ends (free surfaces). A high gradient in through-thickness residual stress (z-direction) at substrate-deposit interface can potentially cause the separation of the component from the substrate (i.e., delamination). The yield strength of Ti-6Al-4V at room temperature is much higher than that of IN 718 which is consistent with the residual stresses that are also higher for Ti-6Al-4V as shown in Figure 6.2.

The strain parameter, as described in Chapter 5 of this thesis, provides a usable scale to estimate and compare the maximum thermal strain in laser-based AM for different alloys. A relatively high value of strain parameter signifies more thermal distortion and a lower printability of the corresponding alloy. Figure 6.3 shows that increasing the number of layers increases thermal strain. This is caused by lower heat conduction from the molten pool into the substrate resulting in higher temperature difference. Thermal strain is the highest for Ti-6Al-4V, which can be attributed to its relatively low density and thermal diffusivity. The ranking of the alloys in Figure 6.3 provides a relative scale of their printability considering their susceptibility to distortion. For alloys that are highly susceptible, appropriate AM variables like power, layer thickness and scanning speed need to be adjusted to reduce the distortion.

Figure 6.4 shows the effect of the laser scanning speed on the calculated strain parameter for PBF-L. Faster scanning speed results in smaller molten pool, smaller volume shrinkage during solidification and reduced strain. Among the four alloys, the susceptibility to thermal distortion is highest for AlSi10Mg due to the largest pool volume under the same processing conditions. Although Ti-6Al-4V exhibits bigger molten pool than SS 316, its volumetric thermal expansion co-efficient is about half of that for SS 316. Therefore, calculated strain values of Ti-6Al-4V and SS 316 build are almost the same. SS 316 and IN 718 builds exhibit nearly the same strain due to their similar thermo-physical and mechanical properties.

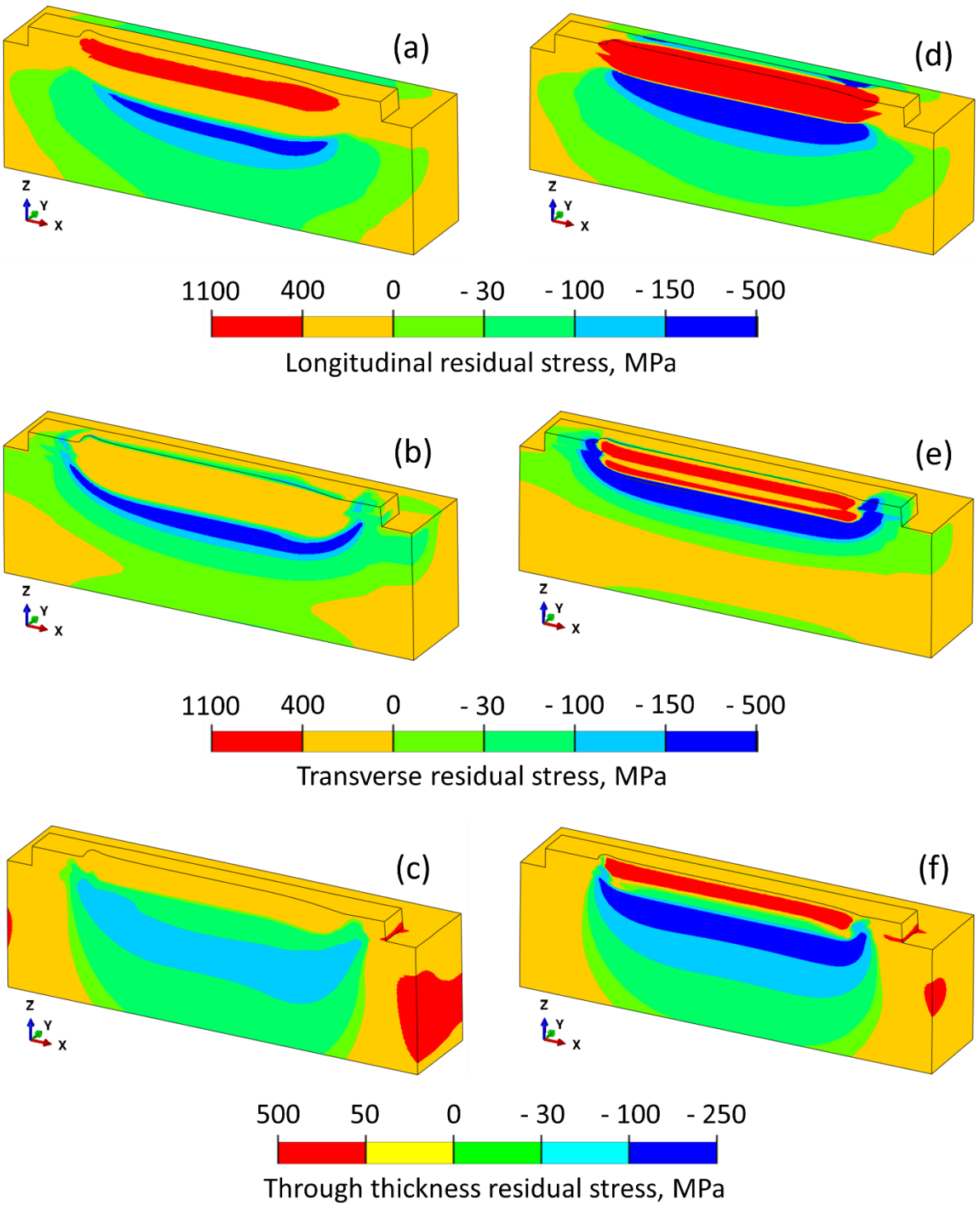

Figure 6.2. Residual stress distribution for IN 718 (a) longitudinal (b) transverse and (c) through-thickness components, and for Ti-6Al-4V (d) longitudinal (e) transverse and (f) through-thickness components of the 2 layers DED-L deposits. Laser beam scanning direction is along the positive x-axis. Half of the solution domain is shown because of the symmetry with respect to XZ plane. The simulations are done for 250 W laser power, 15 mm/s scanning speed, 0.5 mm beam radius, 4 mm substrate thickness and 0.416 g/s powder mass flow rate. Deformation is magnified by 10x.

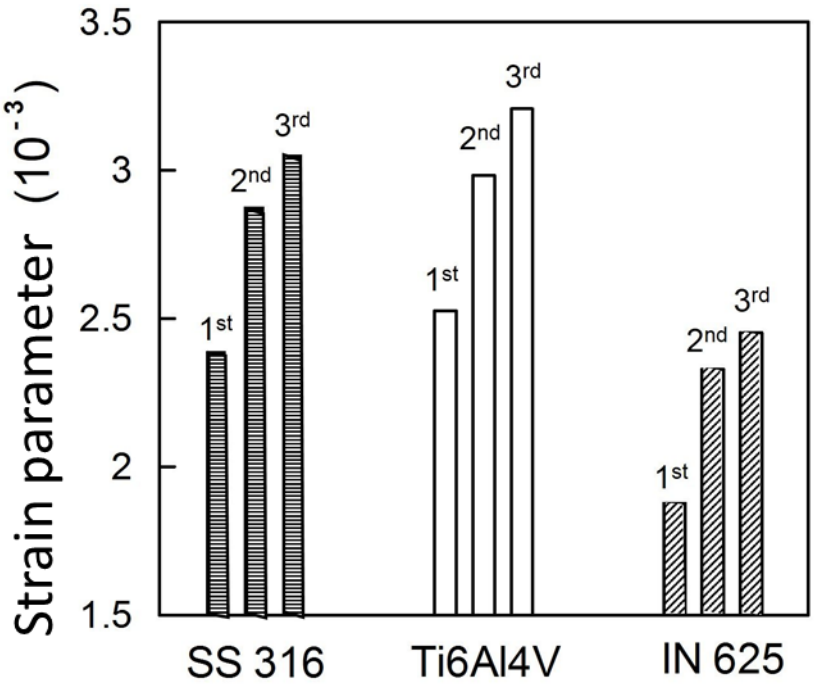

Figure 6.3. Values of the strain parameter in DED-L of single-track, three-layers depositions of SS 316, Ti6Al4V and IN 625. In the figure, 1st, 2nd and 3rd correspond to 1st, 2nd and 3rd layers respectively. The simulations are done for 190 W laser power, 12.5 mm/s scanning speed, 0.5 mm beam radius, 4 mm substrate thickness and 0.416 g/s powder mass flow rate.

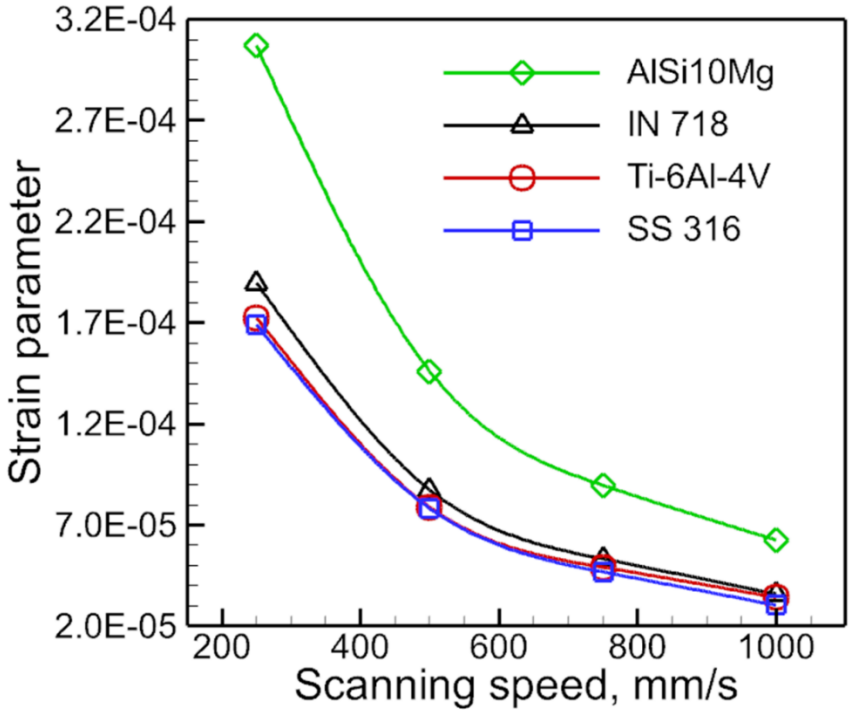

Figure 6.4. Variation of the strain parameter with scanning speed in PBF-L during the fabrication of 1st layer 1st hatch of builds of four alloys. The simulations are done for 60 W laser power, 0.05 mm beam radius, 30 microns layer thickness, 90 microns hatch spacing and 50% packing efficiency.

Figure 6.5 compares the susceptibility of commonly used AM alloys to composition change while printing using DED-L. The figure shows the most volatile alloying elements to be manganese in 2.25Cr-1Mo steel, Alloy 800H and SS 316, chromium in IN 625, and aluminum in Ti-6Al-4V. Figure 6.5 shows that Ti-6Al-4V is the most susceptible and IN 625 is the least susceptible to change in composition, respectively. For alloys highly susceptible to composition change, care should be taken to adjust appropriate AM variables such as laser power density and scanning speed to reduce loss of volatile alloying elements.

As described in Chapter 5 of this thesis, susceptibility to lack of fusion defect for single hatch, multi-layer builds can be quantified by the ratio of molten pool penetration depth (d) to layer thickness (h). Figure 6.6 shows that for a given heat input, Ti-6Al-4V has the highest value of the ratio while SS 316 has the lowest. This is primarily attributed to the largest molten pool of Ti-6Al-4V because it has the lowest density of the four alloys. Therefore, Ti-6Al-4V and SS 316 are the least and most susceptible to lack of fusion defects, respectively, among the four alloys considered. For alloys that are highly susceptible to lack of fusion defects, AM variables like laser power, scanning speed and powder feed rate should be appropriately adjusted to attain an adequate depth of penetration.

For multi-layer, multi-hatch deposits, lack of fusion depends on the extent of overlap between neighboring tracks. Figures 6.7 (a-c) show the computed shapes and sizes of the molten pool transverse sections (YZ plane) for different hatches and layers of five hatches, three layers, PBF-L builds of SS 316, Ti-6Al-4V and AlSi10Mg, respectively. For the SS 316 and Ti-6Al-4V builds, unmelted regions between the molten pools indicating improper fusional bonding among layers and hatches represent the lack of fusion voids. For the same processing conditions, molten pools in the AlSi10Mg build are the largest due to its lowest density. Therefore, AlSi10Mg does not exhibit any lack of fusion voids at the processing condition considered. Figure 6.8 shows the effect of hatch spacing on the lack of fusion voids. The percentage of lack of fusion voids is calculated as a ratio of area in the unmelted region to the total area of cross section of the build expressed in percentage. Higher hatch spacing results in improper fusional bonding between two successive hatches and increases the amount of lack of fusion voids. Among the four alloys, SS 316 exhibits the smallest molten pool. Therefore, under same processing conditions, SS 316 requires the smallest hatch spacing to prevent lack of fusion defect as shown in the figure.

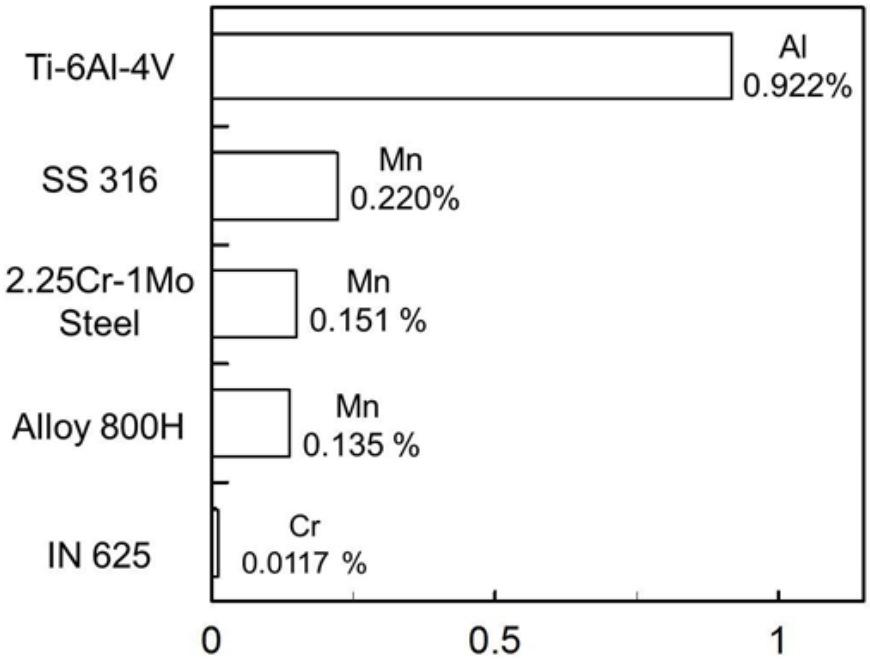

Figure 6.5. Calculated composition change in wt% of the most volatile elements due to vaporization for five alloys during DED-L. The simulations are done for 1000 W laser power, 12.5 mm/s scanning speed, 0.5 mm beam radius, 4 mm substrate thickness and 0.416 g/s powder mass flow rate.

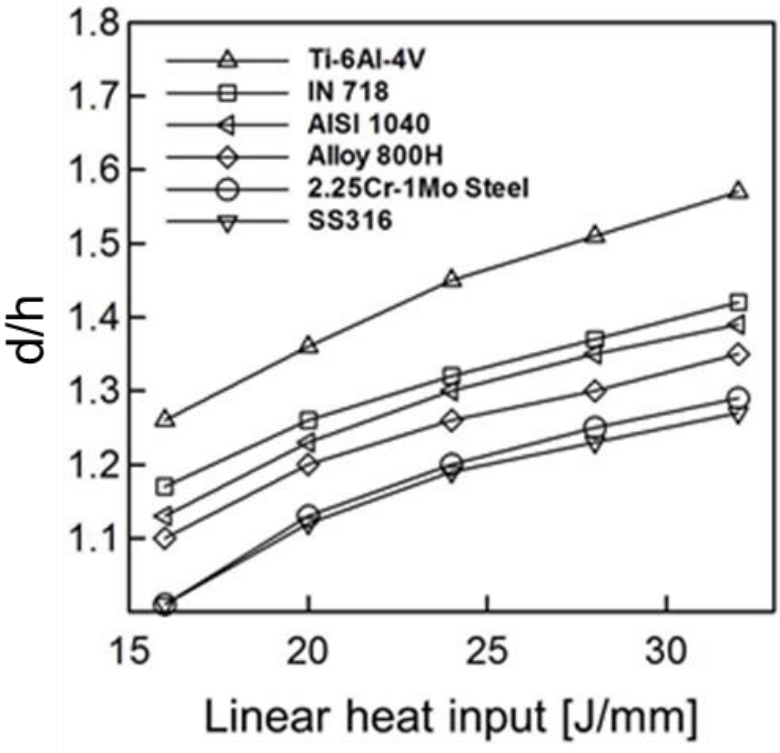

Figure 6.6. Correlation between the ratio of penetration depth (d) to layer thickness (h) to linear heat input for six different alloys with a constant layer thickness of 0.38mm. The results are for DED-L process using 160-330 W laser power, 10 mm/s scanning speed, 0.5 mm beam radius, 4 mm substrate thickness and 0.416 g/s powder mass flow rate.

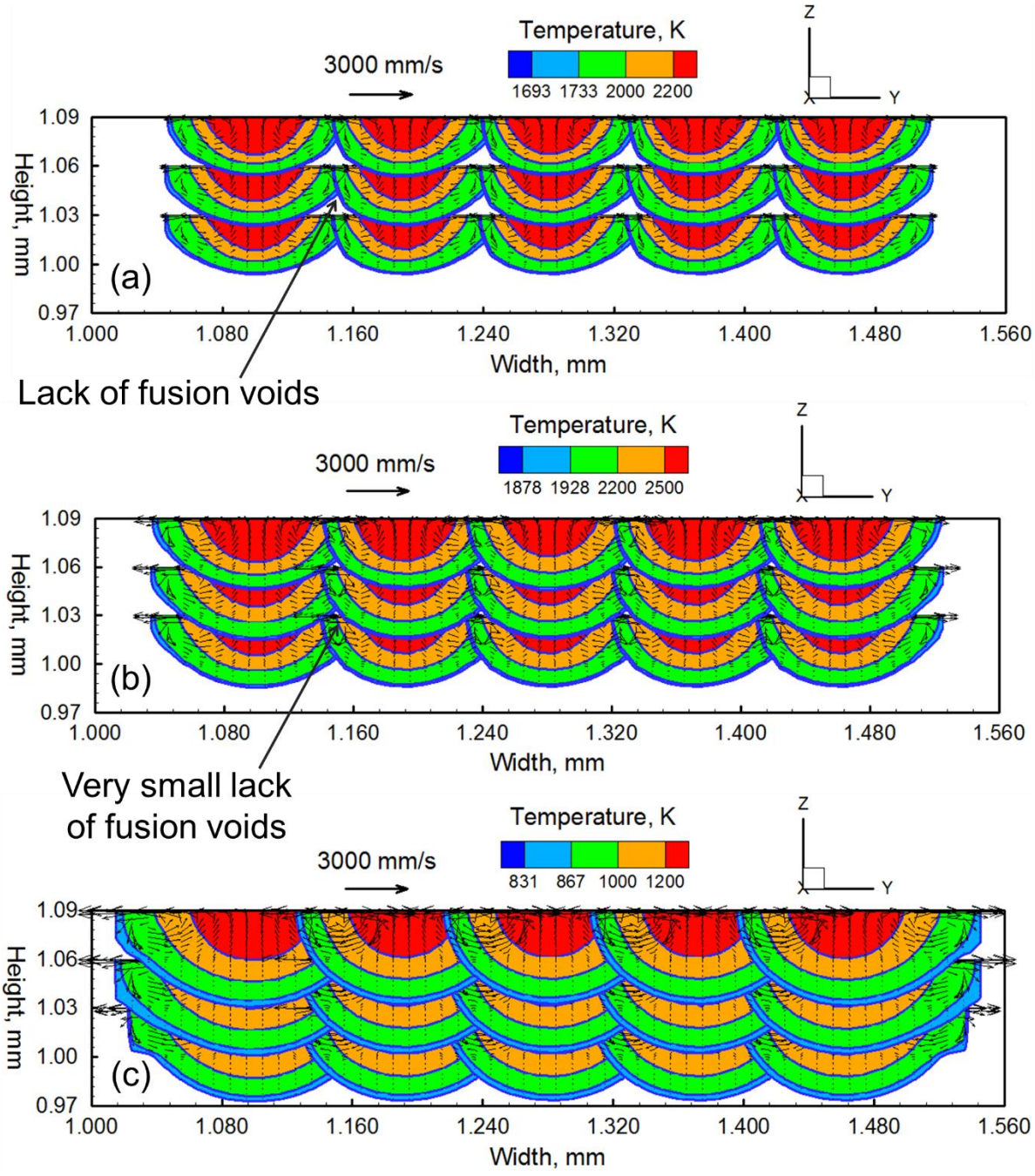

Figure 6.7. Transverse sectional view of the molten pools for 3 layers 5 hatches PBF-L builds of (a) SS 316 (b) Ti-6Al-4V and (c) AlSi10Mg using 60 W laser power, 1000 mm/s scanning speed, 0.05 mm beam radius, 30 microns layer thickness, 90 microns hatch spacing and 50% packing efficiency.

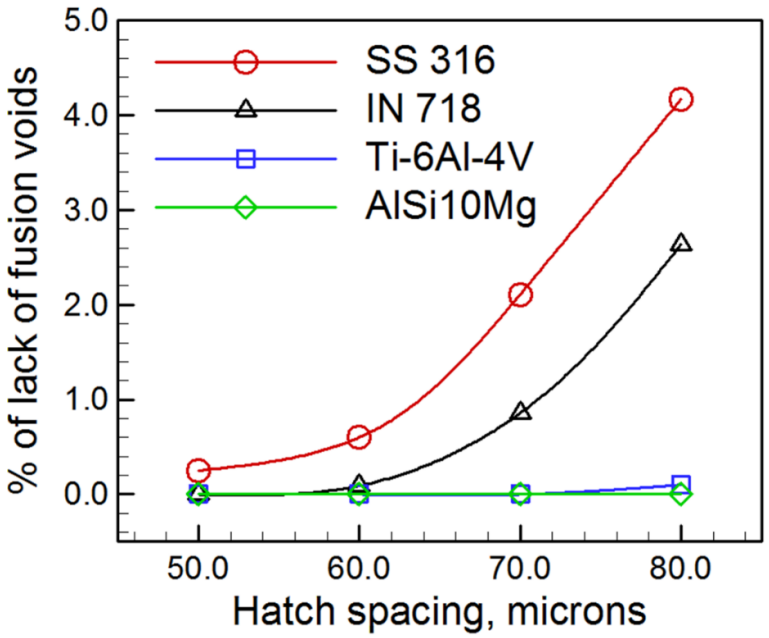

Figure 6.8. Variation of amount of lack of fusion voids with hatch spacing for 5 layers 5 hatches PBF-L build of 4 alloys 60 W laser power, 1000 mm/s scanning speed, 0.05 mm beam radius, 30 microns layer thickness and 50% packing efficiency.

6.2 Printability of different AM processes for a particular alloy

Printability of a particular alloy for different AM processes depends on the diversity in temperature fields and fusion zone geometries during those processes. For example, Figure 6.9 shows both the calculated and experimentally measured shape and size of the transverse (YZ plane) section of single track SS 316 builds printed using three processes [3, 4, 18]. The process parameters are provided in Table 6.1. The molten pool is bounded by the solidus temperature (1693 K). The shape and size of the curved surface of the DED-GMA deposit are determined by the combined effects of arc pressure, surface tension of the liquid metal and volume of the molten droplets. The impingement of the droplets also results in deep penetration in DED-GMA. However, in DED-L the curved pool surface is formed immediately under the laser beam due to the addition of powder particles. In contrast, the top surface of the PBF-L build is flat because of the addition of thin layers of powders during printing. The linear heat input (power/speed) in PBF-L is the lowest of the three processes, of the order of 0.1 J/mm, which results in very small pool whose length, width and depth are measured in micrometers. However, the linear heat inputs in DED-L and DED-GMA are in the order of 10 J/mm and 100 J/mm, respectively. Therefore, the molten pool dimensions in DED-GMA are larger than those in DED-L. Figure 6.9 shows that the pool dimensions in PBF-L are approximately 10% of DED-GMA and 30% of DED-L.

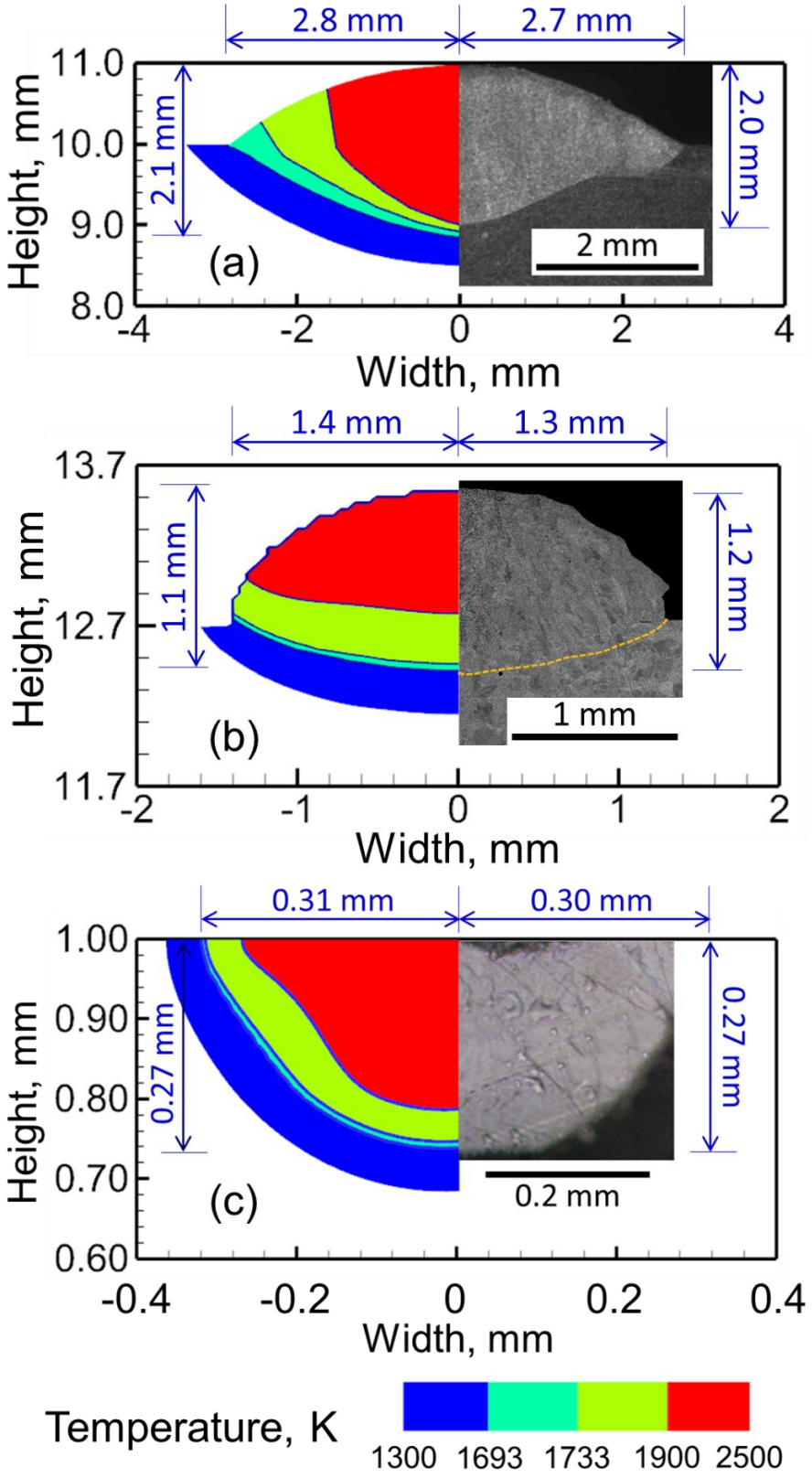

Figure 6.9. Comparison between the calculated transverse sections of SS 316 deposits with the corresponding experimental results [3, 4, 18] for (a) DED-GMA, (b) DED-L and (c) PBF-L. The width and depth of the deposits are provided to clearly indicate the size differences. Process parameters are provided in Table 6.1.

Table 6.1. Process parameters for evaluating printability of SS 316 for three AM processes.

Process parameters	DED-GMA [3]	DED-L [4]	PBF-L [18]
Laser power, W		1500	110
Arc current, A	150		
Arc voltage, V	14.2		
Heat source power, W	2130	1500	110
Scanning speed, mm/s	10	10.6	100
Layer thickness, mm	1.0	0.8	0.25
Wire radius, mm	0.5		
Wire feed rate, m/min	8.0		
Catchment efficiency		0.3	
Deposition rate, g/s	0.5	0.2	
Heat source radius, mm	4.0	2.0	0.3
Substrate thickness, mm	10.0	12.7	0.75

Figures 6.10 (a-c) show the computed longitudinal stress (x-component, σ_{xx} i.e. along the scanning direction) distribution in the SS 316 components printed using the three processes. The wall printed using DED-GMA is the widest because of the biggest molten pool of this process. In addition, DED-GMA components are printed using the thickest layers among the three processes. Thick and wide tracks accumulate high residual stresses during cooling and makes the DED-GMA component the most vulnerable to residual stresses among the three printing processes as shown in Figure 6.10 (a-c). Because of the tiny molten pool and thinnest layers in PBF-L, the component printed using this process accumulates the least residual stresses as shown in Figure 6.10 (c). Similar trend in longitudinal stresses can also be observed at different transverse sections (YZ planes) along the length of the deposit as shown in Figure 6.11. The three processes have the same hierarchy in the susceptibility to the through-thickness (σ_{zz} i.e. along z-direction) residual stress and the corresponding results are provided in Figure 6.12. Figure 6.13 compares the vertical deformation while depositing the SS 316 deposits printed using the three processes. The molten pool in DED-GMA is significantly larger than those for DED-L and PBF-L respectively. Shrinkage of large pools during solidification makes the DED-GMA components the most susceptible to distortion among the three printing processes.

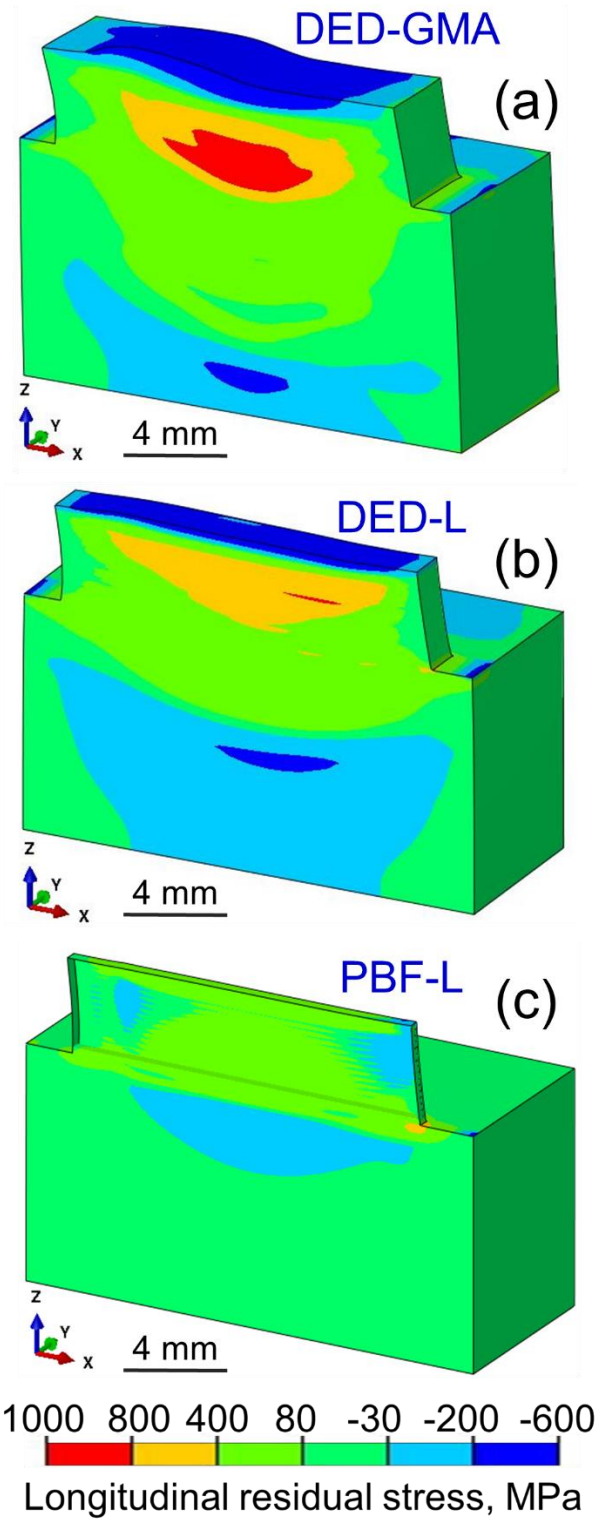

Figure 6.10. Longitudinal residual stress distribution in a SS 316 deposit printed using (a) DED-GMA (b) DED-L and (c) PBF-L. The process conditions are given in Table 6.1. For consistency, all parts are16 mm long, 4 mm high and built on a 20 mm long, 10 mm wide and 10 mm thick substrate. The three parts are printed using 4, 5 and 16 layers for DED-GMA, DED-L and PBF-L, respectively due to the difference in the layer thicknesses of these processes. The scanning direction is along the positive x-axis. Half of the solution domain is shown because of the symmetry with respect to XZ plane.

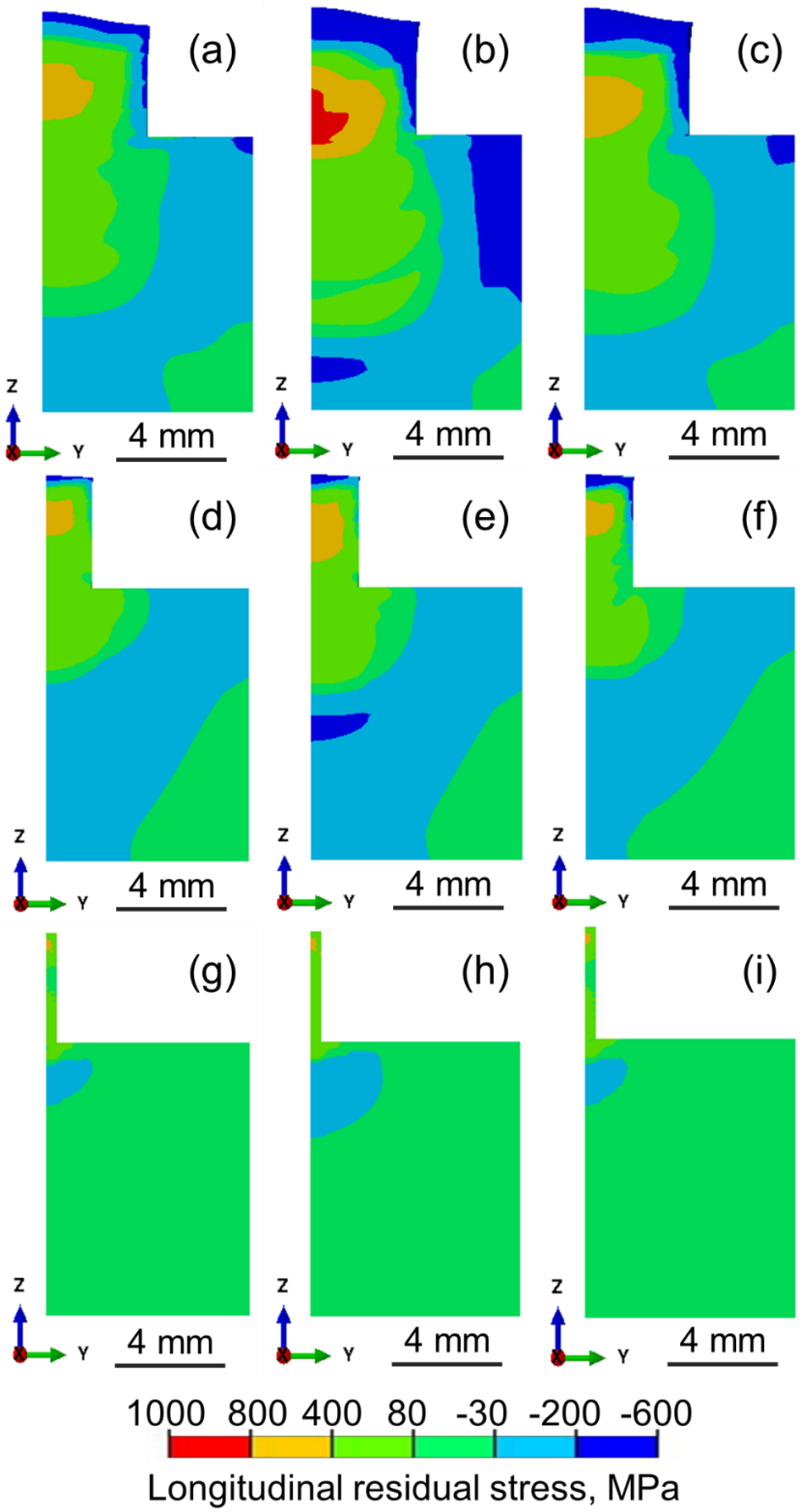

Figure 6.11. Longitudinal residual stress (σ_{xx}) distribution on the transverse planes (YZ) in SS 316 deposits printed using (a-c) DED-GMA (d-f) DED-L and (g-i) PBF-L. Figures (a,d,g), (b,e,h) and (c,f,i) are at x = 6 mm, 10 mm and 14 mm respectively. The process conditions are given in Table 6.1. For consistency, all parts are 16 mm long, 4 mm high and built on a 20 mm long, 10 mm thick substrate. Half of the solution domain is considered because of the symmetry with respect to XZ plane.

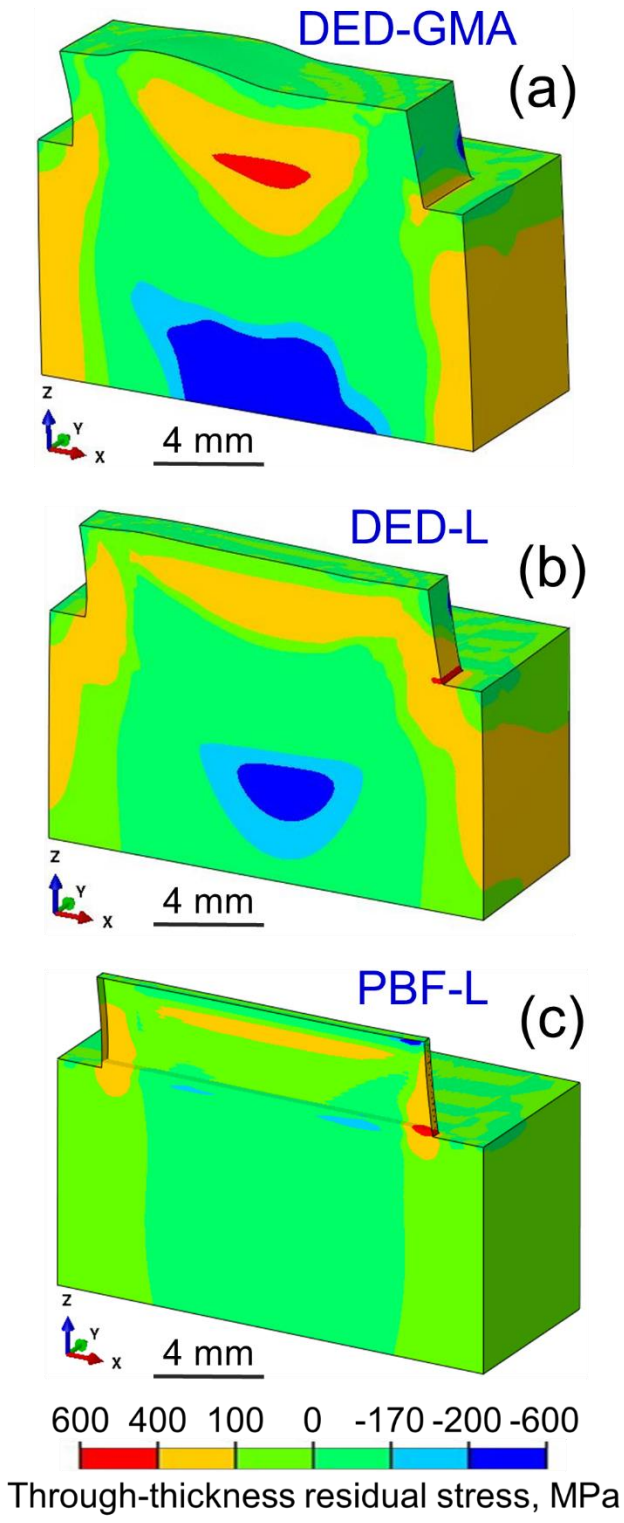

Figure 6.12. Through-thickness residual stress distribution in a SS 316 deposit printed using (a) DED-GMA (b) DED-L and (c) PBF-L. The process conditions are given in Table 6.1. For consistency, all parts are16 mm long, 4 mm high and built on a 20 mm long, 10 mm wide and 10 mm thick substrate. The three parts are printed using 4, 5 and 16 layers for DED-GMA, DED-L and PBF-L, respectively due to the difference in the layer thicknesses of these processes. The scanning direction is along the positive x-axis. Half of the solution domain is shown because of the symmetry with respect to XZ plane.

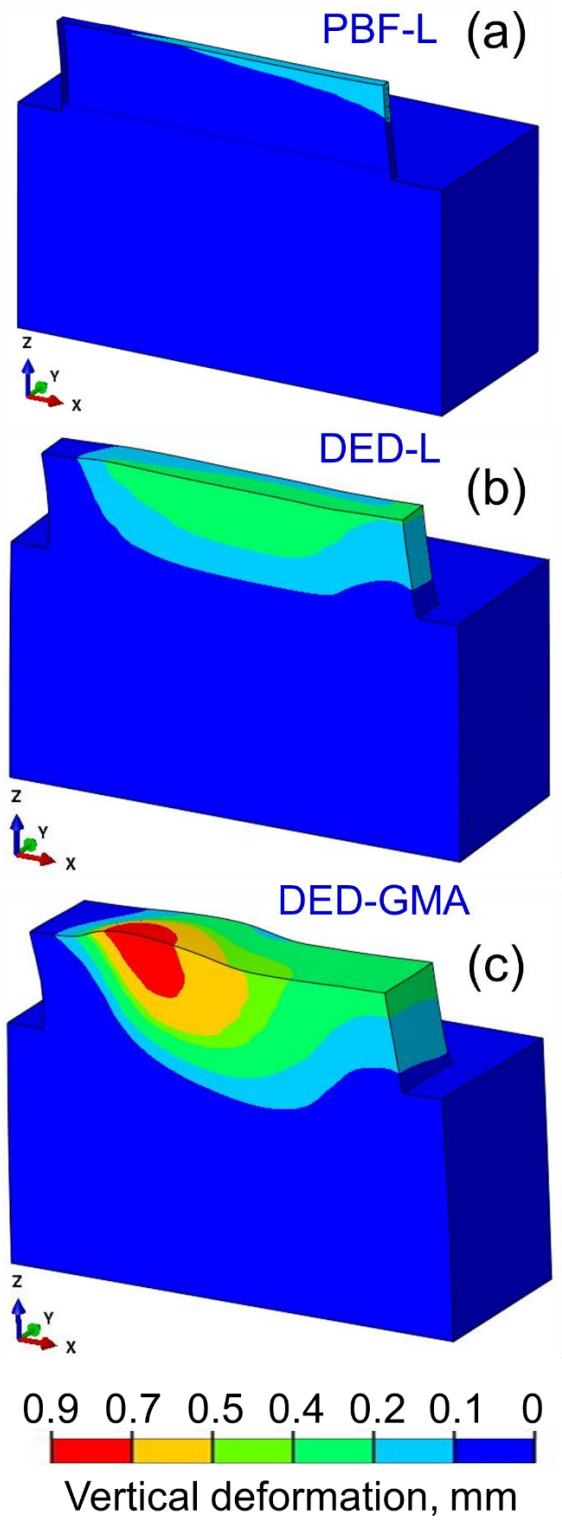

Figure 6.13. Vertical deformation distribution in a SS 316 deposit printed using (a) PBF-L (b) DED-L and (c) DED-GMA. The process conditions are given in Table 6.1. For consistency, all parts are16 mm long, 4 mm high and built on a 20 mm long, 10 mm wide and 10 mm thick substrate. The three parts are printed using 4, 5 and 16 layers for DED-GMA, DED-L and PBF-L, respectively due to the difference in the layer thicknesses of these processes. The scanning direction is along the positive x-axis. Half of the solution domain is shown because of the symmetry with respect to XZ plane.

Accumulation of high residual stresses along the substrate deposit interface may result in detachment of the part from the substrate [2]. In Figure 6.14 (a), the computed longitudinal residual stresses along the substrate deposit interface (AB) for the SS 316 components printed using three processes are compared. Cooling of the largest fusion zone in DED-GMA results in the accumulation of high tensile stress along the substrate deposit interface as shown in Figure 6.14 (a). In contrast, the components printed using PBF-L accumulate the least residual stresses along the substrate deposit interface because it has the smallest fusion zone of the three printing processes.

To provide a quantitative scale for evaluating the relative susceptibilities of DED-GMA, DED-L and PBF-L to distortion, Figure 6.14 (b) compares the values of strain parameter which is a measure of distortion while depositing the 1st layer of SS 316 deposits printed using the three processes. The figure also shows that the molten pool in DED-GMA is significantly larger than those for DED-L and PBF-L respectively. Shrinkage of large pools during solidification makes the DED-GMA components the most susceptible to distortion among the three printing processes.

As discussed in the previous chapter, manganese is the most susceptible element for vaporization among all constituting elements of SS 316. Figure 6.15 (a) compares the percentage change in manganese in single track SS 316 deposits printed using the three processes. Susceptibilities to composition change depends on both the vaporization rate and the ratio of the top surface area to volume of the fusion zone. The amount of mass loss due to evaporation is proportional to the surface area of the fusion zone. However, loss of alloying elements from a smaller molten pool results in a more pronounced change in composition. Because of the smallest volume of molten pool in PBF-L among the three processes, the value of the ratio is significantly higher than those for DED-L and DED-GMA. As a result, PBF-L components are more susceptible to composition change than the other two processes as shown in Figure 6.15 (a). Figure 6.15 (b) also indicates that the SS 316 component printed using PBF-L is the most susceptible to composition change for a wide range of linear heat input among all three printing processes.

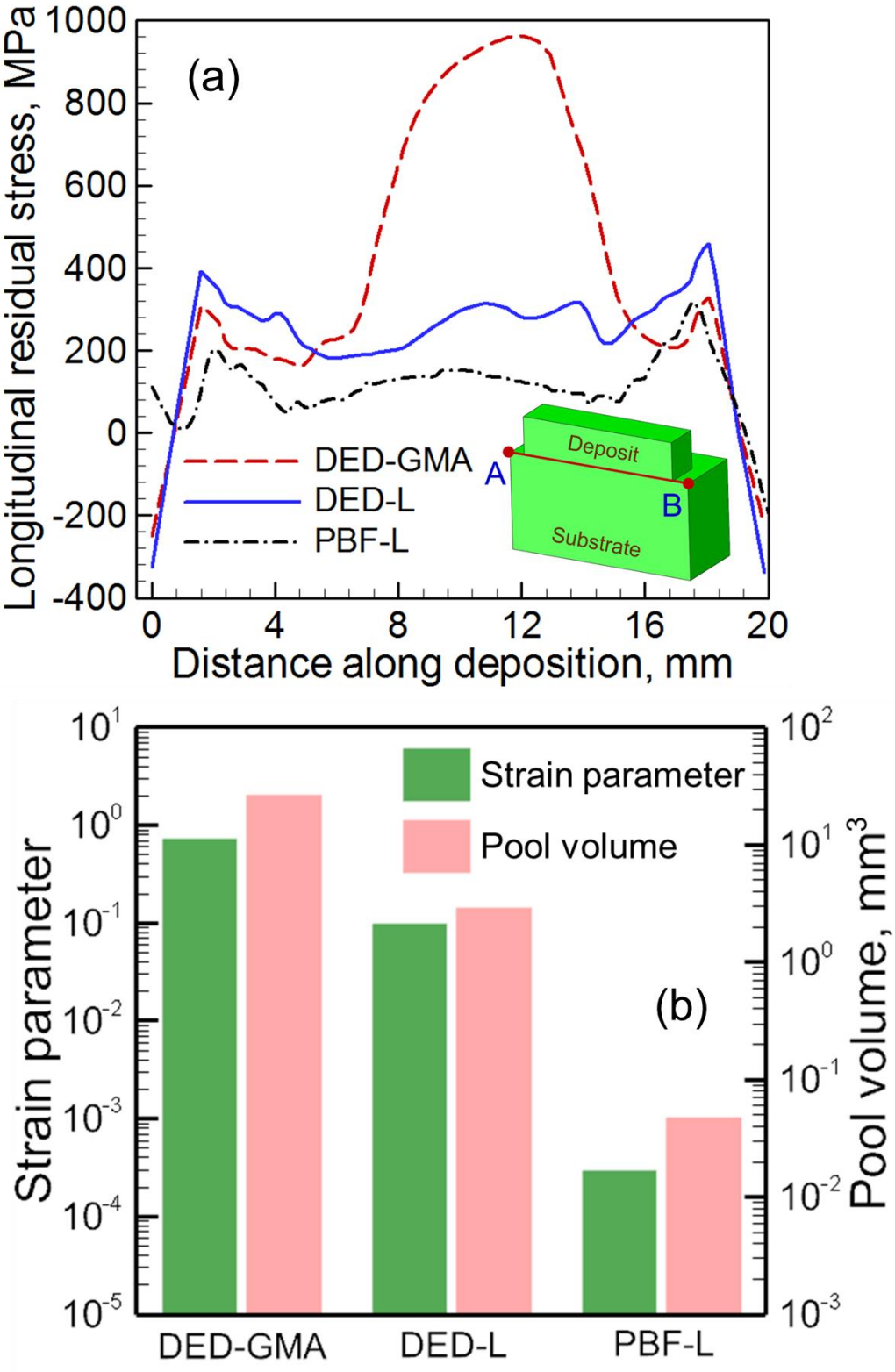

Figure 6.14. (a) Longitudinal residual stress distribution for DED-GMA, DED-L and PBF-L along substrate-deposit interface (AB, where A = 0 mm and B = 20 mm). (b) Strain parameters and maximum pool volume while depositing the 1st layer of SS 316 deposits using the three printing techniques. The process conditions are given in Table 6.1. Same substrate dimensions (20 mm long, 10 mm wide, 10 mm thick) are taken for all three cases for consistency.

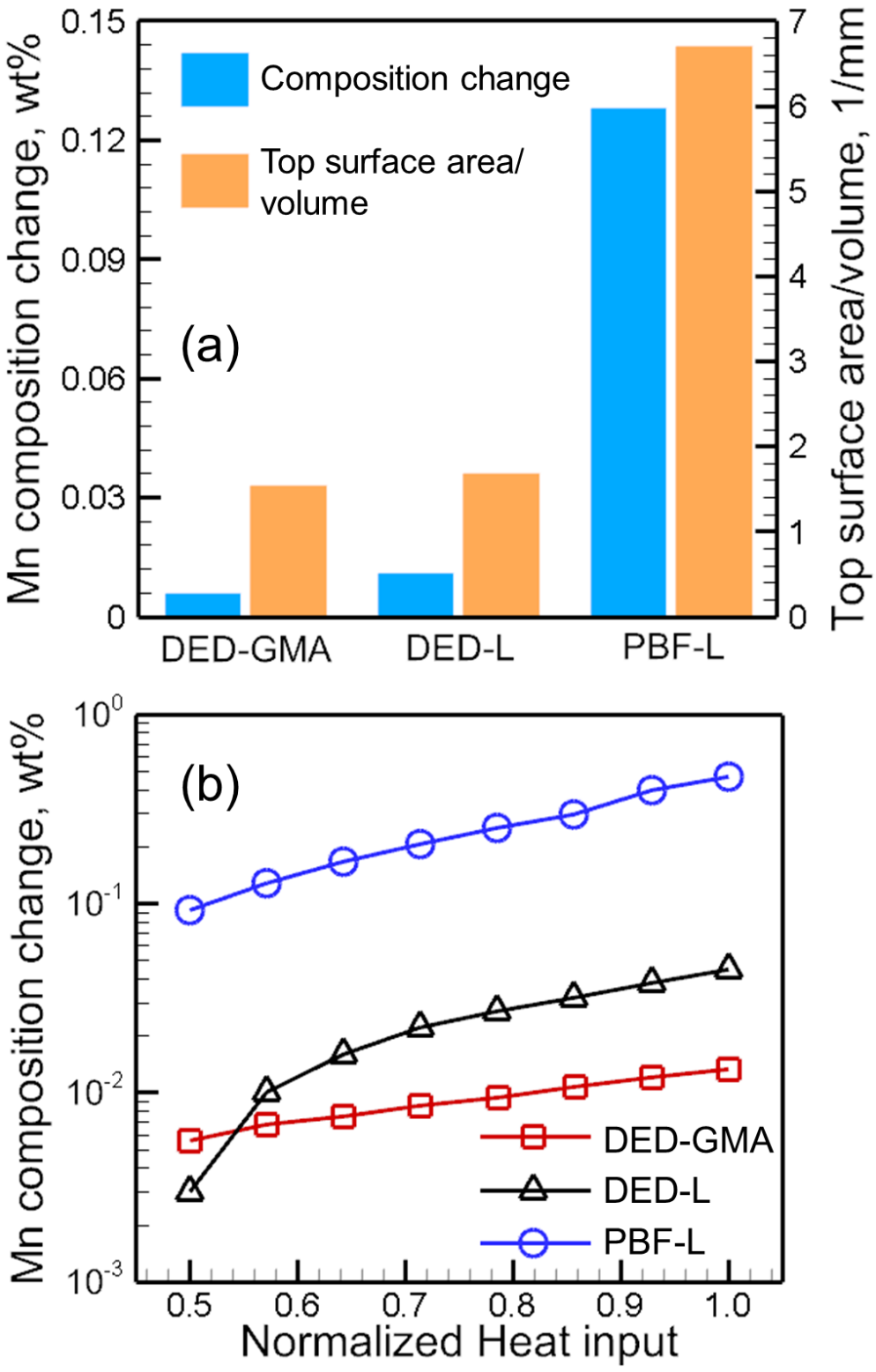

Figure 6.15. (a) Calculated change in manganese composition and the ratio of the top surface area to volume of the fusion zone for a single track SS 316 component printed using three printing techniques. (b) Variations in manganese composition of SS 316 builds printed using the three techniques. The normalized heat input refers to the ratio of heat input to the maximum heat input for the printing process. In both figures (a) and (b) composition change refers to reduction in its concentration. The process conditions are given in Table 6.1.

In order for a deposited layer to bond properly with a previously deposited layer, the depth of the molten pool should exceed the layer thickness considerably. Therefore, the higher the value of the ratio of depth of penetration to the layer thickness, the better the fusional bonding between the layers. Figure 6.16 evaluates the relative susceptibilities to lack of fusion defects of the three printing processes by comparing the corresponding values of the ratio of the pool depth to layer thickness. For all three processes, pool depth increases with the heat input and ensures better fusional bonding among layers. However, deep penetration of the molten pool in the DED-GMA due to the impingement of molten droplets makes this process the least susceptible to lack of fusion defect.

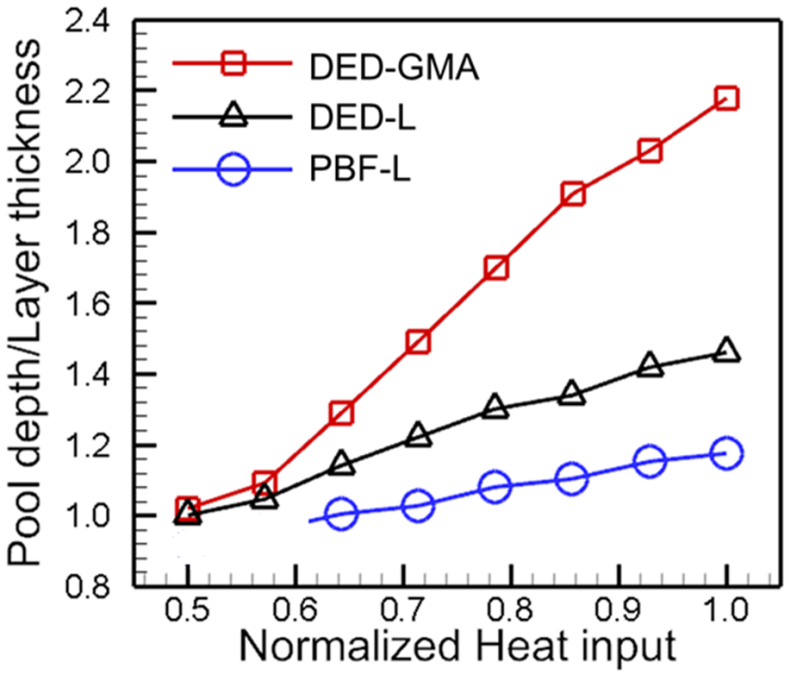

Figure 6.16. Variations in pool depth to layer thickness ratio (an indicator of lack of fusion defect) of single hatch SS 316 builds printed using three AM techniques. All process variables are presented in Table 6.1.

6.3 Summary and conclusions

Printability is defined by the ability of an alloy to resist common defects in AM, residual stresses, distortion, composition change due to evaporative losses and lack of fusion defects. Printability of several commonly used AM alloys for DED-L are evaluated. In addition, printability of stainless steel 316 for DED-L, DED-GMA and PBF-L has been quantitatively examined. The calculations of residual stresses and distortion, composition change and lack of fusion defects are presented in the previous chapters of this thesis. Below are the specific findings.

(1) High deposition rate of DED-GMA allows fabrication of components using thicker layers than DED-L and PBF-L. Deposition of thick layers results in accumulation of the highest residual stresses in DED-GMA components among the three processes. For example, the longitudinal residual stress in DED-GMA component can be around 6 times higher than that in PBF-L component that is printed with layers 4 times thinner than that for DED-GMA using the process conditions considered here.

(2) Rapid scanning speed of PBF-L results in a molten pool that has higher liquid pool free surface to volume ratio than those for DED-L and DED-GMA. Therefore, more materials vaporize per unit volume of the molten pool and make PBF-L components the most susceptible to composition change. Depending on the processing conditions, percentage change in the manganese content in SS 316 component printed using PBF-L can be significantly higher than those in DED-L and DED-GMA components.

(3) Deep penetration of the molten pool in DED-GMA due to the droplet impingement ensures sound bonding with the previously deposited layers. Therefore, DED-GMA components are the least vulnerable to the lack of fusion defect among the components made by the three printing processes.

(4) The typical molten pool size in DED-GMA is significantly larger than those for DED-L and PBF-L. Larger molten pool shrinks more during solidification and makes the DED-GMA component vulnerable to thermal distortion. Therefore, DED-GMA components have the most susceptibility to distortion among the three printing processes considered here.

(5) Ti-6Al-4V is most susceptible to distortion and composition change compared to IN 625 and SS 316 during DED-L under the same processing conditions. However, during DED-L, Ti-6Al-4V exhibits a bigger molten pool than IN 6125 and SS 316 and thus is less susceptible to lack of fusion defects for the same processing conditions.

6.4 References

1) J.C. Lippold. Welding metallurgy and weldability. Hoboken (NJ), Wiley (2014).
2) T. DebRoy et al. Additive manufacturing of metallic components - Process, structure and properties. Prog. Mater. Sci. 92 (2018) 112-224.
3) N. Rodriguez et al. Wire and arc additive manufacturing: a comparison between CMT and TopTIG processes applied to stainless steel. Weld World. 62 (2018) 1083-96.
4) G.L. Knapp et al. Building blocks for a digital twin of additive manufacturing. Acta Mater. 135 (2017) 390-399.

5) T. Mukherjee et al. Dimensionless numbers in additive manufacturing. J Appl. Phys. 121 (2017) 064904.
6) T. Mukherjee et al. A digital twin for rapid qualification of 3D printed metallic components. Appl. Mater. Today. 14 (2019) 59-65.
7) X. Xu et al. Morphologies, microstructures, and mechanical properties of samples produced using laser metal deposition with 316 L stainless steel wire. Optic. Laser. Eng. 94 (2017) 1-11.
8) X. Chen et al. Microstructure and mechanical properties of the austenitic stainless steel 316L fabricated by gas metal arc additive manufacturing. Mater. Sci. Eng. A. 703 (2017) 567-577.
9) Y. Aref Y, Shamsaei N, Thompson SM, Seely DW. Effects of process time interval and heat treatment on the mechanical and microstructural properties of direct laser deposited 316L stainless steel. Mater Sci Eng: A. 2015;644:171-183.
10) G.T. Gray III et al. Structure/property (constitutive and spallation response) of additively manufactured 316L stainless steel. Acta Mater. 138 (2017) 140-149.
11) K. Zhang et al. Characterization of stainless steel parts by laser metal deposition shaping. Mater. Des. 55 (2014) 104-119.
12) M. Ma et al. A comparison on metallurgical behaviors of 316L stainless steel by selective laser melting and laser cladding deposition. Mater. Sci. Eng. A. 685 (2017) 265-273.
13) X. Wang et al. Influences of pulse laser parameters on properties of AISI316L stainless steel thin-walled part by laser material deposition. Optic. Laser. Technol. 92 (2017) 5-14.
14) U.S. Bertoli et al. In-situ characterization of laser-powder interaction and cooling rates through high-speed imaging of powder bed fusion additive manufacturing. Mater. Des. 135 (2017) 385-396.
15) S.A. Khairallah et al. Laser powder-bed fusion additive manufacturing: Physics of complex melt flow and formation mechanisms of pores, spatter, and denudation zones. Acta Mater. 108 (2016) 36-45.
16) V. Manvatkar et al. Heat transfer and material flow during laser assisted multi-layer additive manufacturing. J Appl. Phys. 116 (2014) 124905.
17) F. Caiazzo et al. Laser-Aided Directed Energy Deposition of Steel Powder over Flat Surfaces and Edges. Materials. 11 (2018) 435.
18) A. Foroozmehr et al. Finite element simulation of selective laser melting process considering optical penetration depth of laser in powder bed. Mater. Des. 89 (2016) 255–263.

Chapter 7

CONCLUDING REMARKS

7.1 Summary

In this research, transport phenomena based modeling was used to provide better understanding of the formation of macroscopic defects, residual stresses, distortion, composition change due to evaporative losses and lack of fusion defects during AM of metallic materials. The investigation is carried out for three commonly used AM processes, direct energy deposition with laser (DED-L) and gas metal arc (DED-GMA) heat source and powder bed fusion with laser (PBF-L) source. Three-dimensional, transient heat transfer and fluid flow models for three AM processes, considering the process parameters and alloy properties are developed and used to calculate the fusion zone geometry, temperature and velocity fields. These models solve the equations of conservations of mass, momentum and energy in a solution domain consisting of the substrate, deposit, powder bed (in PBF) and shielding gas. The range of process variables for which calculations are performed is commonly used in practice and is adapted from the literature. Calculations are done for commonly used AM alloys such as stainless steel 316, titanium alloy Ti-6Al-4V, nickel-based superalloys and aluminum alloy AlSi10Mg.

The 3D, transient temperature field, estimated using the heat transfer and fluid flow model, is used to calculate residual stresses and distortion using a finite element based thermo-mechanical model. The thermo-mechanical model solves constitutive equations where the stresses are calculated from the increments in elastic, plastic and thermal strains. Composition change due to evaporative loss of alloying elements is calculated using a vaporization model based on the temperature field and molten pool dimensions. This model first calculates the vaporization flux based on molten pool top surface area, temperature distribution and partial pressure of the alloying elements. Then the net change in composition due to evaporative losses is estimated by mass balance. Since lack of fusion defects depend on the extent of overlap

between neighboring tracks, it is estimated from the calculated fusion zone geometry by the heat transfer and fluid flow model. Back of the envelope calculations are performed to deduce two novel dimensionless numbers to predict the susceptibilities to distortion and lack of fusion defects in real-time shop floor usage.

7.2 Major conclusions

Several important conclusions of this thesis research are summarized as follows.

(1) The residual stresses can be decreased significantly by reducing the thickness of each layer to fabricate the component. High deposition rate of DED-GMA allows fabrication of the component using thicker layers than DED-L and PBF-L. Deposition of thick layers results in accumulation of the highest residual stresses in DED-GMA components among the three processes. For example, the longitudinal residual stress in DED-GMA component of SS 316 can be around 6 times higher than that in PBF-L component of SS 316 that is printed with layers 4 times thinner than that for DED-GMA for the process conditions considered in this research. Apart from printing using thinner layers, increasing the heat input can also reduce the residual stresses. Higher heat input deforms the part which partially alleviate the residual stresses. However, the same condition enhances the thermal distortion significantly. Therefore, an appropriate heat input selected by trading off both distortion and residual stresses will be helpful to fabricate a dimensionally accurate part with good mechanical properties.

(2) A decrease in the heat source power and layer thickness can also result in higher Fourier number indicating low heat storage in the part and lower thermal strain. Alloys with lower heat capacity and higher thermal diffusivity will be susceptible to higher peak temperature, larger pool volume and higher thermal strain. The typical molten pool size in DED-GMA is significantly larger than those for DED-L and PBF-L for the commonly used process parameter range. Larger molten pool shrinks more during solidification and makes the DED-GMA component vulnerable to thermal distortion. Therefore, DED-GMA components have the most susceptibility to distortion among the three printing processes considered here.

(3) The longitudinal residual stresses exhibit a steep gradient at both ends of the deposit that make the parts susceptible to buckling and warping. The through-thickness stresses that are responsible for the possible delamination of a component change sharply at the substrate deposit interface. The residual stresses change from tensile to compressive at the layer

interfaces. In extreme cases, this behavior may result in the separation of layers. Additively manufactured Ti-6Al-4V components suffer higher residual stresses than IN 718 under the same processing conditions. However, IN 718 parts are more susceptible to warping, delamination and buckling because of their higher residual stress to yield strength ratio.

(4) For AM of SS 316, the alloying element that is the most susceptible for composition change is manganese. Rapid scanning speed of PBF-L results in a molten pool that has higher liquid pool free surface to volume ratio than those for DED-L and DED-GMA for commonly used process conditions. Therefore, more materials vaporize per unit volume of the molten pool and make PBF-L components the most susceptible to composition change. Depending on the processing conditions, percentage change in the manganese content in SS 316 component printed using PBF-L can be significantly higher than those in DED-L and DED-GMA parts.

(5) A large heat input per unit length obtained by reduction of scanning speed or an increase in laser power or both results is larger liquid pool that ensures good bonding among the neighboring tracks. Therefore, high heat input is beneficial for reducing lack of fusion defects. A high value of Marangoni number that indicates vigorous circulation of the liquid metal inside the molten pool correlated well with the reduction of the lack of fusion defects. High values of peak temperature also correlated well with the reduction of the occurrence of lack of fusion defects. Since the temperature can be monitored during deposition, this correlation can be used to reduce lack of fusion defects. Deep penetration of the molten pool in DED-GMA due to the droplet impingement ensures sound bonding with the previously deposited layers. Therefore, DED-GMA components are the least vulnerable to the lack of fusion defects among the three printing processes considered in this thesis research.

(6) Ti-6Al-4V is most susceptible to distortion and composition change during DED-L compared to IN 625 and SS 316 processed using the same conditions. However, during DED-L at the same processing conditions, Ti-6Al-4V exhibits a bigger molten pool than IN 6125 and SS 316 and thus is less susceptible to lack of fusion defects.

(7) Since, the mechanical properties of Ti-6Al-4V and 800H are significantly different, dissimilar joints between these two alloys exhibited sharp changes in residual stresses and strains at the interface between the two alloys. These sharp changes in residual stresses and strains have been proved to minimize by fabricating a graded joint using DED-L between these two alloys. Because of the similar mechanical properties of 2.25Cr-1Mo steel and 800H,

graded joints printed using DED-L between these two alloys provided relatively lower benefits for minimizing residual stresses and distortion compared to the dissimilar joints between them.

(8) Droplet impact force and arc pressure result in deep finger penetration under the arc during DED-GMA. The liquid metal depressed under the arc was displaced to the rear end of the molten pool and formed a crown shaped deposit. The resulting wide and deep deposits facilitate high deposition rates that make the DED-GMA process a practical choice for rapid production of large components at low cost. Higher heat input achieved by slow scanning or higher arc power resulted in larger deposits in DED-GMA. Use of thicker wire and rapid wire feeding also increased deposit size because of higher amount of material deposition under those conditions.

(9) A travelling fine grid-system developed in this thesis research is capable of providing good convergence, stability and accuracy of the computed transient three-dimensional temperature and velocity fields for large AM parts with high computational efficiency and limited memory requirement. For example, a 20 mm long SS 316 component fabricated using PBF-L with 5 layers and 5 hatches is simulated within about 5 hours where the conventional model without the traveling grid takes around 25 hours to simulate component of similar dimensions in an i7 PC with 8GB RAM.

7.3 Future work

During this doctoral thesis research, various areas were identified that require further investigation. These areas and probable research needed are described next.

7.3.1 Printability database for new alloys

Printability is the ability of a feedstock material to be successfully converted to components by a given AM process. A ranking of printability of different alloy-AM process combinations provides the relative outcomes of the quality of printed products considering the susceptibilities to common printing defects such as lack of fusion, compositional change, residual stresses and distortion for the narrow process conditions commonly considered. However, it does not characterize the printability of the alloys across all combinations of important process parameters. Therefore, currently, there is no generally available printability database for AM of alloys. Developing such a database will facilitate the selection of an appropriate printing process–alloy combination that can be helpful to reduce and, in some

cases, avoid common defects in metal printing of new AM alloys without extensive trial and error testing. Figure 7.1 provides an example where printability is defined by the susceptibilities to lack of fusion (LOF), keyhole pores (KEY), balling (BALL) over a wide range of laser power and scanning speed for PBF-L of a CoCrFeMnNi high entropy alloy [1]. However, this database is only for two process parameters, laser power and scanning speed. Similar database needs to be developed for other process parameters in various AM process-alloy combinations. Development of this database requires simulation of numerous cases and their experimental validations and thus is kept as a future work.

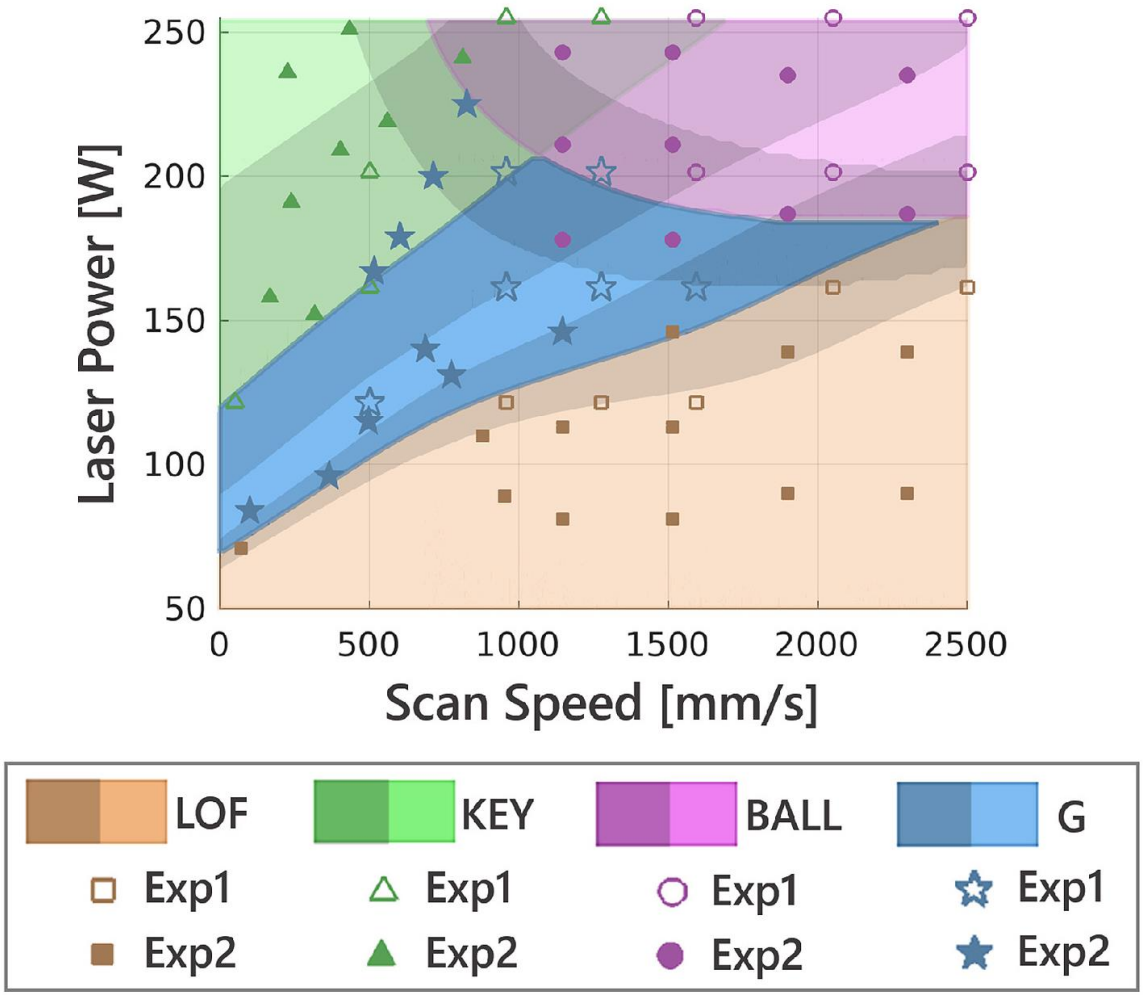

Figure 7.1. Printability database for a wide range of laser power and scanning speed during PBF-L of a CoCrFeMnNi high entropy alloy represented by the susceptibilities to lack of fusion (LOF), keyhole pores (KEY), balling (BALL). 'G' represents the defect free parts. Exp1 and Exp2 represent sets of experiments corresponding to two different substrates. The figure is adapted from Johnson et al. [1].

7.3.2 Machine learning to find hierarchy of important factors

In this research, a better understanding of macroscopic defect formation is provided using transport phenomena based numerical models. Effects of different AM variables on the formation of these defects are also discussed. However, hierarchical influence of important AM variables on the defect formation is not discussed. A knowledge about hierarchical influence is useful for the engineers to know which variables to tune at first in order to mitigate defects. A recent example is in a parallel field of friction stir welding (FSW) where a data driven machine learning approach is used to find the hierarchical influence of the important factors in FSW on void formation [2]. A similar data driven approach can be used for AM. However, this approach requires creation of a large dataset to train, validate and test the machine learning algorithms and thus is kept for future work.

7.3.3 Expanding the model capabilities

In this research, three-dimensional, transient heat transfer and fluid flow models for three AM processes are developed and used to calculate the fusion zone geometry, temperature and velocity fields. Thermomechanical models are also developed and used for the calculations of residual stresses and distortion. However, these models have several assumptions to make the calculations tractable as discussed in Chapter 3 and 4 of this thesis. There are scopes in future to make these models more rigorous and computationally efficient and thus require further research. In addition, these models need to be tested for different combinations of alloys and process parameter combinations. Broadly, there are four areas that require work to broaden the capabilities of the model and need future work.

- The model assumes conduction mode AM processes where peak temperatures are below the boiling point of the corresponding alloy. However, peak temperature during the process may exceed the boiling point depending on the process parameters. A narrow region of metal vapor forms inside the molten pool which is called a keyhole [3]. Keyhole mode AM processes have been observed for PBF-L [3] and PBF-EB [4]. Instabilities of keyhole causes entrapment of vapors inside the fusion zone and results in keyhole porosity [3] as shown in Figure 7.2 (a). Modeling of keyhole mode AM processes is challenging because of the complex mechanism of formation of keyholes and is kept as a future work.
- The model assumes unidirectional scanning strategies for all three AM processes where scanning directions of the heat source for all layers and hatches are the same. However, in practice, complex scanning strategies are often used to minimize defects or to obtain desired

microstructure and properties [5-7]. For example, Figure 7.2 (b) shows that the displacement of the substrate caused by thermal distortion can be minimized by controlling the scanning strategies [6]. In addition, lack of fusion defects were also minimized by adjusting the scanning pattern [5]. Development of the model for different scanning strategies can be a potential future work.

- Heat transfer fluid flow models are developed for laser and electric arc heat sources. However, electron beam is also widely used as a heat source in both PBF and DED processes [4]. Developing the present heat transfer and fluid flow model for electron beam processes requires significant modeling effort because of the unique characteristics of electron beam heat source, preheating of powder bed and low ambient pressure inside the chamber. Therefore, this development work is kept for future work.
- The thermomechanical model developed in this research calculates residual stresses and distortion from the temperature field accurately estimated by considering convective flow of liquid metal inside the molten pool. There are commercial packages such as Ansys (www.ansys.com), NetFab (www.autodesk.com/products/netfabb/overview) that can calculate residual stresses and distortion for large components. As a future work, results of thermomechanical model of this research can be compared with the corresponding data from those commercial packages to justify the unique capabilities of the model.

7.3.4 Future of AM modeling and digital twin

Transport phenomena based numerical models described in this research can be made bi-directional, so that they can switch between input and output variables. In other words, they can compute a set of process variables necessary to achieve a desired product attribute, such as, part dimensions, microstructure, average grain size, and some simple properties. For example, if attaining a target product attribute requires a particular pool dimension, the model can compute the heat input required to achieve that. The bi-directional feature of models has been demonstrated in welding [8] and can be implemented in 3D printing in future.

Outputs from the transport phenomena models may have errors due to several simplifying assumptions in the model, errors in input thermophysical and thermomechanical property data, especially at high temperatures, and the common numerical errors in large complex calculations. In order to minimize these errors these models can be combined with the advanced statistical models [9]. A statistical model can correct the inaccuracies in the predictions of the numerical models based on previous results from a set of classified records

within a large set of data known as the big data. The machine learning, big data, statistical model, sensing control need to be combined under one framework with the numerical model to construct a digital twin as shown in Figure 7.3. While the utility of the digital twin approach is now widely accepted [10] the construction and testing of a digital twin of metal printing is just beginning and is left as a future work.

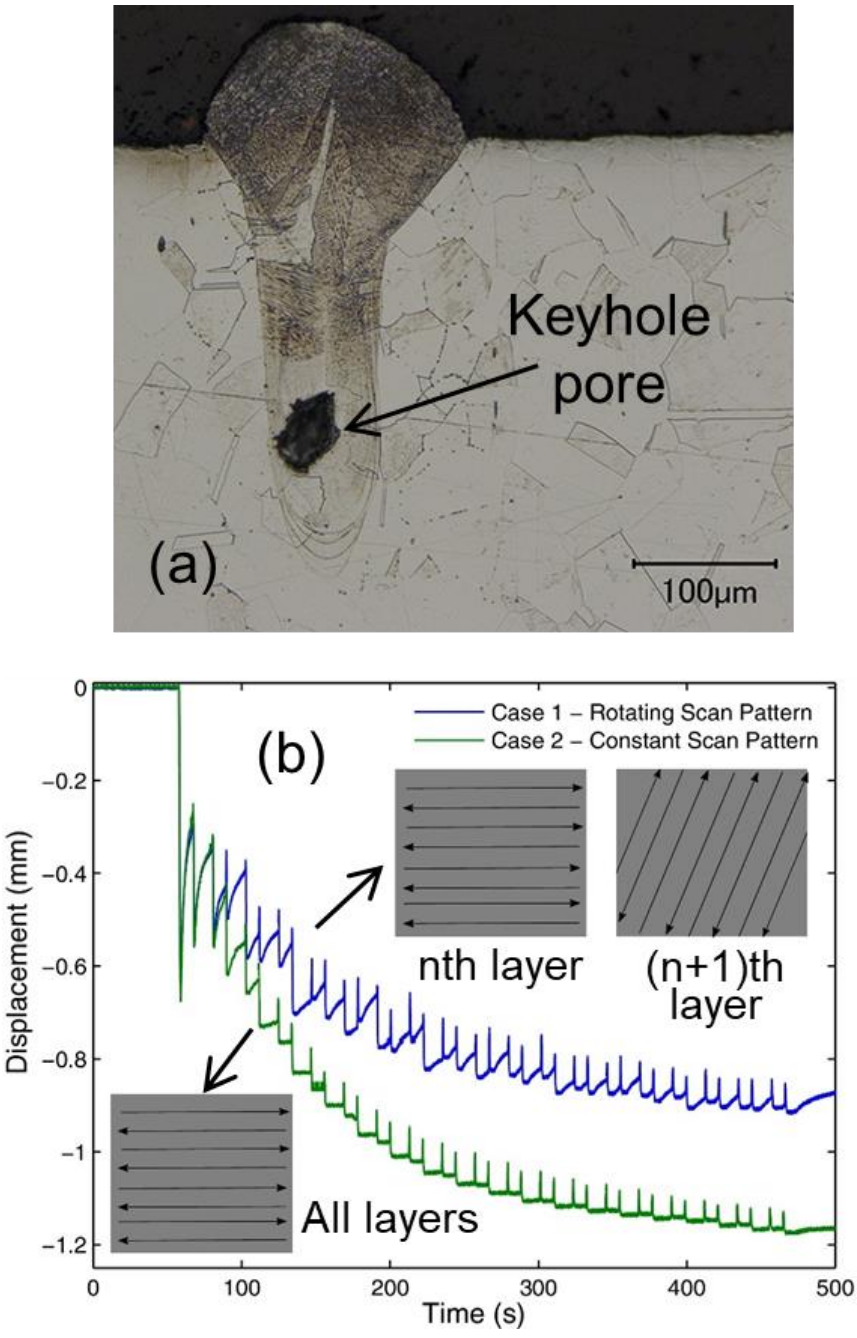

Figure 7.2. (a) Keyhole porosity in PBF-L of SS 316 [3]. (b) Comparison of vertical displacement of substrate due to thermal distortion during PBF-L of Inconel 718 with different scanning strategies [6].

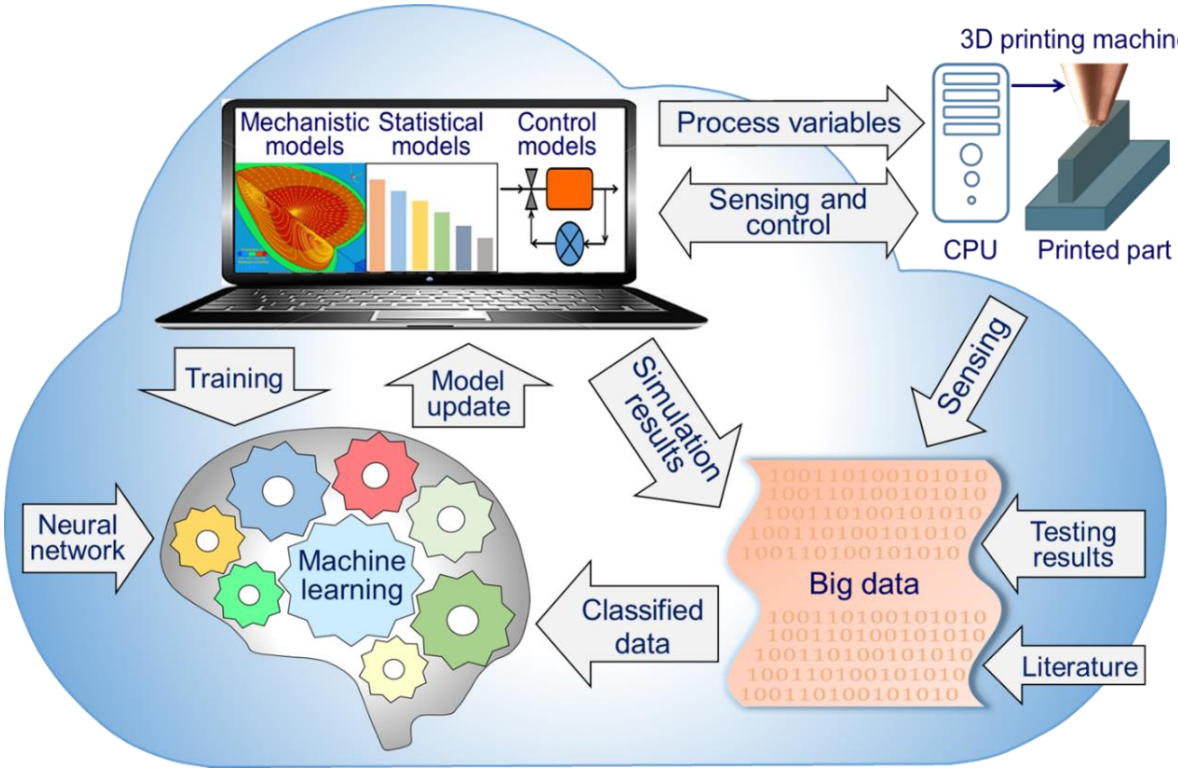

Figure 7.3. Schematic representation of a digital twin of additive manufacturing.

7.4 References

1) L. Johnson et al. Assessing printability maps in additive manufacturing of metal alloys. Acta Mater. 176 (2019) 199-210.
2) Y. Du et al. Conditions for void formation in friction stir welding from machine learning. npj Comput. Mater. 5 (2019) 68.
3) W.E. King et al. Observation of keyhole-mode laser melting in laser powder-bed fusion additive manufacturing. J Mater. Process. Technol. 214 (2014) 2915–25.
4) Y.J. Liu et al. Microstructure, defects and mechanical behavior of beta-type titanium porous structures manufactured by electron beam melting and selective laser melting. Acta Mater. 113 (2016) 56-67.
5) L. Thijs et al. A study of the microstructural evolution during selective laser melting of Ti–6Al–4V. Acta Mater. 58 (2010) 3303-3312.
6) A.J. Dunbar et al. Development of experimental method for in situ distortion and temperature measurements during the laser powder bed fusion additive manufacturing process. Additive Manufac. 12 (2016) 25-30.

7) A.J. Dunbar et al. Comparisons of laser powder bed fusion additive manufacturing builds through experimental in situ distortion and temperature measurements. Additive Manufac. 15 (2017) 57-65.
8) S. Mishra et al. Tailoring gas tungsten arc weld geometry using a genetic algorithm and a neural network trained with convective heat flow calculations. Mater. Sci. Eng. A. 454 (2007) 477–486.
9) T. DebRoy et al. Scientific, technological and economic issues in metal printing and their solutions. Nature Mater. (2019) 1.
10) T. DebRoy et al. Building digital twins of 3D printing machines. Scripta Mater. 135 (2017) 119-124.

VITA

Tuhin Mukherjee

Tuhin Mukherjee was born in Bhatpara, West Bengal, India, on March 19, 1991. In August 2008, he enrolled in the department of Mechanical Engineering at Kalyani Government Engineering College under West Bengal University of Technology, where he was awarded the degree of Bachelor of Technology in July 2012. After that, he began graduate study in the department of Mechanical Engineering at Indian Institute of Technology, Bombay and he was awarded the degree of Master of Technology in July 2014. In the spring of 2015, he joined the Pennsylvania State University to pursue doctoral study in Materials Science and Engineering under the guidance of Professor T. DebRoy. He was awarded by American Welding Society Graduate Research fellowship in 2015 and Robert E. Newnham Research Excellence Award by Penn State University in 2017. He is also a member of American Welding Society (AWS). His list of publications is shown below.

1) T. DebRoy, T. Mukherjee, J.O. Milewski, J.W. Elmer, B. Ribic, J.J. Blecher, W. Zhang. Nat. Mater. 2019, DOI: 10.1038/s41563-019-0408-2.
2) Y. Du, T. Mukherjee, T. DebRoy. npj Comp. Mater. 2019, 5 (68).
3) Q. Wu, T. Mukherjee, C. Liu, J. Lu, T. DebRoy. Add. Manuf. 2019, 29, 100808.
4) T. Mukherjee, T. DebRoy. Sci. Technol. Weld. Join. 2019.
5) T. Mukherjee, T. DebRoy. Appl. Mater. Today. 2019, 14, 59-65.
6) H.L. Wei, G.L. Knapp, T. Mukherjee, T. DebRoy. Add. Manuf. 2019, 25, 448-459.
7) T. Mukherjee, T. DebRoy. J Manuf. Process. 2018, 36, 442-449.
8) W. Ou, T. Mukherjee, G.L. Knapp, Y. Wei, T. DebRoy. Int. J Heat Mass Trans. 2018, 127, 1084-1094.
9) T. Mukherjee, H.L. Wei, A. De, T. DebRoy. Comp. Mater. Sci. 2018, 150, 304-313.
10) T. Mukherjee, H.L. Wei, A. De, T. DebRoy. Comp. Mater. Sci. 2018, 150, 369-380.
11) T. Mukherjee, J.S. Zuback, W. Zhang, T. DebRoy. Comp. Mater. Sci. 2018, 143, 325-337.
12) T. DebRoy, H. L. Wei, J.S. Zuback, T. Mukherjee, J.W. Elmer, J.O. Milewski, A.M. Beese, A. Wilson-Heid, A. De, W. Zhang. Prog. Mater. Sci. 2018, 92, 112–224.
13) G. L. Knapp, T. Muhkerjee, J. S. Zuback, H. L. Wei, T. A. Palmer, A. De, T. DebRoy. Acta Mater. 2017, 135, 390-399.
14) T. Mukherjee, V. Manvatkar, A. De, T. DebRoy. J Appl. Phys. 2017, 121, 064904.
15) T. Mukherjee, W. Zhang, T. DebRoy. Comp. Mater. Sci. 2017, 126, 360-372.
16) T. Mukherjee, V. Manvatkar, A. De, T. DebRoy. Scripta Mater. 2017, 127, 79-83.
17) T. Mukherjee, J. S. Zuback, A. De, T. DebRoy. Sci. Rep. 2016, 6, 19717.